ADVANCED ANALYSIS AND DESIGN OF AXIAL COMPRESSION MEMBERS WITH HIGH-STRENGTH STEEL

LI TIANJI

Ph.D

The Hong Kong Polytechnic University

This programme is jointly offered by

The Hong Kong Polytechnic University and Tongji University

2015

The Hong Kong Polytechnic University

Department of Civil and Environmental Engineering

Tongji University

College of Civil Engineering

Advanced Analysis and Design of Axial Compression Members with High-Strength Steel

LI Tianji

A Thesis Submitted in

Partial Fulfillment of the Requirements for

the Degree of Doctor of Philosophy

December 2014

CERTIFICATE OF ORIGINALITY

I hereby declare that this thesis is my own work and that, to the best of my knowledge and belief, it reproduces no material previously published or written nor material which has been accepted for the award of any other degree or diploma, except where due acknowledgement has been made in the text.

_____________________________ (Signed)

LI Tianji (Name of student)

To my wife & parents

for their love and encouragements

ABSTRACT

High-strength steel is a term usually applied to specific types of steel that have a design yield strength larger than 460 MPa, distinguishing it from the other types of steel having lower strength. Its adoption has become popular in the past decade, initiating certain benefits in fabrication, construction, cost, and so on. Not only does using high-strength steel dramatically reduce the section sizes of members associated with material consumption and member weight, it also considerably alleviates the difficulties in buildmanship and accelerates construction. This can significantly benefit construction in high density urban areas, such as Hong Kong, Shanghai, and New York, where the labor cost is usually more expensive than the material cost. Consequentially, high-strength steel can be viewed as environmental friendly because its use reduces material consumption, thereby decreasing carbon dioxide release.

Although high-strength steel is mass-produced and is widely used in mechanical engineering, its utilization in building construction is still under exploration due to the lack of consummate design and analysis approaches. The current design codes for steel columns used worldwide, e.g., ANSI/AISC 360-10, Eurocode 3 Part 1-1, Hong Kong Code 2011, and China GB50017-2003, mostly provide the formulae and charts for steel with a design yield strength less than 460 MPa, resulting in obstacles in the design and application of high-strength steel members. Eurocode 3 Part 1-12 simply extends the use of high-strength steel to grade S 700. This thesis aims to propose a direct analysis and design approach for high-strength steel members, thereby eliminating the use of the tedious charts and formulae associated with linear elastic assumptions.

By using high-strength steel, the sectional sizes of members can be dramatically reduced and the stability problems associated with the second-order effects would be dominated, which should be properly reflected in the design. In the present study, the pointwise equilibrium polynomial (PEP) element is employed to model the beam-column members and to simulate the P-δ effects due to initial member curvatures. Adopting the high-order shape function for the PEP element and considering the bowing effects, one element per member is sufficient and accurate for nonlinear elastic analysis. Therefore, member design can be simply executed by checking the section strength at critical locations.

For a more accurate representation of the section capacity, the sectional yield surfaces are introduced, which are expressed by a series of strength points in a bi-axial loading space. Two types of surfaces are presented: initial and failure surfaces. These are generated by a cross-sectional analysis technique based on the quasi-Newton algorithm. The sections are automatically meshed into small triangular fibers. This method is valid for arbitrary shapes of the steel sections. The elastic and plastic limit states of a section can be described by the initial yield and failure surfaces, respectively.

To explicitly consider the influences of residual stress, the cross-sectional analysis technique is further developed to take this effect into account. The initial stress inherent in a section is reflected by introducing the residual strains applied to each fiber; therefore, the numerical algorithm can be easily modified on the basis of the current available programs.

Consequentially, residual stress models are vital for the cross section analysis. In real-time applications, Q690 high-strength steel shows a non-negligible potential in applications; however, its residual stress distribution patterns are still being explored and they are seldom reported in the available literature. In this thesis, the magnitudes and distributions of six box and H columns, fabricated by Q690 high-strength steel, will be investigated using the sectioning method. The residual stress patterns on column sections are examined and presented. To simplify the analysis, straight-line models of Q690 high-strength steel are first proposed on the basis of the experimental investigations, which can be further applied to the analysis of the other sections with ranged width-to-thickness or height-to-thickness ratios.

To fulfill the design requirements for simulating the structural behaviors under extreme scenarios, such as progressive collapse analysis, performance-based seismic design, the vital effects inherent to the structural members should be reflected. The P-Δ and P-δ effects related to the frame out-of-plumpness and initial member curvatures, respectively, are directly considered by employing the curved PEP element with the high-order shape function. The influence of residual stress is reflected by explicitly calculating in the cross-section analysis. In addition, a refined plastic hinge model is introduced in order to consider the gradually yielding behaviors at the critical sections. From the present study, it can be observed that the residual stress exerts certain influences on controlling the sectional elastic limit that might cause the fiber to start yielding at a low stress state.

Differing from the conventional method, where the equivalent imperfection is adopted combing initial member curvatures and residual stresses, the proposed method separately considers these two vital effects. Therefore, the design can be more accurate, safe, and economical thereby eliminating the empirical and uncertain considerations found in the conventional design method.

To verify the accuracy and versatility of the proposed method, six fabricated box columns and six welded H columns with different slenderness ratios ranging from 30 to 70 are axially-loaded and studied. All of the columns were prepared by the flame-cut Q690 steel plates with a thickness equal to 16 mm. The numerical simulations of the specimens obtained by the proposed method are presented and compared with the outcomes of the experiments, showing satisfactory results in the comparisons in terms of tracing the load vs. deflection and predicting the ultimate strength.

Extensive research studying the overall buckling behavior of the Q690 columns with different slenderness ratios is conducted, and 132 nos. and 192 nos. columns with box and H sections, respectively, are analyzed by the proposed method. These results are compared with the conventional buckling curves in codes, e.g., GB 50017-2003, Eurocode 3, and ANSI/AISC 360-10. The comparisons show that the axial strengths of the high-strength columns are underestimated, especially for the members with low slenderness ratios. This further proves the importance and necessity of developing an efficient and practical method for the design of high-strength members; otherwise, the material utilization efficiency could be reduced.

To propose an efficient and practical method for the design of high-strength steel members, a second-order design method, based on ANSI/AISC 360-10, is proposed by revising the stiffness reduction factor for a more proper reflection of the residual stress. The optimal design formulae for high-strength steel members are proposed on the basis of an extensive study comprised of over 300 columns.

In this thesis, an efficient advanced analysis and practical second-order design method for structures with high-strength steel members is proposed. A cross-section analysis technique with an explicit consideration of residual stresses is developed. Strength-line models for describing the residual stress patterns of H and box sections fabricated by Q690 steel plates are first proposed. The curved PEP element is employed to simulate the initial member curvature and capture the large deflection effect. A refined plastic hinge model using the sectional surfaces is used to model the inelastic behavior at the gradually yielding sections. Twelve columns are experimentally investigated to verify the proposed theory and extensive research on over 300 nos. columns is conducted. A refined second-order design approach, based on ANSI/AISC 360-10, for high-strength steel members is proposed.

PUBLICATIONS

Journal Papers:

1) Tian-Ji Li, Si-Wei Liu, and Siu-Lai Chan (2015), Cross-sectional analysis of arbitrary sections allowing for residual stresses, *Steel and Composite Structures*, 18(4), 985-1000.

2) Tian-Ji Li, Si-Wei Liu, and Siu-Lai Chan (2014), Direct analysis for high-strength steel frames with explicit-model of residual stresses, Engineering Structures (Submitted).

3) Tian-Ji Li, Guo-Qiang Li, and Yan-Bo Wang (2014), Residual stress tests of welded Q690 high-strength steel box and H-sections, Journal of Constructional Steel Research (Submitted).

Conference Papers:

1) Tian-Ji Li and Guo-Qiang Li, *Studies on residual stress of welded Q690 high strength steel box sections*, The Pacific Structural Steel Conference (PSSC 2013), Singapore, 8 - 11 October 2013.

ACKNOWLEDGEMENTS

The author would like to express his sincere appreciation to his supervisors, Professor S.L. Chan and Professor G.Q. Li, not only for their enlightening guidance, continued support and encouragement throughout this study, but also for their invaluable suggestions on the future work and life. Their broad and deep knowledge in academic fields and engineering problems, sincere attitude and research enthusiasm have encouraged the author.

The author wishes to express his upmost gratitude to Dr. Y.P. Liu, Dr. S.W. Liu and Dr. Y.B. Wang for their valuable suggestions and warmest helps for my research over the past years. Furthermore, much assistance in experimental works provided by Dr. D.H. Wen, Dr. X.L. Yan, Mr. Z.L. Wang, Mr. W.Y. Liu, Mr. H.J. Wang, Mr. X. Sun and Mr. Q. Zhu are gratefully acknowledged.

The author would like to thank The Hong Kong Polytechnic University for providing the financial support during his PhD study.

The author would like to thank the NIDA team members, involving Dr. Z.H. Zhou, Mr. Sam Chan, Mr. Y.Q. Tang, Miss H. Yu, Miss L. Jiang, Mr. R. Bai, Mr. Z.L. Du, Miss W.Q. Tan, and Mr. J.W. He for their great help and constructive discussions. Many thanks also go to the author's friends and colleagues in Tongji University of Shanghai for their generous help during the research life.

Finally, the author would like to express his deepest gratitude to his wife and parents for their patience, unconditional love, support and encouragement all the time.

CONTENTS

LIST OF FIGURES

LIST OF TABLES

LIST OF SYMBOLS

a_i	Coefficients in the polynomial function
A	Cross-section area
A_i	Cross-section area in the individual plate strips or fibers
b_f	Width of outstanding flange
B	Width of flange
c	Specific heat
d_n	Depth of a neutral axis in a section
d_{nk}	Depth of an updated neutral axis
e	Axial shortening of an element
e_0	Eccentricity of members
E	Young's modulus of steel
EA	Axial rigidity
EI	Flexural rigidity
f_y	Yield stress of steel
f_u	Ultimate tensile stress of steel
f_e	Elastic buckling stress
f_{cr}	Critical stress
f_1, f_5	Width of tensile zones on flanges
f_2, f_4	Width of transition zones on flanges
f_3	Width of compressive zones on flanges
h	Height of webs

h_w	Thickness of a weld line
h_f	Fillet weld size
H	Height of an H-section
I	second moment of area
I_v	second moment of area for the minor axis
I_u	second moment of area for the major axis
K_{ij}	Stiffness coefficients of an element
L	Length of members
L_e	Effective length of members
M_u, M_v	Flexural moments about the u and v axes
M_y, M_z	Flexural moments about the y and z axes
M_{er}, M_{pr}	Initial and full yielding moments under axial force
M_1, M_2	Moments at element end 1 and 2
N_d	Design axial load
N_x	Axial force by referring to uov coordinate system
N_{xd}	Current design axial load
N_1, N_2	Shape function parameters for perfectly straight element
q_w	Heat input per unit welded length
S	Initial arc-distance in the arc-length method
S_{s1}, S_{s2}	Spring stiffness at nodes 1 and 2
S_s	Sectional spring stiffness
S_k	Current stiffness parameter
t	Thickness of steel plates

t_f, t_w	Thickness of flanges and webs
T_0	Initial temperature
u	DOFs in an element, or the coordinates in uov system
u_i	Displacement vector
U	Strain energy
v	Lateral displacement function of an element, or the coordinates in uov system
v_0	Lateral initial deflection
v_{mo}	Amplitude of initial deflection at mid-span
V	Work done by external forces
w_1	Width of tensile zones on webs
w_2	Width of transition zones on webs
w_3	Width of compressive zones on webs
x, y, z	Coordinates in local system
X, Y, Z	Coordinates of an element at the original position
Y_i, Z_i	Centroid coordinates of the *i*-th plate strips
Y_{gc}, Z_{gc}	Coordinates of geometric centroid of an entire section
α	Tensile residual stress ratios, or imperfection factor for corresponding buckling curve
α_1, α_2, α_3	Factors corresponding to the appropriate types of cross-sections
β	Compressive residual stress ratios
γ	Parameter to control load magnitude

γ_R	Partial factor for resistance
γ_{M1}	Partial coefficient for the resistance of members to instability assessed by member checks
δ	Lateral deflection of members
δ_0	Pre-determined displacement increment as the steering DOF
$\Delta\%$	Percentage of elongation after rupture
ΔL	Axial deformation increment
ΔP	Axial force increment
ΔM_b	Incremental nodal moments between sectional spring and beam
ΔM_s	Incremental moments of nodes at the joints between sectional spring and global node
$\Delta_m\bar{u}_1$	Displacement vector related to a load parallel to the applied loads
$\Delta_m\bar{u}_i$	Load increment given unbalanced force during iterations
$\Delta\theta_b$, $\Delta\theta_s$	Incremental rotations of nodes associated with the incremental nodal moments
ε	Strain
ε_u	Ultimate strain
ε_{ai}	Axial strain
ε_{ri}	Strain due to residual stresses
θ_1, θ_2	Rotations of an element at nodes 1 and 2

θ_n	Orientation angle of neutral axis
λ	Slenderness ratios
λ_v, λ_u	Slenderness ratios about the minor and major axes
$\overline{\lambda}$	Nondimensional slenderness ratios
$\overline{\lambda}_v$, $\overline{\lambda}_u$	Nondimensional slenderness ratios about the minor and major axes
ρ_0	Steel density
σ	Stress
σ_i	Related stresses that consider residual stresses
σ_{rt}, σ_{rc}	Residual tensile and compressive stresses
σ_{frt}, σ_{frc}	Residual tensile and compressive stresses on the flanges
σ_{frte}	Residual tensile stresses on the flange tips
σ_{wrt}, σ_{wrc}	Residual tensile and compressive stresses on the webs
τ_b	Flexural stiffness reduction factor
ϕ_c	Resistance factor in axial compression columns
ϕ_i	Curvature of strain distribution curves
χ	Reduction factor for overall buckling

CHAPTER 1

INTRODUCTION

1.1. Background

In 2013, consumption of steels in China increased to 701 million tons occupying 90% of total production of crude steel (WSA, 2014). According to statistics from MIIT (Ministry of Industry and Information Technology of the People's Republic China), steel consumption in building industry has accounted for 55.5% of global steel consumption (MIIT, 2014). The information of other industries is shown in Figure 1.1. Before 1990s, the yield stress of primary structural steel for buildings and bridges was between 235 to 275 MPa. In the following decades, however, the yield stress of the steel for buildings and bridges was upgraded to approximately 345 MPa (Bjorhovde, 2004; Veljkovic and Johansson, 2004). Refer to statistics in 2010, the consumed moderate steel plate was reached to 60% in China market, where five grades were widely selected as Q235 (31%), Q345 (62%), Q390 (4%), Q420 (2%), and Q460 (1%) (Wang, 2012).

With the construction of some large steel structure buildings, like the Beijing National Stadium, the CCTV new building, Shanghai World Financial Center, etc., steel products for buildings get dramatic progress in manufacture process, which promote the development and application of the high-strength and performance steel plates of moderate thickness. However, there are many problems in development and application of steel products for buildings including the lower level of development capabilities in new kind of steel products and application technology compared to developed countries, the lower consumption level of high-strength and performance steel applied in building market bringing about the higher amount of steel per unit area, etc. High-strength steel plates (yield strength, 690 MPa) are available in buildings market in China to date with the advance of metallurgical science and technology while high-strength steel plates (1100 MPa) can be gained in developed countries (Veljkovic and Johansson, 2004). Therefore, it is that the gap of using high-strength steel with developed countries cannot be ignored.

1.1.1. Economy and benefits of utilizing high-strength steels

Economic benefits brought about by using high-strength steel is decided largely whether the steels gain ground in building market. A factor for economy is that the strength of high-strength steel can be used effectively. Haaijer (1963) discussed economy of high-strength steel structural members and considered that through the proper design of structural members, the utilization of higher strength steels can give rise to lighter weight structures and frequently to significant material cost savings as well. Collin and Johansson (2006) indicated that the price of structural steel often increases with its strength, as shown in Figure 1.2. The figure illustrates that the trend curve follows the square root of the yield strength. At the same time, they manifested that if the strength can be completely applied, the cost of material will be lowered as the strength is enhanced (see Figure 1.3). In Figure 1.3, it is observed that the material cost from high-strength steels is lower than ordinary steels under same loads.

Raoul and Günther (2005) compiled several references into a book which includes application and investigation of high-strength steel in United States, Canada, Japan and Europe. And they considered that weight reduction can arrive at 20% for medium and long span bridges applying high-strength steels. Long *et al*. (2011) fully investigated the economic interest of the utilization of high-strength steel and normal steel circular in steel and composite columns submitted to static loads. The comparison is based on an optimum design taking into consideration the strength, stability and stiffness conditions. It turned out that the use of high-strength steel becomes economical. In Tominaga's study of bridge high-performance steels (BHS) in Japan, he and his companions demonstrated that about 3% of steel weight and 12% of fabrication cost were decreased through the large scale utilization of BHS to the Tokyo Gate Bridge project (Tominaga *et al.*, 2011). It is noted above that the economic interest of using high-strength steel in buildings and bridges is related to the type of structures, the load distribution form in structures or members, the fluctuation of steel price in different place or time, etc. If employing high-strength steel in tension members or no buckling failure members, the economic benefits will be greater.

Using high-strength steel products not only decreases the construction cost, but also solves some problems in design and construction. These problems are as follows：

1) Compared with ordinary steel products, applying high-strength steel products can reduce the sectional dimension under the same load and consequently drop the consumption of steels. For some larger loaded members, the weight of members can be reduced by applying high-strength steel, which leads to easier handling and transportation and smaller butt weld volume.

2) The structural weight and the foundation load from the upper structure can be declined as a result of utilizing high-strength steel in high-rise buildings. Earthquake action is also weakened in buildings, which contributes to economic seismic design.

In 2013, 380 million tons steels were applied in building industry of China (MIIT, 2014). If high-strength steel can gain ground in China, the consumption of steel products and energy per unit building area must be markedly declined, which is greatly significant to economic benefits and environmental conservation.

1.1.2. Application of high-strength steel in the world

In recent years, high-strength steels have been used in some fields involving building structure, bridge, transmission tower, etc. in Japan, America, Europe and China.

(1) Building structures

High-strength steel (yield strength is between 460 and 690 MPa) has been partially applied in engineering practice, e.g. Sony Center in Berlin, Latitude Tower in Sydney, Star City in Darling Harbour of Sydney, NTV Tower in Tokyo, JR East Main Office in Tokyo, Landmark Tower in Yokohama, Tokyo Skytree, and Otemachi 1-6 Project, which leads to good economic benefits, as shown in Figure 1.4-Figure 1.10 (Raoul and Günther, 2005; MEng, 2006; Shi *et al.*, 2008; Morita *et al.*, 2011).

As shown in Figure 1.11-Figure 1.13, high-strength steel productions (nominal yield strength, 460 MPa) was applied in Beijing National Stadium, CCTV New Building, Shanghai World Financial Center, and Ping'An International Finance Center (under construction), which leads to reduction of thickness of plates and butt weld volume (Chen, 2007; Shi *et al.*, 2008).

(2) Bridge engineering

Refer to Raoul and Günther (2005), in 1990s, many State Departments of Transportation (DOT), including Nebraska DOT, Tennessee DOT and Pennsylvania DOT, have designed and constructed HPS bridges, which promoted the application of high performance steel in bridges. High-strength steels (S460) have been used in Rhine Bridge Düsseldorf-Ilverich of Germany (1998) and Millau Viaduct (2001), as shown in Figure 1.14 and Figure 1.15. Hybrid girder bridge was made in Sweden (Veljkovic and Johansson, 2004; Collin and Johansson, 2006). High-strength steels (S690) were applied in the bottom flange. For the composite highway bridge near Ingolstadt, the semi-rigid connections between the composite piers and steel girders lamellas used high-strength steels (S690QL), which solved some problems about stiffness and strength in design (Collin and Johansson, 2006). Fast Bridge 48 was made of super-high-strength steels (S960 and S1100) in Sweden (Raoul and Günther, 2005; Collin and Johansson, 2006). The bridge reduced greatly weight and fabrication costs. Tokyo Gate Bridge (see Figure 1.16), completed in 2011, utilizes high performance steels (SBHS500), the main span of which is 760 m long (Miki and Kawakami, 2011; Tominaga *et al.*, 2011).

(3) Other structures

According to State Grid Information Network (SG, 2009), Q460 steels were used in towers of the transmission line between Jiao Zuo and Xin Xiang. Utilizing Q460 steels in transmission towers declines 9.4% of the global weight and 2% of the cost per unit. LI *et al*. (2008) evaluated the application of Q460 steels in transmission towers and obtained the result of 5-10% weight savings and 1-8% the total cost reduced.

High-strength steels can also be well employed in the market of offshore platforms, oil and gas transmission pipelines, pressure vessels, automobiles, etc. Lücken *et al*. (2008) discussed the benefits of applying high-performance steel in ships and offshore platforms. Corbett *et al*. (2003) investigated the economic interests of using X120 (Grade 825) in oil and gas transmission pipelines. They considered that utilization of X120 in higher pressure can reduce 5-15% of global cost and provide methods of achieving these savings as well.

1.2. Problem statements

In order to promote more uses of high-strength steel, it is significantly important to know disadvantages concerning material property of high-strength steels. According to material test data existed, the yield ratio increases with the rise of the yield strength while the elongation after fracture declines with the rise of the yield strength. The length of yield plateau observed in the stress-strain curve becomes shorter or vanishes, which leads to unapparent strain hardening effects compared with ordinary steel, as seen in Figure 1.17 (Fukumoto, 1996).

Because of differences between high-strength steel and ordinary steel, the investigation based on the utilization of high-strength steel includes three phases, which are as follows:

1) Initial geometrical imperfection, residual stress and material mechanical properties should be investigated because they greatly impact on ultimate capacity of members. Due to the difference of the stress-strain curve between high-strength steel and ordinary steel, the effects of residual stress and initial geometrical imperfection are also diverse (Ban *et al.*, 2008; Li *et al.*, 2011).
2) Compared to ordinary steel, the yield ratio and elongation after fracture of high-strength steel are negative, which will affect the deformation capacity of members. In terms of plastic design, it is important to note that the ductlity and deformation capacity are very significant. Consequently, these aspects should be well studied and improved for high-strength steel members.
3) Enough ductlity is required in seismic design as well. In addition, utilizing high-strength steel in right structural layout that contributes to consume energy from earthquake should be discussed.

1.3. Objectives

The primary objective of the research project is to research and promote the application of high-strength steel in structures and bridges. To this, the research project aims to investigate the material properties and the basic mechanical behavior of Q690 high-strength steel members. Furthermore, this thesis tends to discuss the residual stresses distribution on the box and H members and propose the stress models for numerical simulation of the steel members. An advanced analysis method that is suited for Q690 welded box and H members is presented and applied in a parametric study. The method can account for residual stresses and initial geometric imperfections separately. Finally, the effects of certain factors (i.e., residual stress and geometric imperfections) on ultimate capacity of the members are discussed. Some recommendations of the first-order linear design method specified in some codes are provided and a second-order elastic design method based on the advanced analysis method is proposed.

The research objectives can be summarized below:

1) To propose an advanced analysis method and a second-order elastic design method for design of high-strength steel members under axial compression members. In the advanced analysis method, an efficient sectional analysis technique for arbitrary built-up sections with consideration of residual stress effects is developed on the basis of quasi-Newton iterative scheme.
2) To determine the residual stress distribution of box and H columns fabricated from Q690 steels via an experiment study on the stress measurment and propose the stress models for the columns. The models are applied into the proposed method.
3) To investigate the overall buckling behavior of the welded columns under axial compression and discuss the mechanical behavior of the columns with varied width-to- thickness and slenderness ratios.

4) To employ the advanced analysis method to the columns and verify the accuracy and efficiency of the proposed method and traditional codified method against the experiments.
5) To implement parametric analysis via the proposed method accounting for the effects of certain factors on ultimate capacity of Q690 welded box and H columns and present some design recommendations for the columns; to promote the application of Q690 high-strength steel in engineering practice.

1.4. Layout of the thesis

The outline of this thesis is presented as follows:

Chapter 1 presents the background of the research project. The economy, benefits and problems of utilizing high-strength steel in engineering are discussed. And then, the objectives and the layout of this research project are given as well.

Chapter 2 widely reviews the development of the material properties, bearing capacity and deformation capacity of high-strength steel, the structural behavior of welded joints and bolted joints, seismic behavior of material and members in recent decades. The advance of beam-column elements for nonlinear analysis and design are also reviewed.

Chapter 3 introduces several methods for measuring residual stresses. The chapter also presents the residual stress magnitude and distribution of the welded box and H section (Q690) through sectioning method. Idealized models of the residual stress based on the test result is proposed.

Chapter 4 covers the experiment investigation of welded box and H columns (Q690) under axial compression. In this chapter, the experimental results are discussed and the data from the experiment is compared with the results from existed design codes, which is used to confirm the feasibility of the codes for the columns.

In Chapter 5, an advanced analysis method for design of welded high-strength steel box and H members is proposed. In order to explicitly allow residual stresses, an efficient cross-sectional analysis method for arbitrary welded sections is developed on the basis of quasi-Newton iterative scheme. PEP element allows for the effects of initial member imperfection and geometrical nonlinearity. The effects of material nonlinearity are considered in the refined plastic hinge approach. Two examples concerning Q460 welded box and H columns are used to validate the accuracy of the method.

Chapter 6 carries out the numerical simulation concerning the experiment of Q690 welded box and H members under axial compression by the proposed advanced analysis method. During the simulation, the residual stress models are selected as the models proposed in Chapter 3 and the initial geometric imperfections are determined from the realistic measurement. Then, parametric analysis is conducted to reveal the effects of certain factors on ultimate bearing capacity of the columns. The results from the analysis are compared with those from traditional codified method. Some recommendations for design of Q690 high-strength steel columns with welded box and H sections is proposed. Finally, a direct analysis method (second-order elastic design method) is proposed and validated against the proposed advanced analysis method.

Finally, Chapter 7 summarizes the findings of this thesis and highlights the significance of the research project. Suggestions and recommendations for future works are provided.

Figures

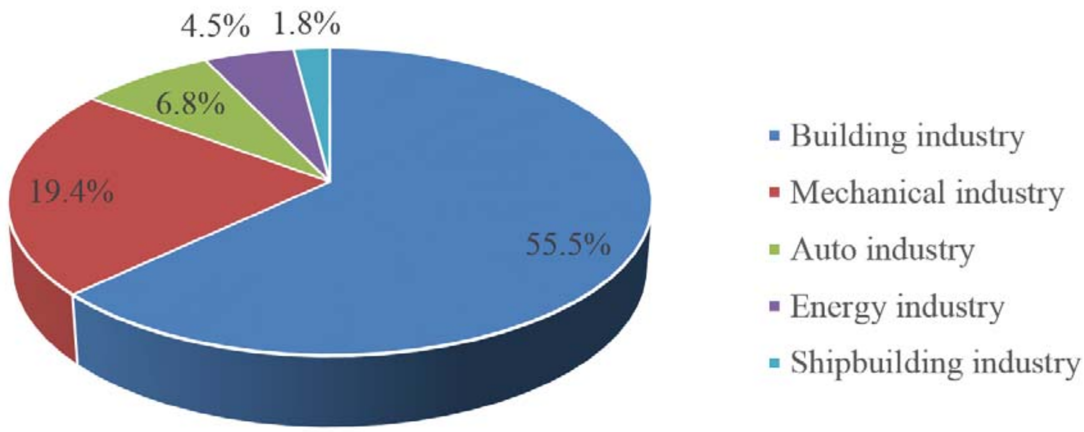

Figure 1.1 Steel consumption proportions (MIIT, 2014)

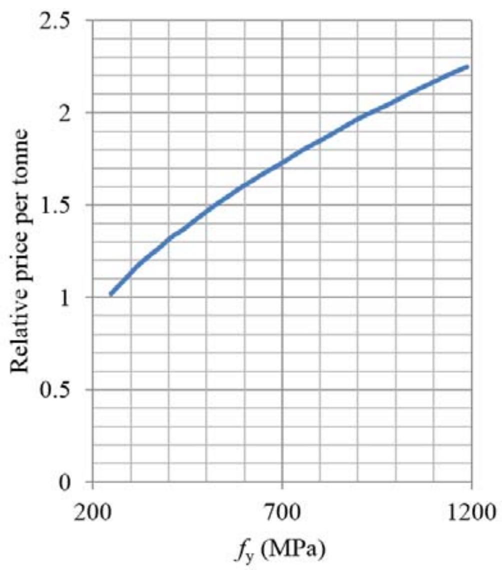

Figure 1.2 Relation between unit price and yield strength (Collin and Johansson, 2006)

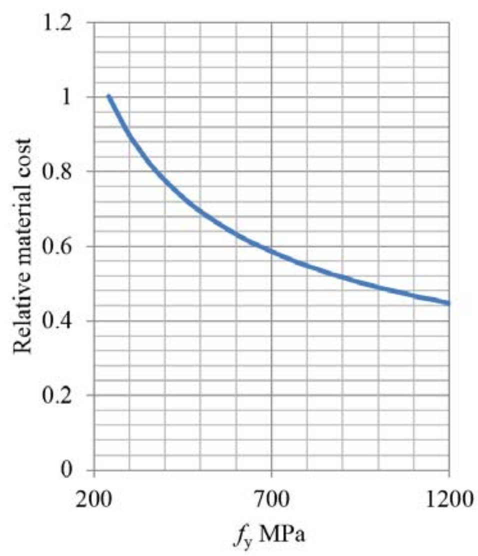

Figure 1.3 Relation between material cost and yield strength (Collin and Johansson, 2006)

Figure 1.4 Sony Center (Lindner, 2005)

Figure 1.5 Latitude (Ernst & Young) Tower (Randwicked, 2005)

Figure 1.6 Star City (Saberwyn, 2011)

Figure 1.7 NTV Tower (Tyoron, 2006)

Figure 1.8 JR East Japan Main Office (Ons, 2006)

Figure 1.9 Yokohama Landmark Tower (Tyoron, 2008)

Figure 1.10 Tokyo Skytree (Kakidai, 2012)

Figure 1.11 Beijing National Stadium (Peter, 2011)

Figure 1.12 CCTV New Building (Proffer, 2008)

Figure 1.13 Shanghai World Financial Center (LERA, 2014)

Figure 1.14 Rhine Bridge Düsseldorf-Ilverich (Michael, 2006)

Figure 1.15 Millau Viaduct (Capper, 2008)

Figure 1.16 Tokyo Gate Bridge (Tashiro, 2011)

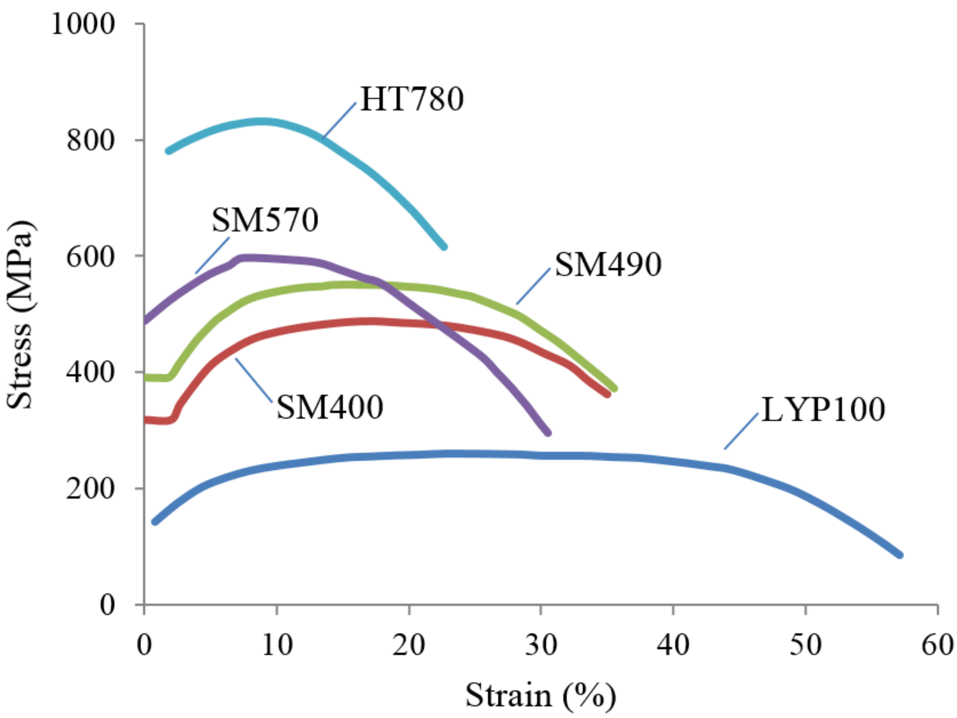

Figure 1.17 Stress-strain curves of different steel grades (Fukumoto, 1996)

CHAPTER 2

LITERATURE REVIEW

This chapter presents a review on the research and investigation of high-strength steel products. Generally, the steel strength is able to be enhanced by the addition of beneficial chemical elements in steel products, the control of heat treatment or cold hardening processes. The steel products are categorized by the type of processes as different processes give rise to diverse mechanical behavior. The study of stability is particularly important for the basic high-strength steel members. The seismic performance of the steel members or structures is also a key point which has a significant influence on the application of high-strength steel in multi-story and high-rise steel structures. Moreover, the reviews on the advance of beam-column elements for nonlinear analysis are presented and the characteristics of some elements are discussed. The plastic hinge and the plastic zone methods are reviewed, which are used to account for material nonlinearity.

2.1. Study of residual stresses

Residual stresses due to the non-uniform distribution of plastic or thermal strains can reduce the ultimate capacity of steel members under compression and the fatigue resistance of the members under cyclic or dynamic loads. An accurate distribution of the stresses is necessary for numerical simulation and design of high-strength steel members or structures. Odar and Nishino (1965) presented the residual stress distribution of box and H sections fabricated by A514 steels. Nishino *et al*. (1967) and Usami and Fukumoto (1982, 1984) experimentally studied the local stability of welded box columns made of high-strength steels (A514 and HT80 steels), and obtained the distribution of residual stresses. Rasmussen and Hancock (1992, 1995) carried out the experiments concerning local and overall stabilities of high-strength steel columns (nominal yield strength, 690 MPa), and presented the residual stress distribution of welded box, H, and cruciform sections. The focus of these studies is mainly on the local stability of columns with large plate slenderness ratios, and no simplified residual stress model is provided.

Wang *et al*. (2012a, 2012b) measured the residual stress distribution of welded box and H sections made of Q460 steels via two methods (the sectioning method and hole drilling method) and provided the stress models for the sections. Lee *et al*. (2012a, 2012b) adopted the hole-drilling method to determine the residual stress distribution of thin-walled T and Y joints welded with RQT701 high-strength steels and established a numerical modeling for parametric analysis. Ban *et al*. (2013a) experimentally investigated the residual stresses of box sections fabricated from Q460 steels and presented an ideal model of the sections. Kim *et al*. (2014) carried out an experimental investigation on the local buckling behvior of H stub columns fabricated by HSA800 high-strength steels and utilized the non-destructive indentation method to measure the residual stress distribution of the columns. Lee *et al*. (2014a, 2014b) studied the residual stress distribution near the weld of box T-joints made of high-strength steels (nominal yield stress is 690 MPa) by the hole-drilling method. They discussed the stress distributions of the joints under the different welding processes (i.e., with preheating and without preheating) and executed numerical study on the joints by the finite element method. Ma *et al*. (2015) experimentally investigated the residual stress distributions of cold-formed high-strength steel hollow sections including square, rectangular, and circular sections. The nominal yield strength of the steel plates were 700, 900, and 1100 MPa. The longitudinal and transverse residual stresses on the sections were measured.

2.2. Mechanical behavior of materials

The difference between high-strength steels and ordinary steels in the mechanical behavior of materials is significantly important to the application of high-strength steel in structures. In the 1960s, the quenched and tempered (Q&T) steel products were occurred in the market of Japan and USA. In Japan, high-strength steels (tensile stress, 600 MPa) were initially utilized in bridges in 1960 and the occurrence of steels with 800 MPa tensile stress was in 1964 (Raoul and Günther, 2005). Two years later, the steels were standardized as JIS SM58 (now equal to SM570). In United States, the first ASTM standard was A514 (yield strength, 690MPa) in 1969 (Bjorhovde, 2004). The material test data were successively obtained from the investigation concerning basic members of high-strength steel in Japan, America, Australia and Europe (Nishino *et al.*, 1967; McDermott, 1969a, 1969b; Usami and Fukumoto, 1982; Usami and Fukumoto, 1984; Rasmussen and Hancock, 1992, 1995; Beg and Hladnilk, 1996). In terms of the early high-strength steel products, it is not uncommon that achieving sufficient deformation capacity is difficult due to the inferior weldability, ductility, and cold forming performance.

Responding to a market demand for high performance and strength steels, the steels with higher strength, modified weldability, and expected fracture toughness and ductility were developed in the 1990s. The improved performance of the steels are obtained via lower levels of carbon and other elements, together with advanced steel-making practices employing thermo-mechanical control process (TMCP) (Raoul and Günther, 2005). In the last decade, high-strength steel (e.g., BHS 500, BHS 700, YP 500, YP630 in Japan and HPS 70W, HPS 100W in USA) was gradually used in bridge and building structures. Fukumoto (1996) reviewed the mechanical properties of mild steels and high-strength steels with TMCP (a controlled rolling and accelerated cooling process). He also discussed the ultimate plate strength and ductility of high-strength steel with a low yield-to-tensile strength ratio under compression. Galambos *et al*. (1997) provided the results of mechanical properties of high-performance steels and stress-strain curves many scholars studied. The mechanical properties of high-strength steels in China and other countries were presented by Ban *et al*. (2011). In the following year, they carried out a test of high-strength steel (Q460D) under cyclic loads. The cyclic performance of high-strength steel and monotonic and hysteretic stress-strain curves were exhibited (Shi *et al.*, 2012c).

Chen *et al.* (2006) experimentally studied the mechanical properties of high-strength steels (BISPLATE 80) and mild steels (XLERPLATE Grade 350) at elevated temperatures. They compared the experimental results with the evaluations from the American, Australian, British and European codes and then suggested that the reduction coefficients of yield strength and elastic modulus of these two steels are greatly similar at the temperatures varying from 22 °C to 540 °C. Tensile and spring-back behaviors of DP600 high-strength steel were studied at the temperatures ranging from room temperature to 300 °C (Ozturk *et al.*, 2009). Scholars from Tsinghua University investigated the mechanical properties of Q460C high-strength steels at low temperature (Wang *et al.*, 2011). Liu *et al.* (2012) used two methods (i.e., steady-state test and dynamic method) to obtain the strength and elastic modulus of Q460 high-strength steels at elevated temperatures. Qiang *et al.* (2012a) carried out an experimental investigation to reveal mechanical properties of S690 high-strength steels at the temperatures varying from 20 °C to 700 °C. Two methods, i.e., steady state and transient state methods, are adopted in the experiment. In the same year, another experimental study was conducted in order to investigate the post-fire mechanical behaviors of S460 and S690 high-strength steels (Qiang *et al.*, 2012b). In the experiment, the maximum temperature was up to 1000 °C. They demonstrated the behaviors of the steels differed from that of ordinary steels. In the following year, Qiang *et al*. (2013) reported the post-fire mechanical properties of S960 ultra-high–strength steels and the specimens were exposed to the maximum temperature up to 1000 °C. They found the post-fire properties of steels depended on steel grades. Chiew *et al*. (2014) experimentally studied the mechanical performance of heat-treated high-strength steels (grade S690) during and after a fire circumstance.

Yan *et al*. (2014) presented the mechanical properties of ordinary steel and S690 steel at various temperatures varying from -80 °C to +30 °C. They discussed the effects of the low temperatures on the properties of the two steels and developed empirical formulae to determine the elastic modulus, yield stress, and ultimate stress of the steels at the low temperatures. This research is significantly important to the application of high-strength steels in Arctic environment.

2.3. Ultimate bearing capacity and deformation ability of high-strength steel members

For high-strength steel members, the ultimate capacity and deformation ability are vital because the application of the members depends on these mechanical behaviors.

2.3.1. Compression members

Domestic and overseas researchers experimentally and theoretically investigate the mechanical behaviors of welded box, cruciform and H section members made of high-strength steels. The studies focus on local buckling, overall buckling, and both interaction buckling behavior (see Table 2.1). With reference to these studies, it is found that residual stresses have less influence on the ultimate bearing capacity of high-strength steel members. For the compression members with built-up box and H sections, the reduction factors for overall buckling about two principal axes are larger than that of the ordinary steel members. The width-to-thickness ratio limits of local buckling specified in current codes is suitable for the high-strength steel compression members. The normalized strength of stub columns fabricated by the steels is lower than that of ordinary steel because the post-buckling hardening performance of the former is inferior to that of the latter.

2.3.2. Flexural members

McDermott (1969a, 1969b) from America initially investigated the mechanical behavior of flexural members fabricated by A514 high-strength steels. Then, rotation capacity of high-strength steel members was studied by scholars of Japan (Kuwamura, 1988; Kato, 1990). For A514 steel flexural members, McDermott thought that they had enough ductility for plastic design. In contrast, some researchers indicated that the failure mode of the tension flange in some high-strength steel beams was brittle fracture (Freuhan, 1998; C. Earls, 2000; Bjorhovde, 2001). Rotation capacity of some of the beams had not been sufficient even though their failure mode was plastic failure. Therefore, the researchers suggested that the high-strength steel produced by early process and technology was unsuitable for plastic design because of its insufficient ductility and inferior weldability.

In 1994, the Federal Highway Administration (FHWA) launched a cooperative research program with the U.S. Navy and the America Iron and Steel Institute (AISI) in order to develop high performance steels involving HPS 70W and HPS 100W with toughness Zone 3 requirements and excellent weldability (Lwin, 2002). In the following decade, many experimental and theoretical studies on mechanical behavior of flexural members made of high-strength steels were carried out by researchers in the world. The studies concentrate on the influence of failure modes, material properties, cross-sectional proportions and bracing configuration on flexural capacity of high-strength steel bending members, as listed in Table 2.2. In addition, several scholars from America and Canada discussed mechanical properties and design method on I-girders with double web plates, corrugated webs and tubular flanges (Sause *et al.*, 2001; Driver *et al.*, 2002). Veljkovic and Johansson (2004) investigated design of hybrid steel beams to fully utilize the strength of high performance steels.

Research results are obtained as follows:

1) In terms of flexural members with same cross-sectional dimension and material property, rotation capacity of high-strength steel (HSLA-80) members under uniform moment is reduced from 51% to 69% compared to moment gradient. As for bending members with same cross-sectional dimension and loading condition, rotation capacity of high-strength steel (HSLA-80) members is decreased from 70% to 83% compared to A36 steel members because of different material properties.
2) In order to obtain sufficient flexural ductility, some methods involving control of material yield ratio and decrease of limiting width-to-thickness ratio can be adopted.
3) Compared with early high performance steel beams, fatigue and fracture resistance of current high performance steel beams is obviously improved (Fisher and Wright, 2001).

2.4. Connections with high-strength steel members

Connections between steel members as the basic components of a structure are essential to steel structures because the mechanical behavior (e.g., strength and ductility) of structures depends on the performance of the connections. Generally, bolted and welded connections are applied in structures.

2.4.1. Bolted connection

After 1998, the mechanical behavior of bolted connections made of high-strength steels was investigated by numerous researchers. They mainly discussed effects of material properties, edge distances, end distances, bolt spacing, and edge conditions on bearing capacity and ductility. They also studied the influence of surface treatment on the slip coefficient and the feasibility of the current design specifications for bolted connections with high-strength steels and presented suggestions for design of the connections (see Table 2.3).

Research findings are given as follows:

1) Bearing capacity of bolted connections with high-strength steel can be effectively predicted by America specification (AISC LRFD 1993) while the predicting value calculated by America specification (AISC LRFD 1999) is smaller than the former because of a variation from center distance of hole to edge distance of hole in AISC LRFD 1999.
2) For S460 steel connections, the reduction of bearing resistance is too large in Eurocode 3 (2005). Design of the edge distance and bolt spacing can be greater than limits specified in the code. The bearing resistance formula in EN 1993-1-8 gives greatly uncertain results.

3) On the one hand, a low ultimate-to-yield stress ratio does not markedly impact bolted connections with high-strength steels on local ductility. On the other hand, a low ultimate-to-yield stress ratio does not allow the yielding of total section and thus the net section check is very important.
4) End distances of bolts significantly affect local ductility and ultimate deformation capacity of connections is reduced with the decrease of end distances.
5) For a tension member with weaker section, the deformation of the member made of high-strength steels mainly occurs the position of the weaker section and therefore the global ductility is insufficient.
6) The slip coefficient of slip resistant joints is strongly affected by surface treatment and moderately by steel grades.

2.4.2. Welded connection

Some researchers mainly investigated the ductility, toughness, and fatigue properties of welded joints with high-strength steels. Huang *et al.* (1996) perform a cyclic loading experiment on high-strength steel weld connections with six kinds of different grade steels (400-800 MPa). They found the inelastic deformation capacity was markedly declined against the test results without weld connections because of the effect of weld connections. And they suggested that the high-strength steels (strength > 600 MPa) can be applied in structures located in seismic zone via the use of elastic deformation capacity substituting plastic deformation capacity.

Olden *et al.* (2002) introduced a method of notch tensile testing to obtain the tensile properties of welded connections with 690 MPa yield strength steels. They found that actual stress and strain data for the transversal orientation of the heat-affected-zone and weld metal can be recovered in association with a geometry correction factor. Butt welds with high-strength steels was investigated experimentally and the results were presented by Collin and Johansson (2005). It is concluded that reasonably undermatching electrodes can be applied to sustain sufficient ductility of butt welds. The developed design formula covers undermatching and overmatching electrodes. The deformation capacity of high-strength steel (S600 and S1100) welded connections with overmatching and undermatching electrodes was investigated via experiments and finite element methods (Kolstein *et al.*, 2007). It was suggested that weld connections with overmatching electrodes had enough deformation capacity. When the undermatching electrodes were adopted in connections, the strength issues should be emphasized.

Zrilic *et al.* (2007) studied toughness and crack properties of welded joints with low-alloy steel of nominal yield strength equal to 700 MPa. It was found that the crack toughness behavior of the weld metal was lower than that of the heat-affected-zone and the parent metal. Muntean *et al.* (2009) obtained the material properties of S235, S460, and S690 steels and performed the monotonic and cyclic loading experiment on welded connections (fillet, K, 1/2V bevel weld). For the types of weld details and combinations of S235, S460, and S690 base materials, each connection failed in the base material rather than at weld. Therefore, they concluded that the strength and ductility of the connections between high-strength steel and ordinary steel specimens satisfied requirements.

Some scholars from Europe experimentally studied the fatigue performance of weld joints made from high-strength steels whose nominal yield strength was from 460 MPa to 690 MPa (Mang *et al.*, 1993; Barsoum and Gustafsson, 2009; Costa *et al.*, 2010). They found that the fatigue strength of high-strength steel welded joints was higher than the prediction of Eurocode EN 1993-1-9 and the welded joints had good fatigue performance. Dancette *et al.* (2012) investigated the tensile shear failure of high-strength steel spot welds and developed a finite element model to clarify the failure mechanisms contributing to understand macroscopic failure types. Lazić *et al.* (2012) carried out the tensile and impact tests on S690QL high-strength steel welded joints and evaluated the weldability and optimal welding procedure and technology for the high-strength steel.

2.4.3. Joint connection

Girão Coelho *et al.* (2004) carried out an experimental study of eight extended end plate joints under static loads and discussed the influence of parameters involving the end plate thickness and steel grade between S355 and S690 on the rotation capacity. Girão Coelho *et al.* (2006) experimentally investigated the nonlinear behavior of end plate connections fabricated from S690 and S960 high-strength steels. It was found that EC3-1-8 specifications gave predictions of design resistance which shows a good agreement with experiment results. The mechanical behavior of end plate joints with

S690 high-strength steels was experimentally studied by Girão Coelho and Bijlaard (2007). It was noticed that the joints coincided with the requirements of rigidity, resistance, and rotation specified in Eurocode 3 (2005).

Jordao *et al.* (2007) obtained the preliminary results of the test on internal steel joints with various heights beams made up of S690 high-strength steels. Based on an experimental investigation on thirteen internal joints with various heights beams made of S355 and S690 steels, the numerical models were provided by da Silva *et al.* (2007). They also gave preliminary guidelines for the type of issues in accordance with Eurocode 3. Girão Coelho *et al.* (2009) undertaken an experimental investigation of beam-column joints with web shear panels fabricated from S690 and S960 high-strength steels. They discussed the deformation capacity and ductility of the panels and compared test results with the predictions of EN 1993-1-8 specification. Experimental results indicated that the panels fabricated by increasingly higher steel grades had less deformation capacity and ductility and panels with identical dimensions revealed higher resistance with the increase of yield strength.

An experimental study was conducted on end plate joints fabricated from S460, S690, and S960 high-strength steels in order to explore the mechanical behavior of the joints (Girão Coelho and Bijlaard, 2010). It was turned out that EN 1993-1-8 specification provided precise predictions compared with the experimental results and the rotation capacity of the joints satisfied the requirements indicated in the specification.

2.5. Seismic performance of high-strength steel structures

To date, the seismic performance on high-strength steel received more attention from researchers in seismic countries. Kuwamura and Kato (1989) performed tension, stub column, and pseudo dynamic tests on high-strength steels with low yield ratio. The test results demonstrated that the high strength steel showed higher ductility and larger energy dissipating capacity than the common mild steel. Low-cycle fatigue performance of beam-to-column weld joints made of high-strength steels (yield stress, 430 MPa) with a yield ratio less than 0.8 was experimentally investigated by Kuwamura and Suzuki (1992). The experimental results exhibited that the joints had enough ductility to resist a violent earthquake specified in Japanese seismic design code. Nevertheless, it should be noted that the results were based on several simplifications with a few limitations.

Ricles *et al.* (1998) discussed ductility capacity of high-strength steel flexural members under static and cyclic loads. They found that yield ratios significantly influenced the rotation capacity and energy dissipating capacity under cyclic loading and recommended that the ratios should be limited for guaranteeing sufficient ductility and energy dissipating capacity of high-strength steel members in seismic design.

Dual structural frames incorporating a stiff subsystem with removable ductile links and a flexible subsystem was presented by Dubina *et al.* (2008). They experimentally investigated ductility behavior of the eccentrically braced frames with the removable links connecting the beams by utilizing flush end-plate bolt connections.

They thought that using the structural system improved seismic behavior of the structure via limiting plastic deformations to the links and decreasing structure drifts. Dubina *et al.* (2010) evaluated the ductility performance of beam-to-column joints under static and cyclic loads based on extensive tests and implemented numerical analysis for the joints by the finite element software ABAQUS.

Wang *et al.* (2010) discussed the relations between yield ratios and steel mechanical behavior, such as plastic design and seismic performance of steel structures. Deng *et al.* (2010) investigated the seismic behavior of high-strength steel columns with a box section via the finite element method. Shi *et al.* (2012b) experimentally studied hysteretic performance of Q460 high-strength steel box columns under cyclic loading. Experimental investigation on material properties of Q460C high-strength steels subjected to monotonic and cyclic loads was conducted by Sun *et al.* (2013). And they proposed the hysteretic model of the high-strength steels.

Li *et al.* (2013a) evaluated the hysteretic behavior of welded box and H columns made of Q460C high-strength steels by an experiment. Based on the experiment results, they proposed the hysteretic models for the welded box and H columns. Li *et al.* (2013b) built a finite element model to fully investigate the seismic performance of the two types of columns under axial and horizontal cyclic loads. Li *et al.* (2013c) reviewed previous studies on high-strength steels, involving material properties, mechanical behavior of basic members, bolted and welded joints, and effective and economic seismic design. They proposed two design ideas for applying high-strength steels in seismic areas on the basis of the existing seismic design principle adopted in Chinese code for seismic design of buildings.

2.6. Beam-column element for nonlinear analysis

With the rapid advance of computer hardware, a considerable amount of research on nonlinear analysis of framed structures has been conducted since 1970s. Therefore, numerous scholars had made substantial efforts on nonlinear engineering problems (Meek and Tan, 1984; Chan and Kitipornchai, 1987; Chan, 1988; Bridge *et al.*, 1990; Chan and Zhou, 1994; Chen and Chan, 1995; Izzuddin and Smith, 1996; Izzuddin, 1996; Spacone *et al.*, 1996; Liew *et al.*, 1997; Neuenhofer and Filippou, 1998; Pi *et al.*, 2006a, 2006b). Effective and workable beam-column elements have been developed for the purpose of solving nonlinear engineering problems.

In this section, some beam-column elements have been reviewed and the concise introduction to the shape function of these elements is presented.

2.6.1. Displacement-based cubic element

Displacement-based cubic element is the most prevalent and common element for engineering analysis, which is also termed as Hermite element adopted by numerous researchers, such as Connor *et al.* (1967), Bathe and Bolourchi (1979), Meek and Tan (1984), Chan and Kitipornchai (1987), Kassimali and Abbasnia (1991), and Teh (2001). The shape function of this element can be written as,

$$v = \sum_{i=0}^{3} a_i x^i = N_1 L\theta_1 + N_2 L\theta_2 \tag{2.1}$$

where v is the lateral displacement along element length; L denotes the element length; a_i represents the coefficients of the shape functions; θ_1 and θ_2 are the rotations at two ends respectively. Substituting Equation (2.2) into (2.3) and (2.4), N_1 and N_2 are obtained,

$$\xi = 2x / L \tag{2.2}$$

$$N_1 = \frac{1}{8}(1-\xi)(1-\xi^2) \tag{2.3}$$

$$N_2 = -\frac{1}{8}(1+\xi)(1-\xi^2) \tag{2.4}$$

in which ξ is the dimensionless coordinate.

Furthermore, the axial elongation caused by element bowing can be expressed as,

$$u_b = \int_0^L \left(\frac{dv}{dx}\right) dx = \frac{L}{30}\left(2\theta_1^2 - \theta_1\theta_2 + 2\theta_2^2\right) \tag{2.5}$$

P is the axial force expressed as,

$$P = EA\left[\frac{e}{L} + \frac{1}{30}\left(2\theta_1^2 - \theta_1\theta_2 + 2\theta_2^2\right)\right] \tag{2.6}$$

in which EA represents the axial stiffness and e is the global axial shortening. Via the principle of minimum potential energy, the bending moments at two ends of the element can be established as,

$$M_1 = \left(\frac{4EI}{L} + \frac{4PL}{30}\right)\theta_1 + \left(\frac{2EI}{L} - \frac{PL}{30}\right)\theta_2 \tag{2.7}$$

$$M_2 = \left(\frac{2EI}{L} - \frac{PL}{30}\right)\theta_1 + \left(\frac{4EI}{L} + \frac{4PL}{30}\right)\theta_2 \tag{2.8}$$

where M_1 and M_2 are the end moments and EI is the flexural stiffness.

As can be seen from the foregoing equilibrium equation of the element, the analytical results are precise if the deflection of the element is moderate whereas if the deflection is too large, the results could be erroneous because of the cubic shape function and the element under fixed shear. Accordingly, simulating a single member commonly requires two or more elements for the sake of the inaccuracies. A research indicated that Hermite element overestimated 21.6% of the buckling capacity for a simple-supported strut when the member was modeled by only one single element (So and Chan, 1991). Additionally, this element has failed to consider the initial member deflection and the relevant P-δ effect. Hence, the element directly applied in second-order nonlinear analysis is inappropriate.

2.6.2. Stability function element

Livesley and Chandler (1956) initially proposed the stability function element applied in a steel frame analysis. The stability function was determined via the solution of differential equilibrium equations related to the element forces and deformation. Oran (1973a, 1973b) developed the stability function by the co-rotational formulation and recommended a tangent stiffness matrix in analysis of plane and space frames as well as a kinematic motion equation. The equilibrium equation of the element is written as,

$$M_1 = \frac{EI}{L}\left[c_1\theta_1 + c_2\theta_2\right] \tag{2.9}$$

$$M_2 = \frac{EI}{L}\left[c_2\theta_1 + c_1\theta_2\right] \tag{2.10}$$

$$P = EA\left[\frac{u}{L} - b_1\left(\theta_1 + \theta_2\right)^2 - b_2\left(\theta_1 - \theta_2\right)^2\right] \tag{2.11}$$

where c_1 and c_2 represent the stability function; b_1 and b_2 denote the curvature function caused by axial forces. These parameters are diverse under different load conditions. The parameters under the compression case are given by,

$$c_1 = \frac{\phi\left(\sin\phi - \phi\cos\phi\right)}{2\left(1-\cos\phi\right) - \phi\sin\phi} \tag{2.12}$$

$$c_2 = \frac{\phi\left(\phi - \sin\phi\right)}{2\left(1-\cos\phi\right) - \phi\sin\phi} \tag{2.13}$$

$$b_1 = \frac{\left(c_1 + c_2\right)\left(c_2 - 2\right)}{8\pi^2 q} \tag{2.14}$$

$$b_2 = \frac{c_2}{8\left(c_1 + c_2\right)} \tag{2.15}$$

where

$$\phi^2 = \frac{PL^2}{EI} = \pi^2 q \tag{2.16}$$

$$q = \frac{PL^2}{\pi^2 EI} \tag{2.17}$$

The parameters under the tension case can be expressed as,

$$c_1 = \frac{\psi\left(\sinh\psi - \psi\cosh\psi\right)}{2\left(\cosh\psi - 1\right) - \psi\sinh\psi} \tag{2.18}$$

$$c_2 = \frac{\psi\left(\psi - \sinh\psi\right)}{2\left(\cosh\psi - 1\right) - \psi\sinh\psi} \tag{2.19}$$

where

$$\psi^2 = -\frac{PL^2}{EI} = -\pi^2 q \tag{2.20}$$

when the axial load is equal to zero, the parameters are obtained as,

$$c_1 = 4 \tag{2.21}$$

$$c_2 = 2 \tag{2.22}$$

Referring to the aforementioned parameters, if the axial load is pretty small, there is perhaps a potential risk bringing about the numerical instability of the stability functions during analysis.

The stability functions were further developed by Chen and Lui (1987) through a power series without truncations. Following this research, the power series was formulated and corresponding tangent stiffness matrix used to nonlinear analysis was given by Goto and Chen (1987). Ekhande *et al.* (1989) recommended a new expression of the stability function for the sake of the practicability for spatial frames. Chan and Gu (2000) developed the stability function considering the initial imperfection of members and then suggested a second-order analysis method with only one single element per member considered initial imperfections. A stability function applied to considerate lateral-torsional buckling was proposed by Kim *et al.* (2006). The function exhibited the adequate efficiency and reliability for engineering practice.

2.6.3. Pointwise Equilibrating Polynomial (PEP) element

Chan and Zhou (1994) originally proposed the Pointwise Equilibrating Polynomial (PEP) element that was widely used in second-order nonlinear analysis over the past decade. The element is particularly effective and workable for the type of analyses even if utilizing a single element models a member. There are four compatibility and two equilibrium conditions in the element (PEP). The shape function of the element is a fifth-order polynomial. It is noted that the element has a significant advantage which can consider initial imperfection of members and simulate large deflection via only a single element per member.

PEP element used to the elastic-plastic and large deflection analysis of steel frameworks was developed by Zhou and Chan (2004). An elastic-perfectly plastic hinge can be formed at an arbitrary location along the element length. The element (PEP) was employed to second-order nonlinear analysis of angle trusses and further validated the numerical results by comparison with experiment results (Chan and Cho, 2008; Cho and Chan, 2008; Fong *et al.*, 2009). PEP element was extended to the nonlinear analysis of composite steel and concrete members and frameworks and verified the efficiency and accuracy of the analysis against experiment results (Fong *et al.*, 2010; Fong *et al.*, 2011).

Liu *et al.* (2010) adopt PEP element to conduct the pushover analysis in terms of performance-based seismic design. Liu *et al.* (2012a, 2012b) extended the element (PEP) to advanced analysis of composite members and hybrid frameworks. The applicability and efficiency of the element were confirmed again in this research.

2.6.4. Other elements

Many scholars such as King *et al.* (1992), Pi and Trahair (1994a, 1994b), Neuenhofer and Filippou (1998), Barsan and Chiorean (1999), El-Tawil and Deierlein (2001a, 2001b), Nukala and White (2004) devote to the exquisite element research. Although the elements proposed by the scholars are utilized well to numerous frame analyses, they cannot effectively model initial imperfections existing in practical members and structures or specified in certain codes because of the straight geometry assumption. That means these elements are unsuitable for nonlinear analysis because of the absence of the capacity considering initially curved geometry and large deflection.

2.7. Plastic hinge and plastic zone approaches for beam-column element

Material nonlinear issues are essential for advanced nonlinear analysis since material yield has a strong influence on ultimate bearing capacity and buckling behavior of members and structures. Generally, two approaches for simulating material yield are the plastic hinge (i.e. the lumped–plasticity method) and plastic zone methods (i.e. the distributed–plasticity method) which were extensively utilized for material nonlinear analysis. In this section, some studies with regard to the plastic hinge and the plastic zone methods are reviewed in this section.

2.7.1. Plastic hinge method

The principle of plastic hinge method is to concentrate plasticity at beam-column element ends whereas the other part of the element are controlled in elastic range during analysis. In order to simulate the plastic hinge, two zero-length springs are added to the two ends of the traditional beam-column element (see Figure 2.1). Figure 2.2 illustrates the models of the conventional plastic hinge and the refined plastic hinge which have been extensively used in nonlinear analysis.

The basic assumption of the conventional plastic hinge method is that the stiffness of plastic hinge is infinite before the failure of section located at the plastic hinge. In contrast, the hinge stiffness tends to be zero after the section failure. The stiffness transition from infinity to infinitesimal potentially brings about an abrupt variation in load–displacement curves during analysis. There is only one failure criterion in terms of a section in this method which can be easily understood. This method has been frequently used to plastic analysis of members and frames by numerous scholars. The plastic hinge method was adopted to analyze the inelastic behavior of H columns under biaxial flexure by Harstead *et al.* (1968). Alvarez and Birnstiel (1969) suggested an approach for analyzing the plastic behavior of multi-story multi-bay steel frameworks. A numerical solution procedure applied in large deformation analysis of elasto-plastic steel frameworks was proposed by Kassimali (1983) and the nonlinear response of three structures were determined by the numerical method. Wong and Tin-Loi (1990) presented an approach that explicates the geometrical and physical nonlinear effects in incremental analysis of steel frames.

In order to obtain the elasto-plastic response of imperfect space trusses, a numerical approach allowing for geometrical and material nonlinearities was suggested by Freitas and Ribeiro (1992). Guralnick and He (1992) developed a finite element formulation used for the incremental analysis of ideal elastic-plastic planar steel frames. The analysis approach was applied in pushover analysis for performance-based seismic design by Liu *et al.* (2010) and verified that the conventional plastic hinge is effective and workable for analysis of common structures.

Compared with the conventional plastic hinge method, the moment-rotation curve obtained from the refined plastic hinge approach exhibits a smooth path between ideal elasticity and plasticity (see Figure 2.2). Because of the degradation of section springs with loading, the material gradual yield can be simulated. There are two sectional criteria with respect to elastic limit and plastic failure states in this method. Numerous researchers have devoted to the investigation of the refined plastic hinge method over the past few years. An effective and reasonable approach, based on sectional assemblage principle, for advanced elasto-plastic analysis of steel frames was proposed by Chan and Chui (1997).

Kim and Chen (1998) used the refined plastic hinge method to simulate the buckling behavior of a beam under distributed transverse loads and discussed the sensitivity issues for element number in this method. Liew *et al.* (2000) presented an improved plastic hinge method employed to second-order nonlinear analysis of spatial framed structures. Kim *et al*. (2002, 2003) utilized the refined plastic hinge method for advanced nonlinear analysis of members, planar and space steel frames. The effects of lateral torsional and local buckling were considered during analysis. Cuong *et al*. (2007) conducted a second-order nonlinear analysis for three-dimensional steel frameworks by a plastic fiber hinge concept and adopted an ESSC residual stress model during analysis.

Liu *et al.* (2014a, 2014b) propose a new beam-column element (i.e. arbitrarily–located–plastic–hinge element) that can be applied in advanced analysis of plane and space steel frames. The element allows for the effects of geometrical and material nonlinearities via one element per member because the plastic hinge can occur at arbitrary location along member length.

2.7.2. Plastic zone method

In the plastic zone method, all analyzed members and relevant sections are meshed into numerous sub-elements and fibers as shown in Figure 2.3. The determination of total member deformation uses numerical integration through the meshed fibers at the integration points along element length. The plasticity spread in elements and fibers of members can be explicitly monitored. The number of the integration points along the sectional fiber and element length has a strong influence on the accuracy of predictions given by the plastic zone method. The method was adopted in the advanced nonlinear analysis of members and simple framed structures by numerous researchers.

Because of the accurate predictions of the plastic zone method, it is commonly employed to validate other plastic analysis methods. Chu and Pabarcius (1964) analyzed the elastic and plastic buckling behavior of portal frames by the method. El-Zanaty *et al.* (1980) conducted the inelastic and elastic-plastic analysis for a beam-column, single story frames, and multi-story steel frames. Yang and Saigal (1984) developed a six degrees-of-freedom beam element and the relevant numerical procedures for nonlinear analysis of beams under static and dynamic loads allowing for geometric and physical nonlinearities.

White (1985) utilized interactive computer graphics, based on the plastic zone method, to conduct an elastic analysis of plane steel frameworks. Meek and Lin (1990) employed the plastic zone method in conjunction with the updated Lagrangian formulation to study inelastic behavior of thin-walled beam-columns after local buckling. The effects of geometric imperfection and residual stress were considered during analysis. Toma and Chen (1992) proposed three calibration frames as benchmark examples to calibrate second-order plastic analysis methods for steel frames. Teh and Clarke (1999) studied inelastic analysis of plane and space steel frames by the plastic zone method and validated the efficiency of the presented spatial beam element.

Fang *et al*. (1999, 2000) developed the plastic zone approach and discussed the plastic analysis of composite beams and frames with semi-rigid joints. Jiang *et al.* (2002) extended the plastic zone method for investigating the plastic behavior of spatial steel frames and confirm the accuracy of analysis results by comparison with established benchmark results. Alvarenga and Silveira (2009) presented a numerical method based on the plastic zone method for inelastic analysis of planar steel frames and discussed the effects of geometric imperfections and residual stresses on design of steel frameworks.

2.8. Cross-sectional analysis methods

The cross-section analysis technique has been widely investigated since the 1960s, which mainly focuses on members and structures with reinforced concrete sections or steel and concrete composite sections. Many researchers devote to the development of the methods (Bresler, 1960; Furlong, 1961; Fleming and Werner, 1965; Moreadith, 1978; Hsu, 1987, 1988, 1989; De Vivo and Rosati, 1998; Rodriguez and Aristizabal-Ochoa, 1999; Chen *et al.*, 2001; Sfakianakis, 2002; Charalampakis and Koumousis, 2008; Chiorean, 2010; Papanikolaou, 2012).

Santathadaporn and Chen (1968) investigated the strength limit states of rectangular and wide-flange H sections under biaxial bending and axial loading. The interaction equations based on an equilibrium method to evaluate the lower and upper boundaries of ultimate strength for the two sections were proposed. Yen (1991) presented a quasi-Newton iterative method that can be applied in computer application for analysis and design of reinforced concrete sections under uniaxial or biaxial loads. Yau *et al*. (1993) proposed a numerical method for analyzing arbitrary reinforced concrete cross-sections subjected to axial loading and biaxial bending. Herein, an iterative scheme is employed to determine the position of neutral axis. Recently, Liu *et al.* (2012a) proposed a rigorous cross-sectional analysis method for arbitrarily-shaped sections.

2.9. Discussion

Residual stresses extensively existed in practical steel members and structures have an influence on mechanical behavior of the members and structures under static or cyclic loads. From the aforementioned studies on numerical methods, the effects of residual stresses are not taken into account in most of the studies. Even though the effects are considered in analysis, the models of residual stress are based on ordinary carbon steels, which are unsuitable for high-strength steels. Consequently, the models suitable for high-strength steels are essential for analysis.

In the present study, actual residual stress distribution of high-strength steel box and H sections are provided by a residual stress experiment and the stress models for the two sections are proposed and adopted in analysis. The section analysis scheme based on the quasi-Newton iterative scheme is utilized to explicitly take into consideration the residual stress effects. The use of PEP element can consider initial geometric imperfection and relevant second-order effects. To reflect the yielding behavior of steels, a plastic hinge model with sectional strength iterative surfaces is adopted. In order to verify the proposed method, an experiment on overall buckling behavior of high-strength steel box and H columns under axial compression is conducted.

2.10.Concluding remarks

In this chapter, the mechanical behavior of high-strength steel materials, members, structures, and joints under static or cyclic loads are reviewed. Then, certain beam-column elements applied in nonlinear analysis are introduced and the plastic hinge and plastic zone methods for inelastic analysis are discussed. Finally, the sectional analysis techniques are summarized.

Figures

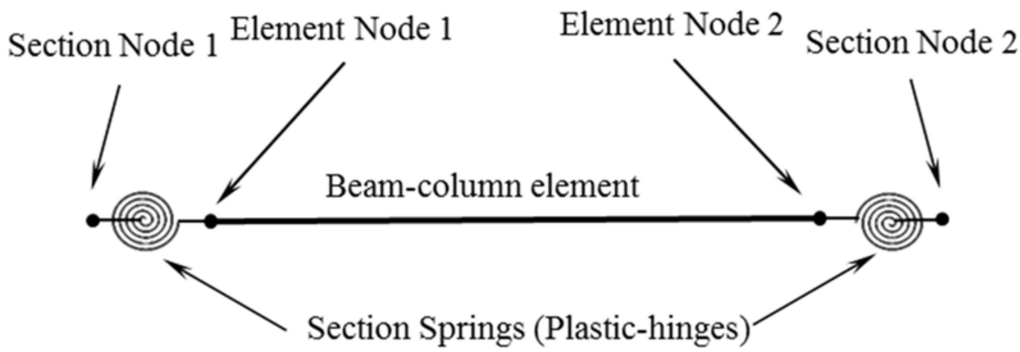

Figure 2.1 Illustration of plastic hinge approach

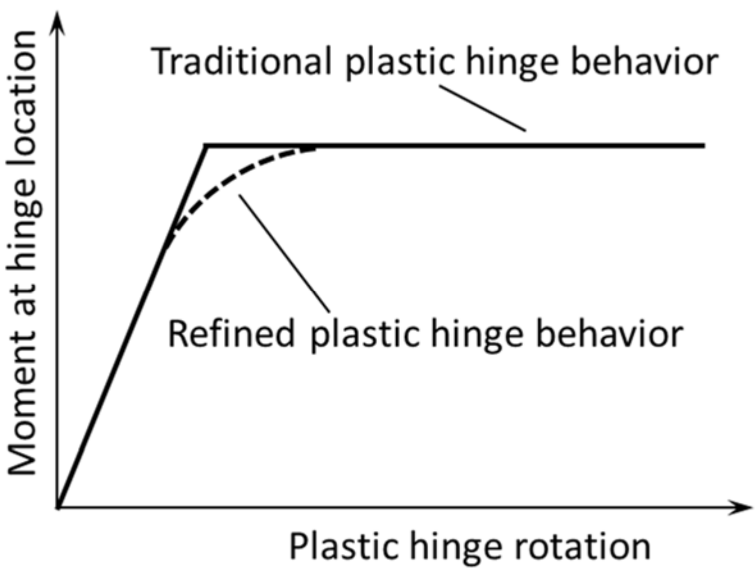

Figure 2.2 Behaviors of plastic hinge and refined plastic hinge

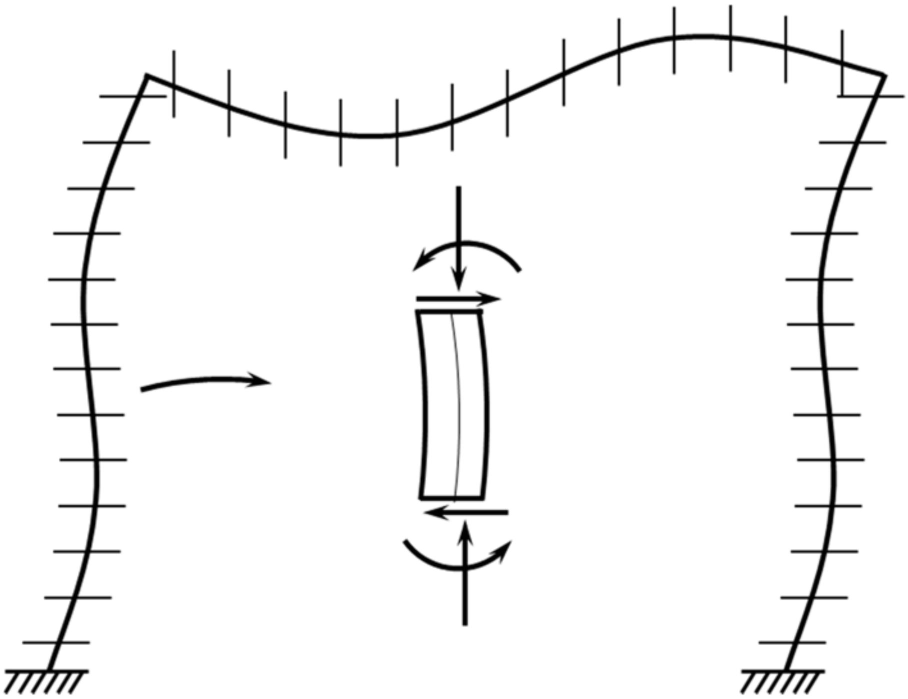

(a) Discrete frame structure

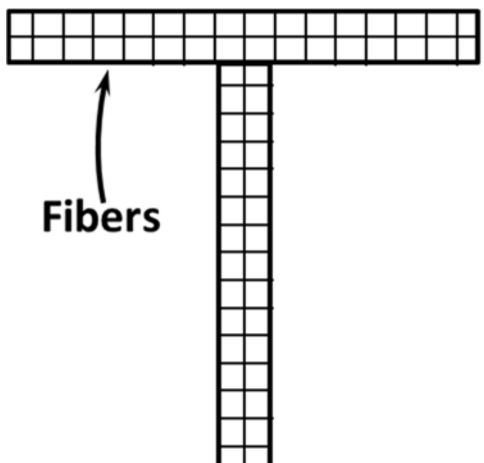

(b) Meshed section with monitored fibers

Figure 2.3 Illustration of plastic zone method

Tables

Table 2.1 Study of High Strength Steel Members under Compression Load

Author (Year)	Country	Type of Research	Steel Grade Actual Yield Strength	Research Contents
Nishino *et al.* (1967)	Japan America	Experiment	A514 717-799MPa	Local buckling behavior of high strength welded box columns; stub column test; residual stresses.
McDermott (1969a)	America	Experiment	A514 752MPa	Local buckling behavior of high strength cruciform stub columns; stub column test; width-to-thickness ratio limits.
Usami and Fukumoto (1982)	Japan	Experiment	HT80/A514 741MPa	Local and overall interaction buckling behavior of high-strength steel column with a welded box section; stub column test; ultimate bearing capacity test; empirical design formula for predictions of interaction buckling strength.
Usami and Fukumoto (1984)	Japan	Experiment	SM58 568MPa	Local buckling of high- strength steel columns under concentric and eccentric compression; post-buckling strength; effective width concept.

Author (Year)	Country	Type of Research	Steel Grade Actual Yield Strength	Research Contents
Rasmussen and Hancock (1992)	Australia	Experiment	BISALLOY80 670MPa	Local buckling behavior of welded box, cruciform, and I columns made of high-strength steels; stub column test; width-to-thickness ratio limits; residual stresses; comparison with AS4100, AISC-LRFD and Eurocode 3.
Rasmussen and Hancock (1995)	Australia	Experiment	BISALLOY80 705MPa	Overall stability of high-strength steel columns with welded box and I sections; ultimate bearing capacity test; residual stresses; comparison with AS4100, AISC-LRFD, BS5950 and Eurocode 3.
Jiao and Zhao (2003)	Australia	Experiment	1350 MPa	Stub columns test; circular tubes; residual stresses; initial geometric imperfections.
Shi and Bijlaard (2007)	China Netherland	Numerical simulation	690MPa	Finite element analysis; residual stresses; initial geometric imperfections.
Gao *et al.* (2009)	China	Experiment	18Mn2CrMoBA 793.3MPa	Local stability of high-strength steel columns with built-up box section; stub column test; parametric study; comparison with AISI.

Author (Year)	Country	Type of Research	Steel Grade Actual Yield Strength	Research Contents
Cao (2010)	China	Experiment and Numerical simulation	Q460	Local buckling and overall buckling behavior of high-strength equal-leg single-angle; ultimate bearing capacity test; numerical simulation; parametric study; buckling curves; comparison with ASCE 10-97.
Wang *et al.* (2012c)	China	Experiment and Numerical simulation	Q460 464-540.9MPa	Overall buckling behavior of welded H columns fabricated by high-strength steels; ultimate carrying capacity test; numerical simulation; parametric analysis; buckling curves; comparison with GB50017-2003 and Eurocode 3.
Ban *et al.* (2012)	China	Experiment and Numerical simulation	492.3-531.9 MPa	Overall buckling of 460MPa high-strength steel columns with welded box and I sections; ultimate bearing capacity test; numerical simulation; buckling curves; parametric analysis and design method for axial compression columns;

Author (Year)	Country	Type of Research	Steel Grade Actual Yield Strength	Research Contents
Shi *et al.* (2012a)	China and Netherlands	Experiment and Numerical simulation	S690&S960 733.7-1019.8 MPa	Overall buckling about the strong axis of welded I columns made of high-strength steels with end constraints; ultimate capacity test; numerical simulation; buckling curves; comparison of Eurocode 3 and GB50017-2003.
Ban *et al.* (2013b)	China and Australia	Experiment Numerical simulation	973.2MPa	Overall buckling behavior of welded box and I columns fabricated by 960MPa high-strength steel; ultimate strength test; numerical simulation; parametric analysis; buckling curves; comparison with Eurocode 3, ANSI/AISC360-10, and GB50017-2003.
Yan *et al.* (2013)	China	Numerical simulation	Q460 505.8MPa	Numerical simulation on global buckling of high-strength steel columns with a box section using the numerical integration method and finite element method; comparison of test and analysis results.

Author (Year)	Country	Type of Research	Steel Grade Actual Yield Strength	Research Contents
Shi *et al*. (2014)	China	Experiment and Numerical simulation	492-532 MPa	Local stability of high-strength steel stub columns with built-up box and I sections; stub column test; parametric study; comparison of results anticipated by GB 50017-2003, ANSI/AISC 360-10, and Eurocode 3.
Wang *et al.* (2014)	China	Experiment and Numerical simulation	Q460 505.8MPa	Overall buckling behavior of welded high-strength steel columns with a box section; ultimate carrying capacity test; numerical simulation; parametric analysis; buckling curves; comparison with results predicted by GB50017-2003 and Eurocode 3.

Table 2.2 Study of High Strength Steel Flexural Members

Author (Year)	Country	Type of Research	Steel Grade Actual Yield Strength	Research Contents
McDermott (1969b)	America	Experiment	A514 765.3-882.6MPa	Lateral buckling, local buckling, and interaction buckling of high-strength steel flexural members with I sections; pure bending test; combination of bending and shearing test; rotation capacity and theoretical analysis of plastic hinge.

Author (Year)	Country	Type of Research	Steel Grade Actual Yield Strength	Research Contents
Beg and Hladnilk (1996)	Slovenia	Experiment and Numerical simulation	NIONICRAL70 775-873MPa	Local buckling of welded high-strength steel I shaped beams categorized as Class 3 cross-section; pure bending test; residual stresses; parametric analysis; the analytical formula for delimitation between slender and semi-compact I sections accounting for the interaction between flange and web.
Ricles *et al.* (1998)	America	Reviews, Experiment, and Numerical simulation	HSLA80 607MPa	Local buckling of high-strength steel flexural members with I sections; pure bending test; combination of bending and shearing test; influence factors about rotation capacity of high-strength steel flexural members under cyclic load; numerical simulation; comparison with AISC-LRFD.
Earls (1999)	America	Numerical simulation	HSLA80 586MPa	The simulation on the inelastic failure of high strength steel I section beams under moment gradient; effects of bracing configuration, sectional proportions, and geometrical imperfections on failure modes and ductility of the beams.

Author (Year)	Country	Type of Research	Steel Grade Actual Yield Strength	Research Contents
C. J. Earls (2000)	America	Numerical simulation	345-690MPa	The investigation on mechanical behavior of compact I section beams subjected to moment gradient; parametric analysis; effects of yield strength, strain hardening modulus, material hardening law, and yield plateau on structural ductility.
Barth *et al.* (2000)	America	Numerical simulation	HPS70W 480MPa	The simulation on the flexural behavior of I-section girders; parametric analysis; effects of geometric and material parameters on bending resistance of the girders; comparison of AASHTO LRFD and predicting formula in previous research.
Earls (2001)	America	Numerical simulation	HSLA552 586MPa HPS483W 539MPa	Simulating the mechanical behavior of high-performance steel I section beams under constant moment; parametric analysis; effects of width-to-thickness ratio of flanges, height-to-thickness ratio of webs, and lateral bracing configuration on ultimate bearing capacity and flexural ductility of the beams; comparison with AISC LRFD.

Author (Year)	Country	Type of Research	Steel Grade Actual Yield Strength	Research Contents
Sause and Fahnestock (2001)	America	Experiment	HPS100W 789MPa	The test of high-strength steel I shaped girders under three-point loading; ultimate bearing capacity and flexural ductility; comparison with results predicted by AASHTO LRFD and previous test results of ordinary steels.
Green *et al.* (2002)	America	Experiment and Numerical simulation	HSLA80 576-609MPa	Ultimate bearing capacity test of high-performance steel flexural members; effects of material properties, sectional proportions and loading conditions on the strength and ductility; numerical simulation; comparison with the results of ordinary steel members and AISC-LRFD; recommendations for design of the flexural members.
Earls and Shah (2002); Thomas and Earls (2003)	America	Numerical simulation	HPS483W 539MPa	Numerical simulation on mechanical behavior of I shaped bridge girders made from high-performance steels; parametric analysis; influence of geometric dimensions and lateral bracing configuration on rotation capacity and strength; comparison with AASHTO LRFD; suggestions for design.

Author (Year)	Country	Type of Research	Steel Grade Actual Yield Strength	Research Contents
Greco and Earls (2003)	America	Numerical simulation	276-540.6MPa	Investigation on mechanical behavior of hybrid high-performance steel beams with I section by numerical simulation; parametric study; effects of flange and web slenderness ratios and bracing configuration on flexural ductility.
Jiao and Zhao (2004)	Australia	Experiment	1350 MPa	Bending behavior of ultra-high strength steel tubes; circular sections; full plastic moment capacity; plastic slenderness limits.
Wheeler and Russell (2005)	Australia	Experiment	Bisplate80	Ultimate bearing capacity test of high-strength steel beams with welded box sections; limiting width-to-thickness ratios; comparison with AS 4100-1998.
Lee *et al.* (2011)	South Korea America	Experiment and Numerical simulation	HSB800 680MPa	Study on rotation capacity of high-strength steel I shaped girders subjected to bending moment; ultimate bearing capacity test; finite element analysis; influence of yield strength and bracing configuration on flexural ductility.

Table 2.3 Bolted Connection of High-Strength Steel

Author (Year)	Country	Type of Research	Steel Grade Actual Yield Strength	Research Contents
Kim and Yura (1999)	America	Experiment	267&483MPa	Bearing shear strength test of lap connections with one and two bolts; effects of various steel grades, end distances and bolt spacing on bearing capacity; comparison with AISC-LRFD specification and Eurocode 3.
Puthli and Fleischer (2001)	Germany	Experiment	S460 524MPa	Bearing shear capacity experiment on two-bolt connections in double shear; effects of edge distance and bolt spacing on bearing strength; comparison the experimental results with the predictions of Eurocode 3.
Rex and Easterling (2003)	America	Experiment and Numerical simulation	301-507MPa	Bearing behavior of single bolt connections in double shear; finite element analysis; effects of edge conditions on bearing strength; a developed model for determining the initial stiffness of the load-displacement curve; estimation of the existing model for design of the plate strength; comparison with AISC Specification (LRFD 1993& LRFD 1999) and Eurocode 3.

Author (Year)	Country	Type of Research	Steel Grade Actual Yield Strength	Research Contents
Može *et al.* (2007)	Slovenia	Experiment and Statistical evaluation	S690 847MPa	Net cross-section failures test of plate with holes and bolt connections fabricated by high-strength steels; local ductility and design resistance; validation of different strength formulae; determination of a partial factor by statistical analysis.
Williams *et al.* (2009)	UK	Experiment and Numerical simulation	590&880MPa	Bearing capacity test on a simple single-bolted-joint under external loads; verification of finite element analysis results via experimental results; comparison with classical theory.
Dusicka and Lewis (2010)	America	Experiment	HPS70W 555-586MPa	Bearing behavior of bolted connections with filler plates made of high-strength steels; influence of filler thickness and multiple filler on connection strength; design recommendations for the bolted connections.
Može and Beg (2010)	Slovenia	Experiment	S690 847MPa	Bearing capacity test of S690 high-strength steel tension splices with one or two bolts; ductility and resistance of the splices; comparison with bearing resistance specified in Eurocode 3; development of a new resistance formula.

Author (Year)	Country	Type of Research	Steel Grade Actual Yield Strength	Research Contents
Može and Beg (2011)	Slovenia	Experiment and Numerical simulation	S690 796MPa	Bearing capacity test on high-strength steel tension splices with three or four bolts in double shear; numerical simulation; validation of finite element results by experimental results; verification of the bearing resistance formula indicated in EN 1993-1-8.
Cruz *et al.* (2012)	Portugal	Experiment	S275&S690	Slip test of slip resistant bolt connections made of mild steel, weather resistant steel and high-strength steel; effects of various surface treatments and steel grades on the slip factor; recommendations for the factor.

CHAPTER 3

EXPERIMENTAL INVESTIGATION ON THE RESIDUAL STRESSES OF WELDED BOX AND H SECTIONS

This chapter presents several techniques for measuring residual stresses, including destructive and nondestructive methods. The sectioning method is selected to determine the residual stress distribution of box and H section specimens fabricated by Q690 high-strength steel. Then, idealized models of residual stress are proposed on the basis of the experimental results. These models can be simply applied to the numerical analysis of basic steel members as the initial imperfection.

3.1. Introduction

Residual stresses are present in steel members and structures because of structural mismatch, non-uniform distribution of inelastic or thermal strains during manufacture or fabrication. These strains can be induced by cold forming, uneven cooling, flame cutting or welding and are frequently investigated because they are influential in changing the member capacities and measurable in laboratory. Three types of residual stresses occur in fabricated members, that is, stresses that are distributed in the longitudinal, transverse, and thickness directions of a weld. The residual stresses in the thickness direction acting on thin welded members can be disregarded because such stresses are of a small magnitude. The residual stresses along a weld are frequently studied because they influence the mechanical behavior of fabricated members. The stress near a weld not only affects the resistance of steel against stress-induced corrosion, cracking, and fatigue but also adversely affects the stability of compression members.

High-strength steel (yield strength ≥460 MPa) possesses more varied mechanical properties under normal and elevated temperatures than ordinary steel and such difference affects the distribution and magnitude of residual stress in welded high-strength steel members. Given these considerations, residual stress investigations on such steel members should be carefully conducted.

In this chapter, six specimens with three H sections and three box sections were fabricated with Q690 steel plates. The sectional dimension and welding process of the specimens are identical to those of the compression members discussed in Chapter 4. The residual stress distribution of these specimens can be determined by the sectioning method. On the basis of the test results, idealized residual stress models that correspond to various sections are proposed, after which several patterns of residual stresses are discussed.

3.2. Measurement methods

The techniques for measuring residual stress can be categorized into two classes namely as destructive and nondestructive methods. The principle that underlies the destructive methods employed by many researchers are the removal of materials and the measurement of subsequent strain alteration. Released stresses can be evaluated by the Hooke's law. For nondestructive measurements, researchers adopt many state-of-the-art techniques, including X-ray diffraction, neutron diffraction, and magnetic Barkhausen noise methods. These approaches are preferable to destructive methods in stress measurements for certain situations such as existing structures or buildings under construction, because specimens are not be damaged during measurement. However, these techniques present more expensive testing costs and equipment than the destructive methods.

3.2.1. Destructive measurement methods

The hole drilling method is classified into blind (center) hole drilling and deep hole drilling. In the blind hole method, every strain rosette is arranged around a corresponding hole, the center of which coincides with the strain rosette. The depths of holes can be selected as partial or complete thicknesses of specimens. To determine the distribution of residual stresses through the thickness of specimens, the material can be incrementally removed. The deep hole method, on the other hand, is typically used in circumstances wherein the residual stress distribution of thick plates needs to be determined. In this method, a small hole is drilled for reference and the diameter of the reference hole is precisely measured. After a column that has the same center as the reference hole is trepanned from the specimen, the diameter of the reference hole should be re-measured. The difference between the two measurements can be used to determine the relieved residual stresses in the radial and axial directions.

Another method, called the sectioning method, involves separating a specimen into strips or layers and then measuring strain alteration. Test results on strips and layers indicate that stresses change on the plane and through the thickness of specimens. Mechanical instruments or strain gauges are commonly regarded as effective tools for measuring the elongation of sectioned strips. Elongation can be mechanically measured with a Whittemore strain gage. Relieved strains should be determined by measuring the distance (length) between the reference holes before and after sectioning. For this purpose, using Whittemore strain gages in measurement requires an identical operation.

3.2.2. Nondestructive measurement methods

This section discusses diffraction measurement and magnetic measurement methods. X-ray diffraction and neutron diffraction methods are used to measure residual stress via diffraction. In the X-ray diffraction method, the depth of measurement ranges from 8 to 20 μm, whereas in the neutron diffraction method, depth can reach 38 mm. This difference indicates that the stress levels presented by the former are suitable for measuring specimen surfaces. The latter relies on the neutron reflection principle, in which residual stresses can be calculated by the reflection angle from the crystals in a material when the neutron crosses through the material.

A magnetic measurement method, called the magnetic Barkhausen noise method, determines residual stress levels on the surface of specimens by exploiting a high-resolution probe where a read head is installed between the poles of ferromagnetic U-shaped cores. This approach is based on the sharp domain wall motions of ferromagnets, the magnetization levels of which vary. Before stresses are measured, calibration should be effectively conducted because this procedure is highly sensitive to the accuracy of test results.

3.3. Experimental program for residual stresses

3.3.1. Measurement technology for residual stresses

In this experiment, the sectioning method proposed by Kalakoutsky (1888) was adopted to measure the longitudinal residual stresses of the specimens. This method is based on the theory that cutting a specimen into a number of strips releases the residual stress present in a cross-section (see Figure 3.1(a) and (b)). Under this approach, the effects of transverse stresses are disregarded. That is, the lower the levels of transverse residual stresses, the more precise the measurement results. This method, which has been used to determine the residual stress distribution of structural steel members for decades, confirms that appropriate specimen preparation and measurement present economic advantages (cost savings) and guarantee accuracy (Tebedge *et al.*, 1973).

3.3.2. Design and manufacture of specimens

Specimens with box and H sections were welded from flame-cut steel plates (nominal yield strength, 690 MPa) by gas metal arc welding (GMAW), as shown in Figure 3.2. In this experiment, the gauge length of the specimens was 200 mm. To eliminate end-effects, the established length of each specimen was equal to the sum of 4B and 200, where B is the lateral dimension of a cross-section; this length was adopted even though multiplying lateral dimension by 2.0 is a theoretically sufficient value. All component plates were connected by complete penetration welding. The filler wire used was ER120S-G, which has the same nominal yield strength as that of Q690 steel. Adopting an optimal welding sequence (i.e., antisymmetric welding sequence) is necessary to avoid shrinkage deformations. The welding parameters applied to the welding process are listed in Table 3.1, and the geometric dimensions of the specimens are shown in Table 3.2 and Table 3.3. The width-to-thickness ratios of the box section specimens were 6.7, 9.9, and 12.5, which correspond to R-B-7, R-B-10, and R-B-13, respectively. The ratios of the flange of the H section specimens were 5.9, 7.0, and 7.5, which correspond to R-H-6, R-H-7, and R-H-8, respectively.

3.4. Measurement of residual stresses

3.4.1. Basic works

Five tension coupons were prepared in accordance with GB/T 2975-1998 (1998), which requires a cutting direction that is orthogonal to rolling direction. An extensometer was used to measure longitudinal strains, which accurately determine the Young's modulus. The experiment was carried out in accordance with GB/T 228-2002 (2002), and the loading rate was 0.5 mm/min. The stress-strain curve is plotted in Figure 3.3, which illustrates the average values of the results for the five tension coupons. A distinct yield point elongation (755–785 MPa) exists in the curve and differs from that observed in common high-strength steels. In Figure 3.3, E is the Young's modulus of Q690 steel, Δ% denotes the percentage of elongation after rupture, ε_u is the ultimate strain, and f_y and f_u represent the yield stress and ultimate tensile stress, respectively. The comparisons between the test results and requirements of Eurocode 3 Part 1-12 are as follows: f_u/f_y = 1.08 > 1.05 (Eurocode 3); ε_u = 0.0612 > $15f_y/E$ = 0.0496 (Eurocode 3); Δ% = 21% > 10% (Eurocode 3). Through the comparison, it is concluded that the Q690 high-strength steel satisfies the corresponding requirements specified in Eurocode 3 and possesses high quality and good ductility.

3.4.2. Sectioning method procedures

The main steps for measuring the residual stresses on the sections of steel specimens by the sectioning method are described below.

(1) Determination of sectioning positions

Cutting lines and the centers of gage holes were marked in the middle of the specimens. The strips in the sectioning zone were also marked (see Figure 3.4).

(2) Drill holes

In accordance with the marks, a punch was used to create gage holes that penetrate the full thickness of the specimens. After the holes were drilled, another drill head was used to enlarge the fillet angle of the holes to 45°, thereby ensuring the accuracy of measurement results.

(3) Measurement before sectioning

After preparation of gage holes and before succeeding measurements was conducted, an important step was to clean the holes by using an air pump. The gage lengths were initially measured and recorded using the Whittemore strain gage shown in Figure 3.5. For the box section specimens, the exterior surface was measured. By contrast, for the H section specimens, the interior and exterior surfaces were measured. Three sets of measurement results for every gage length were recorded when the errors among them were around 0.005 mm. To eliminate the temperature effect on readings, the reading of a reference bar should be gauged at the beginning and end of every measurement.

(4) Sectioning specimens

The sectioning areas were cut from the specimens by using a sawing machine (see Figure 3.6). Then, a wire cutting machine was used to slice the sectioning areas into strips in accordance with the marked lines, as shown in Figure 3.7. To eliminate the effect of heat release from the gasification of steel, a cooling liquid was used in the sectioning procedure. The widths of the strips located on the weld were 14 mm (specimen R-B-7), 15 mm (specimen R-B-10), and 12 mm (specimen R-B-13), whereas that of the other strips and the strips of the H section specimens was about 10 mm.

(5) Measurement after sectioning

The completely sectioned strips are shown in Figure 3.8. Before a new round of measurement is initiated, iron dust and grease should be cleaned, especially around the gage holes. Three sets of readings were re-obtained following the measurement procedure implemented before sectioning. The released strains were calculated by excluding the temperature strains from the measured results. If bending deflection exists in the strips after sectioning, deflection measurement is also necessary. Some curved strips formed after sectioning.

3.4.3. Test results

The magnitudes and distributions of residual stresses on sections can be calculated by using Hooke's law and measured strains. For the curved strips, the measurement results required modification. The specific process used was that presented by Tebedge *et al.* (1973) and Cruise and Gardner (2008). Figure 3.9 shows the experimental results for the exterior surfaces of the box section specimens. Figure 3.10 displays the results for the exterior and interior surfaces of the H section specimens; in the figure, the solid block represents the findings on the exterior (left) surface, and the hollow block denotes the findings on the interior (right) surface. Measurement with a Whittemore strain gage cannot be performed for the H section specimens, specifically near the junction between the flange and web because of the narrow space of this junction. However, the stress magnitudes in these positions can be computed by using sectional self-equilibrating conditions under residual stresses.

3.5. Idealized models of residual stress

The residual stress on a welded section is induced by non-uniform temperature during welding. The experimental results show that the width of the tensile area remains nearly constant for the box and H section specimens, with different width-to-thickness ratios (see Figure 3.9 and Figure 3.10). Barroso *et al.* (2010) proposed a thermal envelope model that can be used to explain this phenomenon:

$$T - T_0 = \sqrt{\frac{2}{\pi e}} \frac{q_{\mathrm{w}}}{2h_{\mathrm{w}} c \rho_0 x} \tag{3.1}$$

where q_{w} is the heat input per unit welded length, c denotes the specific heat, ρ_0 is the density of steel products, T_0 represents the initial temperature, h_{w} is the thickness and x is the distance to the weld line.

On the basis of Equation (3.1), the conclusion that the diverse sections possess an identical heat envelope curve near the welds can be deduced provided that the adopted heat input per unit welded length, specific heat, density, and thickness of plates are identical. The deduction suggests that the widths of the residual tension areas are very close in terms of the various width-to-thickness ratios of each section.

Figure 3.11 shows a simplified residual stress distribution for the box sections. This distribution was determined on the basis of the results of the sectioning experiment, where α and β are the tensile and compressive residual stress ratios listed in Table 3.4. The determination of w (the width of the tensile area) was uncomplicated by equilibrium conditions. The residual stress model of the H section welded by flame-cut plates is proposed in Figure 3.12. In Table 3.5 and Figure 3.12, α_i and β_i are the ratios of the tensile and compressive residual stresses about the actual yield strength, in which subscript i represents the different positions of residual stress blocks.

3.6. Concluding remarks

Although residual stresses may not be detrimental to the plastic strength of cross-sections, it can diminish the stiffness and buckling resistance of compression members and reduce the fatigue life of structural steel members under cyclic or dynamic loading. Investigations on this issue are therefore necessary for high-strength steel members. The present study employed the sectioning method to measure the residual stress distribution of box and H section specimens fabricated with Q690 high-strength steel. Simplified models of residual stresses were then proposed on the basis of the analysis of the experimental results. These models can be incorporated as initial imperfections into the numerical analysis of basic members. Additionally, the rectangular pattern of residual stresses is a favorable characteristic in that it can be more simply incorporated into numerical analysis than the trapezoidal and triangular models.

Figures

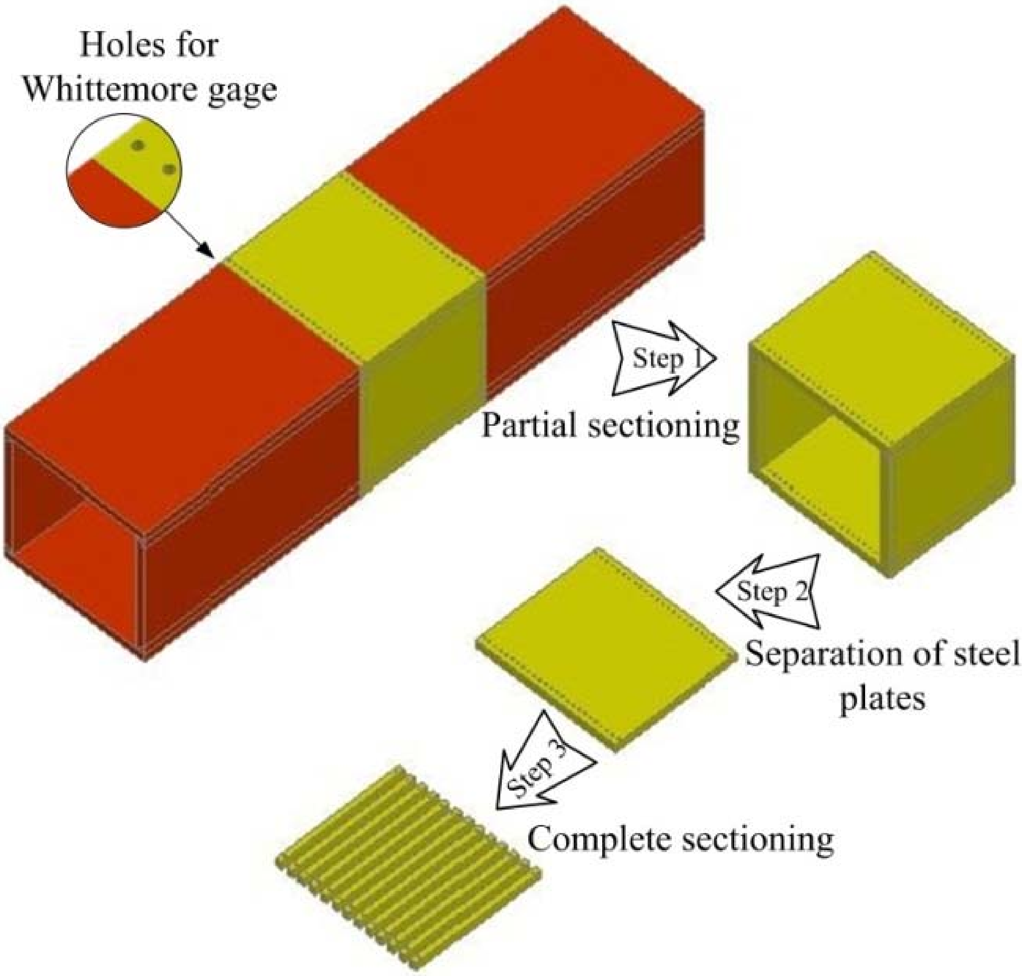

(a) Box section specimen

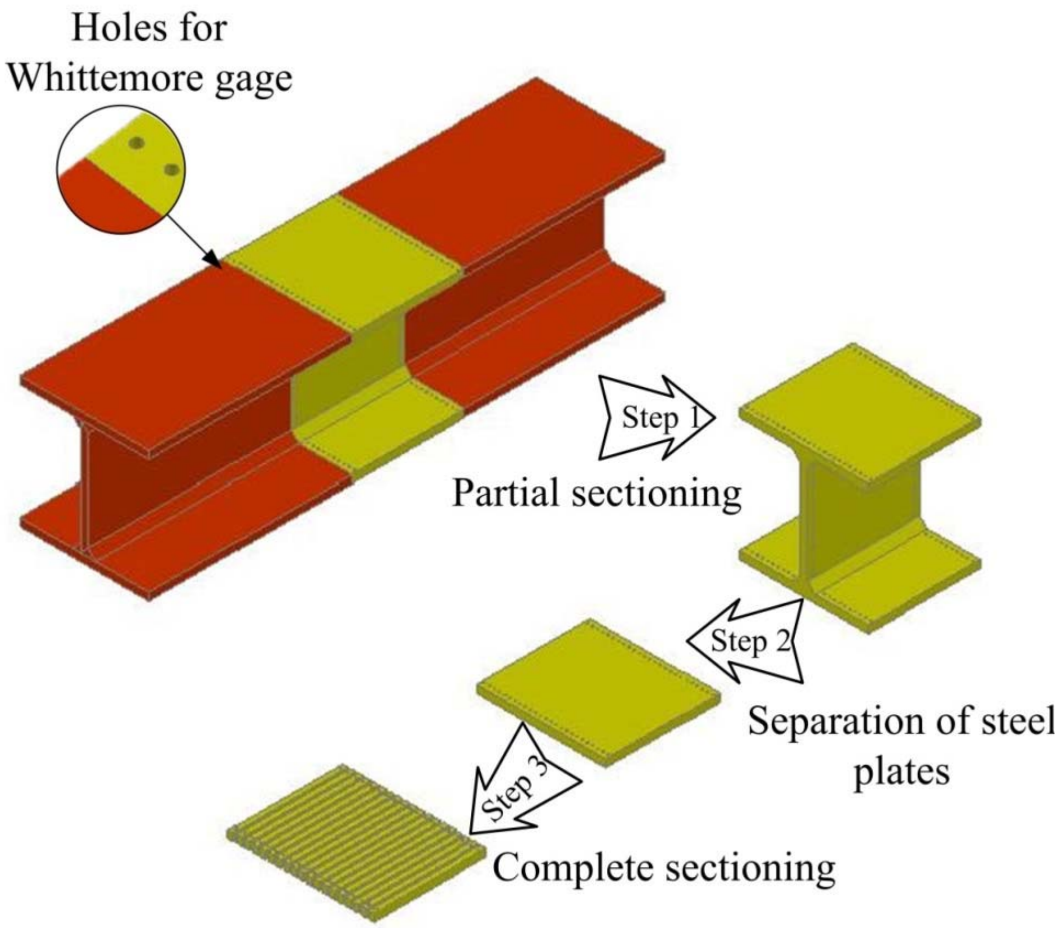

(b) H section specimen

Figure 3.1 Sectioning method steps

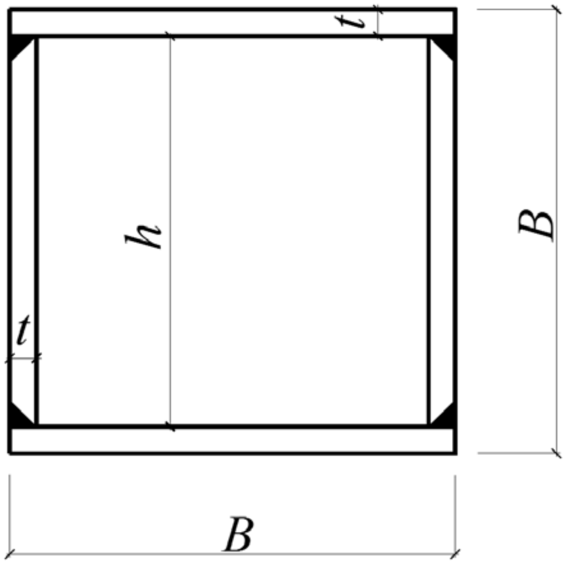

(a) Box section

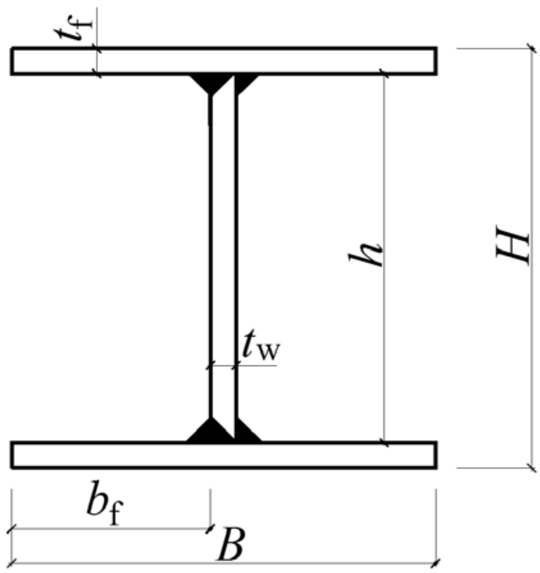

(b) H section

Figure 3.2 Definition of symbols

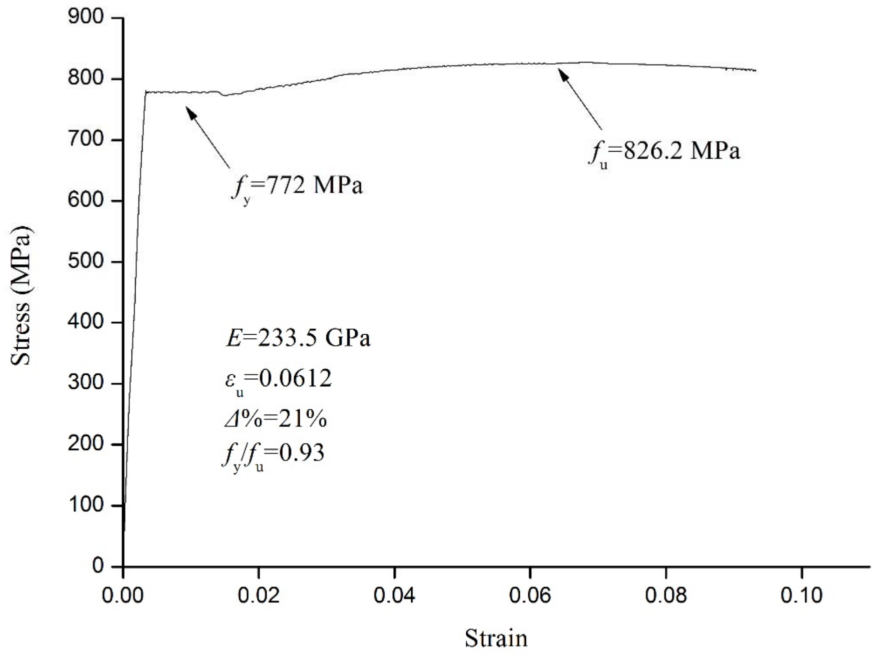

Figure 3.3 Stress-strain curve of Q690 steels

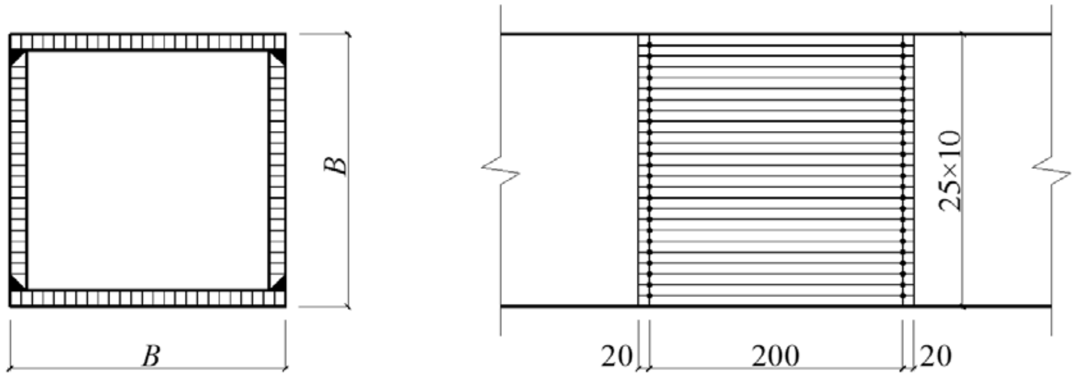

(a) Box section

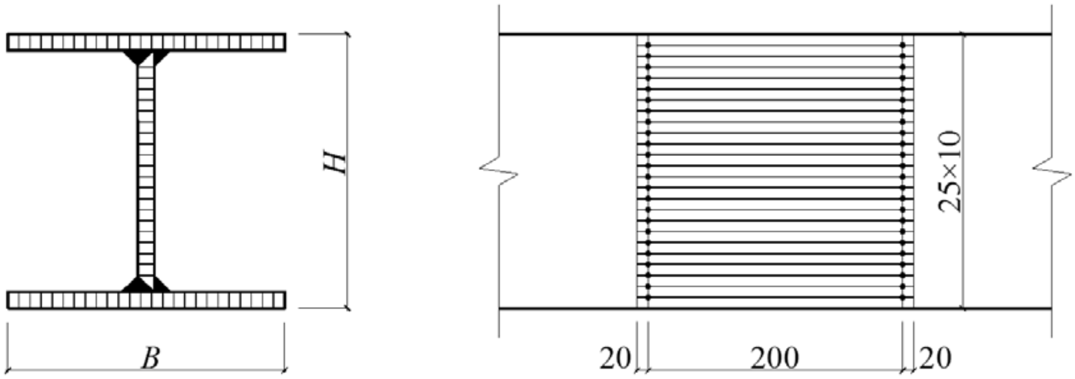

(b) H section

Figure 3.4 Diagram of sectioning locations

Figure 3.5 Initial measurement

Figure 3.6 Sectioning of measurement zones

(a) Partial sectioning

(b) Complete sectioning

Figure 3.7 Sectioning with a wire cutting machine

Figure 3.8 Sectioning strips

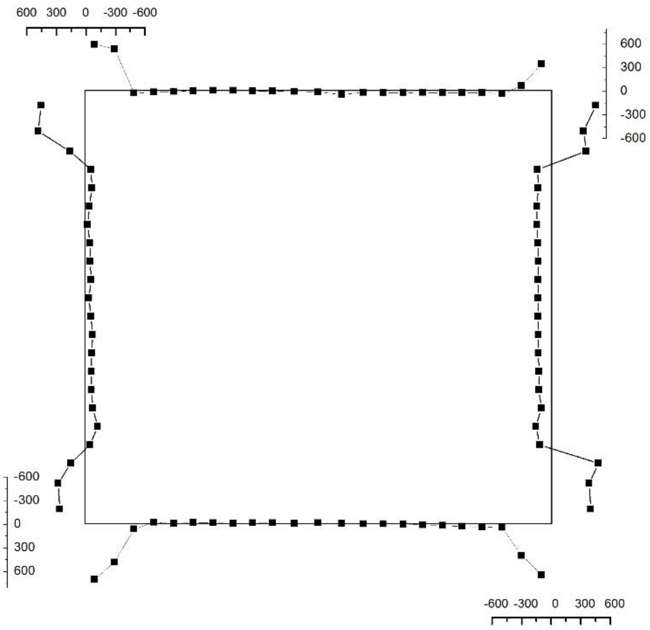
600 300 0 -300 -600
600
300
0
-300
-600
-600
-300
0
300
600
-600 -300 0 300 600

(a) R-B-13

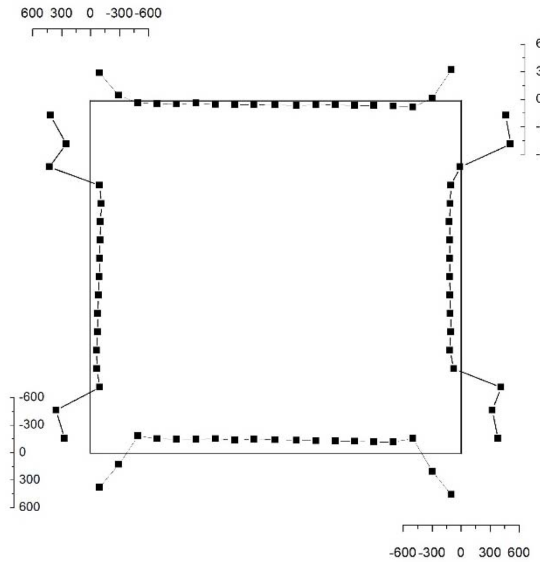
600 300 0 -300 -600
600
300
0
-300
-600
-600
-300
0
300
600
-600 -300 0 300 600

(b) R-B-10

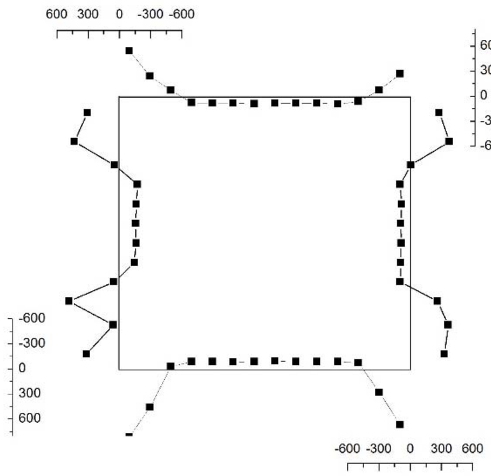

(c) R-B-7

Figure 3.9 Experimental results of box section specimens

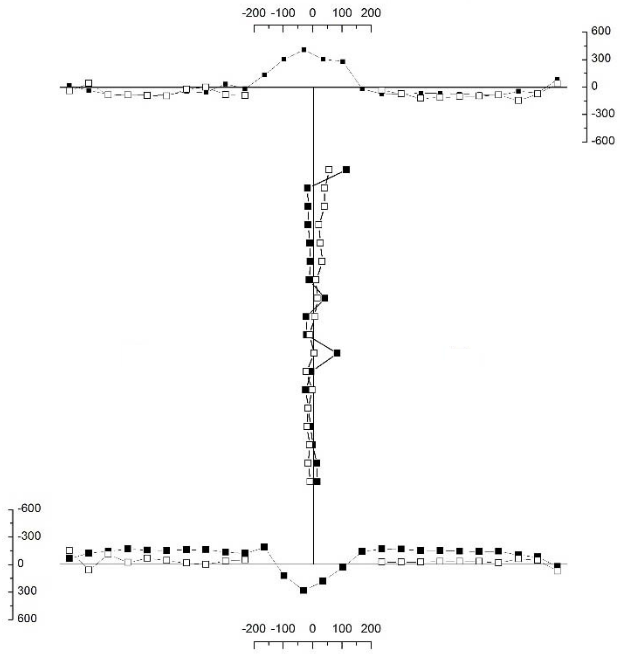

(a) R-H-8

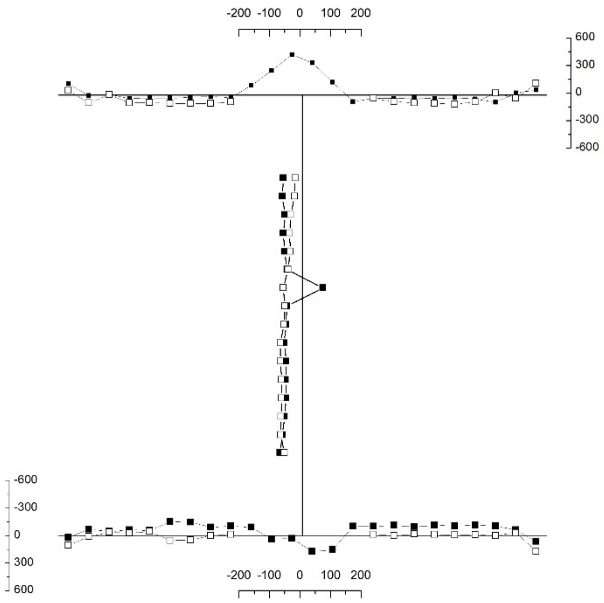

(b) R-H-7

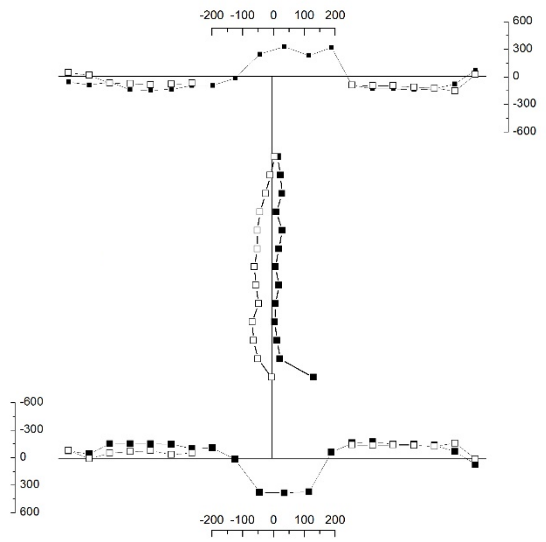

(c) R-H-6

Figure 3.10 Experimental results of H section specimens

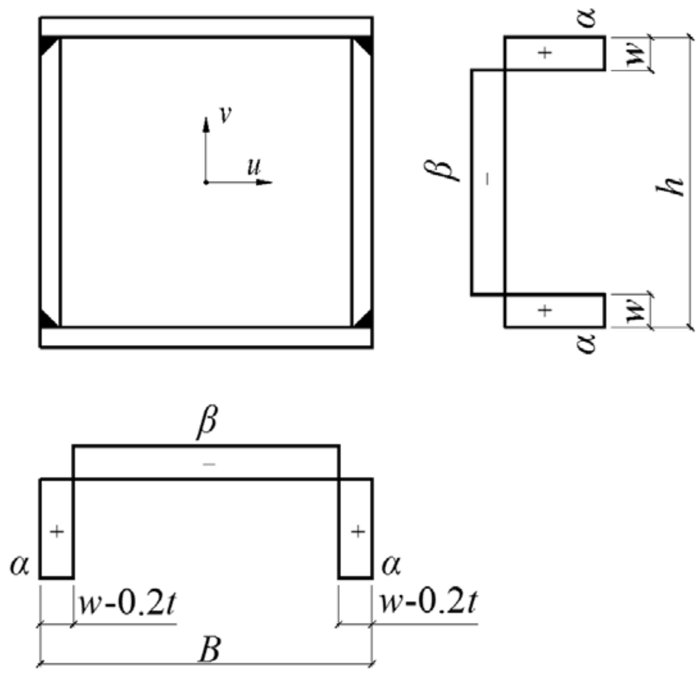

Figure 3.11 Residual stress model of box section

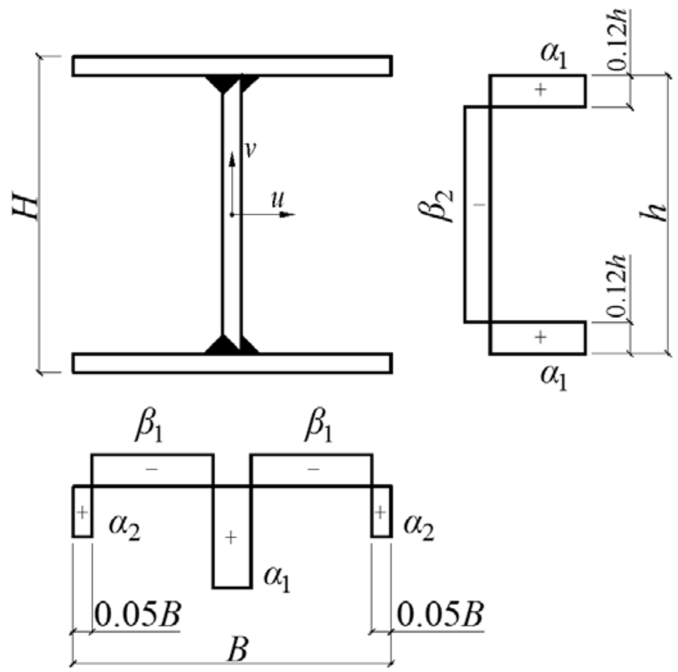

Figure 3.12 Residual stress model of H section

Tables

Table 3.1 Welding parameters

Diameter (mm)	Type	Current Type	Gas Composition	Flow Rate (L/min)	Electric Current (A)	Volts (V)	Travel Speed (cm/min)
φ1.2	Semi-Auto	DCEP	80%Ar+ 20%CO_2	15~20	260~290	28~30	25~35

Table 3.2 Actual dimensions of box section specimens

Specimen label	B (mm)	h (mm)	t (mm)	h/t	L (mm)
R-B-7	141.21	108.83	16.19	6.7	802
R-B-10	192.04	159.78	16.13	9.9	1009
R-B-13	235.64	203.04	16.30	12.5	1187

Table 3.3 Actual dimensions of H section specimens

Specimen label	B (mm)	b_f (mm)	t_f (t_w) (mm)	H (mm)	h (mm)	b_f/t_f	h/t_w	L (mm)
R-H-6	209.03	96.40	16.22	206.30	173.86	5.9	10.7	1075
R-H-7	240.25	112.07	16.11	239.63	207.42	7.0	12.9	1202
R-H-8	261.60	122.67	16.27	258.40	225.87	7.5	13.9	1283

Table 3.4 Residual stress ratios of box section specimens

Specimen label	α	β
R-B-7	0.394	-0.137
R-B-10	0.445	-0.126
R-B-13	0.496	-0.119

Table 3.5 Residual stress ratios of H section specimens

Specimen label	α_1	α_2	β_1	β_2
R-H-6	0.432	0.06	-0.136	-0.027
R-H-7	0.311	0.101	-0.078	-0.063
R-H-8	0.286	0.07	-0.103	-0.012

CHAPTER 4

EXPERIMENTAL STUDY ON AXIALLY LOADED COMPRESSION MEMBERS WITH WELDED BOX AND H SECTIONS

This chapter presents an experimental investigation on the overall buckling behavior of Q690 welded box and H columns under axial compression. The initial geometric imperfections of the specimens are provided, and the test results are discussed. Q690 steels exhibit a yield plateau, which differs from that of other high-strength steels. After flame heating, the yield plateau disappears and the yield strength tends to decrease when flame temperature exceeds 600°C. Additionally, the test data are compared with the buckling curves indicated in Chinese, European and American codes. Recommended curves that are suitable for Q690 steel columns are also presented.

4.1. Introduction

The local and overall buckling behaviors of high-strength steel columns with welded box and H sections have been investigated by Nishino and Tall (1970), Usami and Fukumoto (1982, 1984), Rasmussen and Hancock (1992, 1995), Sivakumaran and Yuan (1998), Ban *et al*. (2012, 2013b), and Wang *et al*. (2012c, 2014). The research findings indicate that the limits of plate slenderness ratios for ordinary steels are also suitable for high-strength steels, and that the residual stress-to-yield stress ratios of the welded sections of ordinary steels are larger than that of high-strength steels. The aforementioned studies, except those of Nishino and Tall (1970), Ban *et al*. (2012, 2013b), and Wang *et al*. (2012c, 2014), mainly focus on local stability and plate slenderness ratios. A few researchers have studied the overall buckling behavior of Q690 high-strength steel with box section and H section columns.

To investigate the mechanical behavior of high-strength steel columns, an axial compression experiment on Q690 steel members with welded box and H sections is conducted. The experimental results for the members fabricated from 16-mm thick steel plates are compared with the predictions indicated in the codes.

4.2. Experimental overview

4.2.1. Design and manufacture of specimens

Twelve columns with welded box and H sections were made from flame-cut Q690 steel plates (thickness = 16 mm), which were then subjected to axial compression. Their slenderness ratios were 30, 50 and 70, and each set of slenderness ratios corresponds to two specimens. The weld sizes and welding process of the columns were the identical with those adopted for the investigation on residual stresses as shown in Figure 3.2. These specimens were fabricated by GMAW, for which an ER120S-G filler wire with a nominal yield strength identical to that of Q690 was used. All component plates were connected by complete penetration welding. The adopted electric current ranged from 260 to 290 A and the voltage ranged from 28 to 30 V. The travel speed was 25 to 35 cm/min. An optimal welding sequence (anti-symmetric welding of sections) was adopted to reduce shrinkage deformation.

Given that the study focuses on determining overall buckling behavior, the width-to-thickness ratio of the specimens should not exceed the limiting ratio stipulated in the related codes. This restriction prevents local instability. The ratio limits for the box and H sections are expressed as follows:

For box sections:

In GB 50017-2003 (2003):

$$\frac{h}{t} \leq 40\sqrt{\frac{235}{f_{\mathrm{y}}}} \tag{4.1}$$

In Eurocode 3 (2005):

$$\frac{h}{t} \leq 42 \cdot \varepsilon = 42\sqrt{\frac{235}{f_{\mathrm{y}}}} \qquad \text{Class 3 cross-sections} \tag{4.2}$$

In ANSI/AISC 360-10 (2010):

$$\frac{h}{t} \leq 1.40\sqrt{\frac{E}{f_{\mathrm{y}}}} = 1.40\sqrt{\frac{200000}{f_{\mathrm{y}}}} \tag{4.3}$$

Figure 4.1(a) illustrates *h* and *t*. For the box sections, if the specified minimum yield stress, f_{y}, is determined as 690 MPa, the limiting ratios indicated in Chinese (GB 50017-2003, 2003) , European (Eurocode 3, 2005), and American (ANSI/AISC 360-10, 2010) specification are 23.3, 24.5, and 23.8, respectively.

For H sections:

In GB 50017-2003 (2003):

$$\frac{b_{\mathrm{f}}}{t_{\mathrm{f}}} \le (10+0.1\lambda)\sqrt{\frac{235}{f_{\mathrm{y}}}} \qquad 30 \le \lambda \le 100 \tag{4.4}$$

$$\frac{h}{t_{\mathrm{w}}} \le (25+0.5\lambda)\sqrt{\frac{235}{f_{\mathrm{y}}}} \qquad 30 \le \lambda \le 100 \tag{4.5}$$

In Eurocode 3 (2005):

$$\frac{b_{\mathrm{f}}}{t_{\mathrm{f}}} \le 14 \cdot \varepsilon = 14\sqrt{\frac{235}{f_{\mathrm{y}}}} \qquad \text{Class 3 cross-sections} \tag{4.6}$$

$$\frac{h}{t_{\mathrm{w}}} \le 42 \cdot \varepsilon = 42\sqrt{\frac{235}{f_{\mathrm{y}}}} \qquad \text{Class 3 cross-sections} \tag{4.7}$$

In ANSI/AISC 360-10 (2010):

$$\frac{b_{\mathrm{f}}}{t_{\mathrm{f}}} \le 0.64\sqrt{\frac{k_{\mathrm{c}}E}{f_{\mathrm{y}}}} = 0.64\sqrt{\frac{200000 \cdot k_{\mathrm{c}}}{f_{\mathrm{y}}}} \qquad 0.35 \le k_{\mathrm{c}} = 4\Big/\sqrt{h/t_{\mathrm{w}}} \le 0.76 \tag{4.8}$$

$$\frac{h}{t_{\mathrm{w}}} \le 1.49\sqrt{\frac{E}{f_{\mathrm{y}}}} = 1.49\sqrt{\frac{200000}{f_{\mathrm{y}}}} \tag{4.9}$$

Figure 4.1(b) depicts b_{f}, t_{f}, h and t_{w}. For the H sections, if the specified minimum yield stress, f_{y}, is equal to 690 MPa, the limiting width-to-thickness ratios of outstanding flanges indicated in the Chinese code range from 7.6 to 11.7, with a variable slenderness ratio λ; the ratios of webs vary from 23.3 to 43.8. In the European code, the limiting ratios of outstanding flanges and webs are 8.2 and 24.5, respectively. In the American code, such ratios range from 6.4 to 9.5, with varying k_{c}; the limit of webs is 25.4.

With reference to the aforementioned code limits, the width-to-thickness ratios of the designed box columns were 7, 10, and 13, which satisfy the requirements for local stability in the relevant specifications. For the designed H section columns, the ratios of outstanding flanges were 6, 7, and 8, and those of webs were 11, 13, and 14. These values also satisfy the provisions of the codes.

The realistic dimensions of the designed columns are listed in Table 4.1 and Table 4.2, where B-30-1 and H-70-2 represent the first box column with a slenderness ratio of 30 and the second H section column with a slenderness ratio of 70, respectively. B, t, H, t_f, and t_w are illustrated in Figure 4.1. In the two tables, L is the column length; L_e is the effective length between two pinned supports; A denotes the cross-section area; I represents the second moment of area for the box section columns; I_v is the second moment of area for the minor axis of the H section columns; λ and λ_v are the slenderness ratios of the box and H section columns; and $\overline{\lambda}$ and $\overline{\lambda}_v$ are the non-dimensional slenderness of the box and H section columns.

4.2.2. Material properties of Q690 steel products

In accordance with GB/T 2975-1998 (1998), five tension coupons were prepared from the original plates used to manufacture the specimens in the residual stress test and ultimate capacity test (see Figure 4.2). The cutting direction should be perpendicular to the rolling direction when samples are taken. Using an extensometer necessitates the acquisition of longitudinal strains that contribute to a precise elastic modulus. The material test was conducted using the 500-kN material testing machine (see Figure 4.3) of the State Laboratory for Disaster Reduction in Civil Engineering at Tongji University. With reference to GB/T 228-2002 (2002), the monotonic tensile test was carried out with a loading speed of 0.5 mm/min. Figure 4.2(a) shows the geometric dimensions of the tensile coupons. Certain data, such as yield strength, ultimate tension strength, and ultimate tensile elongation, should be collected. Table 4.3 lists the test results on the five tension coupons, where E is the elastic modulus of Q690 steel; Δ% is the percentage of elongation at rupture; ε_u denotes the ultimate strain; and f_y and f_u represent the yield strength and ultimate tension strength. The mean values of the five tension coupons (see Table 4.3) will be applied in numerical simulation. As shown in Figure 3.3, the Q690 steels exhibit a distinct elongation plateau, which differs from that of ordinary high-strength steels.

4.2.3. Loading setup and test arrangement

The axial compression experiment on the welded high-strength steel columns was carried out using the 10000-kN universal testing machine (see Figure 4.4) of the State Laboratory for Disaster Reduction in Civil Engineering at Tongji University. The boundary condition for both ends of the columns was pinned joint. To obtain ideally pinned ends, curved surface supports were adopted, as shown in Figure 4.5. The experimental results indicate that the supports exhibit an ideal rotation capacity. Box section columns were tested, with the pinned end about the u axis and the fixed end about the v axis (see Figure 4.1(a)). H section columns were tested with the pinned end at minor axis v and the fixed end at major axis u (see Figure 4.1(b)).

Before a column was set up on the testing machine, the external dimensions and initial geometric imperfections of the specimens were measured. During specimen setup, curved surface supports should remain horizontal and their neutral axes should coincide with those of the specimens. After specimen setup, preloading is necessary to verify the operating state of a strain data logger and displacement transducers and to determine positive direction. In this work, the preloading force was 10% of the estimated failure load. After the examination, the force was released. The experiment was initiated after the preparations were implemented.

Loading involves two stages: force control and axial displacement control. Within 80% of the assessed failure load, the loading increments were controlled by force. In this stage, each increment constituted 10% of the predicted failure load. When the loading force exceeded 80% of the expected failure load, the load increments were controlled by axial displacement increments at an acceleration of 1 mm/min speed to avoid abrupt instability. If the force reaches the ultimate capacity of the specimens, the monitored load will decrease. In this study, specimen failure was assumed to occur at a tracked load of less than 60% of the failure load of the columns. Under such a situation, unloading should be conducted.

Figure 4.6 displays the layout of the displacement transducers and strain gages in the experiment, wherein 16 displacement transducers were used to monitor the horizontal and vertical deformations caused by axial compression. The in-plane and out-plane deflections at mid-height of the specimens were measured with displacement transducers H01-H03 and H06, respectively. H04 and H05 monitored the lateral deflections at the three-eighth and five-eighth heights of the columns, respectively. The in-plane displacements of the supports were obtained by H08 and H11, and the out-plane displacements of the supports were obtained by H07, H09, H10, and H12. Displacement transducers V1 and V2 measured the vertical deformation of the specimens under axial compression. The rotational displacements at the top and bottom supports were monitored using displacement transducers V3-V6. As shown in Figure 4.6(b), 12 strain gages were attached onto the external surfaces of the box section specimens at mid-height and four gages were attached onto the bottom ends of the columns. For the H-section columns, 13 gages were attached at mid-height of the specimens and five gages were attached onto the bottom ends. The data provided by these strain gages represent strain distribution through the cross-section of the columns, which were used to monitor sectional stress-strain state. Figure 4.7 and Figure 4.8 show the column and experiment setups.

4.2.4. Initial geometric imperfections

Initial geometric imperfections consist of initial out-of-straightness and loading eccentricity, which significantly influence the global buckling behavior of high-strength steel columns. Before the experiment, these imperfections were measured and then applied in numerical simulation. The initial deflections (at $3L/8$, $L/2$ and $5L/8$) were determined by a pretensioned strand as a reference line attached onto both ends of the exterior of each specimen (see Figure 4.9). The maximum deflection was selected as the initial out-of-straightness v_0 at mid-height of each specimen. Table 4.4 lists the out-of-straightness values of all the specimens.

For the designed axially loaded compression columns, the neutral axes of the column end sections should coincide with those of the end plates. However, eccentricity e_0 exists in the specimens because of errors due to manual fabrication; this eccentricity was regarded as the loading eccentricity of the columns. To obtain data on the loading eccentricity in the bending plane, the deviations between the neutral axes of the column end sections and the bending axes of the supports were measured (see Figure 4.10). The mean values of the loading eccentricity at both ends of each specimen are listed in Table 4.4. The ratios of the initial geometric imperfections to the effective lengths of the columns are also summarized in Table 4.4.

4.3. Experimental results and discussion

4.3.1. Load–deflection relationships of columns

The experimental results are shown in Table 4.5, where P_u is the measured ultimate bearing capacity of the specimens; f_y is the realistic yield strength; and A denotes the sectional area. The load–deflection relationships at the mid-height columns are depicted in Figure 4.11 and Figure 4.12. Except specimens B-30 and H-30 series, the mean data from displacement transducers H01-H03 of other specimens were used to determine the mid-height deflection caused by the small deviations between such transducers. The failure mode of the 12 columns is the expected overall instability shown in Figure 4.13 and Figure 4.14. Because of the initial geometric imperfections, slight crookedness gradually occurs with increasing axial load, which leads to the rotation of the curved surface supports shown in Figure 4.15. When the loading force is close to the ultimate capacity of the specimens, the slope of the load–deflection curves gradually decrease. Provided that the specimens reach the limit state (i.e., the occurrence of overall instability), the horizontal deflection substantially increase with the slow descent of the monitored load. If the loading force constitutes 60% of the ultimate bearing capacity of the specimens, the tested column is treated as a complete failure and loading is terminated.

In the experiment, local buckling occurs at mid-height of specimen B-30-2 as the monitored load decreases to 80% of the failure load. Likewise, this behavior occurs near the middle of specimens H-30-1 and H-30-2 at an unloading of 80% of ultimate strength. For B-30-2, the compressed flange generates sunken deformation while the two webs perpendicular to the bending axis create convex deformation (see Figure 4.16(a)). For the H-30 series, the deformation at the compression flanges was treated as a single semi-wave sine shown in Figure 4.16(b). As seen in Figure 4.11(b), after the monitored load declines to 80% of the ultimate capacity of B-30-2, the corresponding displacement obtained by horizontal displacement transducer H02 shows a more distinct increasing trend than do H01 and H03. By contrast, although the H-30 series also brought about local buckling under the same conditions, the increase in this displacement (see Figure 4.12(a) and (b)) for H02 was undetected because of local buckling near mid-height of the specimens shown in Figure 4.16(b).

Additionally, after local buckling, the slope of the descending branch exhibits a rising trend (see Figure 4.11(b), and Figure 4.12(a) and (b)) and the degeneration of bearing capacity accelerates.

Note that the ultimate capacity of B-30-1 accounts for 59% of that of B-30-2 because the initial deflection of the latter expands given the flame heating conducted to prevent loading force from exceeding the capacity of the testing machine. Another factor that prompted the enlargement was that the high temperature (above 600 °C) of the flame detrimentally influences the yield strength of the component plates exposed to flame (Qiang *et al.*, 2012b). After the failure of B-30-1, four tension coupons were prepared to verify the yield strength of the relevant component plates. Specimens B-1, B-3, B-2, and B-4 were cut from the compression flange, tension flanges, and two webs. Figure 4.17(a) shows the geometric dimensions and Table 4.6 lists the testing results. Table 4.6 shows that specimen B-3 was not exposed to flame. Thus, its yield strength remains almost unchanged. The yield stresses of B-1, B-2 and B-4 drop to 80%, 82%, and 81%, respectively, compared with the levels derived from the test described above. Therefore, the increase in initial deflection and decrease in yield strength lead to early failure. Figure 4.18 shows that the yield plateau of the flame-heated specimens vanishes because of the effects of high temperature. Given the breakdown of the extensometer attached onto B-4, the stress-strain curve cannot represent a hardening stage. The above-mentioned results indicate that in conducting flame straightening, the temperature applied to Q690 steel plates should not exceed 600 °C.

Because of the large initial geometric imperfections, H-70-1 was straightened by the flame heating method. After the axial compression experiment, three tensile coupons were prepared. Specimens H-1 and H-3 were cut from the two flanges and H-2 was cut from the web. Figure 4.17(a) shows the external sizes of the specimens and Table 4.6 presents the testing results. Specimen H-1 was not exposed to flame; therefore, its yield strength remains unchanged. The yielding stresses of H-2 and H-3 decline to 97% and 98% compared with the original testing result. The yield plateau of the specimens continues to exist, as shown in Figure 4.19. These results indicate that temperature was not effectively controlled during the straightening of H-70-1.

As depicted in Figure 4.11 and Figure 4.12, the slope of the load–deflection curves and ultimate bearing capacity of the specimens decrease with increasing initial geometric imperfections. The specimens are increasingly sensitive to initial imperfections when slenderness ratios rise. Figure 4.12(c) shows that after the ultimate capacity of the specimens (i.e., H-50 series) is reached, the load drops to about 35% of the failure load. This result is attributed to the abrupt instability that occurs in specimens H-50 series, and to the reaction time lag generated by the pressure sensor of the testing machine.

Vertical displacement transducers V1 and V2 monitored the axial deformation of the specimens. Figure 4.20 shows the load–versus–axial displacement curves, for which the mean values of V1 and V2 were adopted. As shown in the figure, the large sectional specimens (such as B-30 and H-30 series) with high axial rigidity *EA* exhibit a considerable slope of loading branch curves and a nonlinear state before the failure load is reached. For the small sectional columns (e.g., B-70 and H-70 series) with low *EA,* the slope is lower and the specimens maintain an approximately linear state before failure load is reached. The failure modes of these specimens can be regarded as elastic instability.

4.3.2. Load–strain relationships of columns

Twelve and thirteen strain gages (see Figure 4.6) were attached onto the exterior at mid-height of box and H columns, respectively. At 200 mm above the bottom end plate, four and five strain gages were also attached onto the box and H section specimens. These strain gages were used to monitor the stress-strain state of the sections during loading. Data on six specimens were extracted from all the specimens to depict the stress-strain curves shown in Figure 4.21 and Figure 4.22. For the critical section at mid-height of the box columns, strain gages S02 and S08 monitored the strains at mid-width of the webs. The strains at the edges of the flanges of the box sections (see Figure 4.6) were presented by S04, S06, S10, and S12. For the H column sections, S02 and S08 presented the strains at mid-width of the flanges. Strain gages S03, S07, S01, and S09 provided the strains at the tips of the H section flanges. Figure 4.21 and Figure 4.22 show that the strains with varied locations at critical section are almost identical under the initial loading branch; these strains are the characteristic of axial compression. Subsequently, the stress state of the sections becomes the coupling state of axial compression and bending because the initial imperfections (i.e., geometric imperfections and residual stress) strongly influence the stress-strain state of the sections as loading force increases. The compression zone of specimens B-30-

2 and H-30-1 is located at the right side of the sections. By contrast, the compressive areas of B-50-1, B-70-1, H-50-2, and H-70-2 are located at the left side of the sections. Their bending directions coincide with the directions of the initial geometric imperfections.

Figure 4.21 shows that when the ultimate capacity is reached, the compressive strain at mid-width of the webs for specimen B-30-2 accounts for 101.8% of yield strain f_y/E, which indicates strength failure. For specimen B-70-1, which has a large slenderness, this strain constitutes 57.5% of yield strain under the same conditions. This finding reflects the characteristics of elastic instability. The strain of specimen B-50-1, which falls within the strains of B-30-2 and B-70-1, represents 85.9% of yield strain; the compressive flange completely yields. Specimen B-50-1 is significantly affected by the initial imperfections, and its instability model is classified under elastic–plastic instability.

Figure 4.22 shows the stress-strain relationships at the critical section of the H columns. For specimen H-30-1, the compression strain located in the middle of the sectional flanges accounts for 159.2% of yield strain. This phenomenon can be assumed as equivalent to strength failure. The strain of H-70-2 drops to 56% of yield strain under the same conditions, and its instability mode is close to elastic instability. The strain of H-50-2, which falls within those of H-30-1 and H-70-2, constitutes 95.1% of yield strain and the compressive tips of the flanges yield. Initial imperfections can substantially influence these kinds of specimens, and the failure that they exhibit is characteristic of elastoplastic instability.

4.4. Comparison of experimental results and design specifications

4.4.1. Relevant code provisions

In GB 50017-2003 (2003), the design buckling resistance of an axial compression member is expressed as,

$$N_{\mathrm{d}} = \frac{\chi A f_{\mathrm{y}}}{\gamma_R} \tag{4.10}$$

where χ is the reduction factor for overall buckling; γ_R denotes the partial factor for resistance, which can be set as 1.0 with the application of a realistic yield strength under the absence of related provisions for Q690 steel.

When $\bar{\lambda} \le 0.215$,

$$\chi = 1 - \alpha_1 \bar{\lambda}^2 \tag{4.11}$$

When $\bar{\lambda} > 0.215$,

$$\chi = \frac{\left[\left(\alpha_2 + \alpha_3\bar{\lambda} + \bar{\lambda}^2\right) - \sqrt{\left(\alpha_2 + \alpha_3\bar{\lambda} + \bar{\lambda}^2\right)^2 - 4\bar{\lambda}^2}\right]}{2\bar{\lambda}^2} \tag{4.12}$$

where $\bar{\lambda}$ is the non-dimensional slenderness; and α_1, α_2 and α_3 are the factors corresponding to the appropriate types of cross-sections (Class a, b, and c sections).

In Eurocode 3 (2005), the design buckling resistance is taken as,

$$N_{\mathrm{d}} = \frac{\chi A f_{\mathrm{y}}}{\gamma_{\mathrm{M1}}} \quad \text{for Class 1, 2, and 3 cross-sections} \tag{4.13}$$

in which γ_{M1} is the partial factor for the resistance of members to instability assessed by member checks; the recommended value for this factor is 1.0. χ is the reduction factor for overall buckling, which can be given as follows:

When $\bar{\lambda} \leq 0.2$, $$\chi = 1 \tag{4.14}$$

When $\bar{\lambda} > 0.2$, $$\chi = \frac{1}{\Phi + \sqrt{\Phi^2 - \bar{\lambda}^2}} \tag{4.15}$$

where $\Phi = 0.5\left[1 + \alpha\left(\bar{\lambda} - 0.2\right) + \bar{\lambda}^2\right]$, and α is the imperfection factor for the corresponding buckling curve.

In ANSI/AISC 360-10 (2010), the design buckling strength is determined thus:

$$N_{\mathrm{d}} = \phi_{\mathrm{c}} f_{\mathrm{cr}} A \tag{4.16}$$

where ϕ_c is the resistance factor, for which a value of 0.9 is recommended. f_{cr} represents the critical stress, written as follows:

When $\lambda \leq 4.71\sqrt{\dfrac{E}{f_{\mathrm{y}}}}$, $$f_{\mathrm{cr}} = \left[0.658^{\frac{f_{\mathrm{y}}}{f_{\mathrm{e}}}}\right] f_{\mathrm{y}} \tag{4.17}$$

When $\lambda > 4.71\sqrt{\dfrac{E}{f_{\mathrm{y}}}}$, $$f_{\mathrm{cr}} = 0.877 f_{\mathrm{e}} \tag{4.18}$$

in which λ is the slenderness ratio and $f_{\mathrm{e}} = \dfrac{\pi^2 E}{\lambda^2}$.

If non-dimensional slenderness $\bar{\lambda}$ substitutes for the slenderness ratio λ in Equations (4.17) and (4.18), these two equations can be written as follows:

When $\bar{\lambda} \leq 1.5$,
$$\chi = \frac{f_{\mathrm{cr}}}{f_{\mathrm{y}}} = \left[0.658^{\bar{\lambda}^2}\right] \tag{4.19}$$

When $\bar{\lambda} > 1.5$,
$$\chi = \frac{f_{\mathrm{cr}}}{f_{\mathrm{y}}} = \frac{0.877}{\bar{\lambda}^2} \tag{4.20}$$

4.4.2. Comparison of experimental results with GB 50017-2003 (2003)

As indicated in the related provisions of GB 50017-2003 (2003), the buckling curve for Class c section is suited for welded box columns that have a maximum 20 width-to-thickness ratio. The B-30, B-50, and B-70 series satisfy this condition and are therefore classified under Class c section. Figure 4.23(a) shows the comparison of the experimental results for the buckling and Euler curves, where the abscissa is the non-dimensional slenderness and the ordinate is the reduction factor. The figure illustrates that the reduction factors of all the specimens, except B-30-1, are higher than buckling curves “c” and “b” because of the overlarge initial deflection and deterioration of yield strength. This finding suggests that the provisions for welded box columns with Q690 steel are conservative. If the average data in Figure 4.23(a) are adopted, the buckling curve for Class a section could be appropriate for this kind of columns. Consequently, for welded Q690 box-columns with a 20 width-to-thickness ratio or less, the relevant provisions should be appropriately revised. Nevertheless, the experimental data derived are insufficient and the conclusion requires additional numerical support to validate the feasibility of the revision.

The sections of the H-30, H-50, and H-70 series fall under the Class b section in GB 50017-2003 (2003), which categorizes flame-cut welded H columns with plates of less than 40 mm under this classification. As shown in Figure 4.23(b), the reduction factors of all the specimens, except H-70-1, are higher than buckling curve “a” because of the yield strength degradation caused by flame heating. This result indicates that curve “a” is probably suited for Q690 flame-cut welded H columns. The solidity of this conclusion requires further verification with numerical data.

4.4.3. Comparison of experimental results with Eurocode 3 (2005)

For welded box columns with a less than 30 width-to-thickness ratio, buckling curve “c” is appropriate, as specified in Eurocode 3 (2005). The B-30, B-50, and B-70 series are suitable for classification under this provision. Figure 4.24(a) shows the comparison of the experimental results and the predictions of the code, in which the abscissa is the non-dimensional slenderness and the ordinate is the reduction factor. As seen in this figure, the reduction factors of the specimens, except specimen B-30-1, are larger than that depicted by curve “a” because of the considerable initial deflection and degeneration of yield strength. This result indicates that Eurocode 3 (2005) underestimates the ultimate capacity of this type of specimens. The result also suggests that buckling curve “a” is more appropriate than curve “c”. This finding, however, also requires further validation by numerical simulation.

The H columns in this study satisfy the provision specified in Eurocode 3 (2005); that is buckling curve “c” is suited for the welded H columns with plates of less than

40 mm when buckling occurs about the minor axis. Except for the reduction factor of specimen H-70-1, those of the other specimens depicted in Figure 4.24(b) are higher than curve a. This result is attributed to the fact that the degradation of yield strength affects the ultimate capacity of H-70-1. The obtained experimental data suggest that curve “a” is appropriate for this type of H specimens, but that the practicability of the result requires confirmation via numerical testing.

4.4.4. Comparison of experimental results with ANSI/AISC 360-10 (2010)

For the design of axial compression members, multiple buckling curves are recommended in GB 50017-2003 (2003) and Eurocode 3 (2005), whereas only a single curve is employed as stipulated in ANSI/AISC 360-10 (2010). The curve specified in the American code is suitable for compression members without slender elements. Figure 4.25(a) shows that except for the reduction factors of specimens B-30-1 and B-70-2, those of the other box columns are larger than that depicted by the buckling curve. For the H columns, except H-70-1, the reduction factors are close to or higher than the buckling curve (see Figure 4.25(b)). These two findings indicate that the provisions of the American code for welded Q690 box and H columns without slender elements are conservative.

4.5. Concluding remarks

An experimental investigation on the overall buckling behavior of Q690 welded box columns and flame-cut H columns was carried out. The failure mode of the twelve columns is anticipated as equivalent to global instability. For specimens B-30-2, H-30-1, and H-30-2, local buckling increases at mid-height when the monitored load decreases to 80% of the failure load. After local buckling, the degradation of the bearing capacity tends to accelerate. The ultimate capacity of specimens B-30-1 and H-70-1 is considerably impaired by flame heating. If the temperature of a flame exceeds 600 °C, the yield strength of Q690 steel plates may decrease by 20% or lower (Qiang *et al.*, 2012b). When conducting flame straightening, therefore, the temperature applied to steel plates should not exceed 600 °C. High temperatures can also eliminate the yield plateau of Q690 steels.

On the basis of the test results, the Chinese (GB 50017-2003, 2003), European (Eurocode 3, 2005), and American (ANSI/AISC 360-10, 2010) codes underestimate the ultimate bearing capacity of Q690 welded box columns and flame-cut H columns. For GB 50017-2003 (2003), buckling curve "a" is more suitable for the two types of columns rather than curves "c" and "b". In terms of Eurocode 3 (2005), curve "a" more strongly agrees with the experimental data than does curve "c". Nevertheless, these recommendations require more numerical testing to verify their feasibility.

Figures

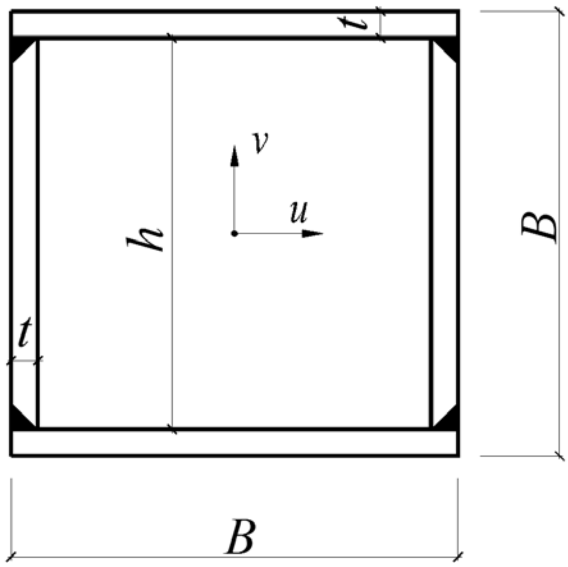

(a) Box section

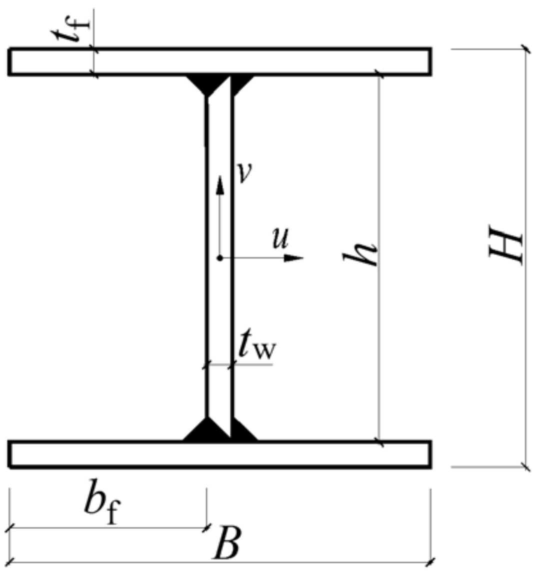

(b) H section

Figure 4.1 Column sections

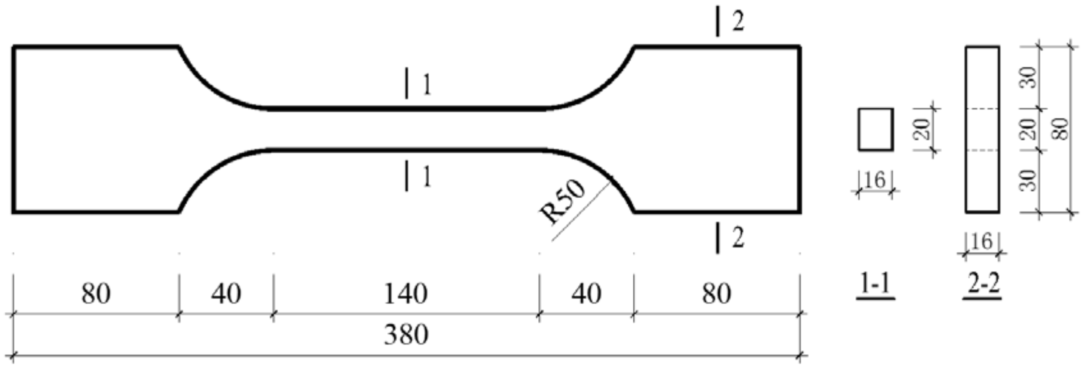

(a) External dimensions of tension coupons

(b) A realistic specimen

Figure 4.2 Tension coupons for material test

Figure 4.3 500-kN testing machine

Figure 4.4 10000-kN universal testing machine

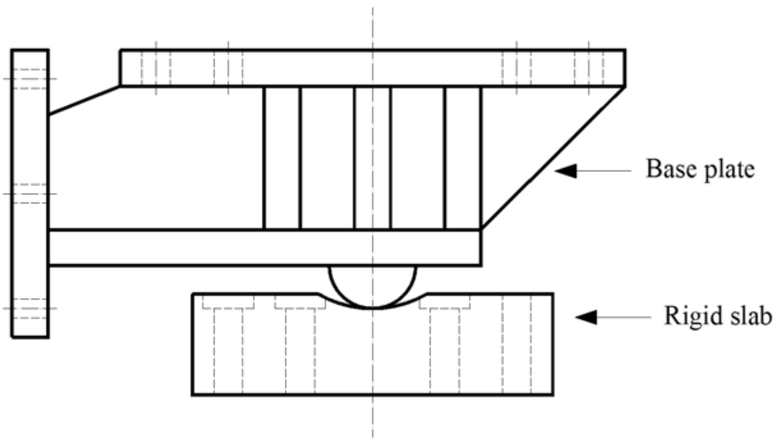

(a) Top support

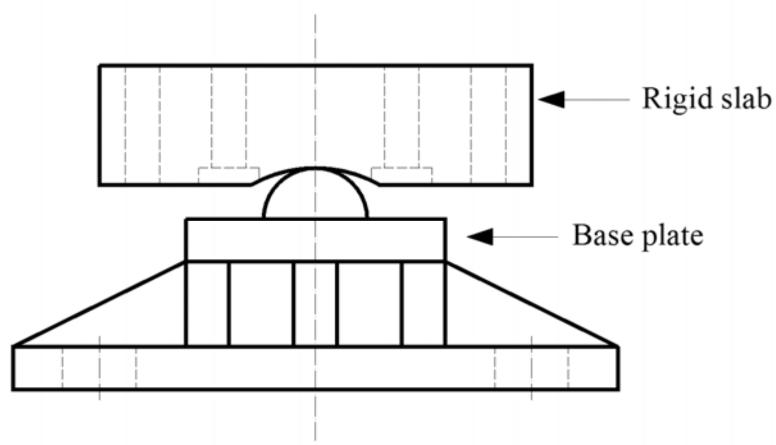

(b) Bottom support

Figure 4.5 Elevation of curved surface supports

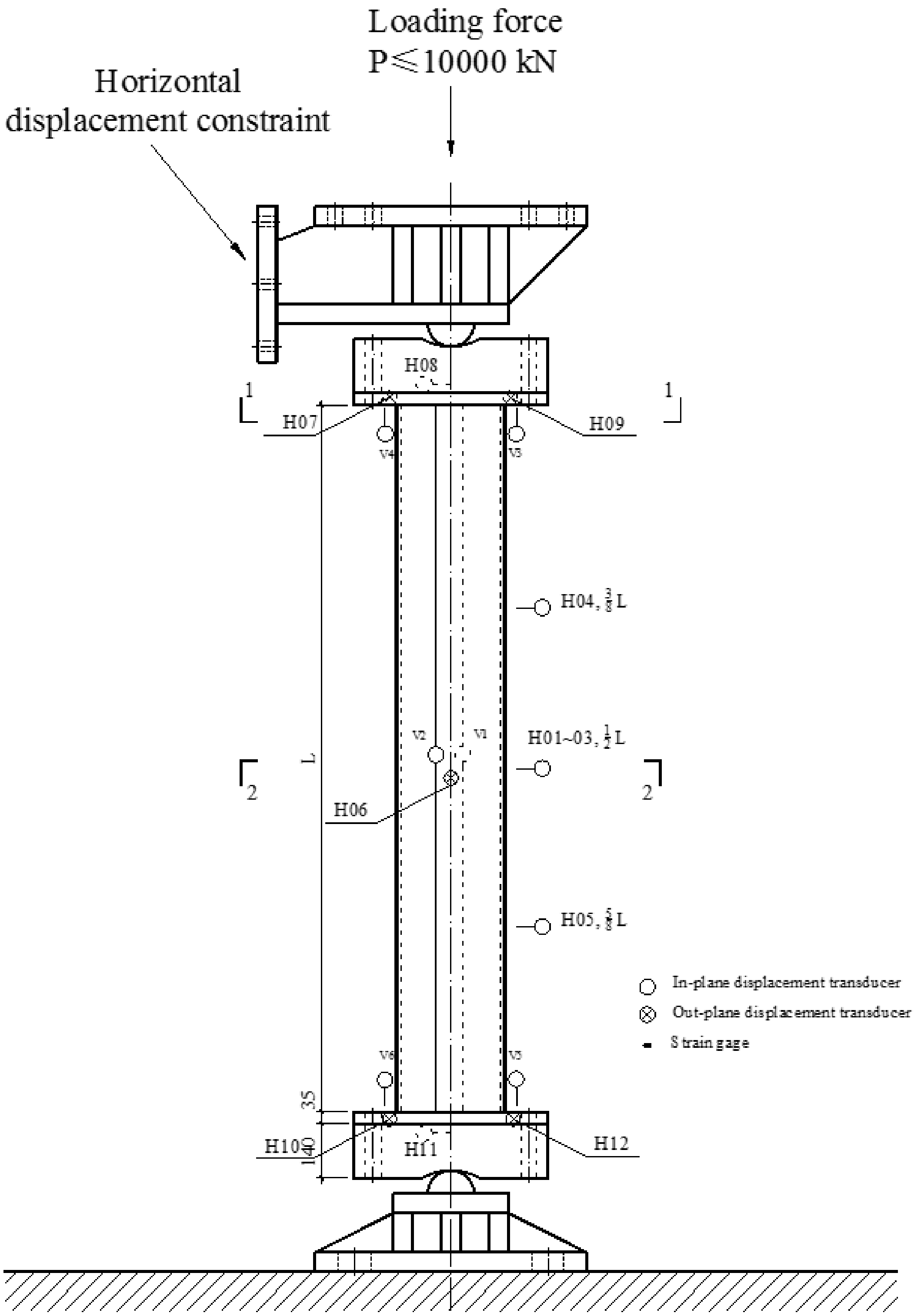
Loading force
P≤10000 kN
Horizontal
displacement constraint
H08
H07
H09
V4
V3
H04, 3/8 L
V2
V1
H01~03, 1/2 L
L
H06
H05, 5/8 L
In-plane displacement transducer
Out-plane displacement transducer
Strain gage
V6
V5
35
140
H10
H11
H12
1
1
2
2

(a) Elevation

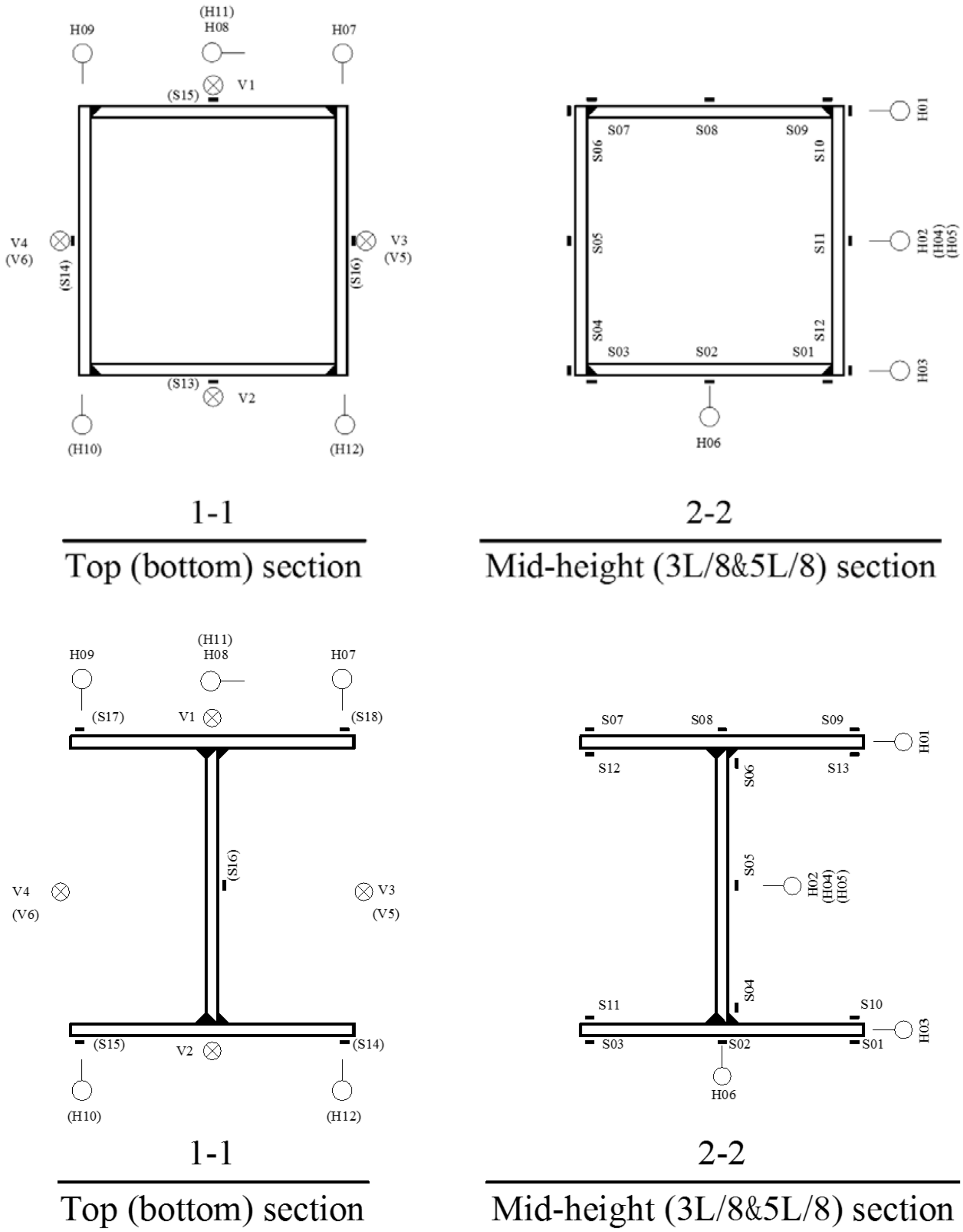

(b) Cross section

Figure 4.6 Arrangement of displacement transducers and strain gages

B-30-2 B-50-1 B-70-2

Figure 4.7 Box columns and experiment setup

H-30-1 H-50-2 H-70-2

Figure 4.8 H columns and experiment setup

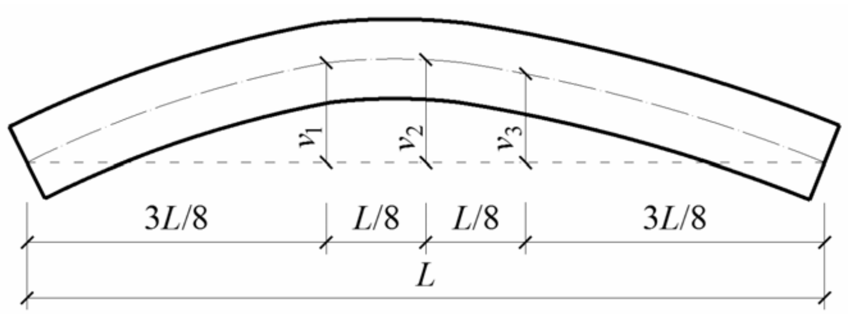

Figure 4.9 Initial out-of-straightness of columns

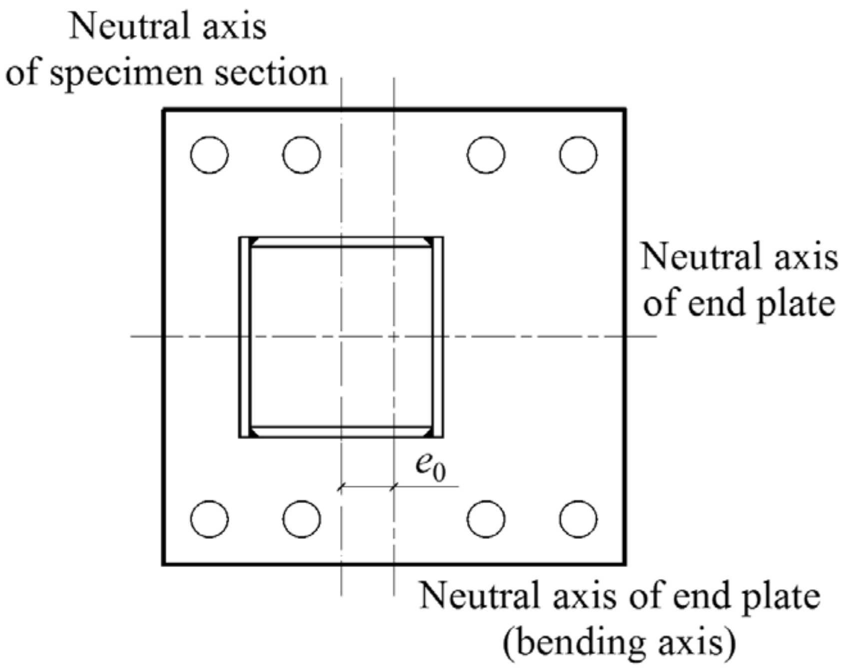

(a) Eccentricity for box section

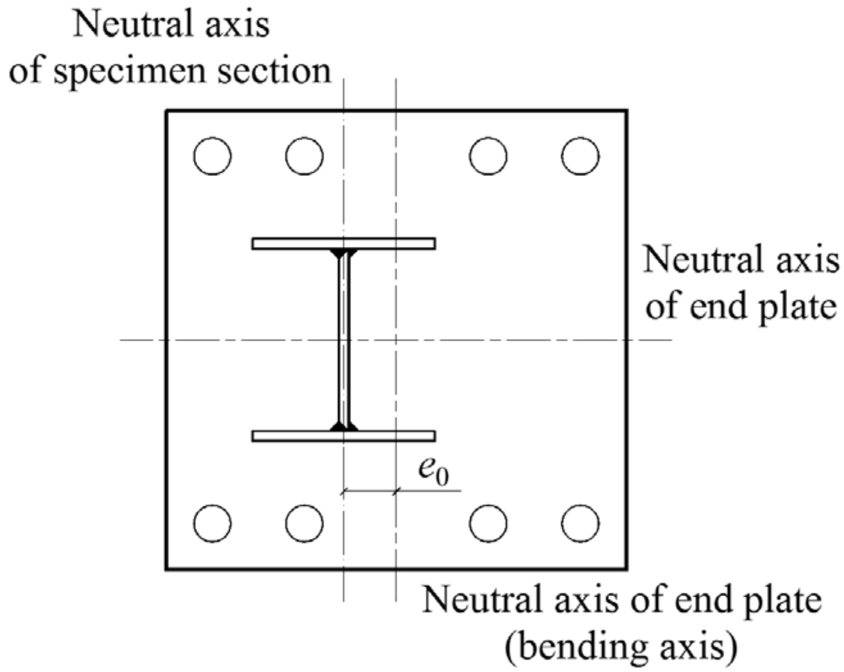

(b) Eccentricity for H section

Figure 4.10 Initial eccentricity of columns

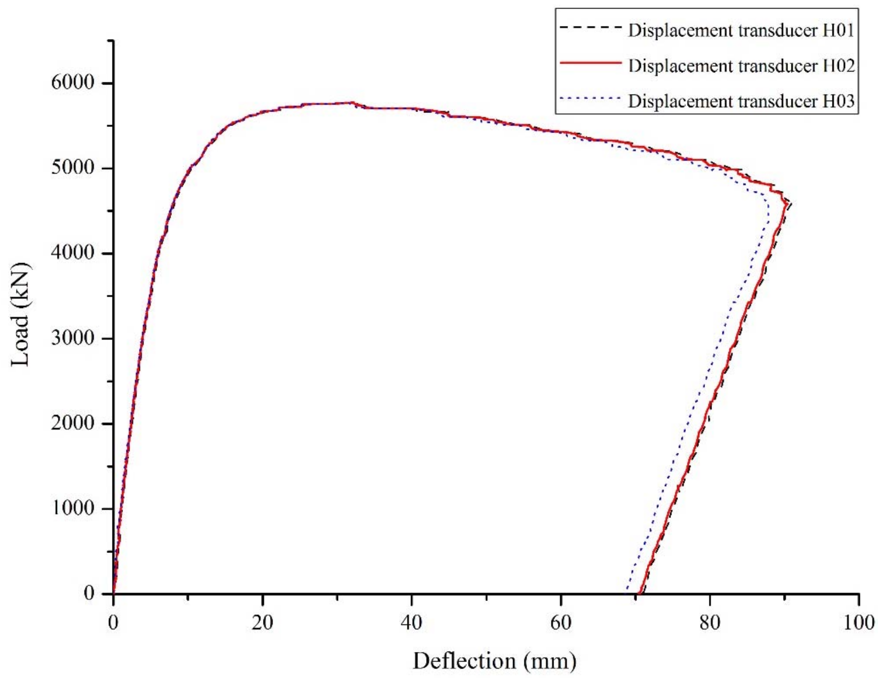

(a) B-30-1

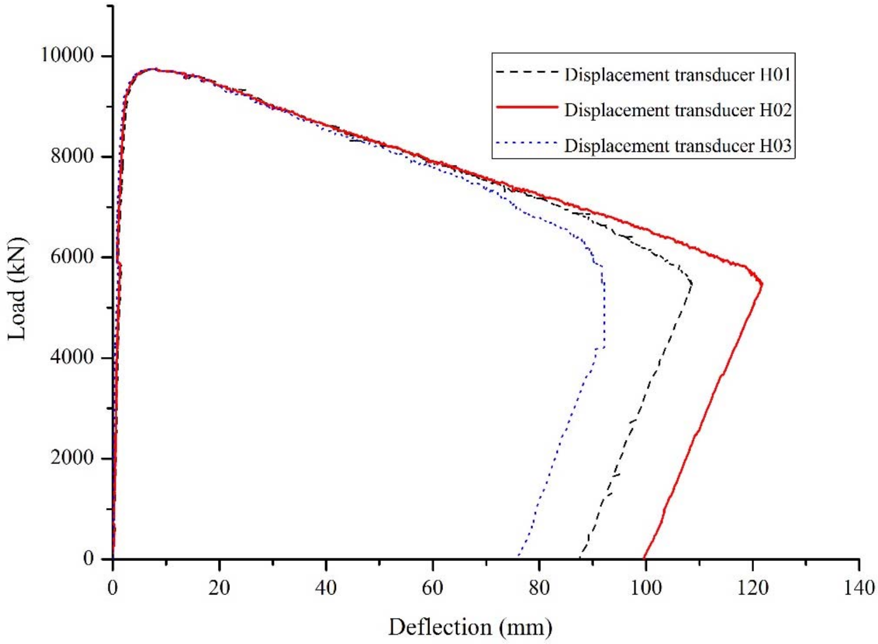

(b) B-30-2

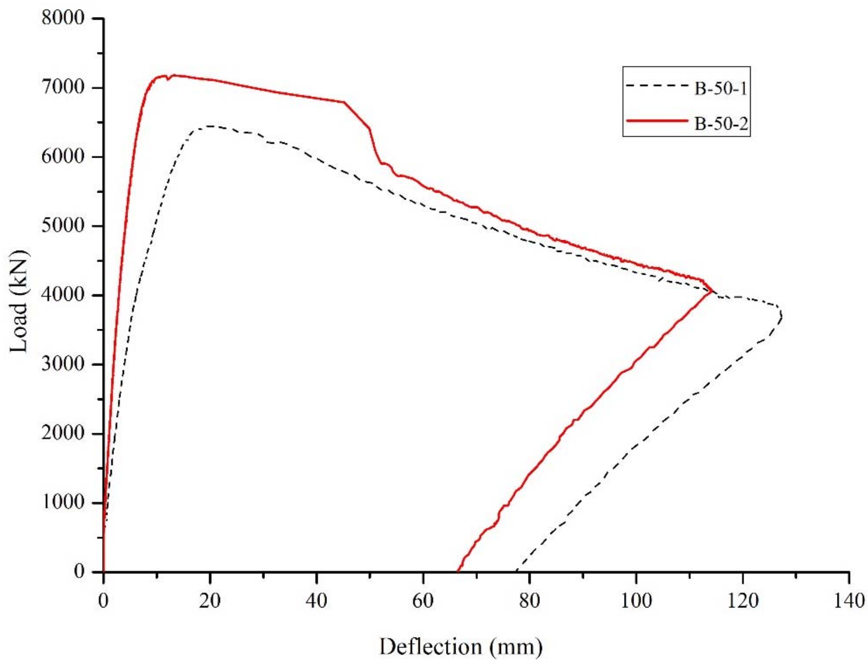

(c) B-50-1 and B-50-2

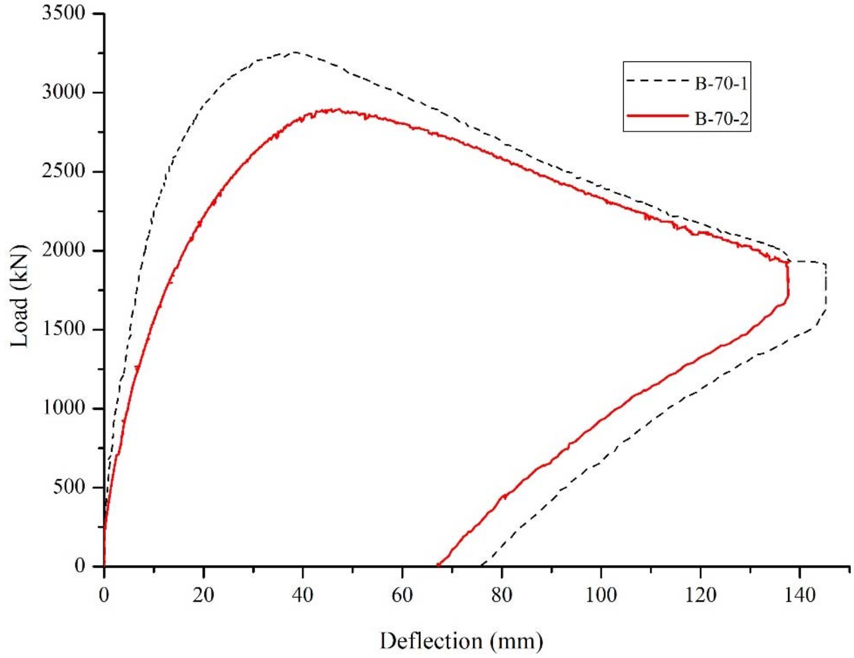

(d) B-70-1 and B-70-2

Figure 4.11 Load–deflection curves for box section specimens

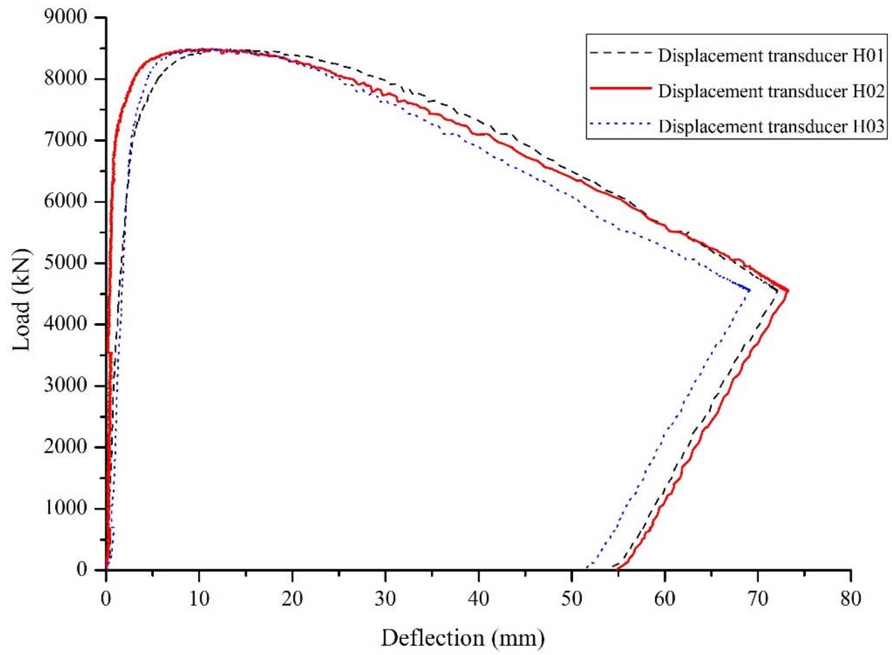

(a) H-30-1

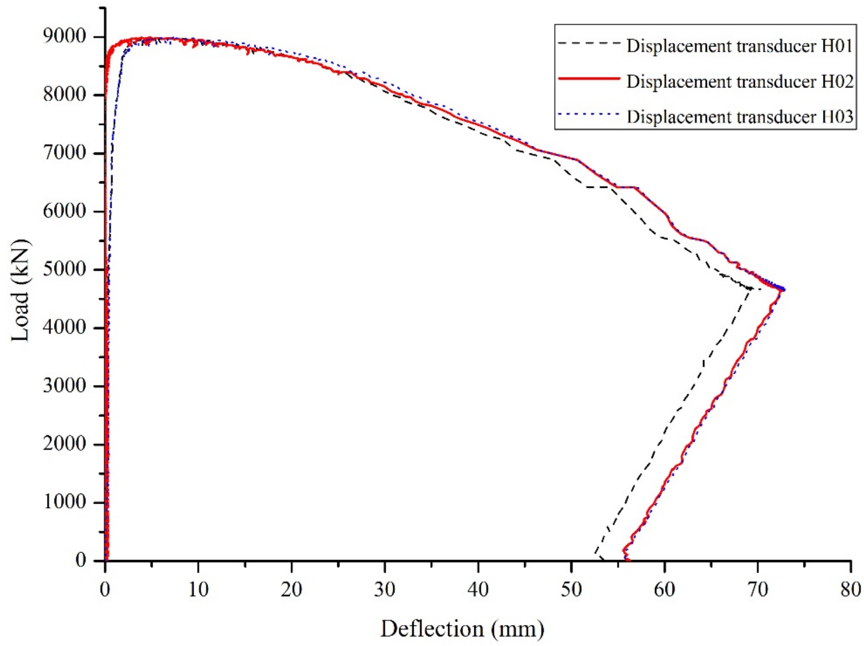

(b) H-30-2

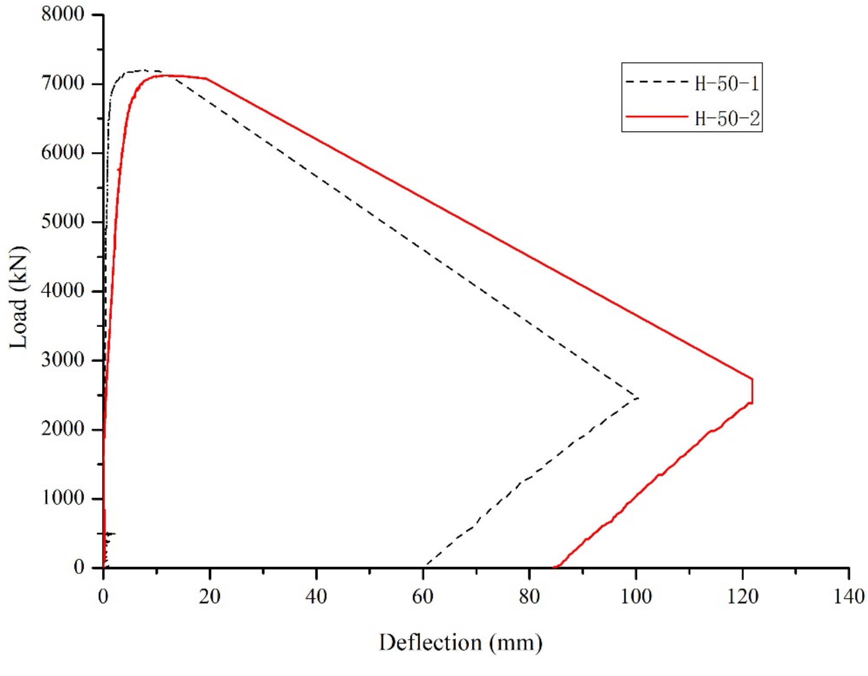

(c) H-50-1 and H-50-2

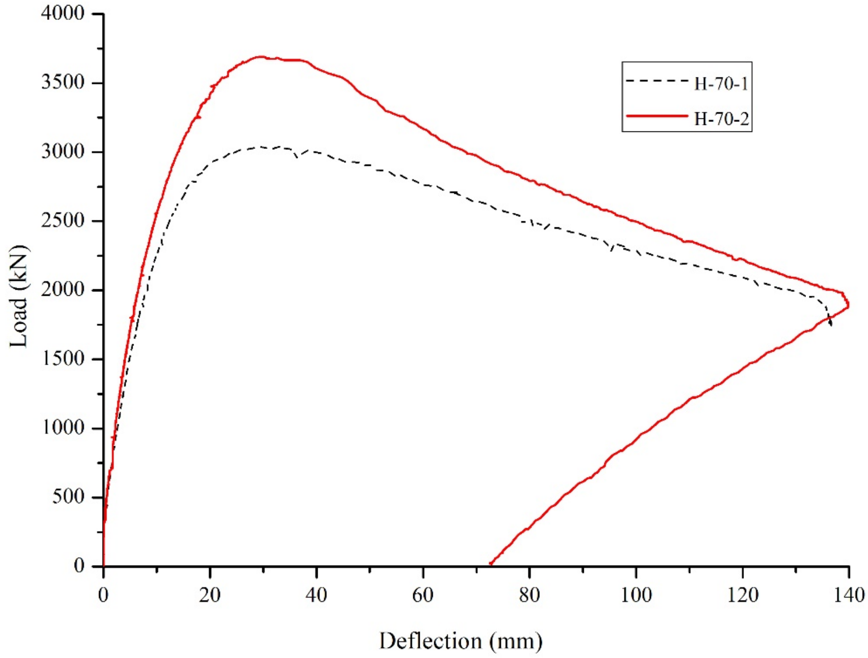

(d) H-70-1 and H-70-2

Figure 4.12 Load–deflection curves for H section specimens

B-30-2 B-50-1 B-70-2

Figure 4.13 Box columns after failure

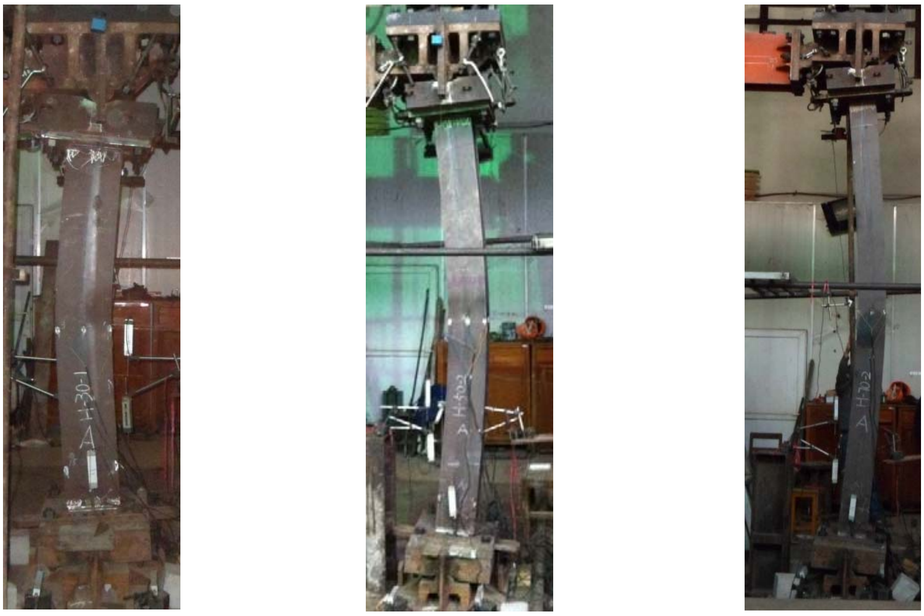

H-30-1 H-50-2 H-70-2

Figure 4.14 H columns after failure

(a) Before loading (b) After failure

Figure 4.15 Rotation of support

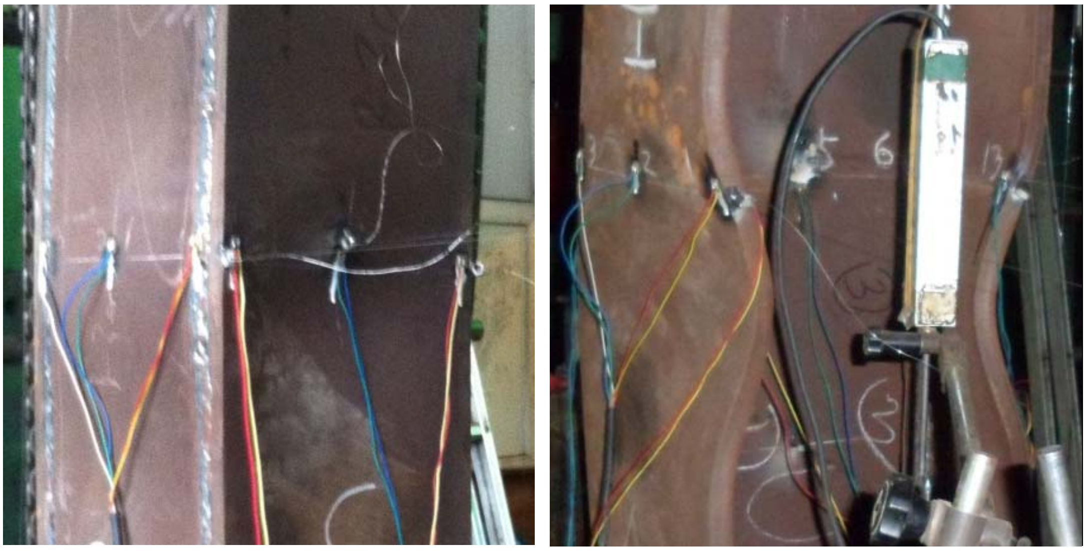

(a) B-30-2 (b) H-30-1

Figure 4.16 Local buckling after failure

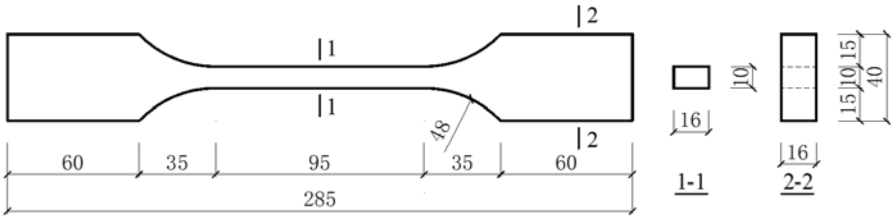

(a) Geometric dimensions of tension coupons

(b) Tension coupons from B-30-1

(c) Tension coupons from H-70-1

Figure 4.17 Tension coupons for material testing

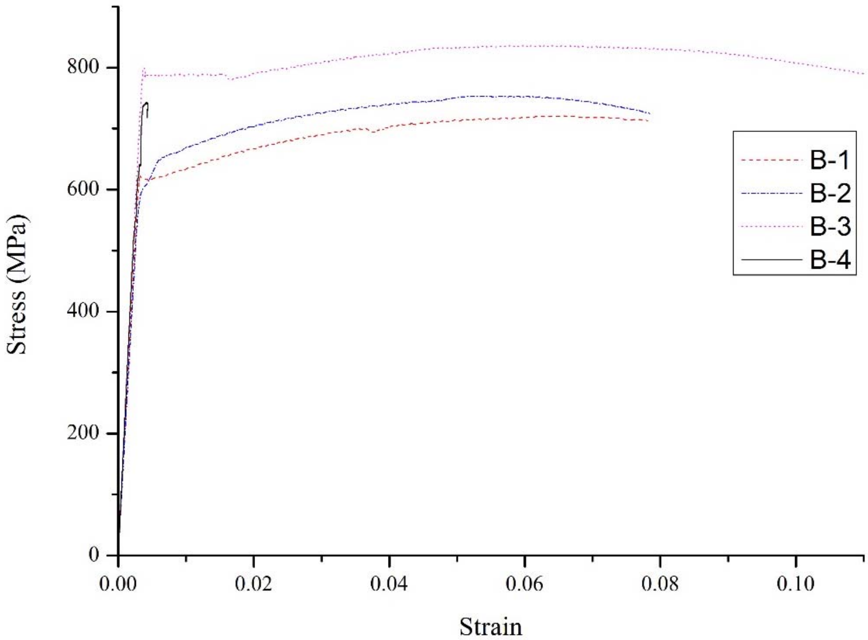

Figure 4.18 Stress-strain curve of B-30-1

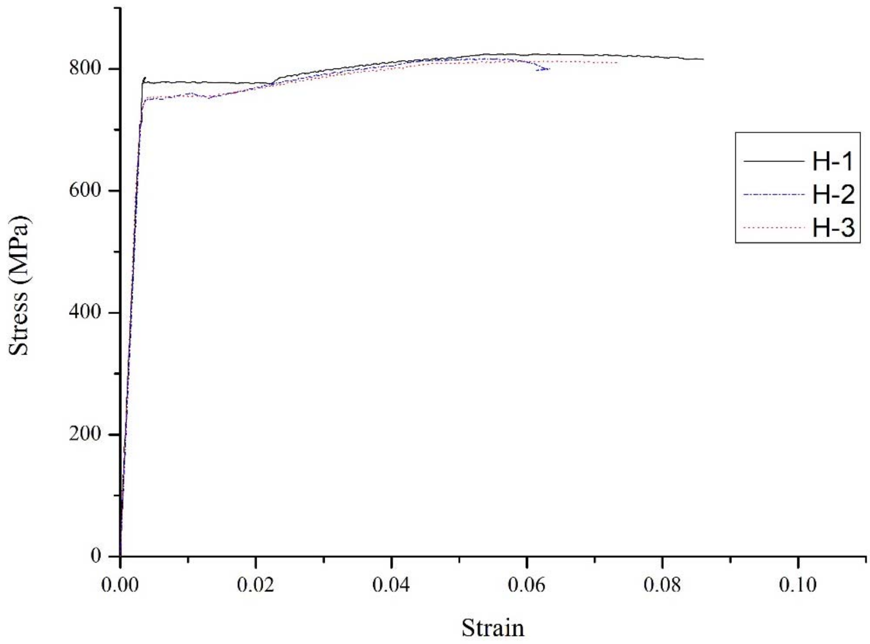

Figure 4.19 Stress-strain curve of H-70-1

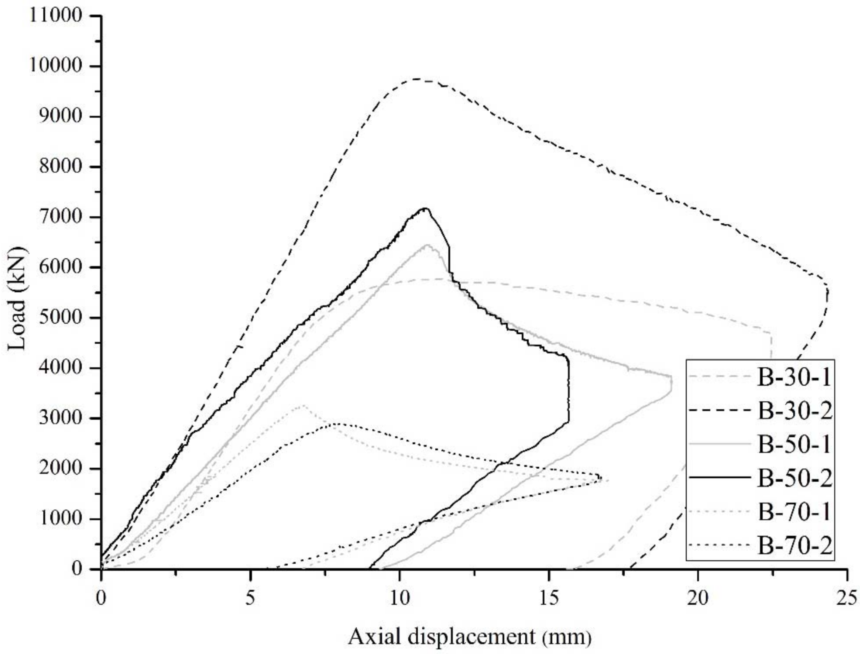

(a) Box section curves

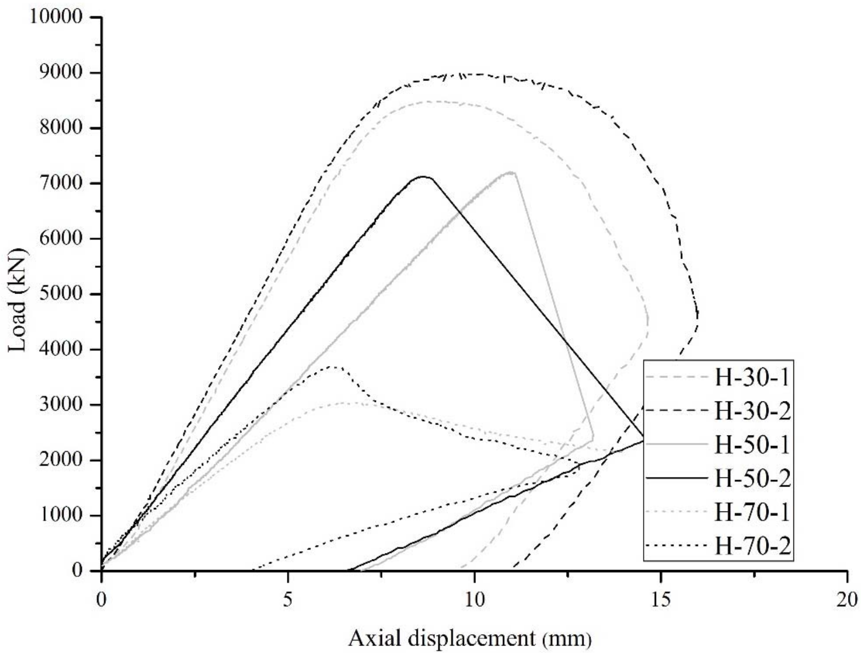

(b) H section curves

Figure 4.20 Load–versus–axial displacement curves

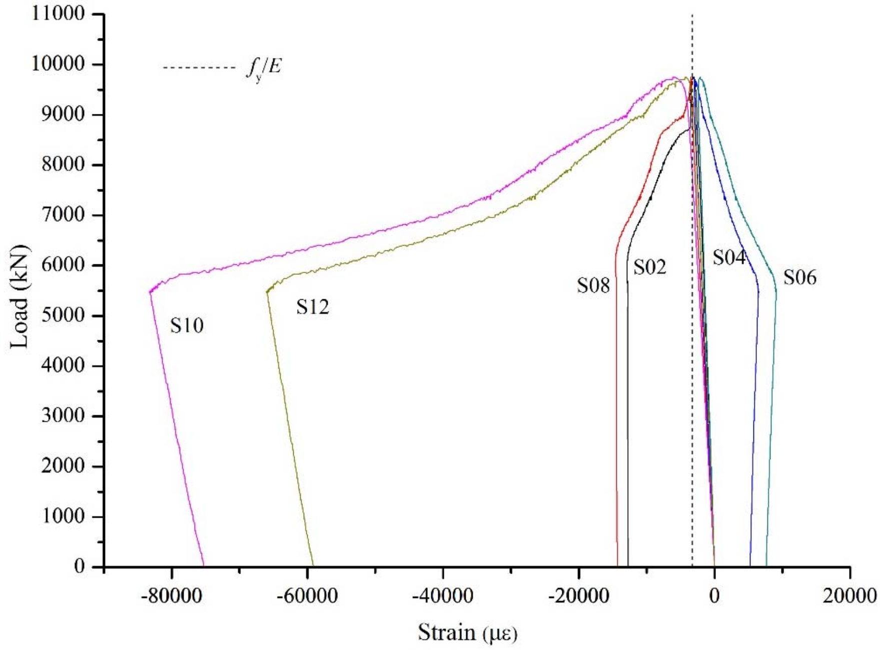

(a) B-30-2

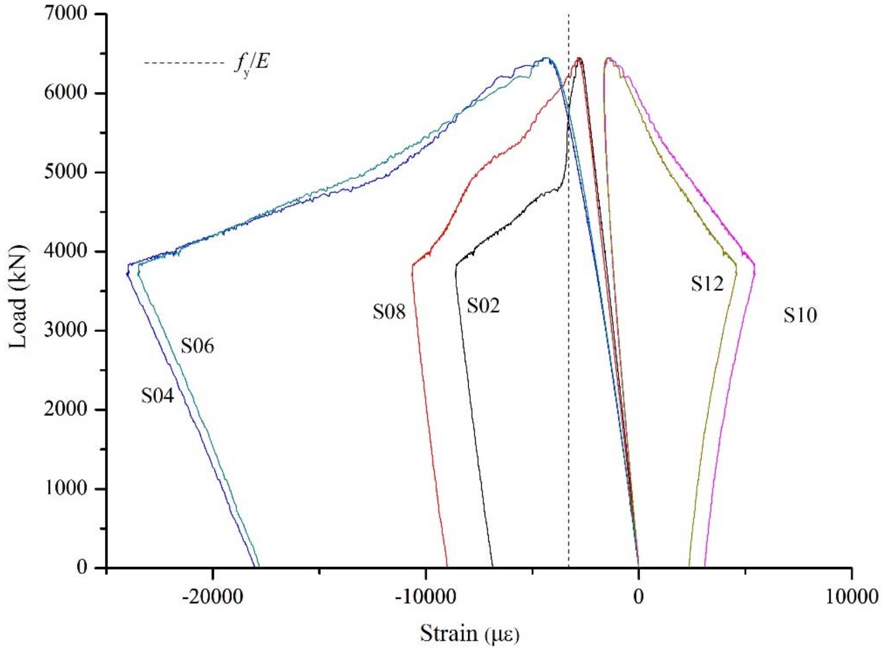

(b) B-50-1

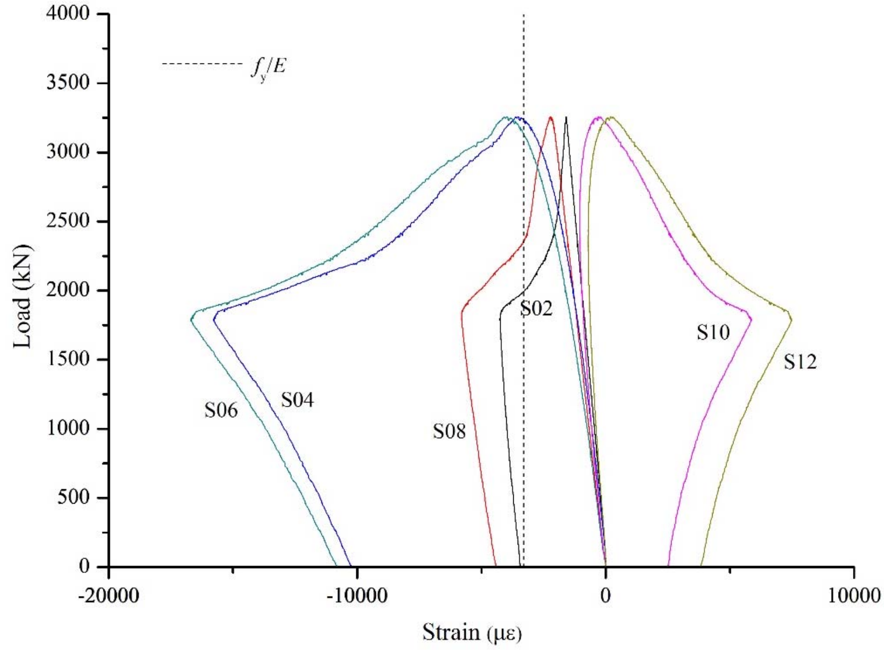

(c) B-70-1

Figure 4.21 Load–strain curves of box columns

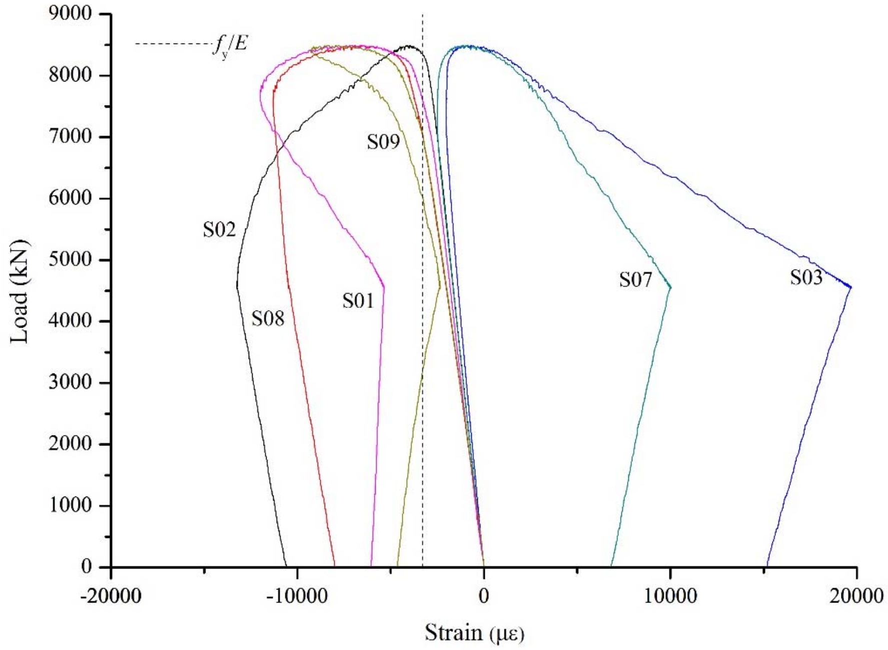

9000
8000
7000
6000
5000
4000
3000
2000
1000
0
Load (kN)
-20000
-10000
0
10000
20000
Strain (με)
f_y/E
S09
S02
S01
S08
S07
S03

(a) H-30-1

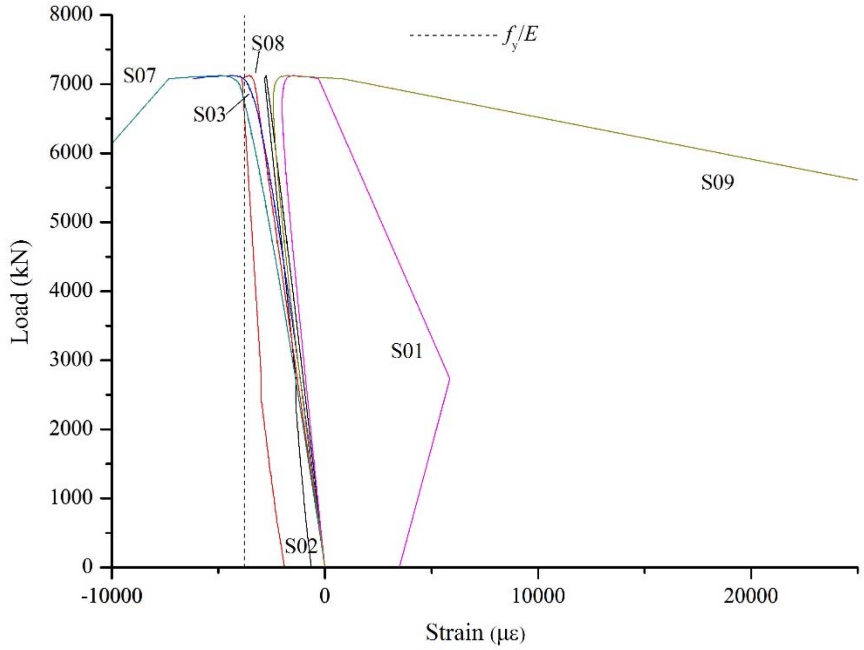

8000
7000
6000
5000
4000
3000
2000
1000
0
Load (kN)
-10000
0
10000
20000
Strain (με)
f_y/E
S08
S07
S03
S09
S01
S02

(b) H-50-2

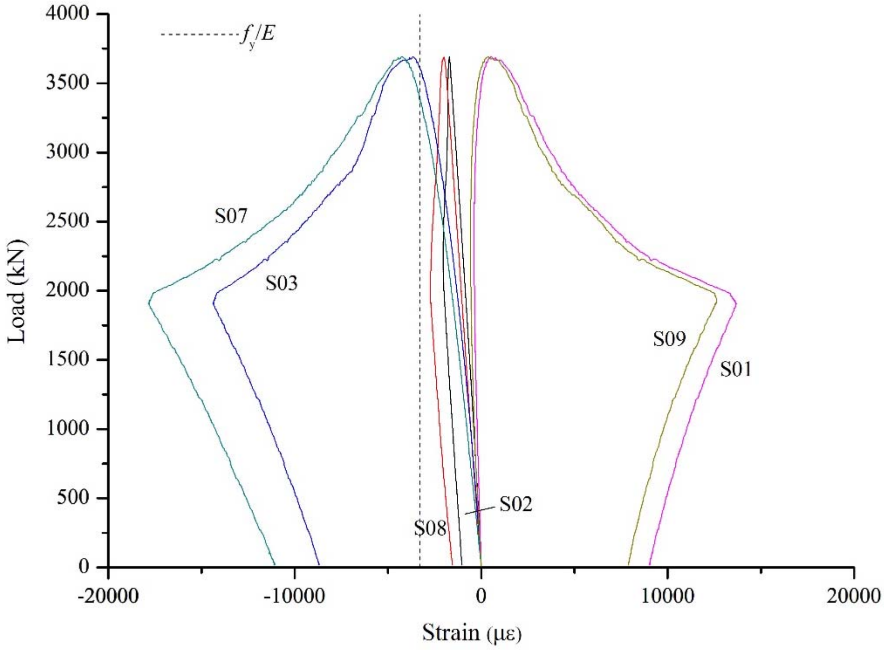

(d) H-70-2

Figure 4.22 Load–strain curves of H columns

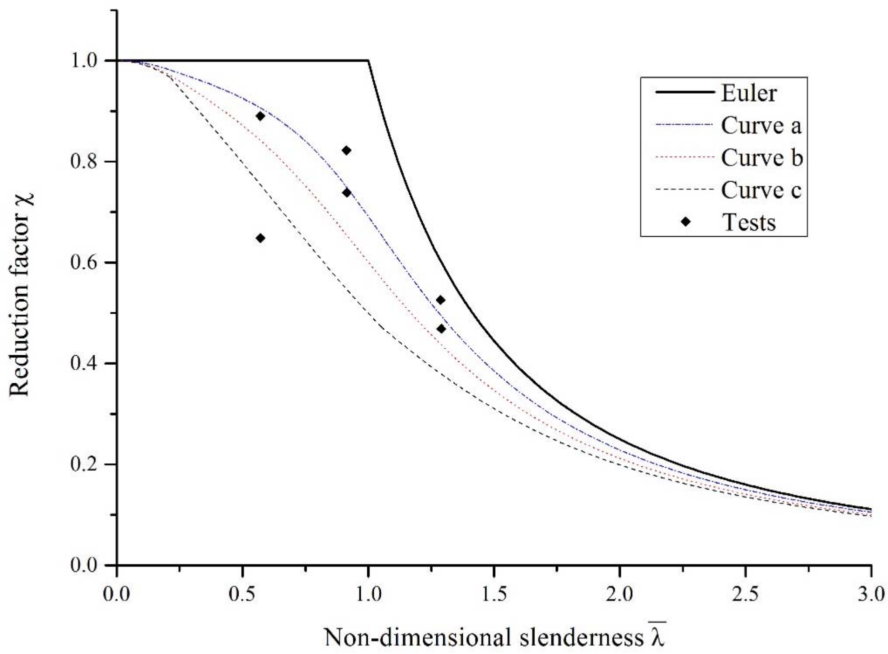

(a) Box section columns

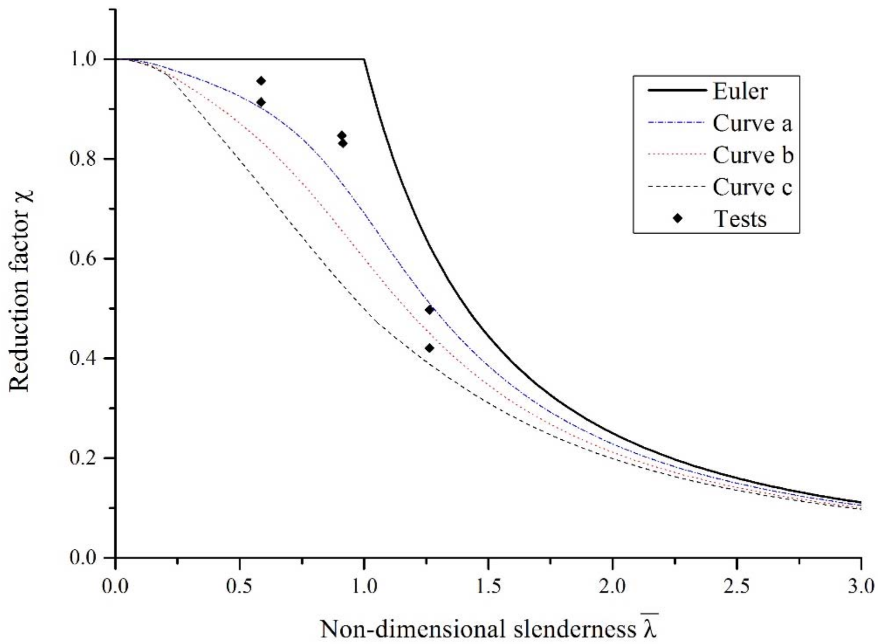

(b) H section columns

Figure 4.23 Comparison between test results and GB 50017-2003 (2003)

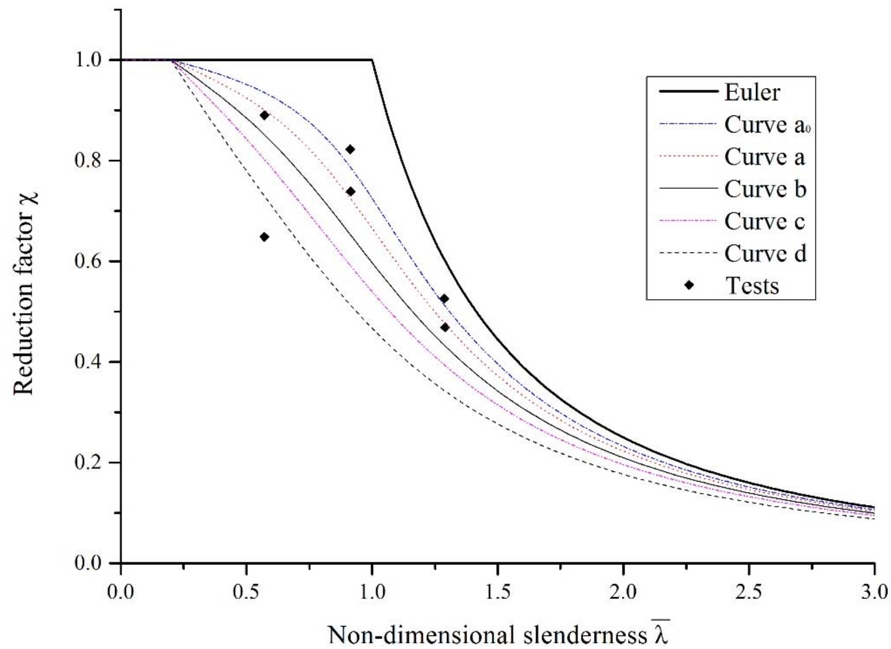

(a) Box section columns

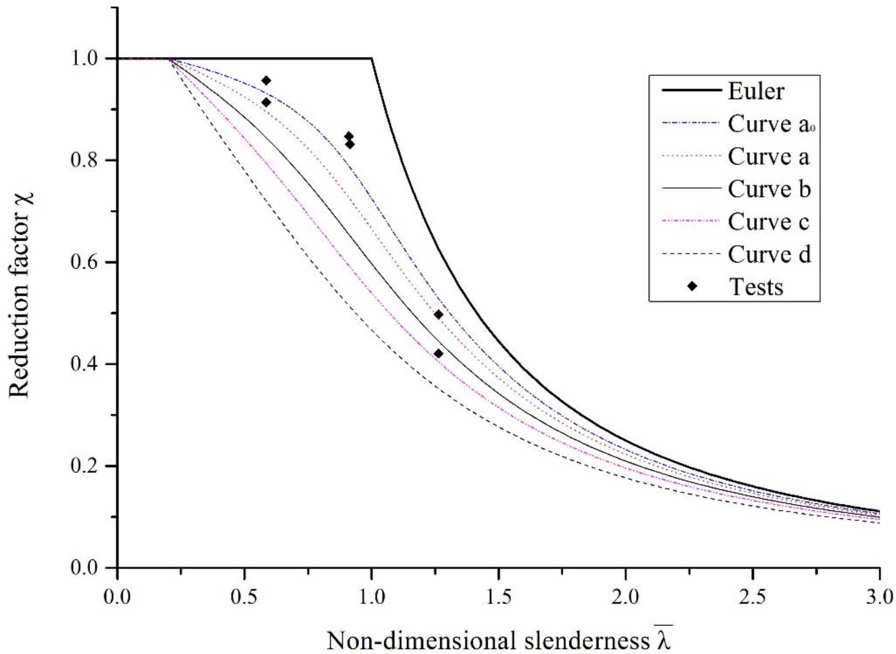

(b) H section columns

Figure 4.24 Comparison between test results and Eurocode 3 (2005)

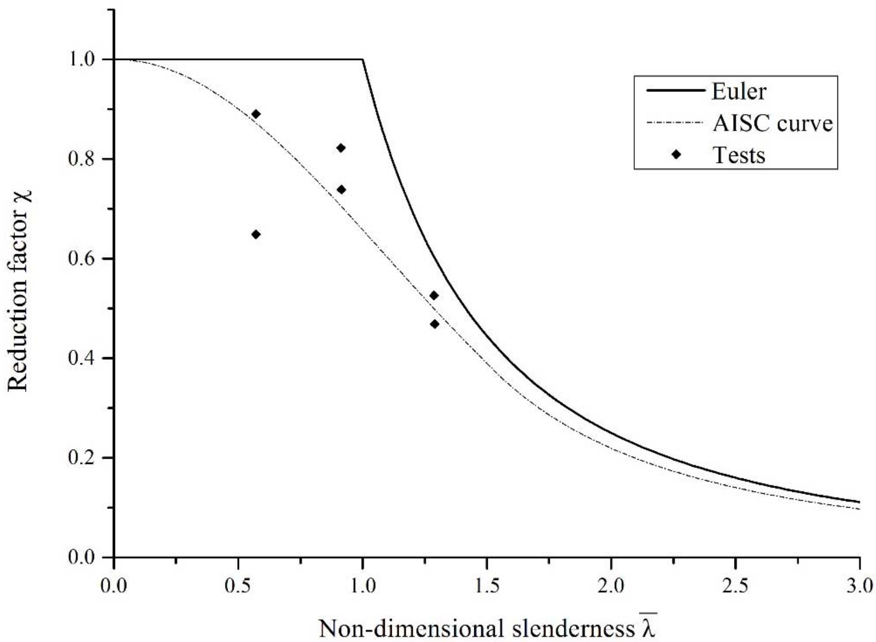

(a) Box section columns

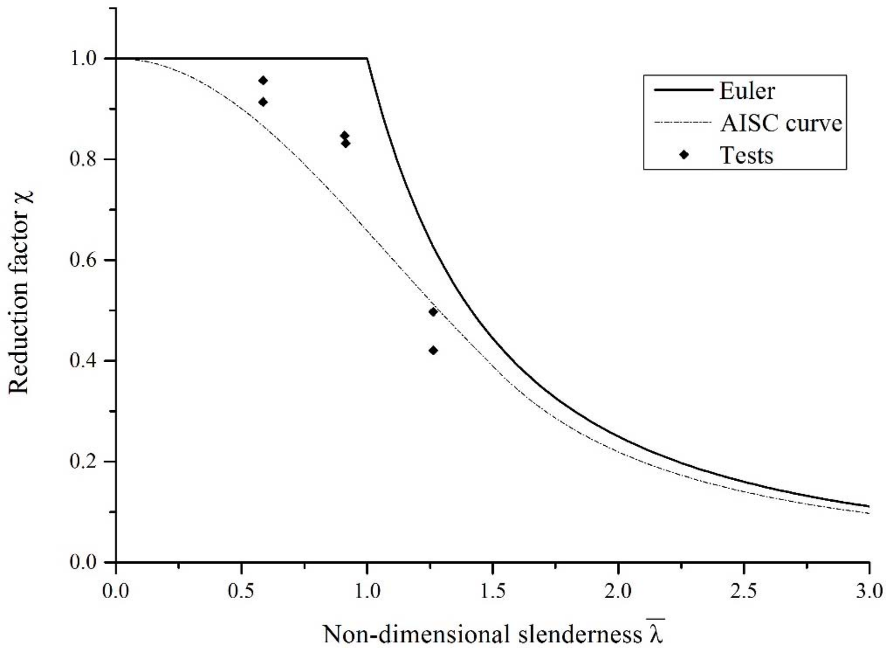

(b) H sections columns

Figure 4.25 Comparison between test results and ANSI/AISC 360-10 (2010)

Tables

Table 4.1 Realistic dimensions of box section columns

Specimen label	B (mm)	t (mm)	L (mm)	L_e (mm)	A (mm^2)	I (cm^4)	λ	$\overline{\lambda}$
B-30-1	236.23	16.20	2501	2811	14258	11567	31.2	0.571
B-30-2	236.47	16.10	2502	2812	14192	11548	31.2	0.571
B-50-1	192.37	16.02	3300	3610	11301	5906	50.0	0.915
B-50-2	192.52	16.02	3302	3612	11310	5921	49.9	0.913
B-70-1	140.88	16.07	3300	3610	8023	2118	70.3	1.287
B-70-2	140.48	16.08	3299	3609	8001	2098	70.5	1.290

Table 4.2 Realistic dimensions of H section columns

Specimen label	B (mm)	H (mm)	t_f, t_w (mm)	L (mm)	L_e (mm)	A (mm^2)	I_v (cm^4)	λ_v	$\overline{\lambda}_v$
H-30-1	260.85	259.19	16.08	1701	2011	12040	4765	32.0	0.586
H-30-2	260.82	260.35	16.25	1700	2010	12179	4814	32.0	0.586
H-50-1	241.75	236.30	16.03	2602	2912	11024	3782	49.7	0.910
H-50-2	240.47	238.15	16.16	2601	2911	11098	3752	50.0	0.915
H-70-1	209.21	204.78	16.26	3201	3511	9605	2488	69.0	1.263
H-70-2	209.38	205.24	16.24	3202	3512	9606	2491	69.0	1.263

Table 4.3 Experimental results for tension coupons

Specimen label	E (GPa)	f_y (MPa)	f_u (MPa)	f_y/f_u	ε_u	$\Delta\%$
L16-A1	243.1	772	827	0.93	0.0682	22
L16-A2	238.9	779	833	0.94	0.0594	23
L16-A3	202.3	779	834	0.94	0.0609	20
L16-A4	243.4	772	827	0.93	0.0583	21
L16-A6	239.6	756	810	0.93	0.0593	21
Mean value	233.5	772	826.2	0.93	0.0612	21

Table 4.4 Initial geometric imperfections

Specimen label	e_0 (mm)	v_0 (mm)	$\lvert(e_0+v_0)/L_\mathrm{e}\rvert\times10^{-3}$
B-30-1	0.8	27.0	9.89
B-30-2	2.4	2.5	1.74
B-50-1	0.1	-1.0	0.25
B-50-2	-0.8	-1.5	0.64
B-70-1	0.9	-1.0	0.03
B-70-2	-0.5	-1.0	0.42
H-30-1	1.0	1.0	0.99
H-30-2	0	0.5	0.25
H-50-1	-1.5	1.0	0.17
H-50-2	-0.5	-0.5	0.34
H-70-1	-0.8	-2.0	0.80
H-70-2	0	-1.5	0.43

Table 4.5 Ultimate capacity of columns

Specimen label	P_u (kN)	P_u/Af_y
B-30-1*	5771.5	0.649
B-30-2	9751.5	0.890
B-50-1	6444.5	0.739
B-50-2	7180.0	0.822
B-70-1	3258.5	0.526
B-70-2	2897.0	0.469
H-30-1	8493.0	0.914
H-30-2	8994.0	0.957
H-50-1	7207.0	0.847
H-50-2	7124.5	0.832
H-70-1*	3039.0	0.421
H-70-2	3690.0	0.498

Note: initial deflection of specimen B-30-1 was enlarged by flame heating; H-70-1 was straightened by flame heating method. Details are presented in Section 4.3.1.

Table 4.6 Material properties of B-30-1 and H-70-1

Specimen	f_y (MPa)	f_u (MPa)	f_y^0 (MPa)	f_y/f_y^0
B-1	617	720	772	0.80
B-2	630	753	772	0.82
B-3	780	836	772	1.01
B-4	625	743	772	0.81
H-1	776	824	772	1.01
H-2	751	816	772	0.97
H-3	753	813	772	0.98

CHAPTER 5

ANALYSIS METHODS FOR SECTIONS AND BEAM-COLUMN ELEMENTS

This chapter discusses a proposed section analysis method suitable for arbitrary steel sections considering residual stress effects. To calculate section capacity, a quasi-Newton method is used to determine the position of the neutral axis of a section. An entire section is automatically meshed into small fibers. Initial yield and failure surfaces with consideration of the effects of residual stress are presented for utilization in an advanced analysis. The method is then validated by comparing its results with those derived using another precise approach. The chapter also presents two effective and robust numerical methods, i.e. the pointwise equilibrium polynomial (PEP) element, and the refined plastic hinge approach in the nonlinear analysis of beam-column members modeled by one element per member. The PEP element takes into account the effects of initial geometric imperfections and simulates geometric nonlinearity. The refined plastic hinge approach is used to model material nonlinear behavior. Moreover, algorithms for nonlinear analysis are reviewed in this chapter. Finally, two numerical examples based on published works are employed to confirm the feasibility of the proposed analysis methods for sections and beam-column elements.

5.1. Introduction

The assessment method based on the concept of sectional yield surface is employed to check the status of the sections used in second-order design and advanced analysis. The failure and initial yield surfaces (see Figure 5.1) used for the section of a beam-column element are presented. Failure surfaces describe the ultimate limit states of cross-sections are exploited to examine member strength in elastic analysis. Initial yield surfaces, as a controlling boundary condition, define the limit states in the elasticity range. With these two surfaces, a loading space is divided into three components—elastic, elastoplastic, and plastic zones—that depict various scenarios of cross-sectional strength. These settings are re-adopted in the refined plastic hinge model.

A failure surface referred to as a full yield surface regularly depicts the ultimate bearing capacity of a section that is used for design practice. Dafalias and Popov (1975) proposed the concept of a failure surface that was used in a model to illustrate material behavior. In their study, a section was subjected to multi-axial and cyclic loads. To improve the traditional design and advanced-plastic-analysis of steel cross-sections, Attalla *et al.* (1994), Chan and Chui (1997), Liew *et al.* (2000), and Jiang *et al.* (2002) presented analogous methods.

In the present study, the position of the neutral axis of a section is determined by a quasi-Newton method. For arbitrary sections made of structural steel, the sectional capacity considering residual stress effects can be further determined. Each section is meshed into many small triangular fibers for stress integration in analysis. The section analysis technique and proposed yield surfaces are gradually represented. The proposed method is then validated with several numerical examples.

The PEP element, which was originally proposed by Chan and Zhou (1994), has been widely applied to the nonlinear analysis of various steel framed structures. Given that the PEP element enables modeling by one element per member, modeling efforts and computational time can be considerably reduced. Unlike other rigorous methods, it does not require the separation of compressive and tensile load cases, and its matrix is applicable to zero, positive, and negative axial forces. Because the polynomial function of the PEP element is of fifth-degree type, the PEP element and the cubic Hermite element in the displacement function exhibit certain differences. The factors of the displacement function can be obtained by enforcing two additional equilibrium constraints at the mid-span of an element and four compatible equations at end nodes. The co-rotational element formulation, tangent stiffness matrix, and secant stiffness matrix are reviewed in this chapter.

Chan and Chui (1997) investigated the refined plastic hinge method applied in the elastoplastic analysis of steel frame structures. Generally, initial yield and failure criteria should be determined because these standards are critical to the monitoring of sectional yielding in elastic-plastic analysis. With initial yield and failure criteria, the progressive plastification of a section can be simulated by gradually adjusting the pseudo-spring stiffness at two ends of an element in accordance with applied forces. The formulation of the hinge element and the verification of element stiffness in extreme cases are discussed in this chapter. Several algorithms for nonlinear analysis are also reviewed. Two numerical cases are then presented to verify the nonlinear analysis method that incorporates the section analysis technique, the PEP element, and the refined plastic hinge approach.

5.2. Assumptions

The basic assumptions employed in this research are as follows:

1) The element based on the Euler–Bernoulli hypothesis is prismatic and elastic.
2) The strain of the element is small, but its deflection is large.
3) Applied loads are conservative and nodal in nature.
4) Warping deformation, the twisting effect, and shear deformation are disregarded.
5) Material nonlinearity is modeled using plastic hinge springs, and the element used is elastic.
6) Compressive strains and stresses are positive during analysis.
7) The sign convention adopted is counterclockwise positive.

In assumption 2, the rotation from the axis connecting both end nodes to the tangent at one node is small while the overall angle of the node rotation can be large. As yielding prohibits the development of large angles at the member ends, assumption 2 is not to be violated for practical steel structures. The above-mentioned assumptions not only meet the requirements for the majority of practical engineering projects, but also for many standards.

5.3. Section analysis method that considers residual stresses

This section presents two types of idealized models of residual stresses and discusses the analysis technique for arbitrary steel sections taking into account effects of residual stresses. Figure 5.2 shows an arbitrary section made with structural steel under bi-eccentric loading. Each section consists of plate strips that are automatically meshed into a given number of small triangular fibers. The mesh method proposed by Niceno (2002) is adopted in section analysis.

5.3.1. Modeling of residual stresses

Numerous researchers devoted investigations to residual stresses of welded high-strength steel box and H sections; in such research, however, the width-to-thickness ratios of the studied specimens were comparatively large because of investigative focus on the local buckling of high-strength steel. In studying the overall buckling behavior of high-strength steel columns (nominal yield strength, 460 MPa) under axial compression, Ban (2012) and Wang *et al.* (2012a, 2012b) presented residual stress models of welded box and H sections. The geometric dimensions and basic parameters of the specimens for residual stress modeling are listed in Table 5.1 and Table 5.2. Figure 5.4 shows the definition of the symbols in the two tables.

(1) Model I

Model I, which was presented by Ban (2012), is plotted in Figure 5.5. This model is suitable for conditions in which the width-to-thickness ratio ranges from 8 to 36 for a box section and from 6 to 14 for an H section. In the experiment, the yield strengths are 532 MPa for 10 mm plates and 493 MPa for 12 and 14 mm plates. Residual stress magnitudes and distributions are detailed below:

For box-section flanges,

$$\sigma_{\mathrm{fr}}(u)=\begin{cases}\sigma_{\mathrm{rt}}, & -B/2\le u\le -B/2+f_1\\ \sigma_{\mathrm{rt}}+\dfrac{\sigma_{\mathrm{rc}}-\sigma_{\mathrm{rt}}}{f_2}\left(u-f_1+B/2\right), & -B/2+f_1<u<-f_3/2\\ \sigma_{\mathrm{rc}}, & -f_3/2\le u\le f_3/2\\ \sigma_{\mathrm{rt}}+\dfrac{\sigma_{\mathrm{rc}}-\sigma_{\mathrm{rt}}}{f_2}\left(-u-f_1+B/2\right), & f_3/2<u<B/2-f_1\\ \sigma_{\mathrm{rt}}, & B/2-f_1\le u\le B/2\end{cases} \tag{5.1}$$

where

$$\sigma_{\mathrm{rt}}=460,\quad h=B-2t \tag{5.2}$$

$$\sigma_{\mathrm{rc}}=-10-\frac{1500}{h/t}-\frac{550}{t},\qquad \text{and } -460\le\sigma_{\mathrm{rc}}\le -46 \tag{5.3}$$

$$f_1=t+h/20 \tag{5.4}$$

$$2\left(f_1+f_2\right)+f_3=B \tag{5.5}$$

$$\iint_{A_{\mathrm{f}}}\sigma_{\mathrm{fr}}\,dA=2\sigma_{\mathrm{rt}}\cdot f_1+\left(\sigma_{\mathrm{rc}}+\sigma_{\mathrm{rt}}\right)\cdot f_2+\sigma_{\mathrm{rc}}\cdot f_3=0 \tag{5.6}$$

With Equations (5.1)-(5.6), the width of the transition zone and the compression zone (f_2 and f_3) on the flanges can be determined as,

$$f_2=\frac{B\cdot\sigma_{\mathrm{rc}}}{\sigma_{\mathrm{rc}}-\sigma_{\mathrm{rt}}}-2f_1=\frac{B\cdot\sigma_{\mathrm{rc}}}{\sigma_{\mathrm{rc}}-\sigma_{\mathrm{rt}}}-\frac{20t+h}{10} \tag{5.7}$$

$$f_3=B-2\left(f_1+f_2\right)=\frac{20t+h}{10}-\frac{B\left(\sigma_{\mathrm{rc}}+\sigma_{\mathrm{rt}}\right)}{\sigma_{\mathrm{rc}}-\sigma_{\mathrm{rt}}} \tag{5.8}$$

For box-section webs,

$$\sigma_{\mathrm{wr}}\left(v\right)=\begin{cases}\sigma_{\mathrm{rt}}, & -B/2+t\le v\le -B/2+t+w_1\\ \sigma_{\mathrm{rt}}+\dfrac{\sigma_{\mathrm{rc}}-\sigma_{\mathrm{rt}}}{w_2}\left(v-w_1-t+B/2\right), & -B/2+t+w_1<v<-w_3/2\\ \sigma_{\mathrm{rc}}, & -w_3/2\le v\le w_3/2\\ \sigma_{\mathrm{rt}}+\dfrac{\sigma_{\mathrm{rc}}-\sigma_{\mathrm{rt}}}{w_2}\left(-v-w_1-t+B/2\right), & w_3/2<v<B/2-t-w_1\\ \sigma_{\mathrm{rt}}, & B/2-t-w_1\le v\le B/2-t\end{cases} \tag{5.9}$$

$$\sigma_{\mathrm{rt}}=460,\ \ h=B-2t \tag{5.10}$$

$$\sigma_{\mathrm{rc}}=-10-\frac{1500}{h/t}-\frac{550}{t},\qquad \text{and} -460\le\sigma_{\mathrm{rc}}\le -46 \tag{5.11}$$

$$w_1=h/20 \tag{5.12}$$

$$2\left(w_1+w_2\right)+w_3=h \tag{5.13}$$

$$\iint_{A_{\mathrm{w}}}\sigma_{\mathrm{wr}}dA=2\sigma_{\mathrm{rt}}\cdot w_1+\left(\sigma_{\mathrm{rc}}+\sigma_{\mathrm{rt}}\right)\cdot w_2+\sigma_{\mathrm{rc}}\cdot w_3=0 \tag{5.14}$$

Combining Equations (5.9)-(5.14) derives the width of the transition zone and the compressive zone (w_2 and w_3) on the webs:

$$w_2=\frac{\sigma_{\mathrm{rc}}\left(2t-B\right)}{\sigma_{\mathrm{rt}}-\sigma_{\mathrm{rc}}}-2w_1=\frac{\sigma_{\mathrm{rc}}\left(2t-B\right)}{\sigma_{\mathrm{rt}}-\sigma_{\mathrm{rc}}}-\frac{h}{10} \tag{5.15}$$

$$w_3 = B - 2t - 2\left(w_1 + w_2\right) = \frac{\left(B - 2t\right)\sigma_{\mathrm{rt}}}{\sigma_{\mathrm{rt}} - \sigma_{\mathrm{rc}}} + \frac{h}{10} \tag{5.16}$$

For H-section flanges,

$$\sigma_{\mathrm{fr}}\left(u\right) = \begin{cases} \sigma_{\mathrm{frte}}, & -B/2 \le u \le -B/2 + f_1 \\ \sigma_{\mathrm{frte}} + \dfrac{\sigma_{\mathrm{frc}} - \sigma_{\mathrm{frte}}}{f_2}\left(u - f_1 + B/2\right), & -B/2 + f_1 < u < -B/2 + f_1 + f_2 \\ \sigma_{\mathrm{frc}}, & -B/2 + f_1 + f_2 \le u \le -f_4 - f_5/2 \\ \sigma_{\mathrm{frc}} + \dfrac{\sigma_{\mathrm{frt}} - \sigma_{\mathrm{frc}}}{f_4}\left(u + f_4 + f_5/2\right), & -f_4 - f_5/2 < u < -f_5/2 \\ \sigma_{\mathrm{frt}}, & -f_5/2 \le u \le f_5/2 \\ \sigma_{\mathrm{frc}} + \dfrac{\sigma_{\mathrm{frt}} - \sigma_{\mathrm{frc}}}{f_4}\left(-u + f_4 + f_5/2\right), & f_5/2 < u < f_4 + f_5/2 \\ \sigma_{\mathrm{frc}}, & f_4 + f_5/2 \le u \le B/2 - f_1 - f_2 \\ \sigma_{\mathrm{frte}} + \dfrac{\sigma_{\mathrm{frc}} - \sigma_{\mathrm{frte}}}{f_2}\left(-u - f_1 + B/2\right), & B/2 - f_1 - f_2 < u < B/2 - f_1 \\ \sigma_{\mathrm{frte}}, & B/2 - f_1 \le u \le B/2 \end{cases} \tag{5.17}$$

$$\sigma_{\mathrm{frt}} = 345, \quad \sigma_{\mathrm{frte}} = 35 \tag{5.18}$$

$$\sigma_{\mathrm{frc}} = 420 - \frac{1200}{b_{\mathrm{f}}/t_{\mathrm{f}}} - \frac{5000}{t_{\mathrm{f}}}, \qquad \text{and} -460 \le \sigma_{\mathrm{frc}} \le -46 \tag{5.19}$$

$$f_5 = t_{\mathrm{w}} + 2h_{\mathrm{f}} \tag{5.20}$$

$$f_1 = f_2 = \frac{b_{\mathrm{f}} - h_{\mathrm{f}}}{10} \tag{5.21}$$

$$2\left(f_1 + f_2 + f_3 + f_4\right) + f_5 = B \tag{5.22}$$

$$\iint_{A_{\mathrm{f}}} \sigma_{\mathrm{fr}} dA = 2\sigma_{\mathrm{frte}} \cdot f_1 + \left(\sigma_{\mathrm{frc}} + \sigma_{\mathrm{frte}}\right) \cdot f_2 + 2\sigma_{\mathrm{frc}} \cdot f_3 + \left(\sigma_{\mathrm{frt}} + \sigma_{\mathrm{frc}}\right) \cdot f_4 = 0 \tag{5.23}$$

Substituting Equations (5.17)-(5.22) into Equation (5.23) yields the width of the compressive zone and the second transition zone (*f_4* and *f_3*) on the flanges as follows:

$$f_4 = \frac{\sigma_{\text{frc}}\left(f_5 - B\right) - \left(\sigma_{\text{frte}} - \sigma_{\text{frc}}\right)\left(2f_1 + f_2\right)}{\sigma_{\text{frt}} - \sigma_{\text{frc}}} \tag{5.24}$$

$$f_3 = \frac{B - 2\left(f_1 + f_2 + f_4\right) - f_5}{2} \tag{5.25}$$

For an H-section web,

$$\sigma_{\text{wr}}\left(v\right) = \begin{cases} \sigma_{\text{wrt}}, & t_{\text{f}} - H/2 \le v \le t_{\text{f}} - H/2 + w_1 \\ \sigma_{\text{wrt}} + \dfrac{\sigma_{\text{wrc}} - \sigma_{\text{wrt}}}{w_2}\left(v + w_2 + w_3/2\right), & t_{\text{f}} - H/2 + w_1 < v < -w_3/2 \\ \sigma_{\text{wrc}}, & -w_3/2 \le v \le w_3/2 \\ \sigma_{\text{wrt}} + \dfrac{\sigma_{\text{wrc}} - \sigma_{\text{wrt}}}{w_2}\left(-v + w_2 + w_3/2\right), & w_3/2 < v < H/2 - t_{\text{f}} - w_1 \\ \sigma_{\text{wrt}}, & H/2 - t_{\text{f}} - w_1 \le v \le H/2 - t_{\text{f}} \end{cases} \tag{5.26}$$

$$\sigma_{\text{wrt}} = 345 \tag{5.27}$$

$$\sigma_{\text{wrc}} = 200 - \frac{2300}{h/t_{\text{w}}} - \frac{2400}{t_{\text{w}}}, \qquad \text{and } -460 \le \sigma_{\text{wrc}} \le -46 \tag{5.28}$$

$$w_1 = h_{\text{f}} \tag{5.29}$$

$$2\left(w_1 + w_2\right) + w_3 = H - 2t_{\text{f}} \tag{5.30}$$

$$\iint_{A_{\text{w}}} \sigma_{\text{wr}} dA = 2\sigma_{\text{wrt}} \cdot w_1 + \left(\sigma_{\text{wrc}} + \sigma_{\text{wrt}}\right) \cdot w_2 + \sigma_{\text{wrc}} \cdot w_3 = 0 \tag{5.31}$$

With Equations (5.26)-(5.30) into Equation (5.31), the width of the transition zone and the compressive zone (w_2 and w_3) on the webs can be given by,

$$w_2 = \frac{\sigma_{\text{wrc}}\left(2t_{\text{f}} - H\right)}{\left(\sigma_{\text{wrt}} - \sigma_{\text{wrc}}\right)} - 2w_1 = \frac{\sigma_{\text{wrc}}\left(2t_{\text{f}} - H\right)}{\left(\sigma_{\text{wrt}} - \sigma_{\text{wrc}}\right)} - 2h_{\text{f}} \tag{5.32}$$

$$w_3 = H - 2t_{\text{f}} - 2w_1 - 2w_2 = H - 2t_{\text{f}} + 2h_{\text{f}} + \frac{2\sigma_{\text{wrc}}\left(H - 2t_{\text{f}}\right)}{\left(\sigma_{\text{wrt}} - \sigma_{\text{wrc}}\right)} \tag{5.33}$$

(2) Model II

As shown in Figure 5.6, model II, which was proposed by Wang *et al*. (2012a, 2012b), is a straight-line model that is appropriate for box-sections with width-to-thickness ratios ranging from 8 to 18 and H-sections with ratios ranging from 3 to 7. The author used yield strengths of 505.8 MPa for 11 mm plates and 464 MPa for 21 mm plates. Residual stress magnitudes and distributions are given with the following equations:

For box-section flanges,

$$\sigma_{\mathrm{fr}}(u)=\begin{cases}\sigma_{\mathrm{rt}}=\alpha\cdot f_{\mathrm{y}}, & -B/2\le u<-B/2+f\\ \sigma_{\mathrm{rc}}=\beta\cdot f_{\mathrm{y}}, & -B/2+f\le u\le B/2-f\\ \sigma_{\mathrm{rt}}=\alpha\cdot f_{\mathrm{y}}, & B/2-f<u\le B/2\end{cases} \tag{5.34}$$

and for webs,

$$\sigma_{\mathrm{wr}}(v)=\begin{cases}\sigma_{\mathrm{rt}}=\alpha\cdot f_{\mathrm{y}}, & -B/2+t\le v<-B/2+t+w\\ \sigma_{\mathrm{rc}}=\beta\cdot f_{\mathrm{y}}, & -B/2+t+w\le v\le B/2-t-w\\ \sigma_{\mathrm{rt}}=\alpha\cdot f_{\mathrm{y}}, & B/2-t-w<v\le B/2-t\end{cases} \tag{5.35}$$

where α and β (Table 5.3) are the residual stress ratios on tensile and compressive areas, respectively, and f_{y} denotes the yield strength of materials.

$$f=w-0.35t \tag{5.36}$$

$$w=\frac{\beta(B+h)}{2(\beta-\alpha)}-f \tag{5.37}$$

From Equations (5.36) and (5.37), the width of the tensile area on a web and flange (w and f, respectively) can be written as,

$$w=\frac{\beta\left(B+h\right)}{4\left(\beta-\alpha\right)}+0.175t \tag{5.38}$$

$$f=\frac{\beta\left(B+h\right)}{4\left(\beta-\alpha\right)}-0.175t \tag{5.39}$$

For H-section flanges,

$$\sigma_{\mathrm{fr}}\left(u\right)=\begin{cases}\sigma_{\mathrm{frte}}=\alpha_2\cdot f_{\mathrm{y}}, & -B/2\le u<-B/2+f_1\\ \sigma_{\mathrm{frc}}=\beta_1\cdot f_{\mathrm{y}}, & -B/2+f_1\le u<-f_3/2\\ \sigma_{\mathrm{frt}}=\alpha_1\cdot f_{\mathrm{y}}, & -f_3/2\le u\le f_3/2\\ \sigma_{\mathrm{frc}}=\beta_1\cdot f_{\mathrm{y}}, & f_3/2<u\le f_3/2+f_2\\ \sigma_{\mathrm{frte}}=\alpha_2\cdot f_{\mathrm{y}}, & f_3/2+f_2<u\le B/2\end{cases} \tag{5.40}$$

and for a web,

$$\sigma_{\mathrm{wr}}\left(v\right)=\begin{cases}\sigma_{\mathrm{wrt}}=\alpha_1\cdot f_{\mathrm{y}}, & -w_1-w_2/2\le v<-w_2/2\\ \sigma_{\mathrm{wrc}}=\beta_2\cdot f_{\mathrm{y}}, & -w_2/2\le v\le w_2/2\\ \sigma_{\mathrm{wrt}}=\alpha_1\cdot f_{\mathrm{y}}, & w_2/2<v\le w_2/2+w_1\end{cases} \tag{5.41}$$

where α_1, α_2 and β_1 (Table 5.4) denote the residual stress ratios of the major tension zones on a flange and web, and the marginal tension and compression zones on a flange; β_2 is the residual stress ratio of the compression zones on a web; and f_y represents the yield strength of materials. The widths of the tensile and compressive zones on a flange and web are given thus:

$$w_1=0.12h;\quad w_2=0.76h;\quad f_1=0.05B \tag{5.42}$$

$$f_3=\frac{\beta_1\left(2f_1-B\right)+\beta_2\left(h/2-w_1\right)-\alpha_1 w_1-2\alpha_2 f_1}{\alpha_1-\beta_1} \tag{5.43}$$

$$f_2=\frac{B-2f_1-f_3}{2} \tag{5.44}$$

For Q460 high-strength steel, model I is more extensively used than model II. However, the applicability of model II is superior to that of model I because it presents simplified equations, although the range of width-to-thickness ratios is not greatly extensive. In this chapter, therefore, model II is employed in the numerical examples. Residual stress effects on the sectional capacities and ultimate bearing capacities of members are discussed in Chapter 6.

5.3.2. Numerical analysis

5.3.2.1. *Reference loading axe**s***

Two variables, namely, the orientation angle θ_n and depth d_n of a neutral axis, can describe the position of the neutral axis (see Figure 5.2). Brondum-Nielsen (1985) and Yen (1991) verified the effectiveness and efficiency of the quasi-Newton method used to determine θ_n and d_n for regular sections. For structural steel sections equipped with many strips of steel plates, the geometric centroid taken as the origin of referenced loading axes is determined by,

$$Z_{gc} = \sum_{i=1}^{n} A_i Z_i \bigg/ \sum_{i=1}^{n} A_i \tag{5.45}$$

$$Y_{gc} = \sum_{i=1}^{n} A_i Y_i \bigg/ \sum_{i=1}^{n} A_i \tag{5.46}$$

in which A_i is the area of the i-th plate strips; Z_i and Y_i are the centroid coordinates of the i-th plate strips; and Z_{gc} and Y_{gc} are the coordinates of the geometric centroid of an entire section. Allowing for Euler–Bernoulli theory in beam-column element analysis generates force and moments that agree with the origin of the geometric centroid.

5.3.2.2. Systems of coordinates

The section analysis features three coordinate systems: ZCY, zoy and uov. The ZCY system is commonly used to illustrate a cross-section that needs to be analyzed. The geometric centroid is taken as the origin of the zoy and uov system coordinates. Twice transformations of coordinates are performed in the total iterative analysis. The first transformation is that from the global coordinate ZCY system to the referenced loading zoy system, and the second is that from the zoy coordinate system to the uov coordinate system, where the u-axis is parallel to the neutral axis.

The transfer equations related to the three coordinate systems are shown below:

$$z = Z - Z_{\mathrm{gc}} \tag{5.47}$$

$$y = Y - Y_{\mathrm{gc}} \tag{5.48}$$

$$u = z\cos\theta_{\mathrm{n}} + y\sin\theta_{\mathrm{n}} \tag{5.49}$$

$$v = y\cos\theta_{\mathrm{n}} - z\sin\theta_{\mathrm{n}} \tag{5.50}$$

where u and v, Z and Y, and z and y represent the coordinates related to the uov, ZOY, and zoy systems, respectively.

5.3.2.3. Stress outcomes and global force and moments

As previously stated, an entire section is meshed into many triangular fibers. Its stress outcomes of the section can be calculated as,

$$N_{\mathrm{x}} = \sum_{i=1}^{\mathrm{n}} \sigma_i A_i \tag{5.51}$$

$$M_{\mathrm{u}} = -\sum_{i=1}^{\mathrm{n}} \sigma_i A_i v_i \tag{5.52}$$

$$M_{\mathrm{v}} = \sum_{i=1}^{\mathrm{n}} \sigma_i A_i u_i \tag{5.53}$$

where A_i denotes the area of individual fibers and σ_i represents the related stresses that consider residual stresses. The stress σ_i imposed on the i-th element is a function of the strain ε_i that features three components. The stress and strain can be expressed as,

$$\sigma_i = f\left(\varepsilon_i\right) \tag{5.54}$$

$$\varepsilon_i = \varepsilon_{\mathrm{a}i} + \varepsilon_{\mathrm{r}i} + \phi_i v_i \tag{5.55}$$

in which $\varepsilon_{\mathrm{a}i}$ is the axial strain, $\varepsilon_{\mathrm{r}i}$ is the residual strain, and ϕ_i is the curvature.

The flexural moments acquired from the above-mentioned equations should be summed, and the moments are transferred to the zoy system through the succeeding conversions. The moments determined from the section analysis are given by the following expressions:

$$M_{\mathrm{z}} = M_{\mathrm{u}} \cos\theta_{\mathrm{n}} - M_{\mathrm{v}} \sin\theta_{\mathrm{n}} = -\left(\sum_{i=1}^{\mathrm{n}} \sigma_i A_i v_i \cdot \cos\theta_{\mathrm{n}} + \sum_{i=1}^{\mathrm{n}} \sigma_i A_i u_i \cdot \sin\theta_{\mathrm{n}} \right) \tag{5.56}$$

$$M_{\mathrm{y}} = M_{\mathrm{u}} \sin\theta_{\mathrm{n}} + M_{\mathrm{v}} \cos\theta_{\mathrm{n}} = -\sum_{i=1}^{\mathrm{n}} \sigma_i A_i v_i \cdot \sin\theta_{\mathrm{n}} + \sum_{i=1}^{\mathrm{n}} \sigma_i A_i u_i \cdot \cos\theta_{\mathrm{n}} \tag{5.57}$$

$$N_{\mathrm{x}} = \sum_{i=1}^{\mathrm{n}} \sigma_i A_i \tag{5.58}$$

in which M_u, M_v, and N_x are the flexural moments and axial force with respect to the uov system; and M_z and My are the global moments in relation to the geometric centroid.

5.3.2.4. Iterative strategy

Accurately determining sectional capacity necessitates changing the neutral axis direction (angle θ_n from 0° to 360°) with variations in depth d_n. Equilibrium, compatibility, and constitutive relationships are derived by the Regula–Falsi method. The cross-section analysis is illustrated in Figure 5.3.

The force capacity N_x in an x-axis can be iterated with regard to d_n by Equation (5.59). In this iterative process, θ_n is constant.

$$d_{\mathrm{nk}} = d_{\mathrm{ns}} + \frac{d_{\mathrm{ng}} - d_{\mathrm{ns}}}{N_{\mathrm{xg}} - N_{\mathrm{xs}}}(N_{\mathrm{xd}} - N_{\mathrm{xs}}) \tag{5.59}$$

in which d_{nk} is the depth of the updated neutral axis; N_{xs} and N_{xg} represent the axial bearing capacities computed at d_{ns} and d_{ng}; N_{xd} denotes the design axial load used in this work; and d_{ns} and d_{ng} are the neutral axis depths that correspond to the axial bearing capacities that are respectively smaller and larger than the design axial load.

5.3.2.5. Strength interaction surfaces

For arbitrary steel sections subjected to a given axial load, flexural moment capacity can be calculated by the aforementioned section analysis approach. The tri-axial yield surfaces of a section are used for second-order design and advanced analysis. The surfaces, i.e., strength interaction surfaces, are described by axial force and related moments. In what follows, failure and initial yield surfaces are discussed (see Figure 5.1).

(1) Failure surface

As shown in Figure 5.1, the outmost surface is a failure surface. The data points in the figure describe the ultimate state of a section and induce failure of steel sections. Accordingly, the significance of this surface is clearly observable when individual load bearing capacity requires determination in traditional steel structure designs.

Numerous codes present the fundamental equations of failure surfaces, but the equations are suitable only under standard conditions. The failure surface generated from a uniaxial flexural case is a specific plane that crosses the sectional yield surface. For computational efficiency, the indexing method proposed by Liu (2014) is adopted. It decreases calculation time through the pre-construction of yield surfaces and the indexing of interaction points.

(2) Initial yield surface

The initial yield surface is an essential condition for controlling strength in the refined plastic hinge approach presented in the succeeding section, as well as the failure surface. Materials do not yield, and the corresponding cross-section maintains elasticity when the initial yield surface can be regarded as a boundary surface under certain load combinations. The elastic limitation, being an approximate hypothesis in cross-section analysis, may give rise to small divergences as the load-displacement path is traced in the elasticity range. In this research, the limitation of steel elastic strains is expressed as ε_e.

Each fiber in a section is inspected, and the outset of the strain that exceeds the elastic limitation is examined when calculating the initial yield surface. Internal force and moments are computed by the integral of the stresses along the cross-section. Thus, sectional capacity can be obtained at initial yield conditions.

5.3.3. Validation of the section analysis method

Two examples involving steel box and H sections are discussed in order to verify the accuracy of the sectional analysis technique. These two sections are analyzed under uniaxial loading. The results—those derived with and without consideration for residual stress—are compared with the findings obtained using a simplified hand calculation method. The steel is used Q460 grade, and the yield strengths are 505.8 MPa for 11 mm plates and 464 MPa for 21 mm plates. The geometric dimensions are shown in Figure 5.7(a) and Figure 5.8(a). The models of residual stresses provided by

Wang *et al*. (2012a, 2012b) are adopted in the present study. The two sections are meshed into small fibers, as shown in Figure 5.7(b) and Figure 5.8(b). Given the double symmetry of the two sections, quarter values of initial yield and failure surfaces are plotted.

The analysis results, as shown in Figure 5.7(c)-(d) and Figure 5.8(c)-(d), verify the accuracy of the proposed section analysis method. The results depicted with solid lines are obtained by the hand calculation method, whereas those denoted by dotted lines are determined by the proposed analysis method. Figure 5.7(c)-(d) and Figure 5.8(c)-(d) illustrate the failure surfaces for the box and H sections with and without residual stress. The slight discrepancies between the results of the two methods may be attributed to the size of the sectional fibers. Guaranteeing satisfactory accuracy commonly suggests a fiber length that is one-fifth of plate thickness. Nonetheless, the number of sectional elements is limited when manual calculation is conducted. This is the reason for the differences between the two methods.

The quarter values of the initial yield and failure surfaces, obtained by the proposed method, are shown in Figure 5.7(e) and Figure 5.8(e). Residual stress strongly influences the initial yield surface but exerts a negligible effect on the failure surface. This finding is attributed primarily to the fact that the existence of residual stresses accelerates the development of yielding on a section. The stress effects on the initial yielding state (i.e., the entire section is elastic) are larger than those on the ultimate state of the sections. Initial yield surfaces are usually symmetric about bi-axes but are not perfectly so. This feature may be caused by the fact that the adopted residual stress models are not absolutely self-equilibrating.

As indicated in Figure 5.7(c)-(e) and Figure 5.8(c)-(e),), the practicability and accuracy of the proposed analysis method can be validated by comparing the results for the box and H sections subjected to axial and uniaxial bending. The diagrams suggest that the effects of residual stress are directed mainly toward the initial yielding state. As shown in Figure 5.7(e), the existence of residual stress diminishes box sectional capacity; the bending axis is the y-axis, which is perpendicular to the flanges. When a large bending moment occurs on a box section, the area of the residual tensile stress on the top flange and the compressive stress area on the bottom flange strongly influence the weakening of the sectional moment capacity (see Figure 5.9(a)-(b)). When this section is subjected to large axial loading, the areas of the tensile stress on the top flange and web upside substantially diminish the moment on the section. This phenomenon suggests that residual stress produces untimely yielding of box sections. The bending axis of the H section is still the y-axis (minor axis). As seen in Figure 5.8(e), the residual stress favorably influences the capacity of the H section subjected to large axial loading but weakens the capacity of this section under a strong bending moment. Under axial load control, the areas of the residual compressive stress on the flange bottom considerably reduces the sectional moment (see Figure 5.9(a)-(b)). If the H-section is under bending moment control, the tensile areas on the flanges underneath considerably increase the sectional moment capacity. These findings indicate that residual stress negatively affects the capacity of an H section subjected to large axial loading in the elasticity range but improves sectional capacity under a strong bending moment. The initial yield surface that considers the effect of residual stress is imperfectly symmetric with respect to the horizontal axis (see Figure 5.7(e) and Figure 5.8(e)) because the adopted residual stress models are not ideally self-equilibrating on the box and H sections.

5.3.4. Summary

As previously discussed, the proposed section analysis method is suitable for box and H sections subjected to axial and uniaxial bending. Residual stress unfavorably affects the elastic capacities of box sections but improves the capacities of H sections under a large bending moment (see Figure 5.7(e) and Figure 5.8(e)). Under axial load control, the capacities of H sections diminish because of residual stress. Nevertheless, this stress exerts minimal influence on the failure surfaces of box and H sections because the cross-section is almost completely yielding.

5.4. Nonlinear beam-column finite element analysis

As previously stated, the PEP element is an extensively used approach in the nonlinear analysis of various steel frame structures. It enables modeling by one element per member, thereby substantially reducing modeling efforts and computational time. In contrast to other rigorous methods, it does not require separation between compressive and tensile load cases, and its matrix is applicable to zero, positive, and negative axial forces. The PEP element also has a fifth-degree polynomial function, a feature that distinguishes it from the cubic Hermite element in the displacement function. The factors of the displacement function can be obtained by applying two additional equilibrium constraints at the mid-span of an element, and four compatible equations at end nodes. A discussion of the co-rotational element formulation, tangent stiffness matrix, and secant stiffness matrix is provided.

The refined plastic hinge method applied in the elastoplastic analysis of steel frame structures (Chan and Chui, 1997) generally requires the identification of initial yield and failure criteria given the criticality of such standards in monitoring sectional yielding during elastoplastic analysis. Initial yielding and failure criteria can be used to simulate the progressive plastification of a section by constantly modifying the pseudo-spring stiffness at two ends of an element in accordance with external forces. The formulation of the hinge element and the inspection of element stiffness in extreme cases are elaborated, and nonlinear analysis algorithms are reviewed.

5.4.1. Co-rotational element formulation for the pointwise equilibrium polynomial element

5.4.1.1. Formulation for the displacement function

Chan and Zhou (1994) proposed the Pointwise Equilibrating Polynomial (PEP) element and applied it to the second-order analysis and design that have been popularly adopted over the last decade. The element is particularly effective and reliable for second-order analysis with only a single element per member. The initial imperfection of the element along a member can be expressed as,

$$v_0 = v_{\text{mo}}\left(1-t^2\right) \qquad t = 2x/L \text{ and } -L/2 \le x \le L/2 \tag{5.60}$$

where v_0 is the initial deflection perpendicular to the member, t is the non-dimensional distance along the element, v_{mo} represents the amplitude of initial deflection at mid-span, and L is the member length (see Figure 5.10).

The PEP element features four compatibility conditions and two equilibrium conditions, which are expressed as follows,

For compatibility,

$$\text{At } x = \pm\frac{L}{2};\ v = 0 \tag{5.61}$$

$$\text{At } x = \pm\frac{L}{2};\ v' = 0 \tag{5.62}$$

For equilibrium,

$$EIv'' = N_x\left(v+v_0\right) + \frac{M_1+M_2}{L}\left(\frac{L}{2}+x\right) - M_1 \tag{5.63}$$

$$EIv''' = N_x v' + \frac{M_1+M_2}{L} \tag{5.64}$$

A fifth-order polynomial function is hypothesized as,

$$v = a_0 + a_1 x + a_2 x^2 + a_3 x^3 + a_4 x^4 + a_5 x^5 \tag{5.65}$$

With consideration for compatibility and equilibrium conditions, the shape function can be expressed thus:

$$v = N_1 \left(L\theta_1 \right) + N_2 \left(L\theta_2 \right) + N_0 v_{\mathrm{m}0} \tag{5.66}$$

where N_1, N_2 and N_0 are

$$N_1 = \frac{A}{H_1} + \frac{B}{H_2} \tag{5.67}$$

$$N_2 = \frac{A}{H_1} - \frac{B}{H_2} \tag{5.68}$$

$$N_0 = -q\left(1\text{-}t^2\right)^2 \Big/ H_2 \tag{5.69}$$

and

$$A = -20\frac{x}{L} + \left(80 - q\right)\left(\frac{x}{L}\right)^3 + 4q\left(\frac{x}{L}\right)^5 \tag{5.70}$$

$$B = 6 - \frac{1}{2}\left(48 - q\right)\left(\frac{x}{L}\right)^2 - 2q\left(\frac{x}{L}\right)^4 \tag{5.71}$$

$$H_1 = 80 + q \tag{5.72}$$

$$H_2 = 48 + q \tag{5.73}$$

$$q = \frac{PL^2}{EI} \tag{5.74}$$

As stated above, the PEP element can consider initial geometric imperfections of members and simulate large deflections via only a single element per member.

5.4.1.2. Secant stiffness matrix

The secant stiffness matrix can be obtained by the minimum total potential energy principle. This matrix is necessary in the computation of equilibrium deviation and in the verification of equilibrium convergence. In the PEP element, the degrees of freedom (DOFs) contain rotations, lengthening along the axis that connects two end nodes, and related axial loads and moments. These components are expressed follows:

$$\begin{cases} u_1 = \theta_1 \\ u_2 = \theta_2 \\ u_3 = e \end{cases} \tag{5.75}$$

$$\begin{cases} F_1 = M_1 \\ F_2 = M_2 \\ F_3 = P \end{cases} \tag{5.76}$$

The formula of the total potential energy can be written as,

$$\Pi = U - V \tag{5.77}$$

in which U is the strain energy, and V is the work done by external forces.

The strain energy is defined as ,

$$U = \frac{1}{2} EA \int_{-L/2}^{L/2} u'^2 dx + \frac{1}{2} EI \int_{-L/2}^{L/2} v''^2 dx + \frac{1}{2} P \int_{-L/2}^{L/2} (v'^2 + 2v'v_0') dx \tag{5.78}$$

where E is the elastic modulus, A is the cross-section area and u denotes the axial displacement. In Equation (5.78), three items represent strain energy because of axial and bending deformations and member curving.

The work exerted by external forces, V is given by,

$$V = \sum_{i=1}^{3} F_i u_i \tag{5.79}$$

The relationships between the displacements and forces can be determined by calculating the first variation in the total potential energy function:

$$
\begin{aligned}
M_1 &= \frac{\partial \Pi}{\partial u_1} + \frac{\partial \Pi}{\partial q}\frac{\partial q}{\partial u_1} = \frac{\partial U}{\partial \theta_1} + \frac{\partial U}{\partial q}\frac{\partial q}{\partial \theta_1} \\
&= \frac{EI}{L}\left[c_1\left(\theta_1+\theta_2\right) + c_2\left(\theta_1-\theta_2\right) + c_0\left(\frac{v_{\mathrm{m0}}}{L}\right)\right]
\end{aligned} \tag{5.80}
$$

$$
\begin{aligned}
M_2 &= \frac{\partial \Pi}{\partial u_2} + \frac{\partial \Pi}{\partial q}\frac{\partial q}{\partial u_2} = \frac{\partial U}{\partial \theta_2} + \frac{\partial U}{\partial q}\frac{\partial q}{\partial \theta_2} \\
&= \frac{EI}{L}\left[c_1\left(\theta_1+\theta_2\right) - c_2\left(\theta_1-\theta_2\right) - c_0\left(\frac{v_{\mathrm{m0}}}{L}\right)\right]
\end{aligned} \tag{5.81}
$$

$$
\begin{aligned}
P &= \frac{\partial \Pi}{\partial u_3} + \frac{\partial \Pi}{\partial q}\frac{\partial q}{\partial u_3} = \frac{\partial U}{\partial e} + \frac{\partial U}{\partial q}\frac{\partial q}{\partial e} \\
&= EA\left[\frac{e}{L} + b_1\left(\theta_1+\theta_2\right)^2 + b_2\left(\theta_1-\theta_2\right)^2 + b_{\mathrm{vs}}\frac{v_{\mathrm{m0}}}{L}\left(\theta_1-\theta_2\right) + b_{\mathrm{w}}\left(\frac{v_{\mathrm{m0}}}{L}\right)^2\right]
\end{aligned} \tag{5.82}
$$

in which θ_1 and θ_2 are the rotations of a node; e is the shortening of a member; and c_1, c_2, b_1, b_2, c_0, b_{vs},and b_{vv} are the factors expressed as follows,

$$
c_1 = \frac{\frac{23}{1260}q^3 + \frac{61}{7}q^2 + 10(80)q + 3(80)^2}{(80+q)^2} \tag{5.83}
$$

$$
c_2 = \frac{\frac{11}{420}q^3 + \frac{29}{5}q^2 + 6(48)q + 48^2}{(48+q)^2} \tag{5.84}
$$

$$
b_1 = \frac{\frac{23}{2520}q^3 + \frac{46}{21}q^2 + \frac{26}{7}(80)q + 2(80)^2}{(80+q)^3} \tag{5.85}
$$

$$
b_2 = \frac{\frac{11}{840}q^3 + \frac{66}{35}q^2 + \frac{14}{5}(48)q + 2(48)^2}{(48+q)^3} \tag{5.86}
$$

$$c_0 = \frac{2q\left(11q^2 + 42\times 48q + 35\times 48^2\right)}{105\left(48+q\right)^2} \tag{5.87}$$

$$b_{vs} = c_0{}' = \frac{2\left(11q^3 + 33\times 48q^2 + 49\times 48^2 q + 35\times 48^3\right)}{105\left(48+q\right)^3} \tag{5.88}$$

$$b_{vv} = -\frac{64q\left(q^2 + 144q + 5376\right)}{35\left(48+q\right)^3} \tag{5.89}$$

Equation (5.82) can be further simplified into,

$$q = \lambda^2\left(\frac{e}{L} + c_{\mathrm{b}} + c_{\mathrm{b0}}\right) \tag{5.90}$$

in which λ, c_{b} and c_{bo} are as follows,

$$\lambda = \sqrt{\frac{AL^2}{I}} \tag{5.91}$$

$$c_{\mathrm{b}} = b_1\left(\theta_1 + \theta_2\right)^2 + b_2\left(\theta_1 - \theta_2\right)^2 \tag{5.92}$$

$$c_{\mathrm{b0}} = b_{\mathrm{vs}}\frac{v_{\mathrm{m0}}}{L}\left(\theta_1 - \theta_2\right) + b_{\mathrm{vv}}\left(\frac{v_{\mathrm{m0}}}{L}\right)^2 \tag{5.93}$$

In Equation (5.90), the first, second and third terms are the linear strain, crookedness owing to the end rotations of a member, and initial bending and end rotation respectively. If a member is straight, the third term is equal to zero.

5.4.1.3. Tangent stiffness matrix

The tangent stiffness matrix reflects the relations between the increments of forces and the related increments of displacements. This matrix, which is employed to evaluate increments in displacement, can be derived by computing the second variation in the total potential energy function:

$$\delta^2\Pi = \frac{\partial^2 \Pi}{\partial u_i \partial u_j}\delta u_i \delta u_j = \left[\frac{\partial S_i}{\partial u_j} + \frac{\partial S_i}{\partial q}\frac{\partial q}{\partial u_j}\right]\delta u_i \delta u_j \quad \text{and } i, j\text{=1\textasciitilde 3} \tag{5.94}$$

in which S_i is the force vector, and u_i is the displacement vector. These variables can be written as,

$$S = \left(M_1 M_2 P\right)^T \tag{5.95}$$

$$u = \left(\theta_1 \theta_2 e\right)^T \tag{5.96}$$

For the axis across two end nodes, the fundamental stiffness matrix is expressed as,

$$\left[k_\mathrm{e}\right] = \frac{EI}{L}\begin{bmatrix} c_1 + c_2 + \dfrac{G_1^2}{H} & c_1 - c_2 + \dfrac{G_1 G_2}{H} & \dfrac{G_1}{LH} \\ & c_1 + c_2 + \dfrac{G_2^2}{H} & \dfrac{G_2}{LH} \\ S.Y.M. & & \dfrac{1}{LH} \end{bmatrix} \tag{5.97}$$

in which G_1, G_2, and H are as follows,

$$G_1 = c'_{\mathrm{b1}} = 2b_1\left(\theta_1 + \theta_2\right) + 2b_2\left(\theta_1 - \theta_2\right) + b_{\mathrm{vs}}\left(\frac{v_{\mathrm{m0}}}{L}\right) \tag{5.98}$$

$$G_2 = c'_{\mathrm{b2}} = 2b_1\left(\theta_1 + \theta_2\right) - 2b_2\left(\theta_1 - \theta_2\right) - b_{\mathrm{vs}}\left(\frac{v_{\mathrm{m0}}}{L}\right) \tag{5.99}$$

$$H = \frac{1}{\lambda^2} - c'_{\mathrm{b}} - c'_{\mathrm{b0}} \tag{5.100}$$

The form of the tangent stiffness matrix in 3D space can be extended by repeating the previously described procedures for the y- and z-axes. The expression is as follows,

$$[K_{\mathrm{T}}] = \sum^{NELE} [L][k_{\mathrm{T}}][L]^T = \sum^{NELE} [L]\left([T]^T [k_{\mathrm{e}}][T] + [N]\right)[L]^T \tag{5.101}$$

where [L] is the matrix used to transform the stiffness matrix from a local to a global coordinate system, [T] is the matrix used to transform a member's basic forces to an element force in the local coordinate system, and [N] is the geometric stiffness matrix used to clarify the work exerted by initial force and translational displacements. For details on [L], [T], and [N], the reader is referred to Meek and Tan (1984).

5.4.2. Refined plastic hinge approach

5.4.2.1. Formulation of element stiffness to account for plastic effects

An essential requirement in plastic analysis is defining a function that detects gradual yielding on a section. Figure 5.11 illustrates the node rotations for a curved PEP element that involves two pseudo-springs at both end nodes.

The rotations of two sectional springs are generally unequal because of incomplete yielding on a section and the softened rotation stiffness of a spring. Taking into account the condition of the moment on a spring, the increment equation becomes,

$$\begin{bmatrix} \Delta M_{\mathrm{s}} \\ \Delta M_{\mathrm{b}} \end{bmatrix} = \begin{bmatrix} S_{\mathrm{s}} & -S_{\mathrm{s}} \\ -S_{\mathrm{s}} & S_{\mathrm{s}} \end{bmatrix} \begin{bmatrix} \Delta \theta_{\mathrm{s}} \\ \Delta \theta_{\mathrm{b}} \end{bmatrix} \tag{5.102}$$

where ΔM_s denotes the incremental moments of nodes at the joints between the sectional spring and the global node, ΔM_b representss the incremental nodal moments between the sectional spring and the beam, and $\Delta\theta_s$ and $\Delta\theta_b$ are the incremental rotations of nodes associated with the incremental nodal moments. Subscripts "s" and "b" refer to external and internal nodes in relation to the element. With the combination of sectional spring rigidity and the ends of an element, the increment equation can be rewritten as,

$$\begin{bmatrix} \Delta M_{s1} \\ \Delta M_{b1} \\ \Delta M_{b2} \\ \Delta M_{s2} \end{bmatrix} = \begin{bmatrix} S_{s1} & -S_{s1} & 0 & 0 \\ -S_{s1} & K_{11}+S_{s1} & K_{12} & 0 \\ 0 & K_{21} & K_{22}+S_{s2} & -S_{s2} \\ 0 & 0 & -S_{s2} & S_{s2} \end{bmatrix} \begin{bmatrix} \Delta\theta_{s1} \\ \Delta\theta_{b1} \\ \Delta\theta_{b2} \\ \Delta\theta_{s2} \end{bmatrix} \tag{5.103}$$

where subscripts "1" and "2" refer to nodes 1 and 2, respectively. If only the global nodes are subjected to loading, ΔM_{b1} and ΔM_{b2} are equal to zero in Equation (5.103). These variables can be expressed thus:

$$\begin{bmatrix} \Delta\theta_{b1} \\ \Delta\theta_{b2} \end{bmatrix} = \begin{bmatrix} K_{11}+S_{s1} & K_{12} \\ K_{21} & K_{22}+S_{s2} \end{bmatrix}^{-1} \begin{bmatrix} S_{s1} & 0 \\ 0 & S_{s2} \end{bmatrix} \begin{bmatrix} \Delta\theta_{s1} \\ \Delta\theta_{s2} \end{bmatrix} \tag{5.104}$$

The sectional spring elements are categorized under the internal DOFs of the beam-column element which can be eliminated by substituting Equation (5.104) into (5.103). The final incremental rigidity relationships of the element can be written as,

$$\begin{bmatrix} \Delta P \\ \Delta M_{s1} \\ \Delta M_{s2} \end{bmatrix} = \begin{bmatrix} \frac{EA}{L} & 0 & 0 \\ 0 & S_{s1} - \frac{S_{s1}^2 \left(K_{22} + S_{s2}\right)}{\beta_s} & \frac{S_{s1} S_{s2} K_{12}}{\beta_s} \\ 0 & \frac{S_{s1} S_{s2} K_{21}}{\beta_s} & S_{s2} - \frac{S_{s2}^2 \left(K_{11} + S_{s1}\right)}{\beta_s} \end{bmatrix} \begin{bmatrix} \Delta L \\ \Delta \theta_{s1} \\ \Delta \theta_{s2} \end{bmatrix}$$
$$= \begin{bmatrix} \frac{EA}{L} & 0 & 0 \\ 0 & k'_{22} & k'_{23} \\ 0 & k'_{32} & k'_{33} \end{bmatrix} \begin{bmatrix} \Delta L \\ \Delta \theta_{s1} \\ \Delta \theta_{s2} \end{bmatrix} \tag{5.105}$$

where K_{ij} is the flexural rigidity of the PEP element that considers axial force, ΔP is the axial force increment, ΔL is the axial deformation increment, and

$$\beta_s = \begin{vmatrix} K_{11} + S_{s1} & K_{12} \\ K_{21} & K_{22} + S_{s2} \end{vmatrix} = \left(K_{11} + S_{s1}\right)\left(K_{22} + S_{s2}\right) - K_{12} K_{21} > 0 \tag{5.106}$$

The sectional spring stiffness, S_s, can be formulated as,

$$\begin{aligned} S_s &= 10^{+10} EI/L &&, \text{For } M_i \le M_e \\ S_s &= \frac{EI}{L} \left| \frac{M_{pr}^i - M_i}{M_i - M_{er}^i} \right| &&, \text{For } M_e \le M_i \le M_p \\ S_s &= 10^{-10} EI/L &&, \text{For } M_i \ge M_p \end{aligned} \tag{5.107}$$

in which EI is the constant flexural rigidity; L is the member length; M^i_{er} and M^i_{pr} are the reduced initial and full yielding moments under axial force, respectively. As can be seen in Equation (5.107), the variation in sectional rigidity from infinite to a small strain-hardening value denotes three sectional phases: elastic, partially plastic and fully plastic.

5.4.2.2. Examination of element stiffness in extreme cases

An important task is to verify the derived element stiffness in extreme cases wherein sectional spring stiffnesses are set at very small and very large values. The element stiffness can be validated by comparing it with theoretical stiffness formulae. Three cases require examination: a case where no plastic hinge is found at element ends, one wherein a single plastic hinge is placed at one element end, and another in which both element ends are equipped with two plastic hinges.

(1) No plastic hinge

Given that no plastic hinge is generated at nodes 1 and 2 in an element, the items in the second and third rows of Equation (5.105) can be simplified by establishing very large S_{s1} and S_{s2} values. This approach simplifies the entries from Equation (5.105) into,

$$
\begin{aligned}
k'_{22} &= \lim_{\substack{S_{s1}\to\infty \\ S_{s2}\to\infty}} \left(\frac{S_{s1} - S_{s1}^2 \left(K_{22} + S_{s2} \right)}{\beta_s} \right) \\
&= \lim_{\substack{S_{s1}\to\infty \\ S_{s2}\to\infty}} \frac{\left(\dfrac{K_{22}}{S_{s2}} + 1 \right) K_{11} - \dfrac{K_{12} K_{21}}{S_{s2}}}{\left(\dfrac{K_{11}}{S_{s1}} + 1 \right)\left(\dfrac{K_{22}}{S_{s2}} + 1 \right) - \dfrac{K_{12} K_{21}}{S_{s1} S_{s2}}} = K_{11}
\end{aligned}
\tag{5.108}
$$

$$
\begin{aligned}
k'_{23} &= \lim_{\substack{S_{s1}\to\infty \\ S_{s2}\to\infty}} \left(\frac{S_{s1} S_{s2} K_{12}}{\beta_s} \right) \\
&= \lim_{\substack{S_{s1}\to\infty \\ S_{s2}\to\infty}} \frac{K_{12}}{\left(\dfrac{K_{11}}{S_{s1}} + 1 \right)\left(\dfrac{K_{22}}{S_{s2}} + 1 \right) - \dfrac{K_{12} K_{21}}{S_{s1} S_{s2}}} = K_{12}
\end{aligned}
\tag{5.109}
$$

$$
\begin{aligned}
k'_{32} &= \lim_{\substack{S_{s1}\to\infty \\ S_{s2}\to\infty}} \left(\frac{S_{s1}S_{s2}K_{21}}{\beta_s} \right) \\
&= \lim_{\substack{S_{s1}\to\infty \\ S_{s2}\to\infty}} \frac{K_{21}}{\left(\frac{K_{11}}{S_{s1}}+1\right)\left(\frac{K_{22}}{S_{s2}}+1\right)-\frac{K_{12}K_{21}}{S_{s1}S_{s2}}} = K_{21}
\end{aligned} \tag{5.110}
$$

$$
\begin{aligned}
k'_{33} &= \lim_{\substack{S_{s1}\to\infty \\ S_{s2}\to\infty}} \left(\frac{S_{s2}-S_{s2}^{2}\left(K_{11}+S_{s1}\right)}{\beta_s} \right) \\
&= \lim_{\substack{S_{s1}\to\infty \\ S_{s2}\to\infty}} \frac{\left(\frac{K_{11}}{S_{s1}}+1\right)K_{22}-\frac{K_{12}K_{21}}{S_{s2}}}{\left(\frac{K_{11}}{S_{s1}}+1\right)\left(\frac{K_{22}}{S_{s2}}+1\right)-\frac{K_{12}K_{21}}{S_{s1}S_{s2}}} = K_{22}
\end{aligned} \tag{5.111}
$$

The final incremental force-displacement equation is converted into a beam-column element as follows,

$$
\begin{bmatrix} \Delta P \\ \Delta M_{s1} \\ \Delta M_{s2} \end{bmatrix} = \begin{bmatrix} \frac{EA}{L} & 0 & 0 \\ 0 & K_{11} & K_{12} \\ 0 & K_{21} & K_{22} \end{bmatrix} \begin{bmatrix} \Delta L \\ \Delta\theta_{s1} \\ \Delta\theta_{s2} \end{bmatrix} \tag{5.112}
$$

(2) Only a single plastic hinge at node 1

If one plastic hinge is generated at node 1 in an element, S_{s1} and S_{s2} are set as very small and extremely large values, respectively. The entries are simplified as,

$$
\begin{aligned}
k'_{22} &= \lim_{\substack{S_{s1}\to 0 \\ S_{s2}\to\infty}} \left(\frac{S_{s1}-S_{s1}^{2}\left(K_{22}+S_{s2}\right)}{\beta_s} \right) \\
&= \lim_{\substack{S_{s1}\to 0 \\ S_{s2}\to\infty}} \frac{S_{s1}\left(K_{11}-\frac{K_{12}K_{21}}{S_{s2}}\right)}{\left(K_{11}+S_{s1}\right)\left(\frac{K_{22}}{S_{s2}}+1\right)-\frac{K_{12}K_{21}}{S_{s2}}} = 0
\end{aligned} \tag{5.113}
$$

$$
\begin{aligned}
k'_{23} &= \lim_{\substack{S_{s1}\to 0\\ S_{s2}\to\infty}} \left(\frac{S_{s1} S_{s2} K_{12}}{\beta_s} \right) \\
&= \lim_{\substack{S_{s1}\to 0\\ S_{s2}\to\infty}} \frac{S_{s1} K_{12}}{\left(K_{11}+S_{s1}\right)\left(\dfrac{K_{22}}{S_{s2}}+1\right)-\dfrac{K_{12}K_{21}}{S_{s2}}} = 0
\end{aligned} \tag{5.114}
$$

$$
\begin{aligned}
k'_{32} &= \lim_{\substack{S_{s1}\to 0\\ S_{s2}\to\infty}} \left(\frac{S_{s1} S_{s2} K_{21}}{\beta_s} \right) \\
&= \lim_{\substack{S_{s1}\to 0\\ S_{s2}\to\infty}} \frac{S_{s1} K_{21}}{\left(K_{11}+S_{s1}\right)\left(\dfrac{K_{22}}{S_{s2}}+1\right)-\dfrac{K_{12}K_{21}}{S_{s2}}} = 0
\end{aligned} \tag{5.115}
$$

$$
\begin{aligned}
k'_{33} &= \lim_{\substack{S_{s1}\to 0\\ S_{s2}\to\infty}} \left(\frac{S_{s2} - S_{s2}^2\left(K_{11}+S_{s1}\right)}{\beta_s} \right) \\
&= \lim_{\substack{S_{s1}\to 0\\ S_{s2}\to\infty}} \frac{\left(K_{11}+S_{s1}\right)K_{22} - K_{12}K_{21}}{\left(K_{11}+S_{s1}\right)\left(\dfrac{K_{22}}{S_{s2}}+1\right)-\dfrac{K_{12}K_{21}}{S_{s2}}} = \frac{K_{11}K_{22}-K_{12}K_{21}}{K_{11}}
\end{aligned} \tag{5.116}
$$

The final element stiffness equation can be written as,

$$
\begin{bmatrix} \Delta P \\ \Delta M_{s1} \\ \Delta M_{s2} \end{bmatrix} = \begin{bmatrix} \dfrac{EA}{L} & 0 & 0 \\ 0 & \dfrac{K_{11}K_{22}-K_{12}K_{21}}{K_{11}} & 0 \\ 0 & 0 & 0 \end{bmatrix} \begin{bmatrix} \Delta L \\ \Delta\theta_{s1} \\ \Delta\theta_{s2} \end{bmatrix} \tag{5.117}
$$

The value of $(K_{11}K_{22}–K_{12}K_{21})/K_{11}$ is equal to $3EI/L$ on the assumption that axial force disappears (i.e. P=0, K_{11}=K_{22}=$4EI/L$, K_{12}=K_{21}=$2EI/L$). The stiffness equation is eventually converted into the stiffness of a beam with one end pinned and another end fixed.

(3) Plastic hinges at nodes 1 and 2

For plastic hinges generated at nodes 1 and 2 in an element, S_{s1} and S_{s2} are defined as extremely small values. Correspondingly, the entries from Equation (5.105) are converted into,

$$\begin{aligned} k'_{22} &= \lim_{\substack{S_{s1}\to 0 \\ S_{s2}\to 0}} \left(\frac{S_{s1} - S_{s1}^2 \left(K_{22} + S_{s2}\right)}{\beta_s} \right) \\ &= \lim_{\substack{S_{s1}\to 0 \\ S_{s2}\to 0}} \frac{K_{11} S_{s1} \left(K_{22} + S_{s2}\right) - K_{12} K_{21} S_{s1}}{\left(K_{11} + S_{s1}\right)\left(K_{22} + S_{s2}\right) - K_{12} K_{21}} = 0 \end{aligned} \tag{5.118}$$

$$\begin{aligned} k'_{23} &= \lim_{\substack{S_{s1}\to 0 \\ S_{s2}\to 0}} \left(\frac{S_{s1} S_{s2} K_{12}}{\beta_s} \right) \\ &= \lim_{\substack{S_{s1}\to 0 \\ S_{s2}\to 0}} \frac{S_{s1} S_{s2} K_{12}}{\left(K_{11} + S_{s1}\right)\left(K_{22} + S_{s2}\right) - K_{12} K_{21}} = 0 \end{aligned} \tag{5.119}$$

The final equation becomes,

$$\begin{bmatrix} \Delta P \\ \Delta M_{s1} \\ \Delta M_{s2} \end{bmatrix} = \begin{bmatrix} \dfrac{EA}{L} & 0 & 0 \\ 0 & 0 & 0 \\ 0 & 0 & 0 \end{bmatrix} \begin{bmatrix} \Delta L \\ \Delta \theta_{s1} \\ \Delta \theta_{s2} \end{bmatrix} \tag{5.120}$$

This expression is identical to a pin-jointed truss element.

5.4.2.3. Force point movement between initial and full yield surfaces

Initial and full yield surfaces divide a loading zone into three parts: elastic, elastoplastic and plastic hardening areas (see Figure 5.12). If a loading combination is falls within the range of the initial yield surface, a section can be regarded as characterized by ideal elasticity without the need to reduce strength or stiffness. If the coordinate of a load point falls in the elastoplastic area, the stiffness of a sectional spring is degraded and the force point may move, as shown in Figure 5.12. Once the loading combination exceeds the full yield surface, sectional hardening occurs.

Elastic moment capacity M_e^n and plastic moment capacity M_p^n are both in the existence of the axial force, the determination of these two values is illustrated in Figure 5.12.

5.4.2.4. Constitutive relationship of materials

Constitutive models are generally obtained by experiments. If experimentation is not possible, an assumed elastic-ideally plastic stress–strain relationship can be adopted in analysis (see Figure 5.13). For structural steel, this relationship takes on the mathematical forms,

$$\sigma = f_y, \qquad \varepsilon_e \le \varepsilon \le \varepsilon_u \tag{5.121}$$

$$\sigma = E \cdot \varepsilon, \qquad -\varepsilon_e \le \varepsilon \le \varepsilon_e \tag{5.122}$$

$$\sigma = -f_y, \qquad -\varepsilon_u \le \varepsilon \le -\varepsilon_e \tag{5.123}$$

where, f_y is the yield stress of steel; E is the Young's modulus of steel; ε_e and ε_u are the strain limits for elasticity and plasticity, respectively.

5.4.3. Algorithm for nonlinear analysis

The non-proportional nature of load-deflection behavior is the main characteristic of nonlinear analysis, indicating that instantaneous loading level and geometric deformation affect the reaction of a structure under incremental force. As one of the methods for nonlinear analysis, the Newton–Raphson method is commonly employed in the regular design of structures. It not only presents ease of use and effective predictions for the analysis of normal structures, but also provides precise structural reactions at given load cases. Nevertheless, if a solution point is in the vicinity of limit points, this approach is inaccurate, thereby making the distinction between numerical failure and structural instability difficult.

Obtaining the full load-deflection reaction of a structure for nonlinear analysis is often difficult owing to numerical divergence. In particular, tangent stiffness is ill-conditioned or a numerical singular value is near limit points. Consequently, the Newton–Raphson method cannot obtain satisfactory results in extreme cases that require only tangent stiffness in the increment procedure. This deficiency gives rise to divergence in equilibrium iterations.

Over the past decades, some state-of-the-art numerical algorithms proposed by researchers have been validated through many examples. Batoz and Dhatt (1979) presented a displacement control algorithm that uses incremental displacement instead of load and introduced a highly valuable approach to restoring symmetry of the system matrix. The approach enables performance analysis when solution points are close to limit points and snap-through points. A flaw of the approach is that it fails to solve the snap-back problem, wherein the loading equilibrium path does not rise with monitored displacement. Riks (1979) initially proposed the arc length method, in which an additional constraint equation is introduced to tangent stiffness equations with changes in arc length for tracing of the equilibrium path. The method was refined by Crisfield (1981) and Ramm (1981) to preserve the symmetry of the tangent stiffness matrix. It is an effective and stable approach to solving numerous nonlinearity problems, but the quadratic equations require solving at each iteration. Chan (1988) indicated that the ultimate purpose of iterations is to minimize divergence error and proposed the minimum residual displacement method, in which a solution point can be obtained by the shortest equilibrium path in this method. Unlike the quadratic equations of the arc length method, the mathematical expression of the minimum residual method is simple and does not require solving a quadratic equation.

The Newton–Raphson method is briefly discussed in the followings, and the incremental iterative procedure of the constraint equation is explained. The arc length control, displacement control, and minimum residual displacement methods are also reviewed.

5.4.3.1. Newton–Raphson approach

The Newton–Raphson method, which integrates the iteration and increment methods, adopts a linear solution in resolving the nonlinearity problem. To diminish the error between external and internal forces, the method may require multiple iterations at each load ΔF. It also uses the norm of an unbalanced force vector $[\Delta R]$ to assess iterative times. The unbalanced force vector, $[\Delta R]$, can be obtained by,

$$[\Delta R]=[F]-[R] \tag{5.124}$$

where, [F] is the external force vector, and [R] is the internal resistance force vector computed by the formula for nodal displacement u.

The tangent stiffness matrix is to be rectified at each iteration in the conventional Newton–Raphson solution method. By contrast, this matrix is to be reformed only at the first iteration in the modified Newton–Raphson technique. The comparison of the two is illustrated in Figure 5.14. The basic steps of the Newton–Raphson method are as follows,

$$[\Delta R]_i=[F]-[R]_i \tag{5.125}$$

$$[\Delta u]_i=[K_T]^{-1}[\Delta R]_i \tag{5.126}$$

$$[u]_{i+1}=[u]_i+[\Delta u]_i \tag{5.127}$$

$$[R]_{i+1}=\text{Function of }[u]_{i+1} \tag{5.128}$$

in which, [K_T] is the tangent stiffness matrix adjusted iteratively in the Newton-Raphson method, and i is the iterative number.

5.4.3.2. Derivation of constraint equation

The incremental equilibrium equation can be expressed as,

$$[\Delta F]=[K_\mathrm{T}][\Delta u] \tag{5.129}$$

where, [ΔF] is the unbalanced force vector, [K_T] is the tangent stiffness matrix, and [Δu] is the unbalanced displacement vector.

The force vector in the constraint equation parallels the applied load vector and the equation can be obtained as,

$$\Delta\lambda\left[\Delta\bar{F}\right]=\Delta\lambda\left[K_{\mathrm{T}}\right]\left[\Delta\bar{u}\right] \tag{5.130}$$

in which $\Delta\lambda$ is the load corrective coefficient for the imposition of the constraint condition; $[\Delta\bar{F}]$ is the force vector of arbitrary length, which parallels the applied load vector; and $[\Delta\bar{u}]$ is the conjugate displacement vector of $[\Delta\bar{F}]$.

With substituting Equation (5.127) into (5.126), the final incremental equilibrium equation is given as,

$$\left[\Delta F\right]+\Delta\lambda\left[\Delta\bar{F}\right]=\left[K_{\mathrm{T}}\right]\left(\left[\Delta u\right]+\Delta\lambda\left[\Delta\bar{u}\right]\right) \tag{5.131}$$

Then, the load vector and displacement vector at every iteration can be reformed as,

$$\left[F\right]_{i+1}=\left[F\right]_{i}+\Delta\lambda_{i+1}\left[\Delta\bar{F}\right] \tag{5.132}$$

$$\left[u\right]_{i+1}=\left[u\right]_{i}+\Delta\lambda_{i+1}\left[\Delta\bar{u}\right] \tag{5.133}$$

where subscript "*i*" represents the *i*-th iterative number in a load increment.

All numerical analysis methods that are based on the incremental-iterative procedure can be formulated as Equation (5.128), with differences in terms of load corrective coefficient $\Delta\lambda$. This equation is converted into the incremental equilibrium equation of the conventional Newton–Raphson method if the load corrective coefficient is set to zero.

5.4.3.3. Arc length control approach

As one of the favorable methods used to solve nonlinear analysis problems, the arc length method was initially presented by Riks (1979) and further developed by Crisfield (1983). In this approach, the load increment related to arc distance S adds a constraint equation. The relative constraint equation at the initial iteration within a load cycle is as follows,

$$\Delta\lambda_1 = \frac{S}{\sqrt{[\Delta\bar{u}]_1^{\mathrm{T}}[\Delta\bar{u}]_1}} \tag{5.134}$$

in which S is the initial arc distance.

Arc distance S is kept constant for succeeding iterations. The constraint equation then becomes,

$$\left([u]_{i-1} + [\Delta u]_i + \Delta\lambda_i[\Delta\bar{u}]_i\right)^{\mathrm{T}}\left([u]_{i-1} + [\Delta u]_i + \Delta\lambda_i[\Delta\bar{u}]_i\right) = S^2 \tag{5.135}$$

The expanded equation can be obtained as,

$$[\alpha_1]\Delta\lambda_i^2 + [\alpha_2]\Delta\lambda_i + [\alpha_3] = 0 \tag{5.136}$$

where,

$$[\alpha_1] = [\Delta\bar{u}]_i^{\mathrm{T}}[\Delta\bar{u}]_i \tag{5.137}$$

$$[\alpha_2]=2\left([u]_{i-1}+[\Delta u]_i\right)^{\mathrm{T}}[\Delta\overline{u}]_i \tag{5.138}$$

$$[\alpha_3]=\left([u]_{i-1}+[\Delta u]_i\right)^{\mathrm{T}}\left([u]_{i-1}+[\Delta u]_i\right)-S^2 \tag{5.139}$$

A necessary task is to select the root associated with a positive angle between the initiation and the updated displacement increment vector after Equation (5.133) is calculated. The load incremental factor at the *i*-th interaction is,

$$\Delta\lambda_i=-\frac{[\alpha_3]}{[\alpha_2]} \tag{5.140}$$

The arc length method is illustrated in Figure 5.15. The quadratic equation requires computation, and the roots should be selected within the iterative procedure.

5.4.3.4. Single displacement control approach

The single displacement control method for nonlinear analysis was presented by Batoz and Dhatt (1979). The selection of a single DOF is adopted to steer displacement with fixed increment. In this method, a pre-determined deflection can satisfy the equilibrium at each load incremental step. The procedure is illustrated in Figure 5.16.

By assuming an *m*-th DOF as the steering displacement DOF, the corrective coefficient can be expressed as,

$$\Delta\lambda_1=-\frac{\delta_0}{\Delta_{\mathrm{m}}\overline{u}_1} \tag{5.141}$$

in which δ_0 is the pre-determined displacement increment as the steering DOF and $\Delta_m \bar{u}_1$ is the displacement vector related to a random load vector parallel to applied loads.

For succeeding iterations within a load increment, $\Delta_m \bar{u}_{i+1}$ is identical to $\Delta_m \bar{u}_i$ because of the absence of displacement at the steering DOF. The corrective coefficient becomes,

$$\Delta\lambda_i = -\frac{\Delta_m u_i}{\Delta_m \bar{u}_i} \qquad (i \geq 2) \tag{5.142}$$

where $\Delta_m \bar{u}_i$ is the load increment given unbalanced force during iterations.

This method exhibits excellent performance for inelastic analysis when solution points are close to limit points and snap-through points. However, it fails to solve the snap-back problem, in which the loading equilibrium path does not increase with monitored displacement. Additionally, an essential requirement is to select the steering DOF during analysis because of its crucial effects on numerical stability. The largest displacement incremental point in a structure is commonly taken as the steering DOF.

5.4.3.5. Minimum residual displacement approach

Given that the ultimate purpose of the iteration process is the elimination of unbalanced forces or residual displacement, Chan (1988) proposed the minimum residual displacement method to satisfy the convergence criterion instead of the constraint arc distance or completed constant work, which are not the objectives of numerical iterations.

Residual displacement can be defined as $[\Delta u]_i + \Delta\lambda_i[\Delta\bar{u}]$, where $[\Delta\bar{u}]$ is the displacement vector associated with the force vector $[\Delta\bar{F}]$ that parallels applied loads $[F]$. Differentiating the formula of convergence criterion about parameter $\Delta\lambda_i$, the minimum residual displacement can be obtained as,

$$\frac{\partial\left[\left(\Delta\lambda_i[\Delta\bar{u}]+[\Delta u]_i\right)^{\mathrm{T}}\left(\Delta\lambda_i[\Delta\bar{u}]+[\Delta u]_i\right)\right]}{\partial\Delta\lambda_i}=0 \tag{5.143}$$

and further rewritten as,

$$\lambda_i=-\frac{[\Delta u]_i^{\mathrm{T}}[\Delta\bar{u}]}{[\Delta\bar{u}]^{\mathrm{T}}[\Delta\bar{u}]} \tag{5.144}$$

This method is graphically depicted in Figure 5.17.

For two or more iterations, $\Delta\lambda_i$ can be obtained by Equation (5.141). Load increment should be small at the initial iteration. For the magnitude of load increment at the first step, the stiffness parameter proposed by Bergan *et al.* (1978) can be adopted as follows,

$$\Delta\lambda_1=\Delta\lambda_1\left(S_{\mathrm{k}}\right)^{\gamma} \tag{5.145}$$

where γ is a parameter defined by users to control load magnitude and S_{k} is the current stiffness parameter written as,

$$S_{\mathrm{k}} = \frac{\left[\Delta\bar{F}\right]_{\mathrm{l}}^{\mathrm{T}}\left[\Delta\bar{u}\right]_{\mathrm{k}}}{\left[\Delta\bar{F}\right]_{\mathrm{k}}^{\mathrm{T}}\left[\Delta\bar{u}\right]_{\mathrm{l}}} \quad \text{and} \quad 0.1 < \left(S_{\mathrm{k}}\right)^{\gamma} < 2.0 \tag{5.146}$$

The minimum residual displacement method is deemed straightforward and effective because quadratic equations do not require resolution, as in the arc length method. Furthermore, the shortest path is selected to acquire a solution point in the iterative process.

5.4.3.6. Convergence criteria

For the iterative processes of finite element analysis, a necessary task is to use convergence criteria on the basis of residual displacements or unbalanced forces to terminate an iteration. Convergence criteria significantly influence the predictive accuracy of engineering analysis. These criteria are as follows,

$$\frac{\left[\Delta u\right]_{\mathrm{g}}^{\mathrm{T}}\left[\Delta u\right]_{\mathrm{g}}}{\left[u\right]_{\mathrm{g}}^{\mathrm{T}}\left[u\right]_{\mathrm{g}}} \leq 0.1\% \tag{5.147}$$

$$\frac{\left[\Delta F\right]_{\mathrm{g}}^{\mathrm{T}}\left[\Delta F\right]_{\mathrm{g}}}{\left[R\right]_{\mathrm{g}}^{\mathrm{T}}\left[R\right]_{\mathrm{g}}} \leq 0.1\% \tag{5.148}$$

in which $[\Delta u]_{\mathrm{g}}$ and $[u]_{\mathrm{g}}$ are the incremental and overall displacements of external nodes in the global coordinate system, respectively; and $[\Delta F]_{\mathrm{g}}$ and $[R]_{\mathrm{g}}$ denote the global unbalanced forces and external resistance forces in global directions, respectively.

5.5. Numerical examples

The accuracy of the proposed analysis method for individual members is validated by comparing its findings with the experimental results presented by Wang (2012). The overall buckling behavior of the members adopted in the succeeding examples are simulated. The verification of member strength is associated with failure surfaces, and the simulation of the unloading process is based on initial yield surfaces. Combining the Newton–Raphson method with the minimum residual displacement (Chan, 1988) or arc length methods (Crisfield, 1981) enables tracing of the path to and beyond limits while maintaining convergence. The minimum residual displacement method is adopted in this analysis because it presents minimal equilibrium deviation at every iteration.

5.5.1. Axial compression member with welded box sections

In this example, the yield strength of the column is 505.8 MPa, and the elasticity modulus is 207800 MPa. Its length is 3260 mm, and its sectional dimensions are illustrated in Figure 5.7(a). The distribution of residual stresses is shown in Figure 5.6(a) and Table 5.3.

For high-strength steel columns with welded box sections, the load-displacement curves obtained by the proposed analysis method and the previous experimental investigation (i.e., Wang, 2012) are plotted in Figure 5.18. The curve derived in the present study is close to the experimental results, indicating that the proposed method is suitable for high-strength steel columns with welded box sections subjected to axial compression.

5.5.2. Axial compression member with welded H sections

In terms of the example with welded H columns, two types of material properties exist because of the different thicknesses of flanges and webs. The yield strengths of the flanges and web are 464 and 505.8 MPa, respectively. Their elastic moduli are 217600 and 207800 MPa, respectively, and the length of the column is 3320 mm. Figure 5.8(a) represents the sectional dimensions, and Figure 5.6(b) and Table 5.4 illustrate the adopted residual stresses model.

Figure 5.19 describes the load-displacement curves acquired using the proposed method and the experimental data on high-strength steel columns with welded H sections. The two curves exhibit moderate divergence (Figure 5.19), indicating that the proposed analysis method can be exploited to simulate H columns made of high-strength steel subjected to axial loading.

5.6. Concluding remarks

This chapter presents analysis methods for sections and beam-column elements, which are used as components in second-order design and advanced analysis. The application of analytical technique of sections contributes to consider the effects of residual stresses. Two examples are illustrated to validate the proposed cross-section analysis technique. The failure and initial yield surfaces are adopted to check the strength of members and simulate unloading process, respectively. Geometrical nonlinearity, i.e., initial out-of-straightness and P-δ effects, is considered via the PEP element. As for material nonlinearity, the refined plastic hinge method is employed. Finally, to verify the efficiency and accuracy of the proposed analysis method, previous experimental results on Q460 welded high-strength steel box and H columns and the current analysis findings are compared.

Figures

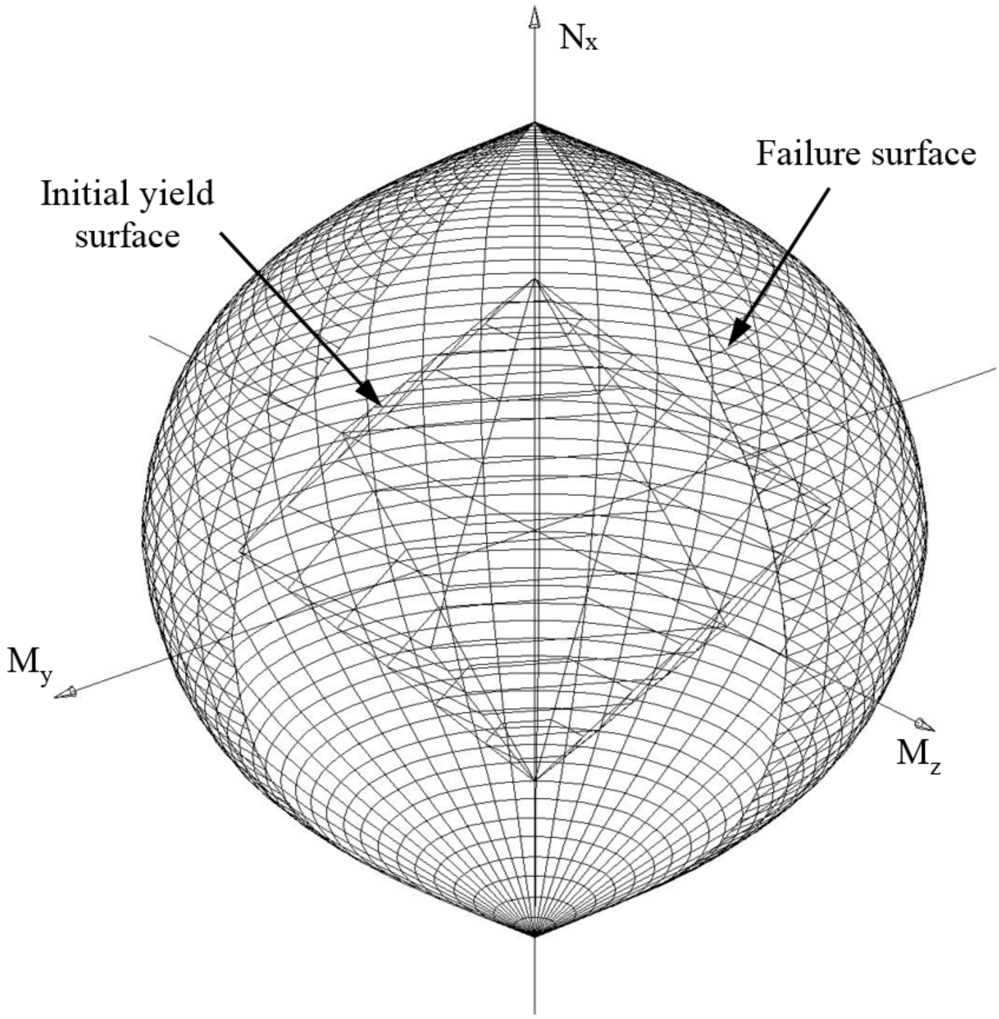

Figure 5.1 Interpretation of initial yield and failure surfaces of steel sections

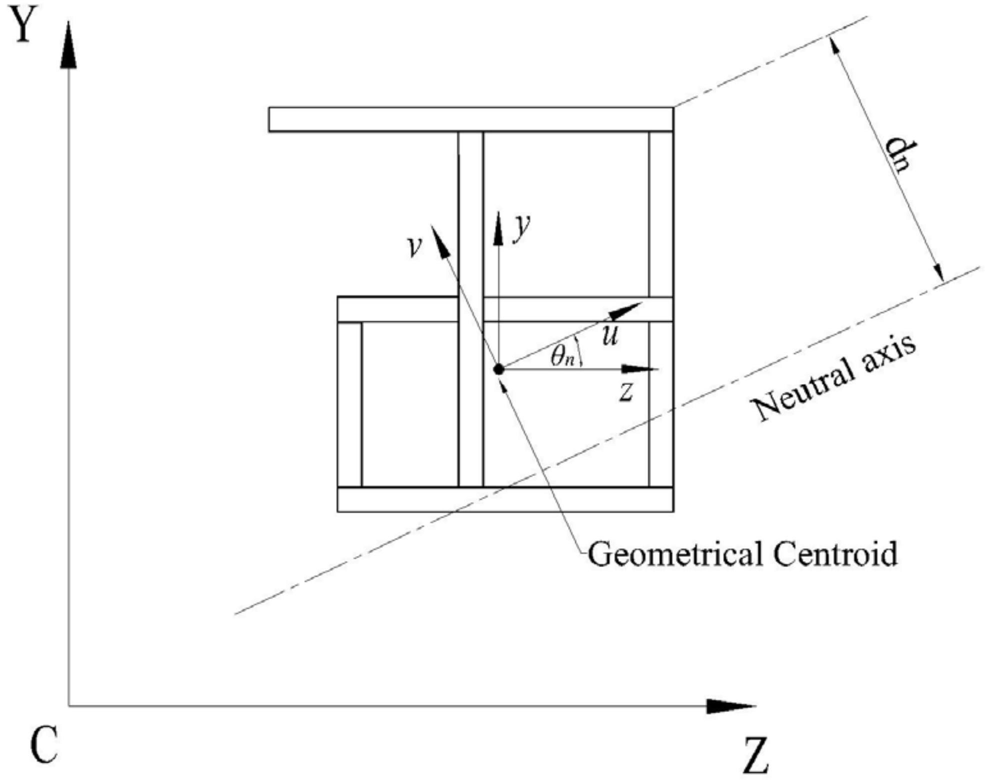

Figure 5.2 Arbitrarily fabricated section

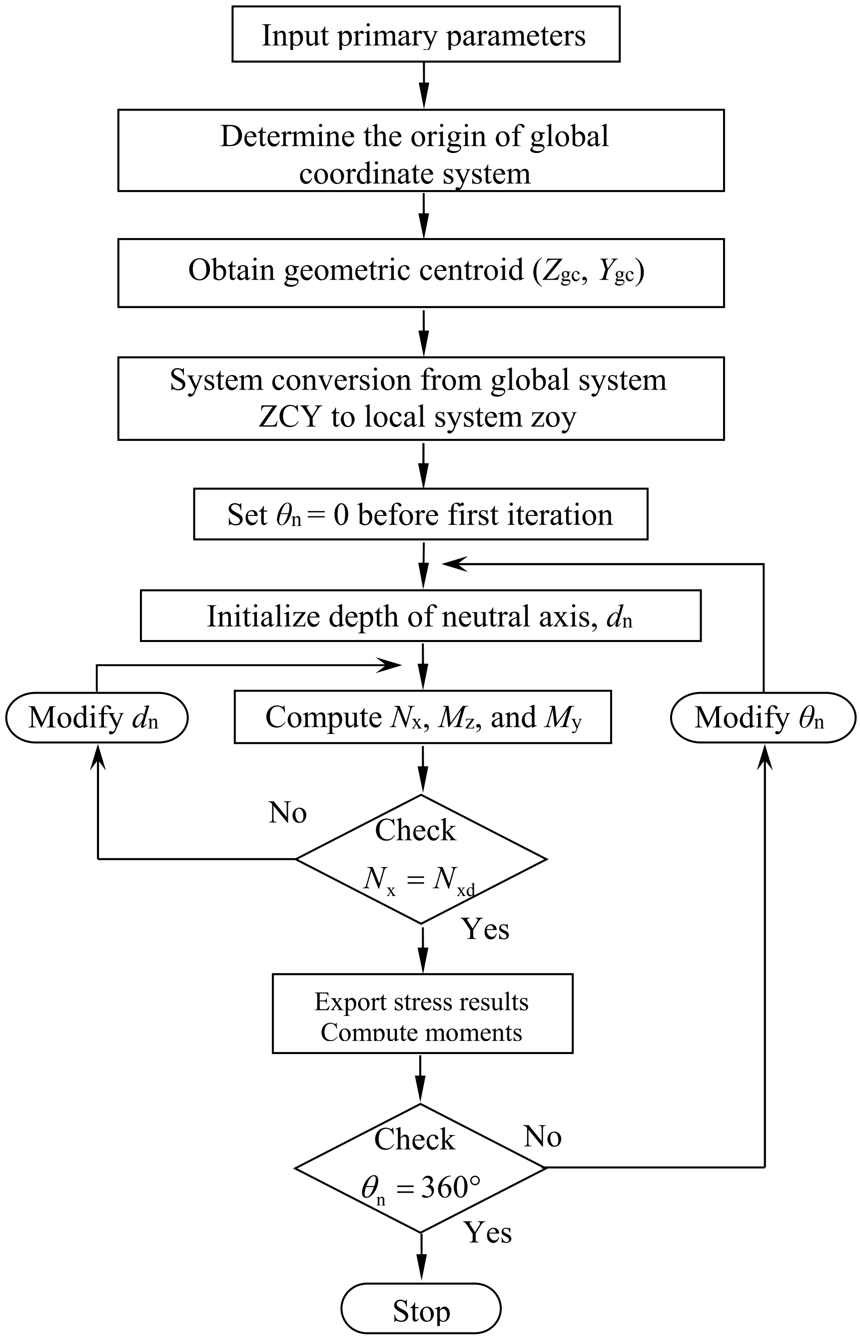

Figure 5.3 Flowchart for sectional analysis under given axial load

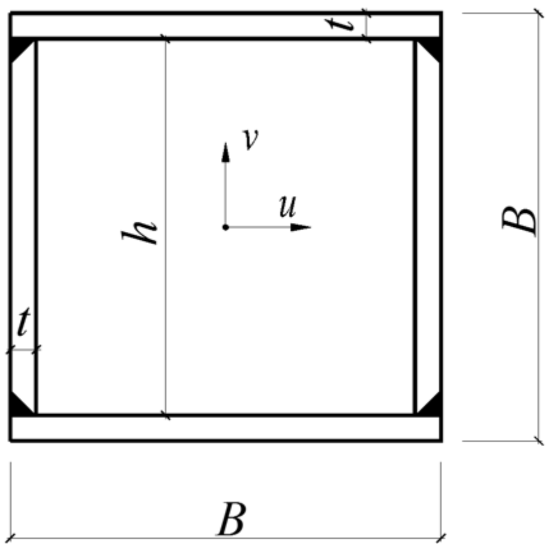

(a) Box section

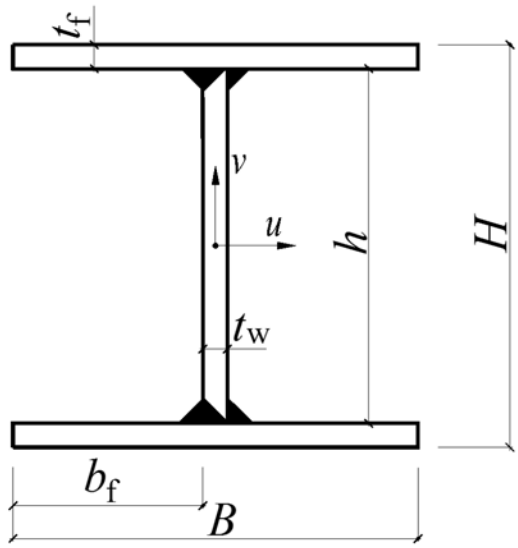

(b) H section

Figure 5.4 Definition of symbols

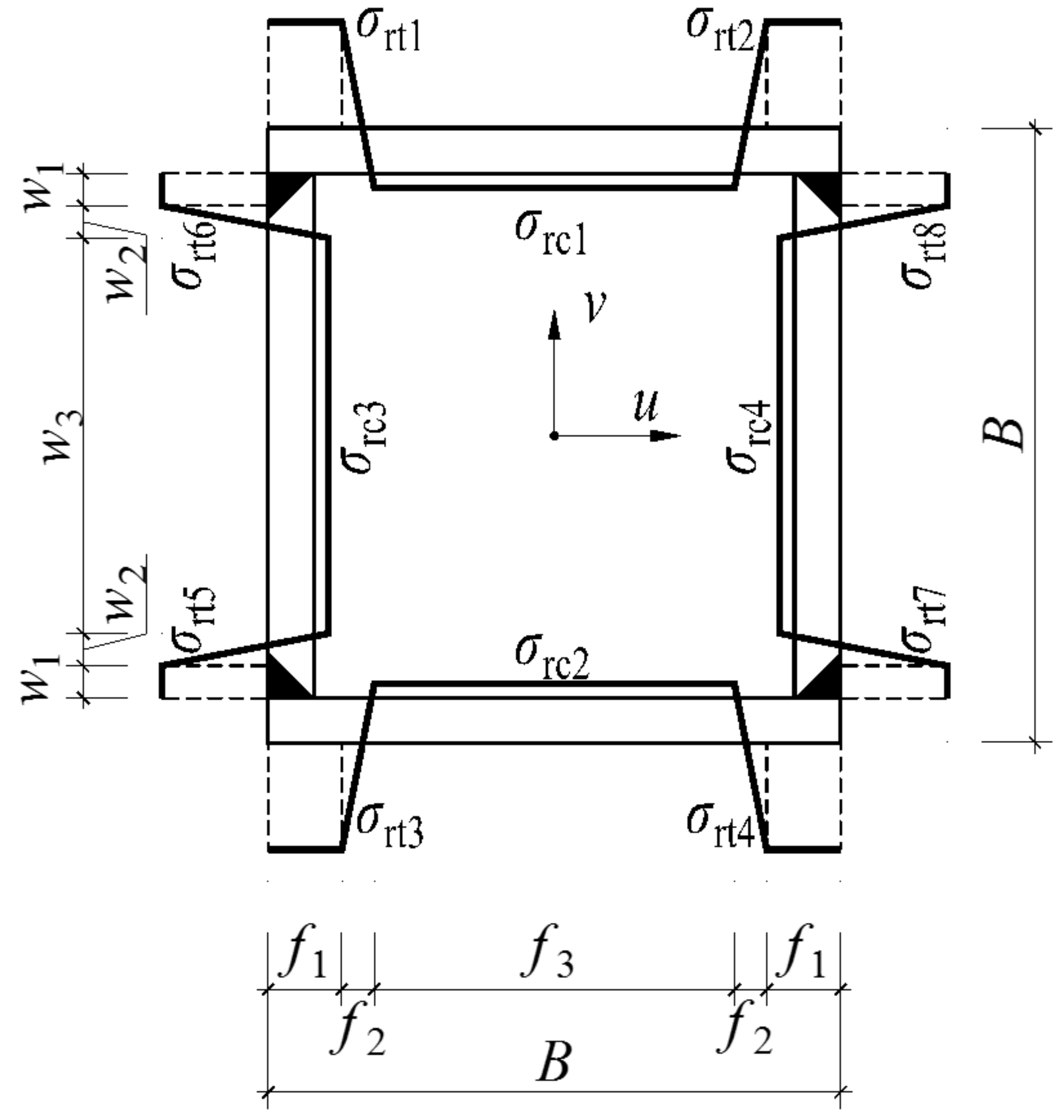

(a) Pattern for a box section

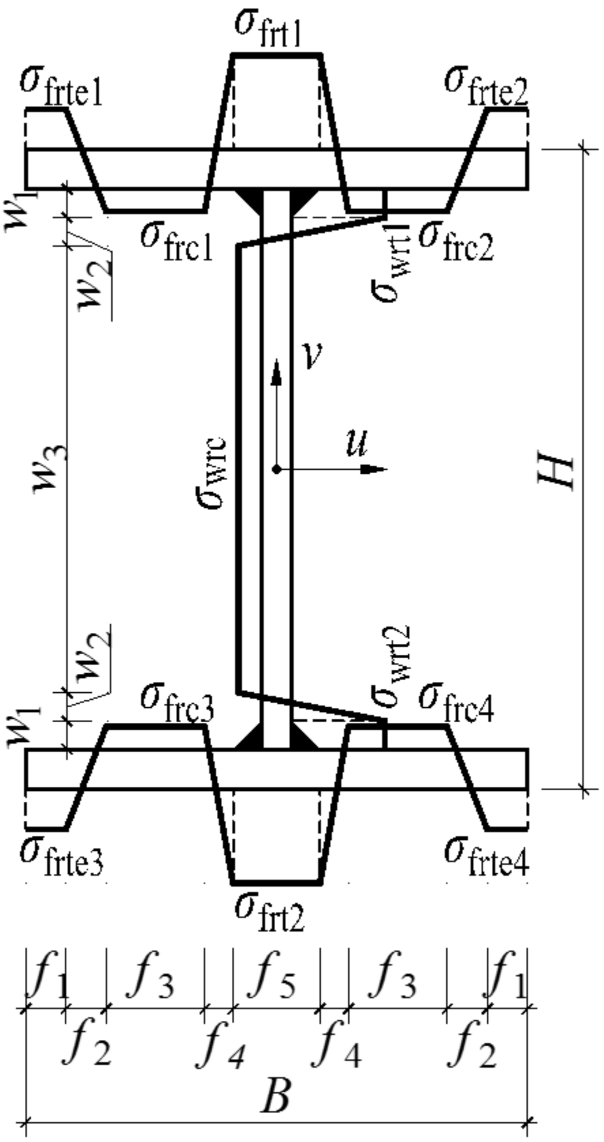

(b) Pattern for an H section

Figure 5.5 Residual-stress model I

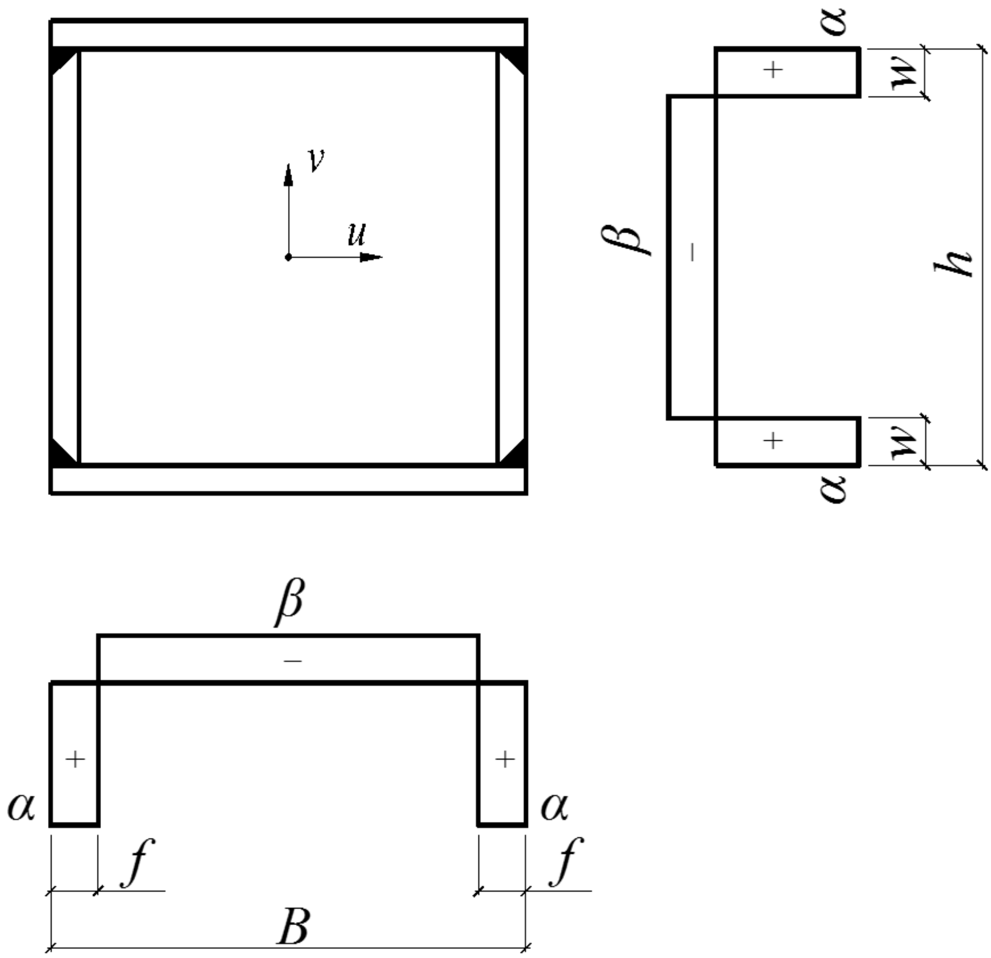

(a) Pattern for a box section

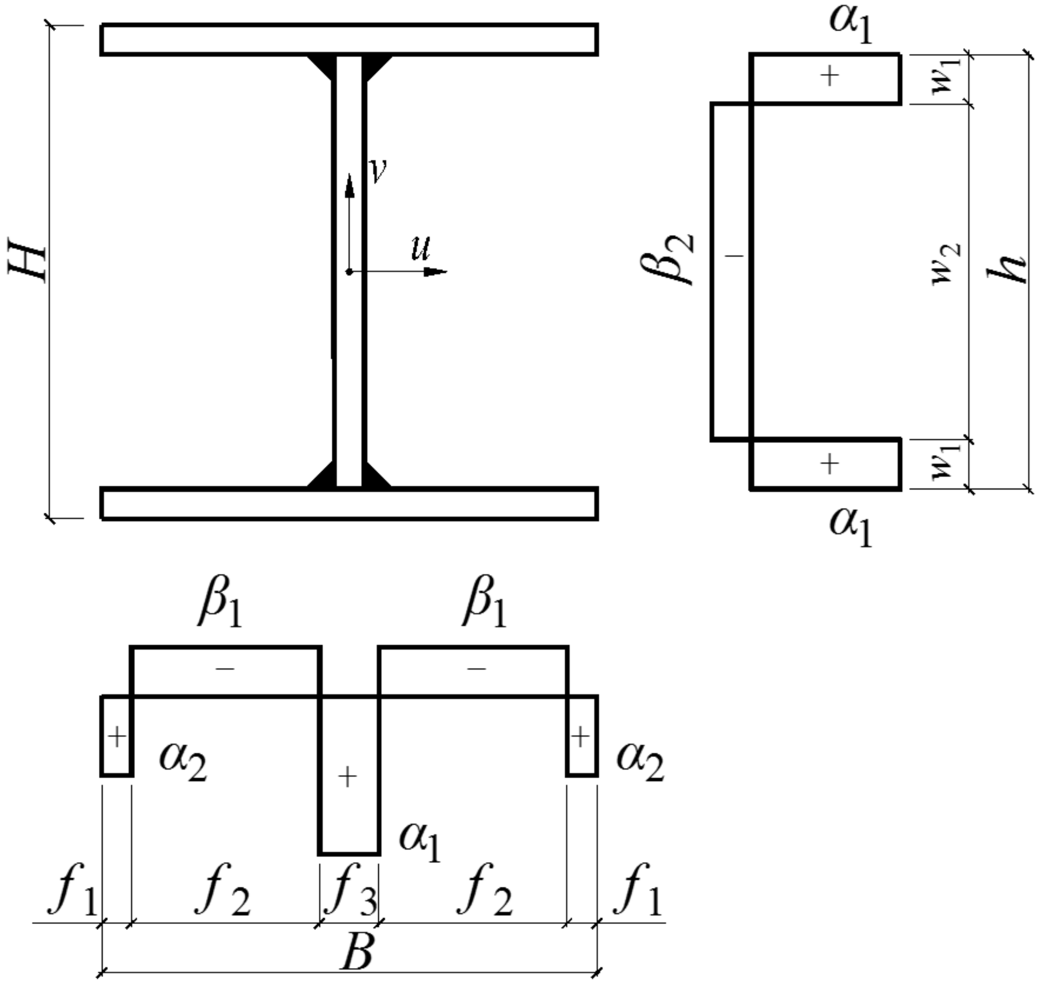

(b) Pattern for an H section

Figure 5.6 Residual-stress model II

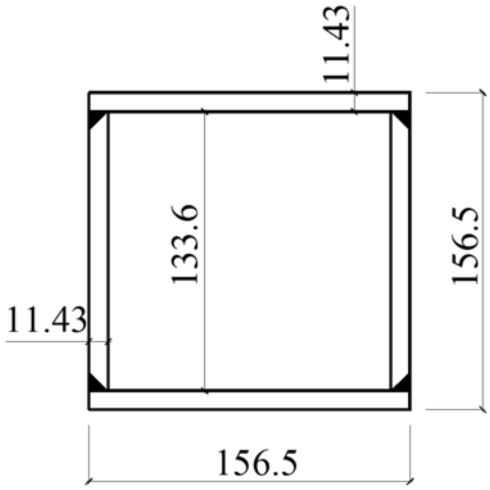

(a) Dimensions

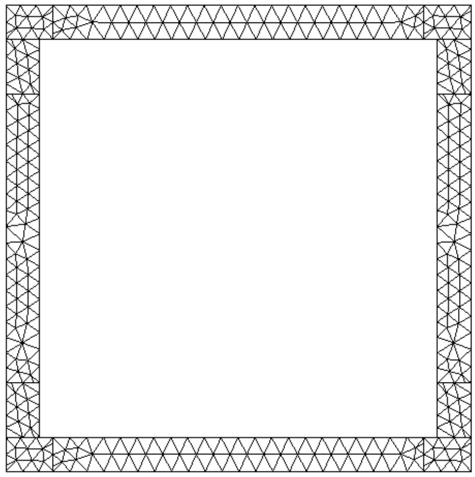

(b) Section fibers

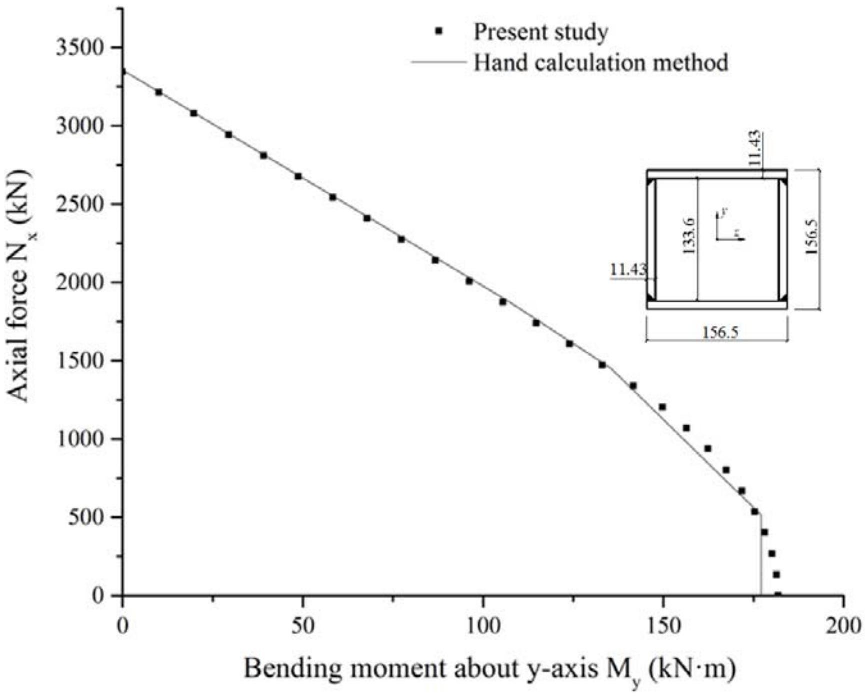

(c) Failure surface without residual stress

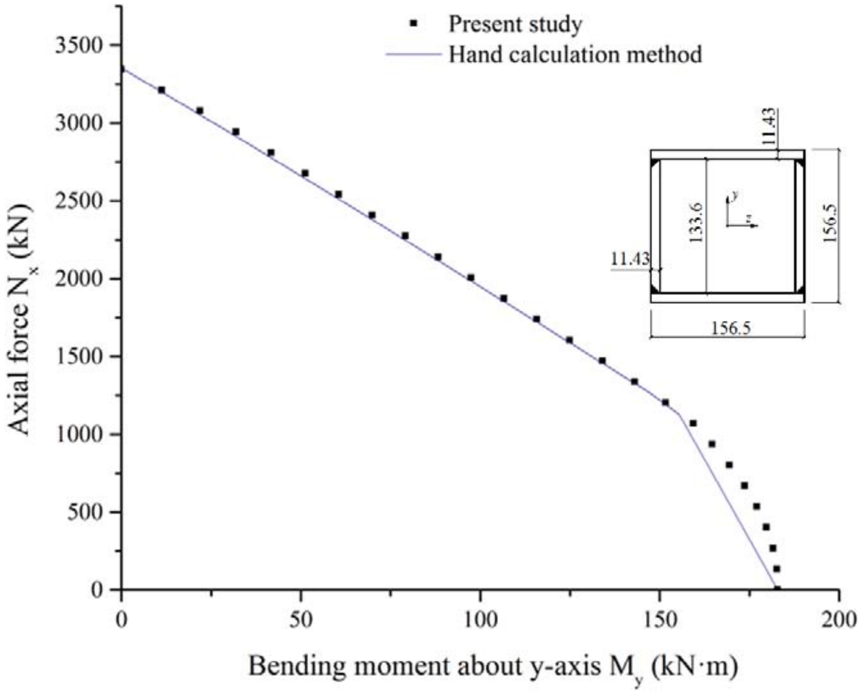

(d) Failure surface with residual stress

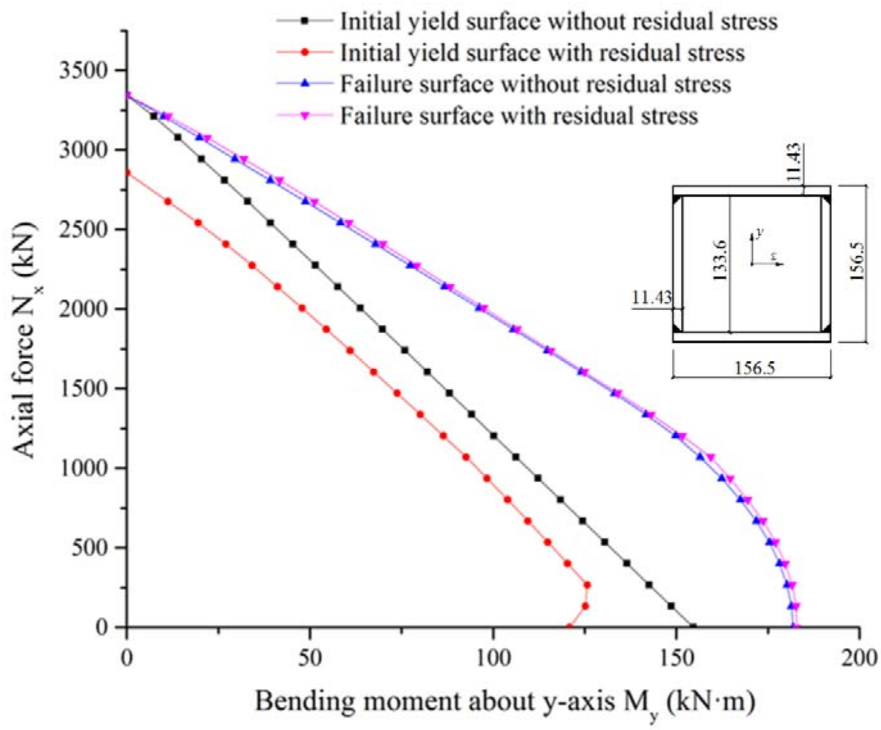

(e) Residual stress effects on initial yield and failure surfaces

Figure 5.7 Comparison results of box-section

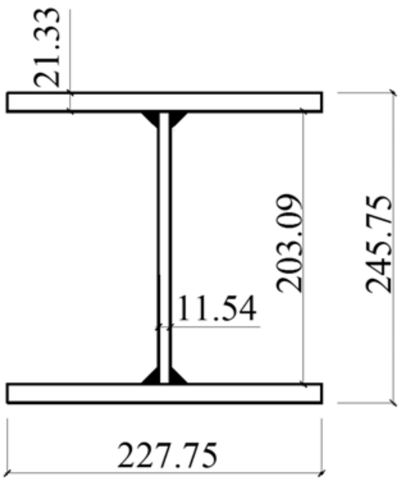

(a) Dimensions

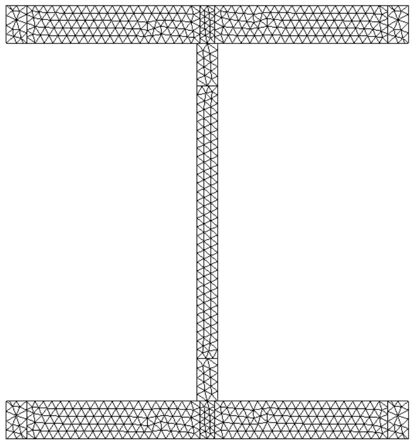

(b) Section fibers

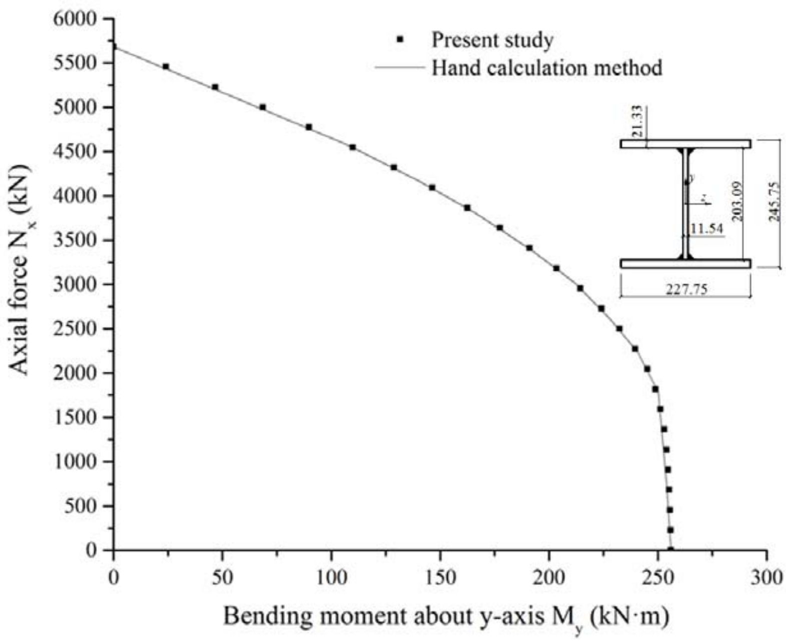

(c) Failure surface without residual stress

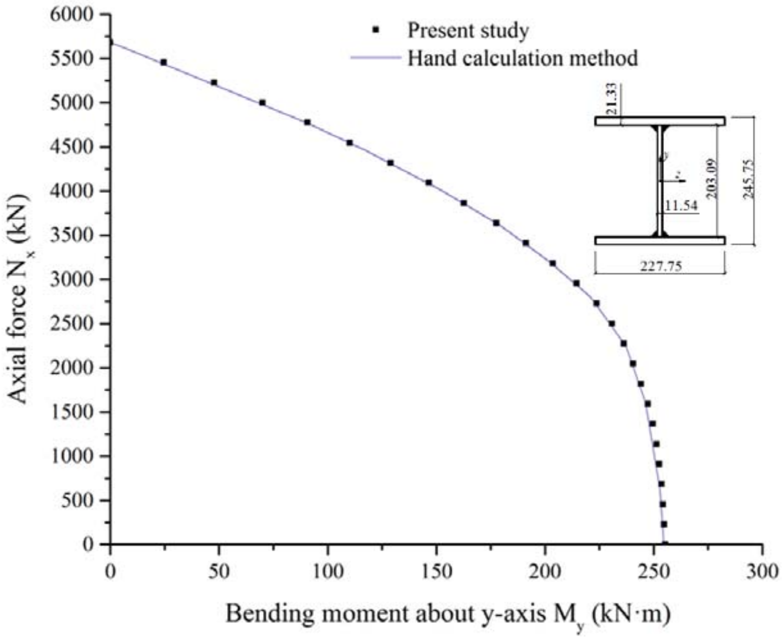

(d) Failure surface with residual stress

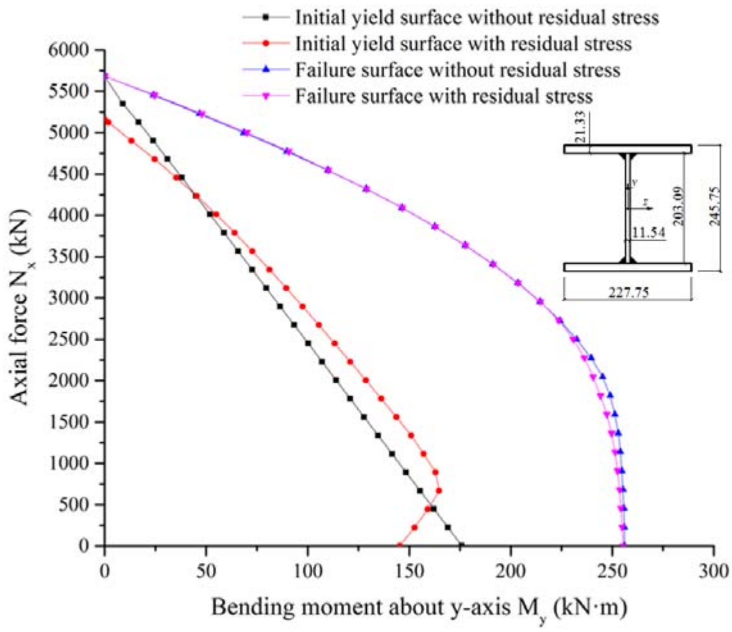

(e) Residual stress effects on initial yield and failure surfaces

Figure 5.8 Comparison results of H-section

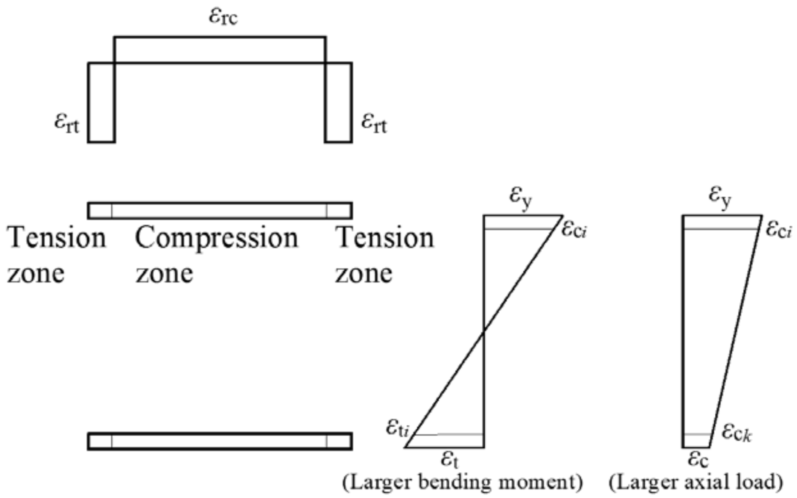

(a) Residual stress influence on flanges

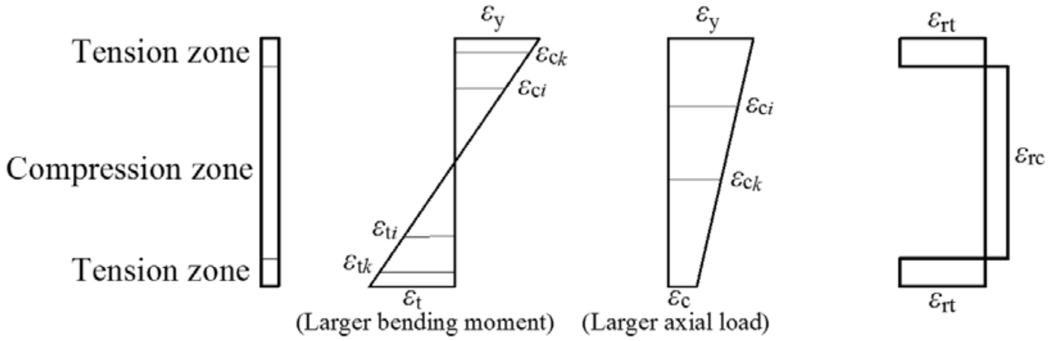

(b) Residual stress influence on a web

Figure 5.9 Residual stress influence on sections

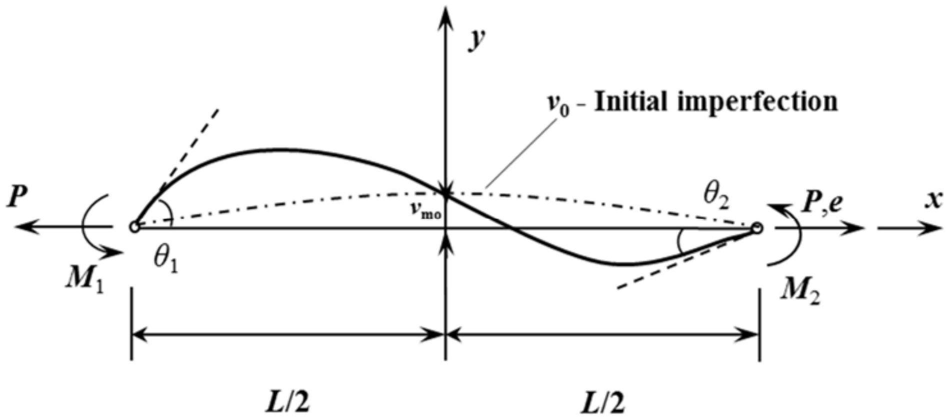

Figure 5.10 Relations between basic forces and displacements in the PEP element

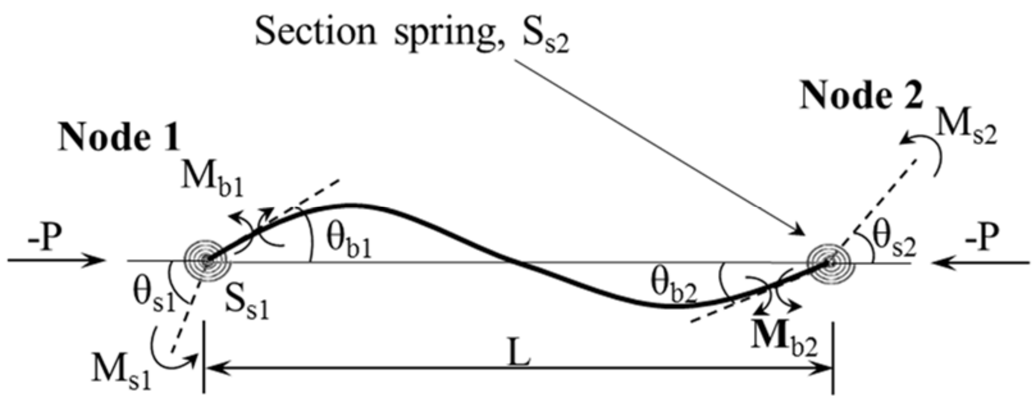

Figure 5.11 Internal forces of an element with end-section springs

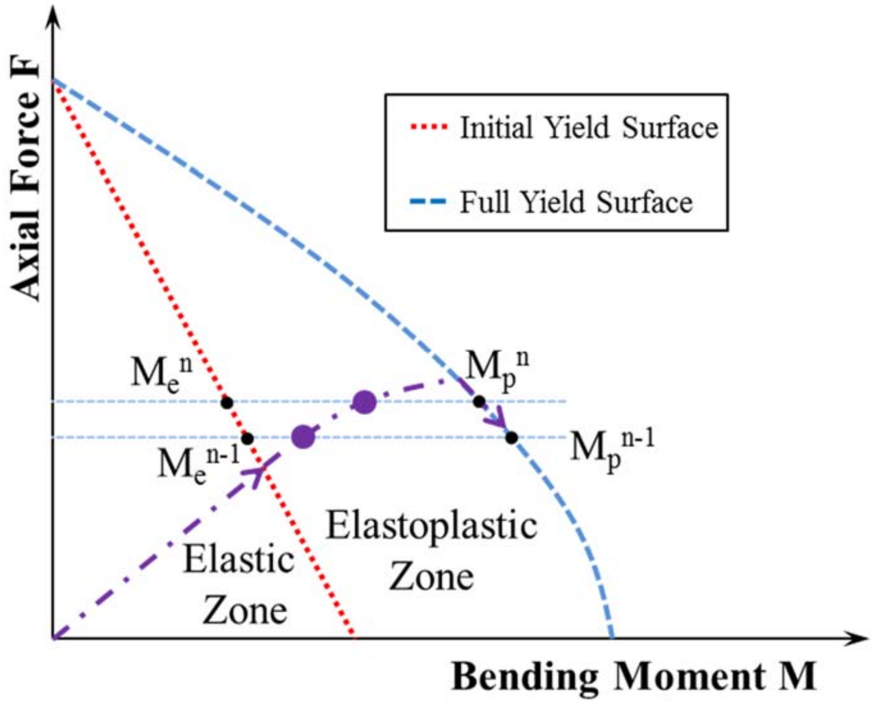

Figure 5.12 Loading path between first and fully yield surfaces under given moment

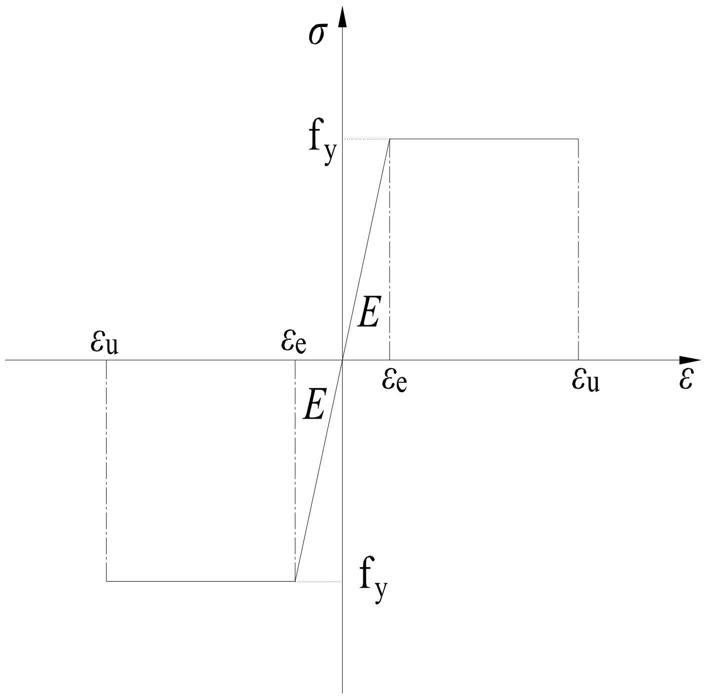

Figure 5.13 Constitutive relationship of steel

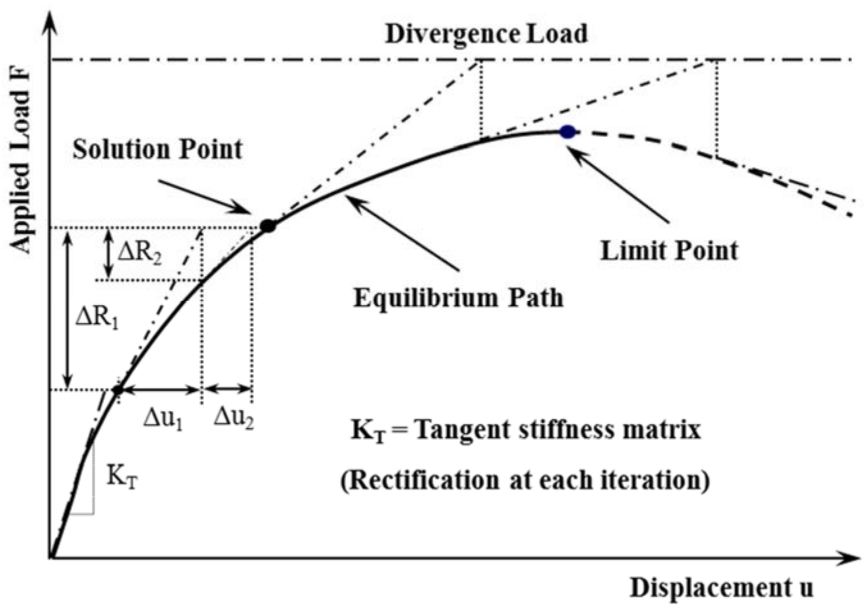

(a) Conventional Newton-Raphson method

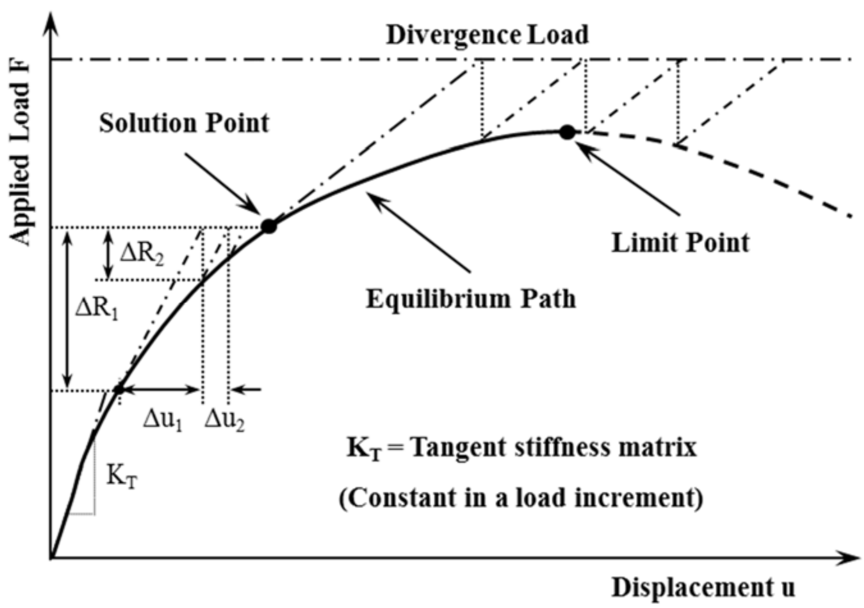

(b) Modified Newton-Raphson method

Figure 5.14 Comparison of two Newton-Raphson methods

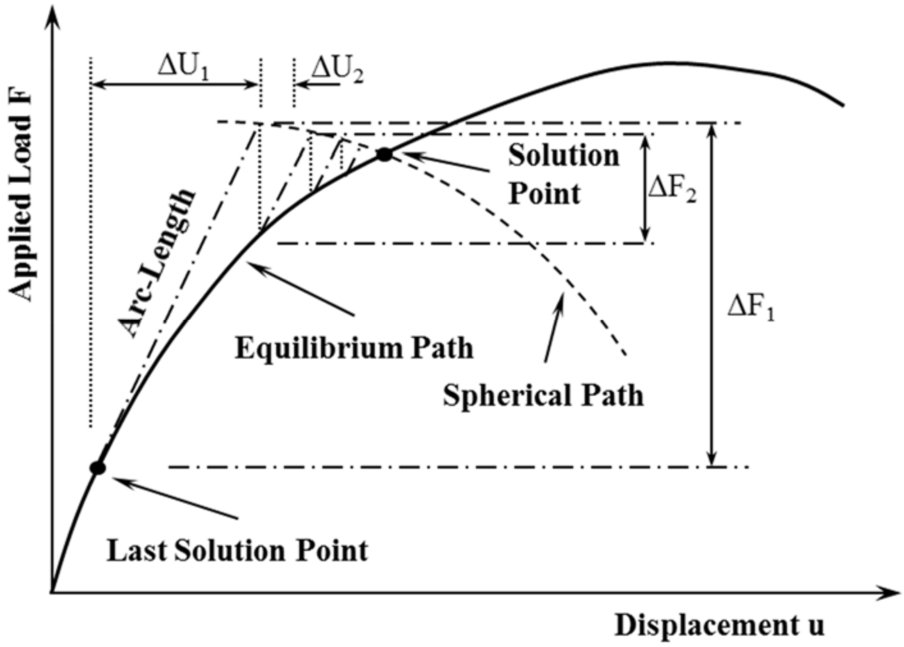

Figure 5.15 The arc-length method

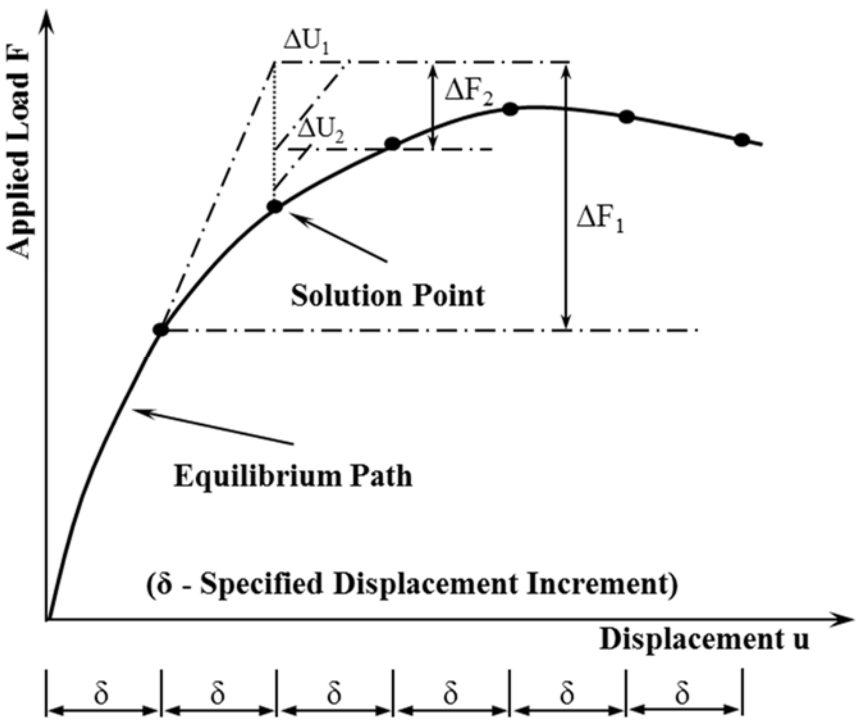

Figure 5.16 The displacement control method

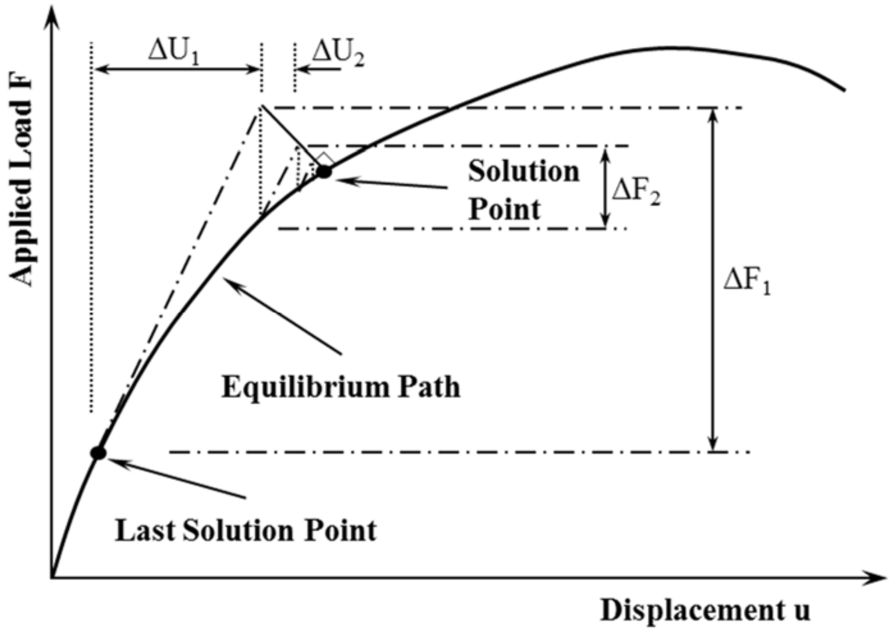

Figure 5.17 The minimum residual displacement method

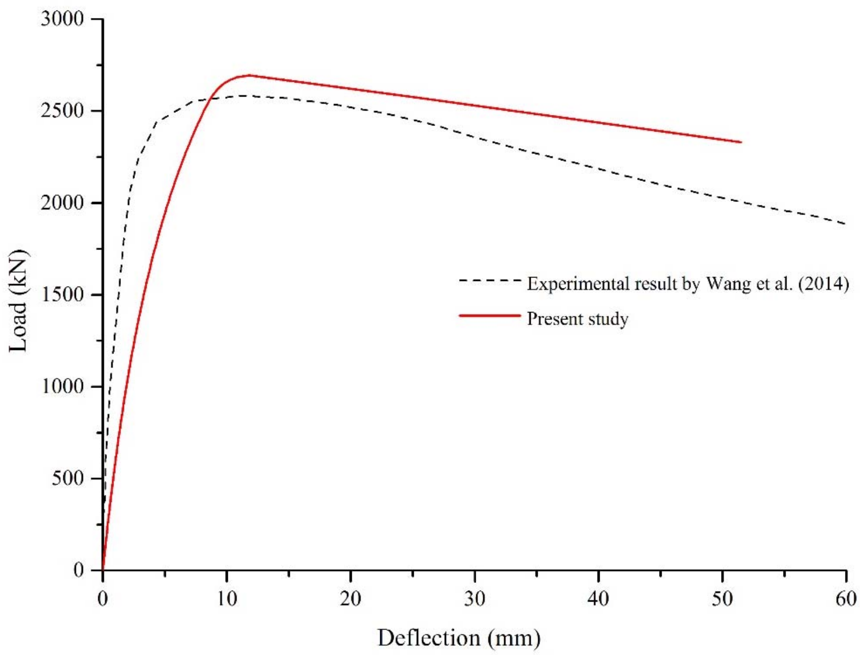

Figure 5.18 Comparison results of load-displacement curves for box-section

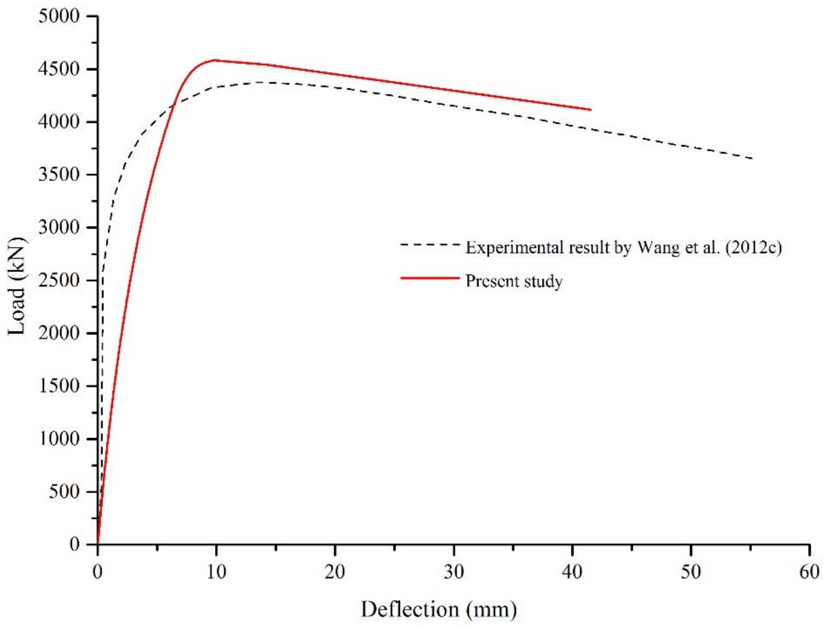

Figure 5.19 Comparison results of load-displacement curves for H-section

Tables

Table 5.1 Dimensions of box-section specimens

Specimen label	B (mm)	h (mm)	t (mm)	h/t
Specimens of model 1				
RB1-460	100.0	80.0	10.0	8.0
RB2-460	140.0	112.0	14.0	8.0
RB3-460	150.0	130.0	10.0	13.0
RB4-460	240.0	216.0	12.0	18.0
RB5-460	330.0	306.0	12.0	25.5
RB6-460	380.0	360.0	10.0	36.0
Specimens of model 2				
R-B-8	110.9	88.2	11.40	7.7
R-B-12	156.5	133.6	11.44	11.7
R-B-18	219.8	196.9	11.42	17.3

Table 5.2 Dimensions of H-section specimens

Specimen label	B (mm)	H (mm)	t_f (mm)	t_w (mm)	h_f (mm)	b_f/t_f	h/t_w
Specimens of model 1							
RI1-460	130.0	110.0	10.0	10.0	6.0	6.0	9.0
RI2-460	150.0	150.0	10.0	10.0	6.0	7.0	13.0
RI3-460	210.0	210.0	14.0	14.0	6.0	7.0	13.0
RI4-460	290.0	150.0	10.0	10.0	6.0	14.0	13.0
RI5-460	348.0	276.0	12.0	12.0	6.0	14.0	21.0
RI6-460	220.0	300.0	12.0	10.0	6.0	8.8	27.6
RI7-460	280.0	360.0	12.0	10.0	6.0	11.3	33.6
RI8-460	150.0	150.0	10.0	10.0	6.0	7.0	13.0
Specimens of model 2							
R-H-3	156.0	168.0	21.39	11.49	–	3.4	10.9
R-H-5	225.3	243.8	21.23	11.33	–	5.0	17.8
R-H-7	314.0	319.5	21.20	11.63	–	7.1	23.8

Table 5.3 Residual stress ratios of box-section specimens

Specimen label	α	β
R-B-8	0.555	-0.255
R-B-12	0.678	-0.195
R-B-18	0.787	-0.142

Table 5.4 Residual stress ratios of H-section specimens

Specimen label	α_1	α_2	β_1	β_2
R-H-3	1.039	0.080	-0.408	-0.152
R-H-5	0.900	0.243	-0.271	-0.235
R-H-7	0.731	0.488	-0195	-0.131

CHAPTER 6

PARAMETRIC STUDY AND DESIGN RECOMMENDATIONS

This chapter discusses the practicability of the proposed advanced analysis method for Q690 welded high-strength steel columns. The effects of factors, such as initial geometric imperfections, residual stresses, and sectional width-to-thickness and member slenderness ratios, are illustrated. Numerical simulation data are compared with the predictions in the Chinese (GB 50017-2003, 2003), European (Eurocode 3, 2005), and American (ANSI/AISC 360-10, 2010) codes. Recommendations that are suitable for designing Q690 welded steel columns are presented. On the basis of the proposed advanced analysis method, a second-order elastic design method for design of Q690 welded box and H columns is put forward.

6.1. Introduction

An experimental investigation on the overall buckling behavior of Q690 welded box and H columns under axial compression is presented in Chapter 4. The experiment involves six welded box columns and six flame-cut welded H columns with three types of cross-sections. The experimental results are compared with the buckling curves indicated in the Chinese (GB 50017-2003, 2003), European (Eurocode 3, 2005), and American (ANSI/AISC 360-10, 2010) codes. Recommended curves that are suitable for Q690 steel columns are presented. Despite the suitability of these curves, however, they require further validation by numerical simulation that considers different sectional width-to-thickness and member slenderness ratios because the experimental data are insufficient.

The advanced analysis method presented in Chapter 5 is used to simulate the mechanical behavior of welded box and H columns made of high-strength steel. This analysis can resolve the deficiency due to the insufficiency of experimental data. It also enables the explicit modeling of residual stresses and initial geometric imperfections, and effectively reflects the mechanical characteristics of Q460 welded high-strength steel columns.

The advanced analysis method requires experimental support to verify its feasibility for Q690 welded high-strength steel columns. The numerical analysis uses the residual stress models proposed in Chapter 3; these models are suitable for Q690 welded box and H columns. Some parameters (i.e., initial geometric imperfections, residual stresses, and sectional width-to-thickness and member slenderness ratios) are then analyzed to determine the factor effects on the ultimate bearing capacities of such columns. The numerical results obtained with the Chinese, European, and American codes are compared, and some suggestions for designing these types of columns are discussed. Finally, a refined second-order elastic analysis method, namely, the DAM, is also proposed for the design of Q690 welded box and H columns. The DAM is based on the proposed advanced analysis technique.

6.2. Numerical models

The advanced analysis method presented in Chapter 5 is also used to analyze and design the Q690 welded box and H columns. A section analysis technique that considers residual stress effects is presented on the basis of a quasi-Newton iterative scheme. To calculate arbitrary sectional capacity, the scheme is employed to determine the neutral axis position of a section. Because residual stress distributions differ among varied steel grades, external dimensions, and sectional shapes, the residual stress patterns proposed in Chapter 3 are adopted in the numerical simulation for the Q690 welded steel columns. Such patterns are derived from residual stress measurements. The related details are discussed in Chapter 3.

To take into account the second-order effects associated with initial geometric imperfections, the PEP element is adopted. A refined plastic hinge approach using sectional strength-iteration surfaces is proposed for modeling material nonlinearity. The relevant details and equations are found in Section 5.4. In the numerical analyses of the Q690 welded high-strength steel columns, the elastic-ideally plastic constitutive model is applied (Figure 6.1). The model is extracted from the experimental data on the material properties discussed in Chapter 4. To validate the practicability of the proposed method for the columns, the measured initial geometric imperfections (i.e., initial eccentricities and deflections) are applied in the analysis. The imperfections are listed in Table 4.4 of Chapter 4.

6.3. Verification of models

As discussed in Chapter 5, the proposed advanced analysis method is practicable and effective for Q460 welded high-strength steel columns. The method’s feasibility for box and H columns fabricated with Q690 high-strength steel is confirmed by comparing the numerical and experimental results in this section.

6.3.1. Comparison of ultimate bearing capacities

As a significant parameter, ultimate bearing capacity can reflect the mechanical characteristics of Q690 welded box and H columns under axial compression. Comparisons between the numerical results calculated from the advanced analysis method that considers the effects of initial geometric imperfections and residual stresses and the test results are listed in Table 6.1 for the box columns and Table 6.2 for the H columns.

For the Q690 welded box and H columns, the average numerical prediction-to-test result ratios are 1.06 and 1.06, with standard deviations of 0.05 and 0.05, respectively (Table 6.1 and Table 6.2). These findings indicate that the numerical method provides effective and accurate predictions for Q690 welded box and H columns subjected to axial compression loading.

6.3.2. Comparison of load-deflection curves

Load-deflection curves indicate not only the ultimate bearing capacities of members, but also variations in member stiffnesses and post-buckling mechanical behaviors. The curves can clearly reveal the overall buckling behavior of box and H columns fabricated with Q690 high-strength steel. The load-deflection curves represented by the experimental data and the numerical results determined using the advanced analysis method are shown in Figure 6.2 and Figure 6.3. Figure 6.2(a)-(c) presents the load-deflection curves of the Q690 welded box columns with 30, 50, and 70 slenderness ratios. In Figure 6.3(a)-(c), the load-deflection curves of the H columns also correspond to 30, 50, and 70 slenderness ratios.

For the numerical simulation and experiments, Figure 6.2 and Figure 6.3 show that the failure modes of the Q690 welded box and H columns under axial compression reflect overall buckling. The shape and path of the load-deflection curves from the numerical analyses and experiments are similar. For certain columns, however, the stiffness variations of the curves in the numerical simulation do not perfectly agree with those in the experiment because loading eccentricities from the loading end of a universal testing machine cannot be avoided. On the basis of the comparison, the proposed advanced analysis method can be regarded as an effective approach to designing and analyzing Q690 welded columns.

6.4. Parametric analysis

Parametric analysis is necessary to determine the effects of certain factors on the ultimate bearing capacities of columns fabricated with Q690 high-strength steel. The factors considered in this work are initial geometric imperfections, residual stresses, and sectional width-to-thickness and member slenderness ratios. Sectional width-to-thickness ratios indirectly influence the ultimate bearing capacities of columns because they alter the residual stress distributions on sections; the residual stresses can directly affect the ultimate capacities of such columns.

6.4.1. Basic parameters

Thirty-six welded box columns and 36 welded H columns made of Q690 high-strength steel are analyzed to determine the ultimate bearing capacity. These columns are subjected to axial compression loading. The box columns include 3 sectional width-to-thickness ratios (7-13) and 12 slenderness ratios (20-130). The external dimensions of such columns are listed in Table 6.3, and the cross-sections of the columns are shown in Figure 6.4. As indicated in Table 6.3, B-x denotes that the section of the column is a box section, and the width-to-thickness ratio is x; the section is symmetric about the u- and v-axes. The H columns also involve three width-to-thickness ratios ranging from 6 to 8 and 12 slenderness ratios ranging from 20 to 130. Table 6.4 lists the sectional dimensions of the columns, and Figure 6.5 displays the bisymmetric sections of the columns. H-xx (Table 6.4) represents the H column with an xx width-to-thickness ratio of flanges.

In the parametric analyses, the initial geometric imperfections of the box and H columns are selected as 1‰ of the corresponding column length. For the box columns, the residual stress model indicated in Figure 3.11 is adopted. For the H columns, the residual stress model depicted in Figure 3.12 is employed.

6.4.2. Analysis results

6.4.2.1. Box columns

The box-section columns are divided into three groups, i.e., B-7, B-10, and B-13, which correspond to realistic width-to-thickness ratios of 6.8, 10.0, and 12.7, respectively. Each group incorporates 12 specimens whose slenderness ratios vary from 20 to 130. For the bisymmetric box-section columns (Figure 6.4), the residual stress distributions on the flanges and webs are not completely identical. Therefore, the columns that bend about the u- and v-axes require analysis. The analytical results for u- and v-axes are listed in Table 6.5 and Table 6.6, respectively. The two tables show that $\bar{\lambda}$ is the non-dimensional slenderness ratio ($\bar{\lambda} = \lambda \cdot \sqrt{f_y / E} / \pi$), χ_u and χ_v denote the reduction factors for overall buckling about the u- and v-axes, respectively.

As shown in Table 6.5 and Table 6.6, the reduction factors about the u-axis are close to those about the v-axis. The maximum error between them is 1% indicating that residual stress distribution slightly affects the buckling reduction factors about the u- and v-axes for welded Q690 box columns.

6.4.2.2. H columns

The H-section columns also comprise three groups, namely, H-6, H-7, and H-8. The realistic width-to-thickness ratios of the columns of these three groups are 5.9, 6.9, and 7.5. The slenderness ratios of each group vary from 20 to 130, and each group comprises 12 columns. The columns that bend about the minor (v-axis) and major (u-axis) axes are calculated by the proposed advanced analysis method. Table 6.7 and Table 6.8 list the calculation results for the minor and major axes, in which $\overline{\lambda}_{\mathrm{v}}$ and $\overline{\lambda}_{\mathrm{u}}$ represent the non-dimensional slenderness ratios about the minor and major axes ($\overline{\lambda}_{\mathrm{v}} = \lambda_{\mathrm{v}} \cdot \sqrt{f_{\mathrm{y}}/E} \big/ \pi$, $\overline{\lambda}_{\mathrm{u}} = \lambda_{\mathrm{u}} \cdot \sqrt{f_{\mathrm{y}}/E} \big/ \pi$), and χ_{v} and χ_{u} are the reduction factors for overall buckling about the minor and major axes, respectively.

6.4.3. Response of varied steel grades to initial deflections

6.4.3.1. Box columns

Thirty-six numerical models for the box-section specimens are established and analyzed, in which only initial geometric imperfections are considered. The initial deflection is set as 1‰ of the corresponding specimen length. The numerical results shown in Figure 6.6 indicate that the three buckling curves for B-7, B-10, and B-13 are coincident. Consequently, the box columns with different width-to-thickness ratios possess the same reduction factor for overall buckling when only initial deflections are taken into account. Width-to-thickness ratios indirectly influence the overall buckling of specimens via varied residual stress distributions.

To determine the sensitivity of box columns with various yield strengths to initial deflections, Q235 and Q460 column models are created, in which only initial geometric imperfections are considered. The Young's modulus of the Q235 and Q460 steel columns is 206 GPa. The yield strengths of the Q235 and Q460 steels are 235 and 460 MPa, respectively. The numerical results are depicted in Figure 6.6.

As shown in Figure 6.6, the buckling curves of the Q690 columns are higher than those of the Q460 and Q235 columns. Similarly, the buckling curve of the Q460 columns is higher than that of the Q235 columns. When the non-dimensional slenderness ratios range from 0.5 to 1.5, a large difference occurs among the buckling reduction factors of the Q690, Q460, and Q235 box steel columns. The largest difference in reduction factors between the Q460 and Q235 columns is 4.4%, and that between the Q690 and Q235 columns is 6.9%. These findings indicate that the effect of initial geometric imperfections on the ultimate bearing capacities of box columns tends to decrease with increasing yield strength. Thus, the buckling reduction factors of the columns with high yield strength improve.

6.4.3.2. H columns

Seventy-two H column models are built, for which only initial geometric imperfections are considered. The models are designed to determine the effects of such imperfections on the ultimate strength of different sections. The initial deflection applied in the models is 1‰ of the corresponding column length. The overall buckling of such columns about the minor and major axes is simulated. The numerical results for the minor and major axes are shown in Figure 6.7(a) and (b), respectively. The three buckling curves (Figure 6.7(a) and (b)) that correspond to H-6, H-7, and H-8 are coincident. Thus, the fact that H columns with different width-to-thickness ratios have the same reduction factors for overall buckling can be determined via analyses that consider only initial deflections.

To examine the sensitivity of H columns with diverse steel grades to initial deflections, Q235 and Q460 column models are established. The models consider only initial geometric imperfections (L_e/1000). The Young's modulus of the Q235 and Q460 steel columns is 206 GPa. The yield strengths of the Q235 and Q460 steels are 235 and 460 MPa, respectively. The ultimate bearing capacities of such columns are calculated with respect to the minor and major axes, and the analysis results are shown in Figure 6.7(a) and (b).

As indicated in Figure 6.7(a) and (b), the buckling curves of the Q690 H columns are higher than the Q460 column curve, which is higher than the curve of the Q235 H columns. A large difference occurs among the buckling reduction factors of the Q690, Q460, and Q235 columns for nondimensional slenderness ratios ranging from 0.5 to 1.5. The maximum ratio between the reduction factors of the Q460 and Q235 columns for overall buckling about the minor axis is 1.041 and that between the Q690 and Q235 column curves is 1.072. For the reduction factor about the major axis, the largest ratio between the Q460 and Q235 column curves reaches 1.047 and that between the Q690 and Q235 column curves reaches 1.073. These findings suggest that the effect of initial geometric imperfections on the ultimate bearing capacities of H columns tend to decrease with increasing yield strength. The reduction factors for overall buckling therefore improve.

6.4.4. Influence of residual stresses

To investigate the effects of residual stresses on the ultimate bearing capacities of Q690 welded box and H columns, 216 models are created and analyzed. The models feature box columns (section types: B-7, B-10, and B-13) and H columns (section types: H-6, H-7, and H-8) that bend about the minor and major axes. Each type of columns consists of 12 slenderness ratios. The models are divided into two groups: one that considers initial deflections (L_e/1000) and another that takes into account combined initial deflections and residual stresses.

The analysis results for the box columns are shown in Figure 6.8. The effects of residual stresses on the box columns are directed primarily toward columns with nondimensional slenderness ratios that range from 0.5 to 1.2. The buckling reduction factor that considers the effects of residual stresses is higher than that which disregards such effects by a maximum of 3.9%. Figure 6.9(a) and (b) displays the analysis results for the H columns that bend about the minor and major axes. For the minor axis, the reduction factor of the H columns decreases by a maximum of 2.0% because of the residual stress effects. For the major axis, the reduction factor decreases by a maximum of 2.8%.

6.5. Design recommendations

As indicated in GB 50017-2003 (2003) and Eurocode 3 (2005), first-order linear theory is used to design axially loaded steel members. This theory considers the buckling effect via effective length factors. The efficiency of the method depends on the appropriateness of an effective length factor. Nevertheless, the factors related to members in real-world structures are not explicitly determined because ideal end conditions (pin and fixed ends) are impractical. ANSI/AISC 360-10 (2010) recommends the direct analysis method (DAM) in designing members and treats the effective length method as an alternative. This approach takes into account geometric nonlinear effects and does not require the determination of factors, thereby reflecting realistic buckling behaviors during analysis.

6.5.1. GB 50017-2003 (2003) Code for steel members subjected to axial compression

As specified in GB 50017-2003 (2003), welded box columns with a width-to-thickness ratio lower than 20 correspond to buckling curve "c." To validate the practicability of the provision for Q690 welded box columns, the numerical results (B-

7, B-10, and B-13 series) are compared with relevant buckling curves “a,” “b,” and “c” (see Figure 6.10). The analysis data are listed in Table 6.9.

In Figure 6.10 and Table 6.9, the buckling reduction factors derived by the numerical analysis are higher than the buckling curves “c,” “b,” and “a” determined by GB 50017-2003 (2003). On average, the numerical analysis yields percentages of 28%, 15%, and 5%. Therefore, in designing welded Q690 box columns with reference to GB 50017-2003 (2003), buckling curve “a” is appropriate.

The sections that categorize flame-cut welded H columns with plates of less than 40 mm fall under Class “b” section in GB 50017-2003 (2003). Buckling curve “b” is suggested for this class. To confirm the feasibility of the term for Q690 welded H columns, the numerical results (H-6, H-7, and H-8 series) for the minor and major axes are shown in Figure 6.11(a) and (b). The numerical analysis results are compared with the curves “a,” “b,” and “c” indicated in the code. Table 6.10 and Table 6.11 provide the numerical analysis data.

As shown in Figure 6.11(a) and Table 6.10, the numerical results for the H columns about the minor axis are higher than the buckling curves “b” and “a” indicated in GB 50017-2003 (2003). On average, the numerically derived percentages are 14% and 4%, respectively. The results for the columns about the major axis are higher than curves “b” and “a”, yielding percentages of 16% and 6%, respectively (Figure 6.11(b) and Table 6.11). Thus, in designing welded Q690 H columns with reference to GB 50017-2003 (2003), buckling curve “a” is suitable.

6.5.2. Eurocode 3 (2005) design of steel members subjected to axial compression

For welded box columns with a width-to-thickness ratio less than 30, buckling curve “c” is appropriate, as indicated in Eurocode 3 (2005). The item for Q690 welded box columns should be verified. The B-7, B-10, and B-13 series are simulated, after which the results are compared with buckling curves “a_0”, “a”, “b”, and “c” (see Figure 6.12). Table 6.12 lists the numerical results.

In Figure 6.12 and Table 6.12, the numerical results for the Q690 welded box columns are higher than buckling curves “c”, “b”, “a”, and “a_0” by an average of 25%, 16%, 8% and 2%, respectively. A potential risk of overestimating the ultimate capacities of box columns arises when curve “a_0” is used for slenderness ratios ranging from 20 to 40. Therefore, curve “a” can be regarded as a reasonable curve for designing welded Q690 box columns.

Eurocode 3 (2005) specifies that buckling curves “c” and “b” are respectively suitable for flame-cut welded H columns (plate thickness < 40 mm) that bent about the minor and major axes. To confirm that the Q690 welded H columns satisfy this provision, the numerical results for the H-6, H-7, and H-8 series versus curves “a_0,” “a,” “b,” and “c” are plotted in Figure 6.13. Figure 6.13(a) and (b) shows the comparison of the results for the minor and major axes, respectively, with the curves indicated in the code. The analysis data are presented in Table 6.13 and Table 6.14.

As shown in Figure 6.13(a) and Table 6.13, the buckling reduction factors of the H columns about the minor axis are higher than buckling curves “c”, “b”, “a”, and “a_0” by an average of 24%, 15%, 7% and 1%, respectively. The reduction factors about the major axis are higher than buckling curves “b”, “a”, and “a_0” by an average of 16%, 8% and 3%, respectively (Figure 6.13(b) and Table 6.14). With consideration of the circumstance that using the curve “a_0” gives rise to the possibility of overestimating the ultimate bearing capacities of Q690 flame-cut welded H columns in slenderness ratios ranging from 20 to 30. Curve “a” is therefore a reasonable choice for designing such columns.

6.5.3. AISC 360-10 (2010) specification for steel members subjected to axial compression

Unlike GB 50017-2003 (2003) and Eurocode 3 (2005), ANSI/AISC 360-10 (2010) adopts only a single curve in the effective length method. To verify the practicability of ANSI/AISC 360-10 (2010) for Q690 welded box columns, the numerical results (B-7, B-10, and B-13 series) are compared with the relevant buckling curve, as shown in Figure 6.14 and Table 6.15. The numerical findings are higher than the buckling curve specified in ANSI/AISC 360-10 (2010) by 8% in average. The curve indicated in ANSI/AISC 360-10 (2010) can be used to design Q690 welded box columns.

The buckling curve indicated in ANSI/AISC 360-10 (2010) is compared with the numerical results (H-6, H-7, and H-8 series) for the minor and major axes (see Figure

6.15, Table 6.16 and Table 6.17) to confirm the feasibility of the code for Q690 welded H columns. As shown in Figure 6.15, Table 6.16 and Table 6.17, the buckling reduction factors for the H columns about the minor and major axes are higher than the curve specified in ANSI/AISC 360-10 (2010), with average percentages of 7% and 9% on average, respectively. Accordingly, using this curve to design Q690 flame-cut welded H columns is relatively safe.

6.5.4. Direct analysis method for axial compression members fabricated with high-strength steel

The DAM indicated in ANSI/AISC 360-10 (2010) considers the effects of residual stresses and partial yielding via stiffness modification. The stiffness reduction factor selected is $0.8\tau_b$, which is suitable provided that no explicit residual stress model is applied in analysis. Equations (6.1) and (6.2) provide the formula for τ_b.

$$\tau_b = 1.0, \qquad \text{when } N_r/N_y \le 0.5 \tag{6.1}$$

$$\tau_b = 4\left(N_r/N_y\right)\left(1 - N_r/N_y\right), \qquad \text{when } N_r/N_y > 0.5 \tag{6.2}$$

where N_r and N_y denote the required axial compressive strength and axial yield strength, respectively.

In this section, the proposed DAM considers initial geometric imperfections and second-order effects with the PEP element. To consider the effects of residual stresses and partial yielding, the stiffness reduction method specified in ANSI/AISC 360-10

(2010) can be adopted in analysis. The elastic-perfectly-plastic yield criterion should satisfy the cross-sectional strength limit (i.e., failure surface) indicated in Section 5.3.

The determination of the stiffness reduction factor specified in the American code is based on the condition that maximum compressive residual stress is equal to 30% of yield strength. However, the ratio is overestimated for Q690 welded high-strength steel columns. For the Q690 welded box and H columns in Chapter 3, the maximum ratios are 0.137 and 0.136. Consequently, the stiffness reduction factor requires validation.

To verify the efficiency of the factor, the box columns (B-7, B-10, and B-13 series) and H columns (H-6, H-7, and H-8 series) are calculated by using the $0.8\tau_b$ factor recommended in ANSI/AISC 360-10 (2010); the initial deflections of these columns are 1‰ of the corresponding column lengths. Then, the analysis results obtained by the proposed DAM are compared with the numerical results from the proposed advanced analysis method that explicitly allows for residual stress effects, as listed in Table 6.18-Table 6.20.

As shown in Table 6.18, the ultimate box column capacities derived with the proposed DAM are lower than those determined using the advanced analysis method by a percentage of 14% on average. Table 6.19 and Table 6.20 shows that for the H columns bent about the minor and major axes, the ultimate capacities determined by the DAM are lower than those derived with the advanced analysis method by 13.3%

and 14.7% on average, respectively. Thus, the stiffness reduction factor requires modification.

According to Section 6.4.3, Q690 welded box and H columns possess higher buckling reduction factors than do Q235 and Q460 steel columns under the same initial geometric imperfections. Combined with the results in Table 6.18-Table 6.20, the stiffness reduction factor for slender columns should appropriately increase. For intermediate and stocky columns, the stiffness reduction factor should slightly increase because the maximum compressive residual stress ratio of Q690 welded columns is lower than that adopted in ANSI/AISC 360-10 (2010). The stiffness reduction factor is modified into $0.85\tau_b$. The details of τ_b are shown in Equations (6.3) and (6.4).

$$\tau_b = 1.05, \qquad \text{when } N_r/N_y \le 0.5 \tag{6.3}$$

$$\tau_b = 4.2\left(N_r/N_y\right)\left(1 - N_r/N_y\right), \qquad \text{when } N_r/N_y > 0.5 \tag{6.4}$$

Table 6.21-Table 6.23 list the numerical results determined by the proposed DAM with the modified factor and the advanced analysis method. For the box columns and H columns bent about the minor and major axes, the ultimate capacities obtained by the proposed DAM with the modified factor are lower than those determined by the advanced analysis method by 7.7%, 6.3% and 8.3% on average. Consequently, the proposed DAM is suitable for the design of Q690 welded box and H columns.

6.6. Concluding remarks

The efficiency and accuracy of the advanced analysis method presented in Chapter 5 for Q690 welded box and H columns are verified by comparing the results with the test findings in this chapter. The method is employed to conduct parametric analysis that involves the calculation of the ultimate capacities of columns with different section and slenderness ratios, to study the sensitivity of varied steel grades to initial geometric imperfections, and to determine residual stress effects. Some recommendations for the design of Q690 welded box and H columns are presented in the chapter. In the Chinese code (GB 50017-2003, 2003), buckling curve “a” is recommended as suitable for the design of welded box and H columns fabricated with Q690 steel. The European code (Eurocode 3, 2005) recommends buckling curve “a,” with consideration for the safety of intermediate and stocky columns. The buckling curve specified in the American code (ANSI/AISC 360-10, 2010) can be employed to design Q690 welded box and H columns. Finally, a DAM based on the American specification (ANSI/AISC 360-10, 2010) is proposed and validated against the proposed advanced analysis method. The proposed DAM (i.e., second-order elastic analysis method) is suitable for the design of Q690 welded box and H columns.

Figures

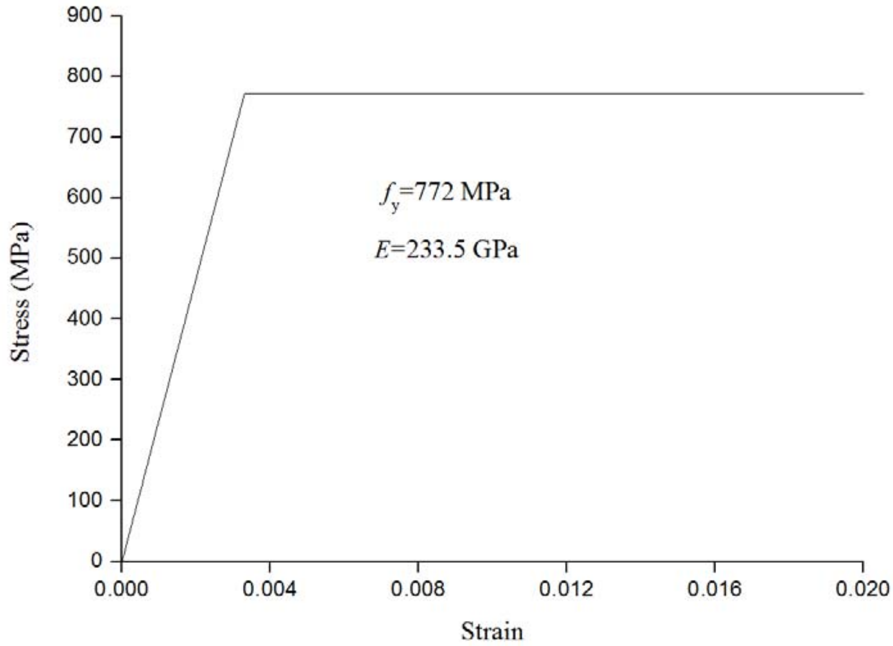

Figure 6.1 Elastic-ideally–plastic constitutive model for Q690 steel

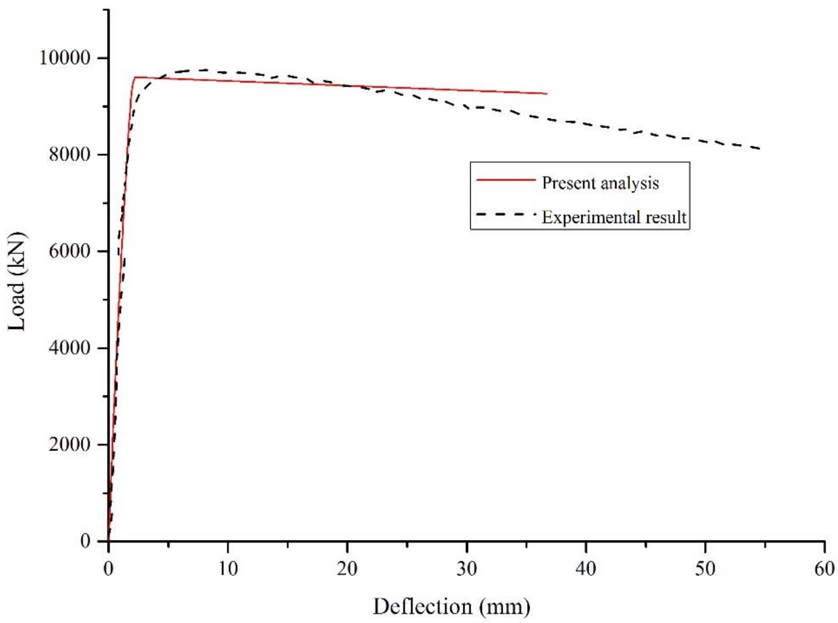

(a) B-30-2

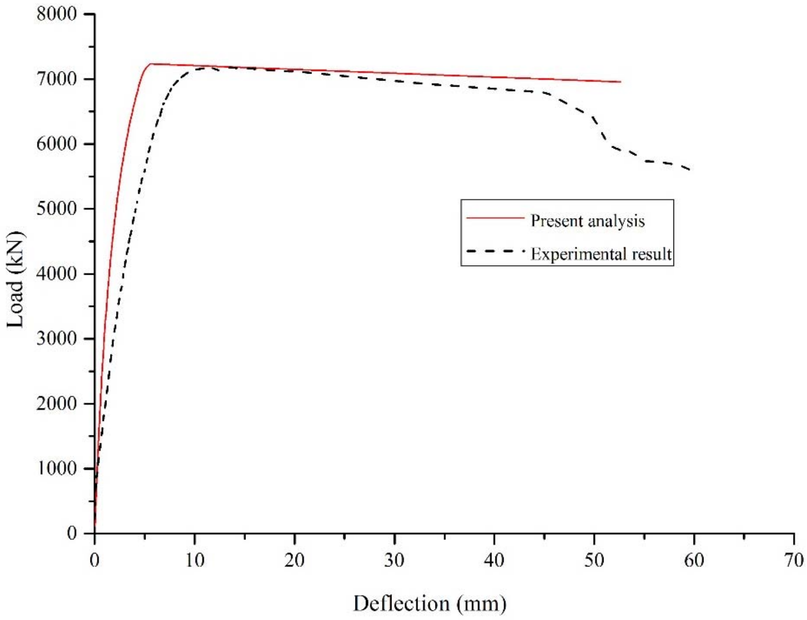

(b) B-50-2

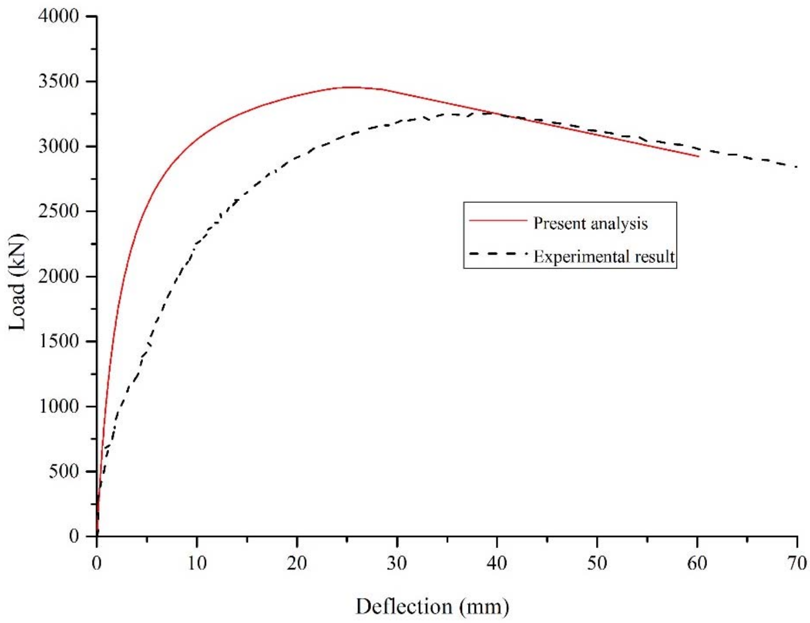

(c) B-70-1

Figure 6.2 Comparison with the test results of the box columns

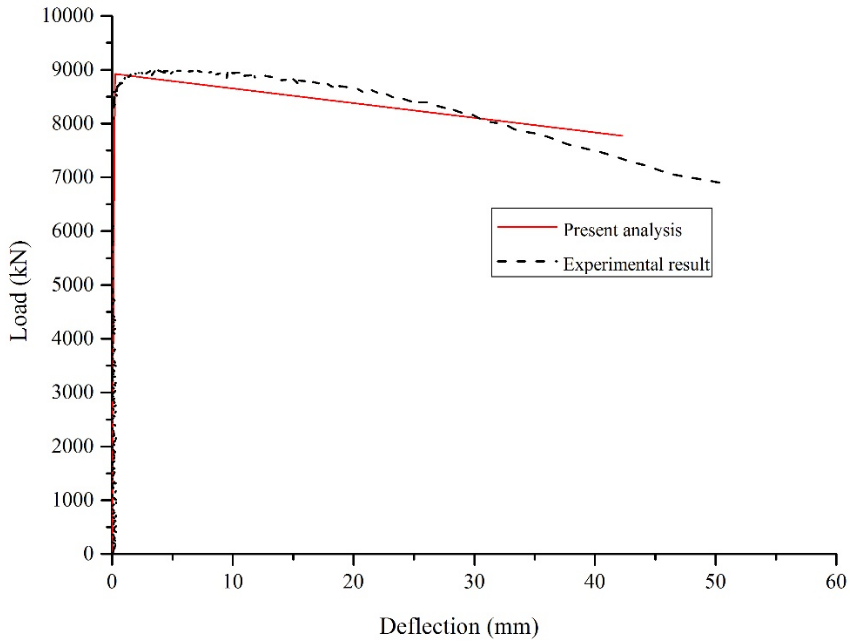

Load (kN)
10000
9000
8000
7000
6000
5000
4000
3000
2000
1000
0
0
10
20
30
40
50
60
Deflection (mm)
Present analysis
Experimental result

(a) H-30-2

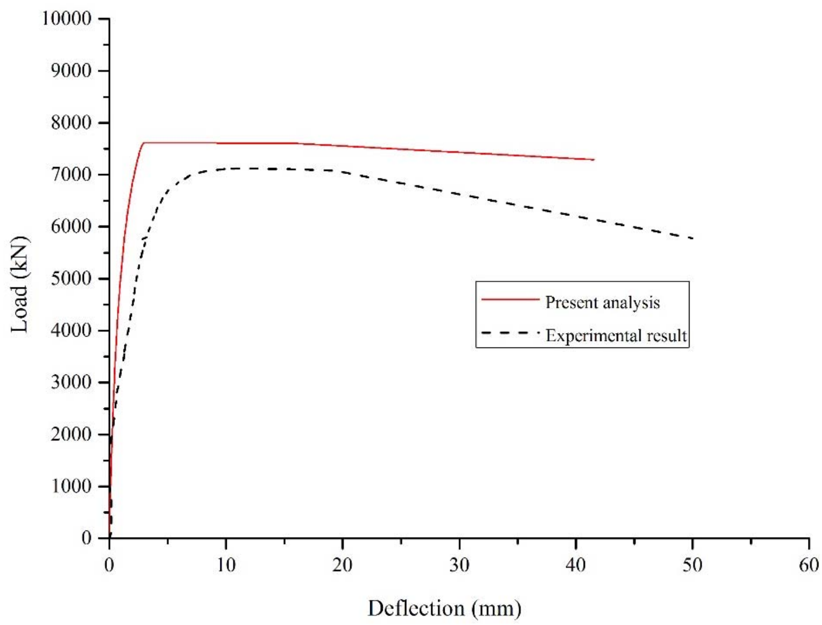

Load (kN)
10000
9000
8000
7000
6000
5000
4000
3000
2000
1000
0
0
10
20
30
40
50
60
Deflection (mm)
Present analysis
Experimental result

(b) H-50-2

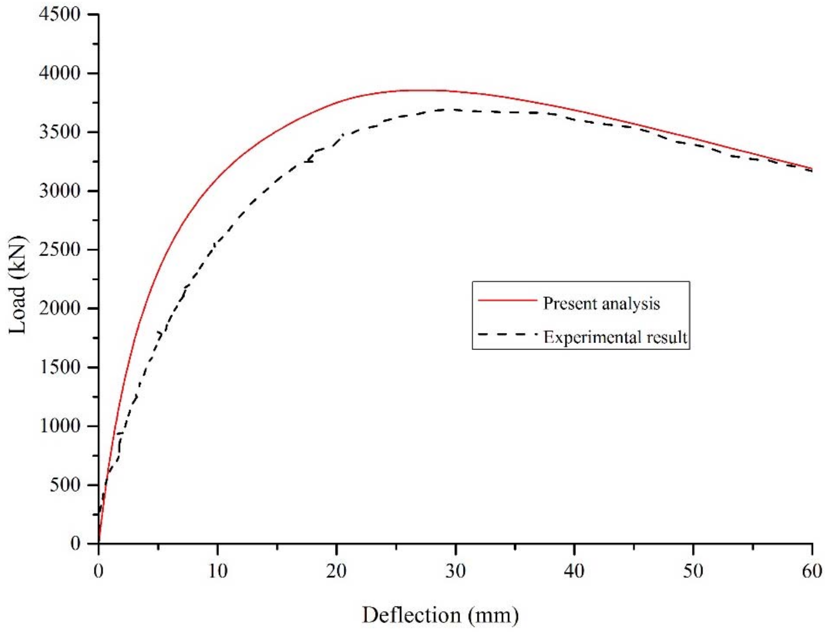

(c) H-70-2

Figure 6.3 Comparison with the test results of the H columns

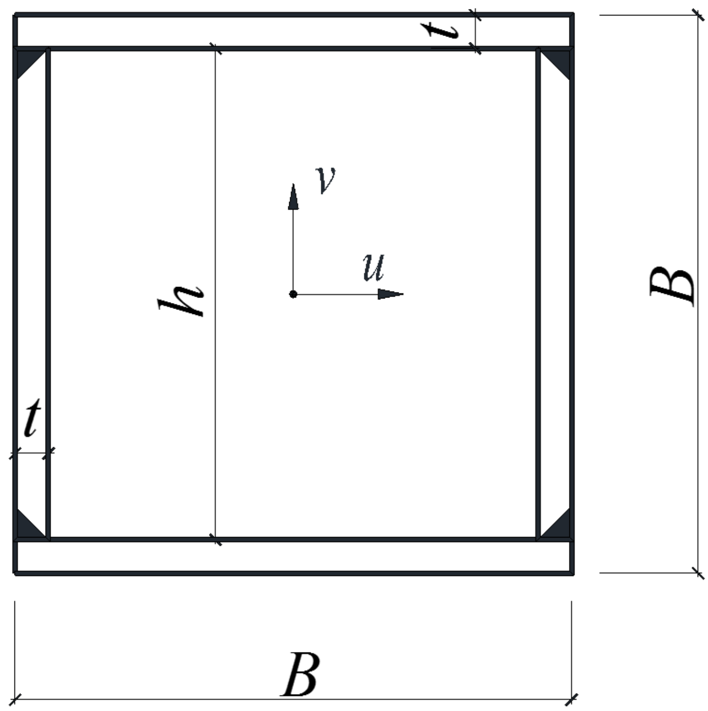

Figure 6.4 Box section in numerical models

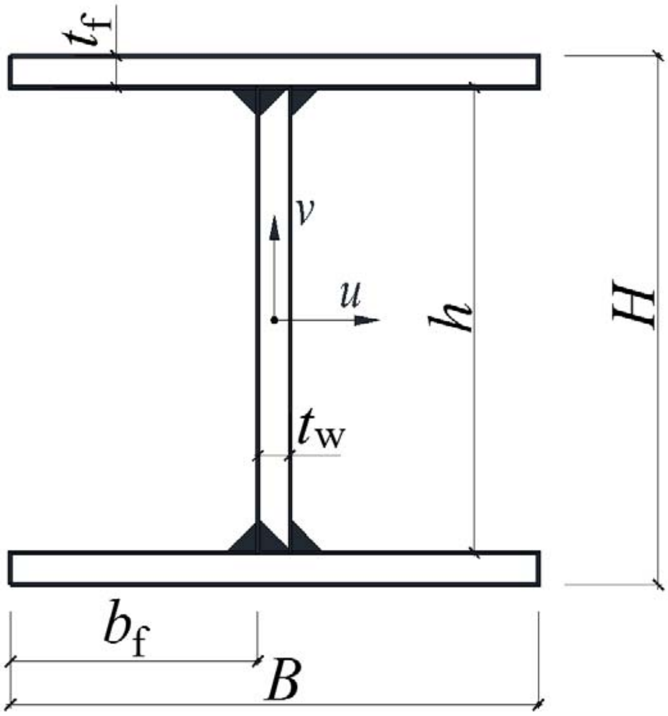

Figure 6.5 H section in numerical models

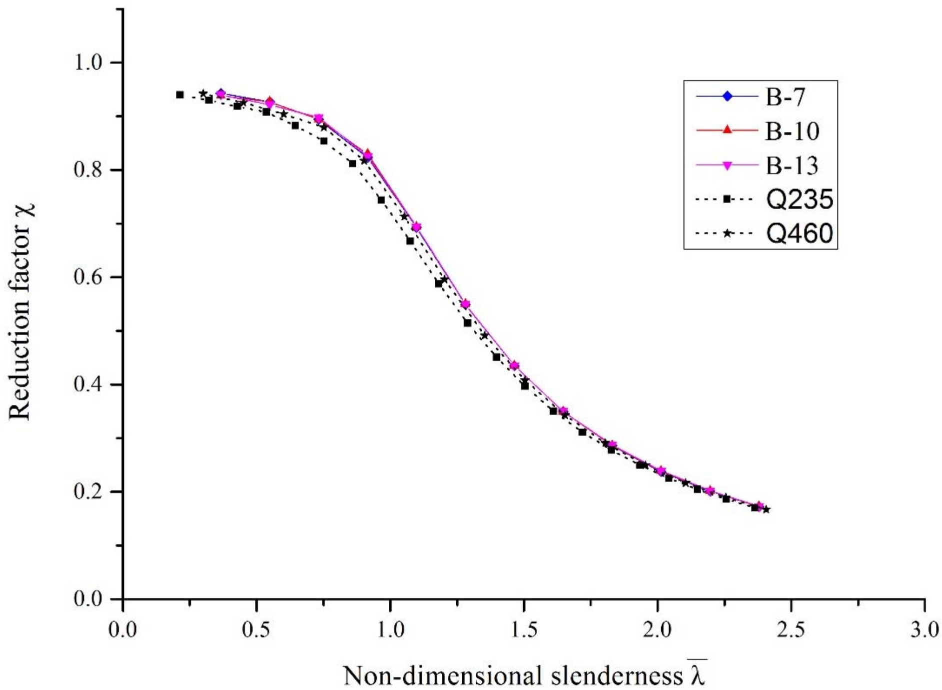

Figure 6.6 The influence of initial geometric imperfection on box columns

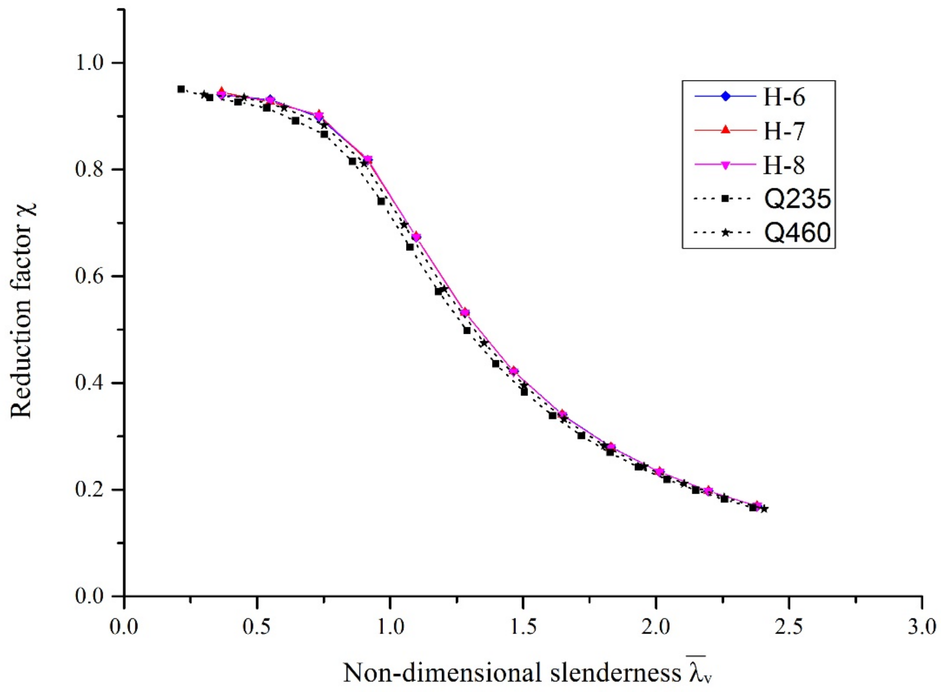

(a) Results about the minor axis

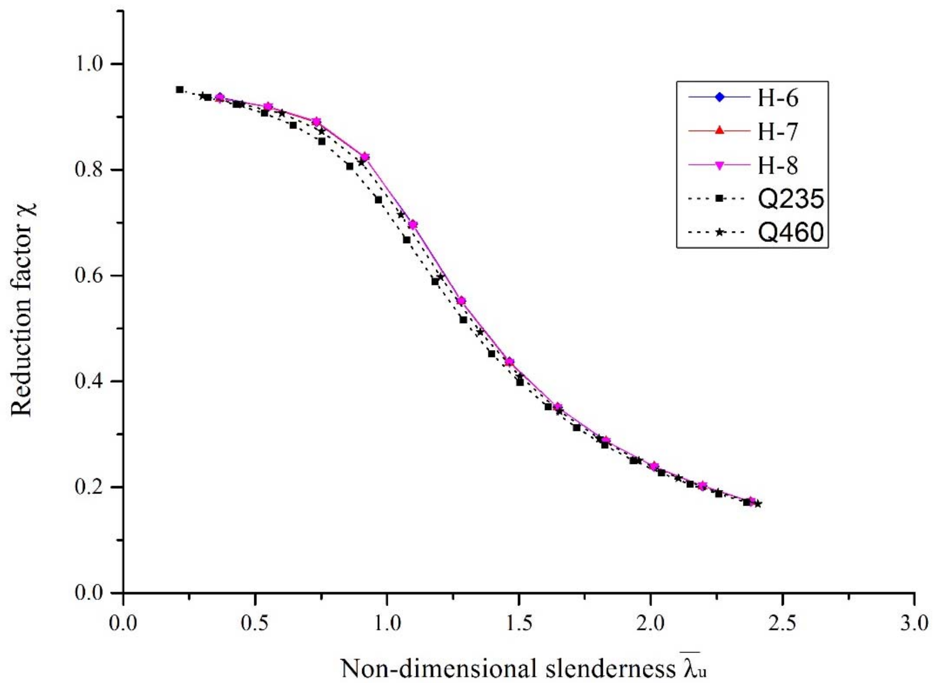

(b) Results about the major axis

Figure 6.7 The influence of initial geometric imperfection on H columns

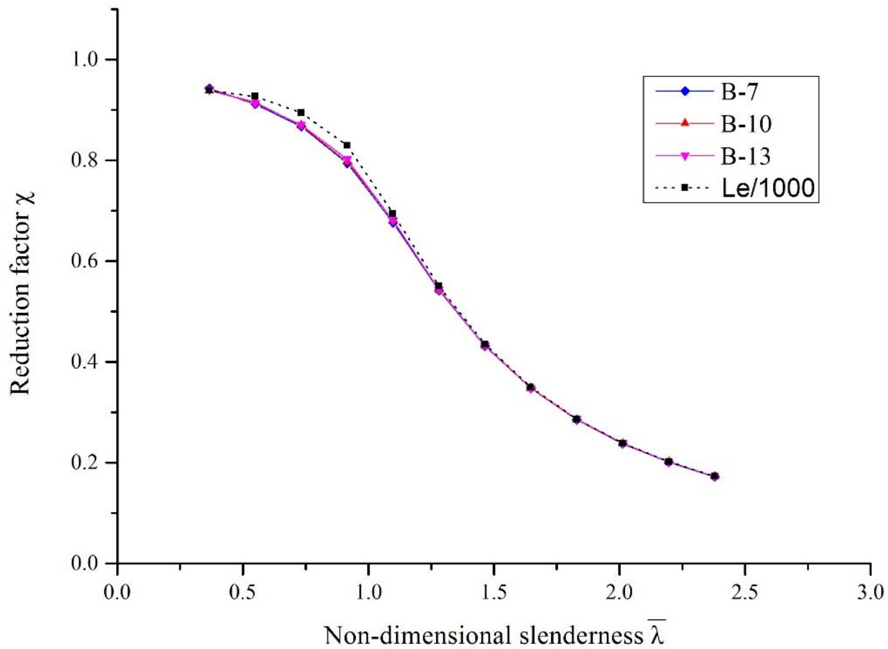

Figure 6.8 The influence of residual stresses on box columns

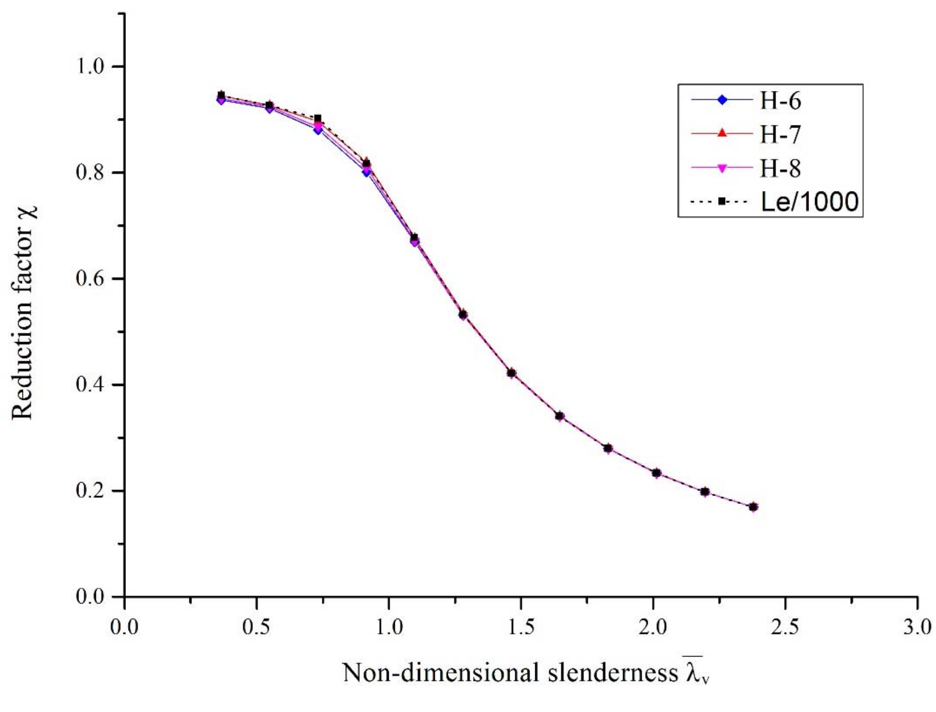

(a) Results about the minor axis

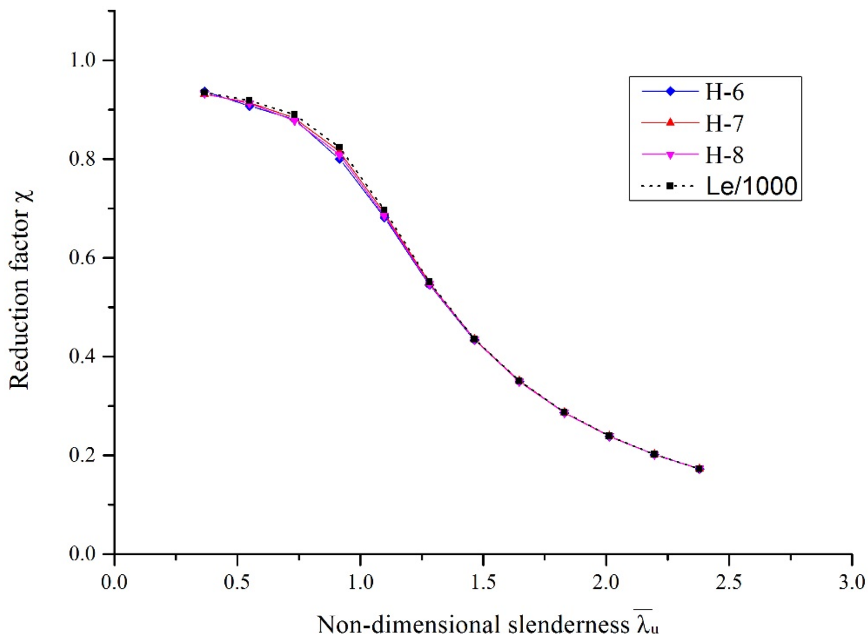

(b) Results about the major axis

Figure 6.9 The influence of residual stresses on H columns

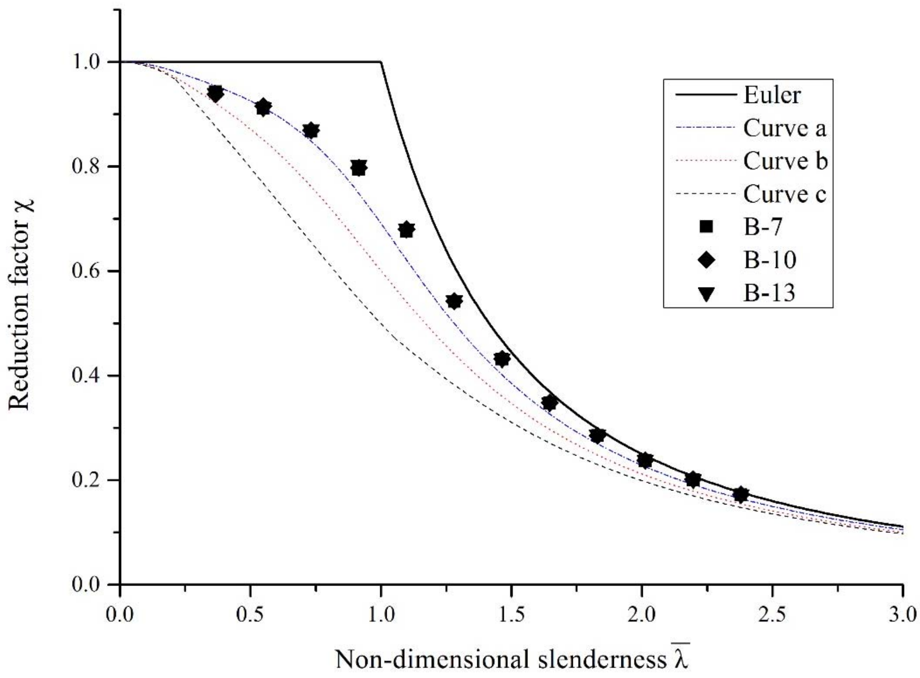

Figure 6.10 Comparison between test results of box columns and GB 50017-2003 (2003)

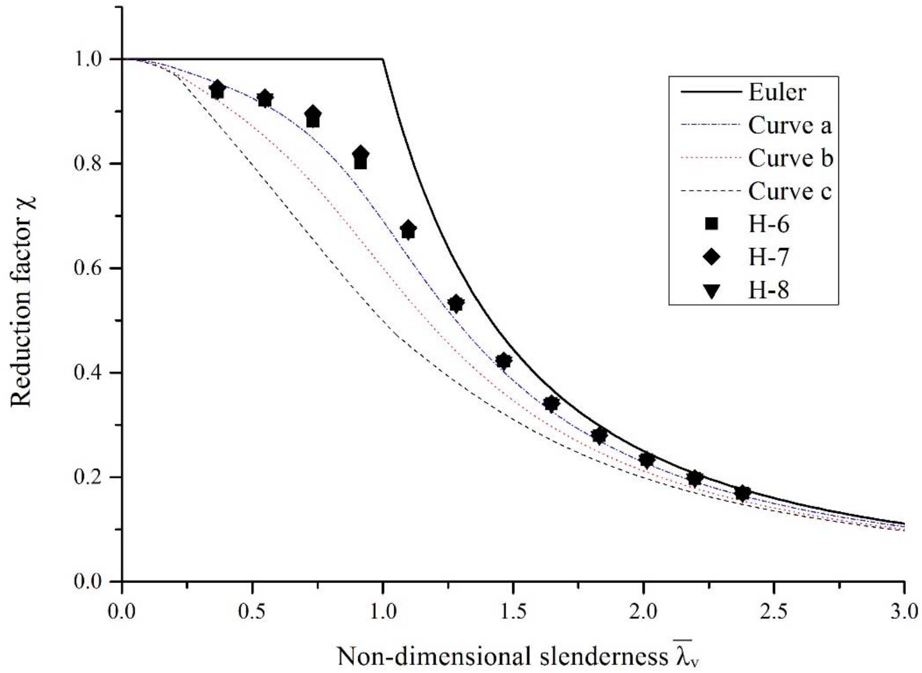

(a) Results about minor axis

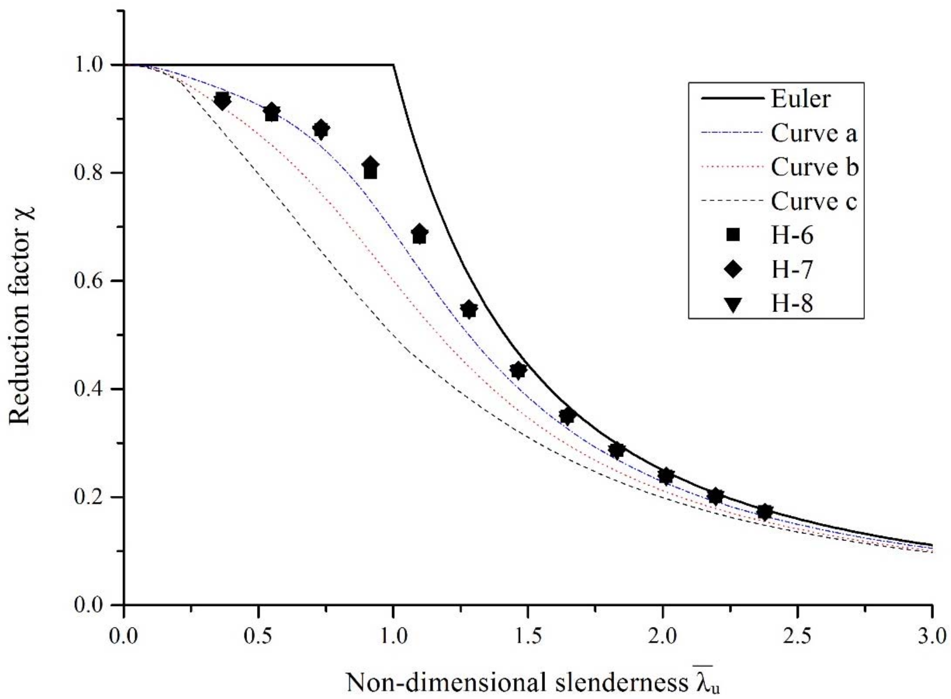

(b) Results about major axis

Figure 6.11 Comparison of test results of H columns and GB 50017-2003 (2003)

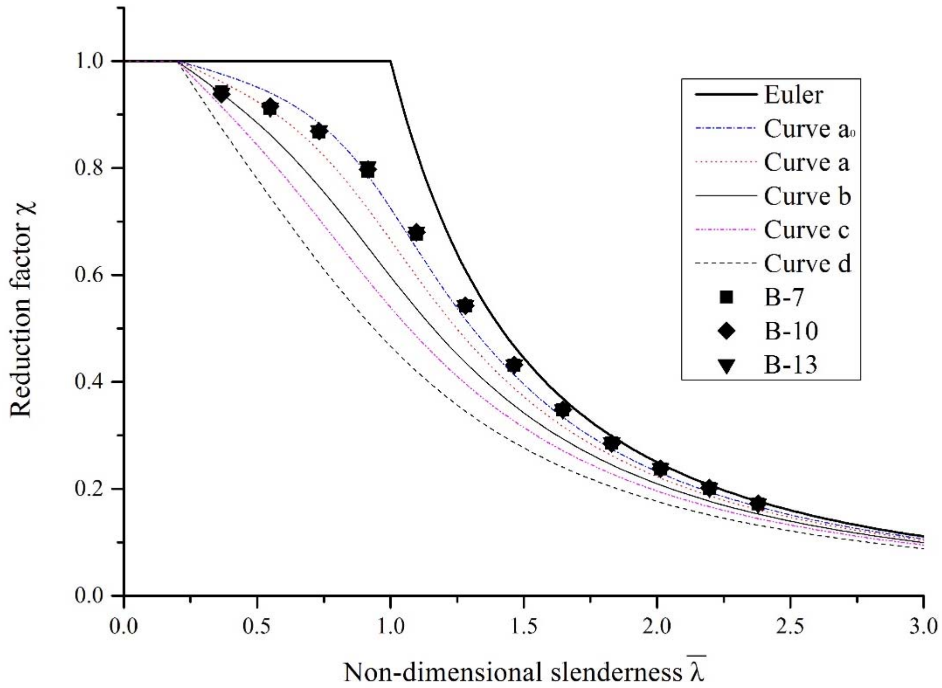

Figure 6.12 Comparison between test results of box columns and Eurocode 3 (2005)

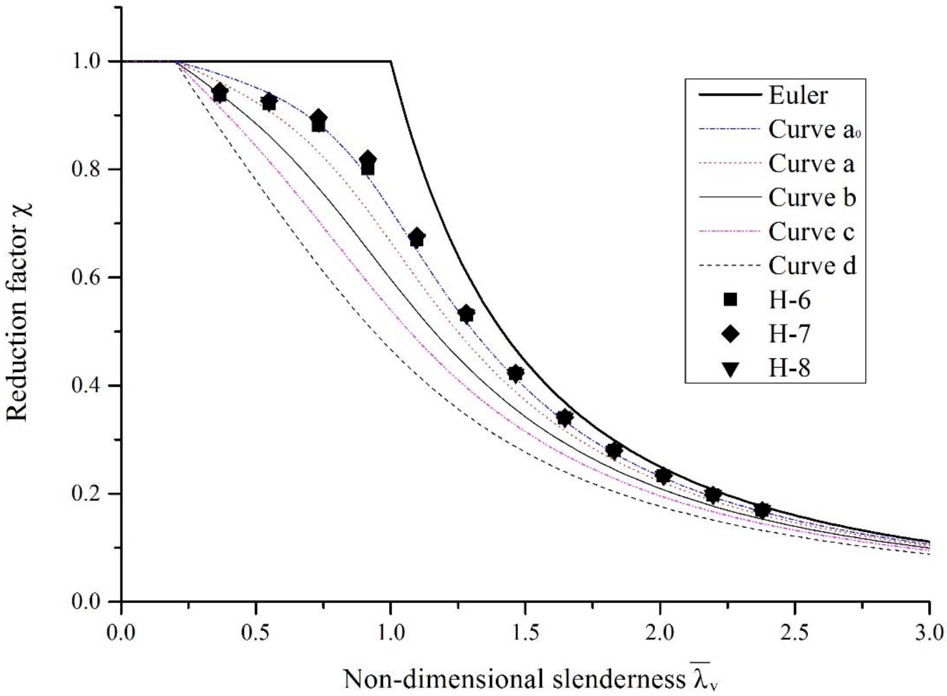

(a) Results about the minor axis

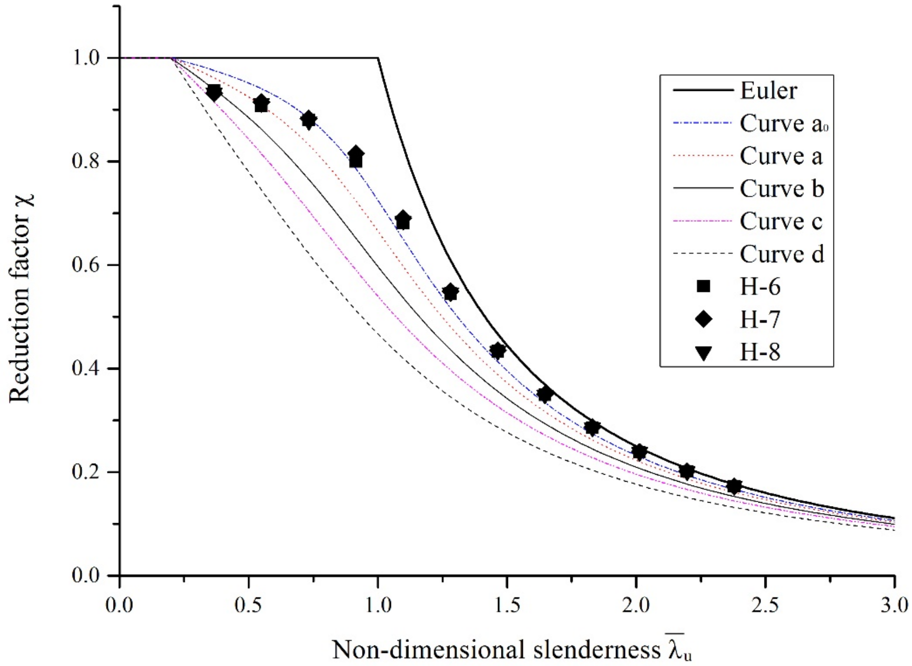

(b) Results about the major axis

Figure 6.13 Comparison of test results of H columns and Eurocode 3 (2005)

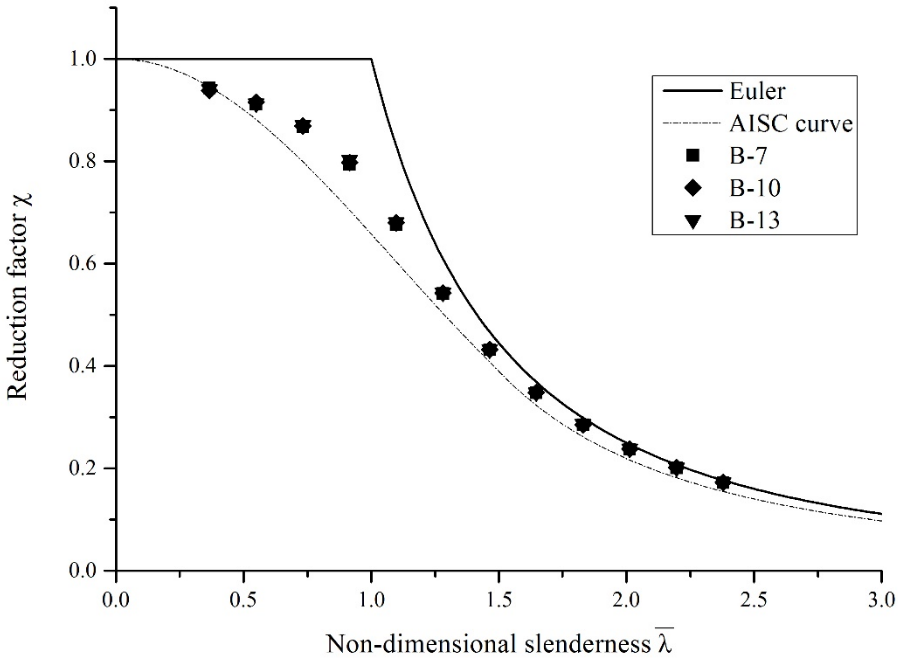

Figure 6.14 Comparison of test results of box columns and ANSI/AISC 360-10 (2010)

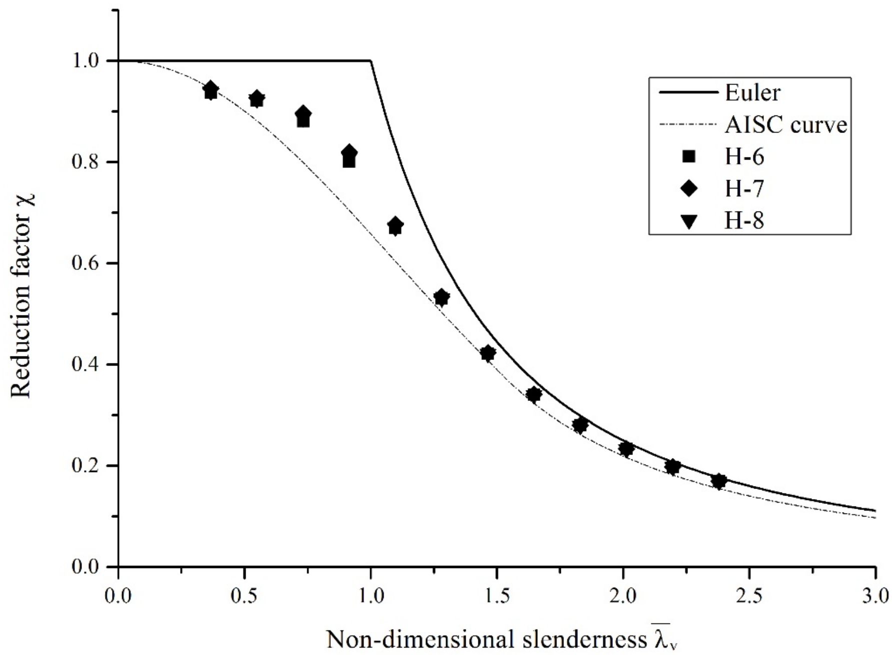

(a) Results about the minor axis

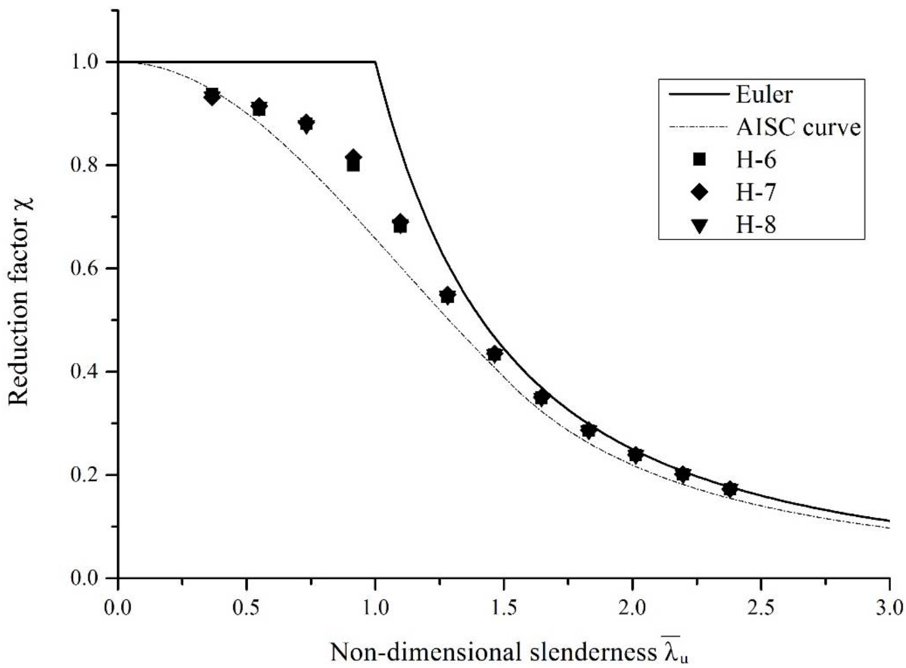

(b) Results about the major axis

Figure 6.15 Comparison of test results of H columns and ANSI/AISC 360-10 (2010)

Tables

Table 6.1 Comparison of test and prediction results of box columns

Specimen label	Test results (kN)	Predict capacity (kN)	Ratio
B-30-1*	5771.5	6352.3	1.10
B-30-2	9751.5	9602.7	0.98
B-50-1	6444.5	6895.7	1.07
B-50-2	7180.0	7234.2	1.01
B-70-1	3258.5	3455.7	1.06
B-70-2	2897.0	3311.2	1.14
Mean			1.06
Standard Deviation			0.05

Note: Initial deflection of specimen B-30-1 was enlarged by flame heating. Details are presented in Section 4.3.1.

Table 6.2 Comparison of test and prediction results of H columns

Specimen label	Test results (kN)	Predict capacity (kN)	Ratio
H-30-1	8493.0	8559.4	1.01
H-30-2	8994.0	8922.9	0.99
H-50-1	7207.0	7815.5	1.08
H-50-2	7124.5	7616.7	1.07
H-70-1*	3039.0	3505.4	1.15
H-70-2	3690.0	3856.6	1.05
Mean			1.06
Standard Deviation			0.05

Note: H-70-1 was straightened by the flame heating method. Details are presented in Section 4.3.1.

Table 6.3 Realistic dimensions of box section columns

Specimen label	B (mm)	h (mm)	t (mm)	h/t	A (mm^2)	I_u (cm^4)
B-7	140.88	108.74	16.07	6.8	8023	2118
B-10	192.37	160.33	16.02	10.0	11301	5906
B-13	236.47	204.27	16.10	12.7	14192	11548

Table 6.4 Realistic dimensions of H section columns

Specimen label	B (mm)	b_f (mm)	H (mm)	h (mm)	t_f, t_w (mm)	b_f/t_f	h/t_w	A (mm^2)
H-6	209.38	96.57	205.24	172.76	16.24	5.9	10.6	9606
H-7	240.47	112.16	238.15	205.83	16.16	6.9	12.7	11098
H-8	260.82	122.29	260.35	227.85	16.25	7.5	14.0	12179

Table 6.5 Buckling reduction factors of box columns about the u axis

λ	$\bar{\lambda}$	χ_u		
		B-7	B-10	B-13
20	0.366	0.943	0.938	0.940
30	0.549	0.911	0.915	0.913
40	0.732	0.867	0.869	0.871
50	0.915	0.794	0.797	0.803
60	1.098	0.676	0.680	0.681
70	1.281	0.542	0.543	0.544
80	1.464	0.431	0.432	0.432
90	1.647	0.348	0.348	0.348
100	1.830	0.285	0.285	0.286
110	2.013	0.238	0.238	0.239
120	2.196	0.201	0.202	0.202
130	2.379	0.172	0.173	0.172

Table 6.6 Buckling reduction factors of box columns about the v axis

λ	$\bar{\lambda}$	χ_v			χ_u / χ_v		
		B-7	B-10	B-13	B-7	B-10	B-13
20	0.366	0.943	0.938	0.940	1.00	1.00	1.00
30	0.549	0.911	0.915	0.913	1.00	1.00	1.00
40	0.732	0.870	0.869	0.871	1.00	1.00	1.00
50	0.915	0.795	0.803	0.804	1.00	0.99	1.00
60	1.098	0.679	0.682	0.683	1.00	1.00	1.00
70	1.281	0.544	0.545	0.545	1.00	1.00	1.00
80	1.464	0.432	0.433	0.433	1.00	1.00	1.00
90	1.647	0.348	0.348	0.348	1.00	1.00	1.00
100	1.830	0.285	0.285	0.287	1.00	1.00	1.00
110	2.013	0.238	0.238	0.239	1.00	1.00	1.00
120	2.196	0.201	0.202	0.202	1.00	1.00	1.00
130	2.379	0.172	0.173	0.173	1.00	1.00	1.00

Table 6.7 Buckling reduction factors of H columns about the minor axis

λ_v	$\bar{\lambda}_v$	χ_v		
		H-6	H-7	H-8
20	0.366	0.937	0.945	0.940
30	0.549	0.921	0.927	0.924
40	0.732	0.881	0.896	0.886
50	0.915	0.801	0.820	0.809
60	1.098	0.669	0.677	0.671
70	1.281	0.531	0.534	0.531
80	1.464	0.422	0.423	0.421
90	1.647	0.340	0.341	0.340
100	1.830	0.280	0.280	0.279
110	2.013	0.233	0.234	0.233
120	2.196	0.198	0.198	0.197
130	2.379	0.169	0.169	0.169

Table 6.8 Buckling reduction factors of H columns about the minor axis

λ_u	$\bar{\lambda}_u$	χ_u		
		H-6	H-7	H-8
20	0.366	0.937	0.932	0.932
30	0.549	0.908	0.915	0.913
40	0.732	0.880	0.883	0.878
50	0.915	0.800	0.816	0.809
60	1.098	0.682	0.690	0.685
70	1.281	0.545	0.549	0.547
80	1.464	0.433	0.435	0.434
90	1.647	0.349	0.350	0.349
100	1.830	0.286	0.287	0.286
110	2.013	0.238	0.239	0.238
120	2.196	0.201	0.202	0.202
130	2.379	0.172	0.173	0.173

Table 6.9 Comparison of numerical results and GB 50017-2003 (2003) for box columns

λ	$\bar{\lambda}$	χ					Ratio			Ratio		
		B-7	B-10	B-13	a curve	b curve	B-7/a curve	B-10/a curve	B-13/a curve	B-7/b curve	B-10/b curve	B-13/b curve
20	0.366	0.943	0.938	0.940	0.954	0.921	0.99	0.98	0.98	1.02	1.02	1.02
30	0.549	0.911	0.915	0.913	0.913	0.851	1.00	1.00	1.00	1.07	1.07	1.07
40	0.732	0.867	0.869	0.871	0.849	0.762	1.02	1.02	1.03	1.14	1.14	1.14
50	0.915	0.794	0.797	0.803	0.749	0.654	1.06	1.06	1.07	1.21	1.22	1.23
60	1.098	0.676	0.680	0.681	0.621	0.541	1.09	1.10	1.10	1.25	1.26	1.26
70	1.281	0.542	0.543	0.544	0.499	0.441	1.08	1.09	1.09	1.23	1.23	1.23
80	1.464	0.431	0.432	0.432	0.401	0.360	1.07	1.08	1.08	1.20	1.20	1.20
90	1.647	0.348	0.348	0.348	0.326	0.297	1.07	1.07	1.07	1.17	1.17	1.17
100	1.830	0.285	0.285	0.286	0.269	0.248	1.06	1.06	1.06	1.15	1.15	1.16
110	2.013	0.238	0.238	0.239	0.226	0.210	1.05	1.05	1.06	1.13	1.13	1.14
120	2.196	0.201	0.202	0.202	0.192	0.179	1.05	1.05	1.05	1.12	1.13	1.13
130	2.379	0.172	0.173	0.172	0.165	0.155	1.04	1.05	1.05	1.11	1.12	1.11
Mean							1.05	1.05	1.05	1.15	1.15	1.15
Standard Deviation							0.03	0.03	0.03	0.06	0.06	0.07

Table 6.9 (Cont.) Comparison of numerical results and GB 50017-2003 (2003) for box columns

λ	$\bar{\lambda}$	χ				Ratio		
		B-7	B-10	B-13	c curve	B-7/c curve	B-10/c curve	B-13/c curve
20	0.366	0.943	0.938	0.940	0.877	1.07	1.07	1.07
30	0.549	0.911	0.915	0.913	0.768	1.19	1.19	1.19
40	0.732	0.867	0.869	0.871	0.655	1.32	1.33	1.33
50	0.915	0.794	0.797	0.803	0.546	1.45	1.46	1.47
60	1.098	0.676	0.680	0.681	0.453	1.49	1.50	1.50
70	1.281	0.542	0.543	0.544	0.382	1.42	1.42	1.42
80	1.464	0.431	0.432	0.432	0.321	1.34	1.34	1.35
90	1.647	0.348	0.348	0.348	0.271	1.28	1.28	1.29
100	1.830	0.285	0.285	0.286	0.230	1.24	1.24	1.25
110	2.013	0.238	0.238	0.239	0.197	1.21	1.21	1.21
120	2.196	0.201	0.202	0.202	0.170	1.18	1.19	1.19
130	2.379	0.172	0.173	0.172	0.148	1.16	1.17	1.17
Mean						1.28	1.28	1.29
Standard Deviation						0.12	0.13	0.13

Table 6.10 Comparison of numerical results and GB 50017-2003 (2003) for H columns about minor axis

λ_v	$\bar{\lambda}_v$	χ_v					Ratio			Ratio		
		H-6	H-7	H-8	a curve	b curve	H-6/a curve	H-7/a curve	H-8/a curve	H-6/b curve	H-7/b curve	H-8/b curve
20	0.366	0.937	0.945	0.940	0.954	0.921	0.98	0.99	0.98	1.02	1.03	1.02
30	0.549	0.921	0.927	0.924	0.913	0.851	1.01	1.02	1.01	1.08	1.09	1.09
40	0.732	0.881	0.896	0.886	0.849	0.762	1.04	1.06	1.04	1.16	1.18	1.16
50	0.915	0.801	0.820	0.809	0.749	0.654	1.07	1.09	1.08	1.23	1.25	1.24
60	1.098	0.669	0.677	0.671	0.621	0.541	1.08	1.09	1.08	1.24	1.25	1.24
70	1.281	0.531	0.534	0.531	0.499	0.441	1.06	1.07	1.06	1.20	1.21	1.20
80	1.464	0.422	0.423	0.421	0.401	0.360	1.05	1.05	1.05	1.17	1.17	1.17
90	1.647	0.340	0.341	0.340	0.326	0.297	1.04	1.05	1.04	1.15	1.15	1.14
100	1.830	0.280	0.280	0.279	0.269	0.248	1.04	1.04	1.04	1.13	1.13	1.13
110	2.013	0.233	0.234	0.233	0.226	0.210	1.03	1.04	1.03	1.11	1.12	1.11
120	2.196	0.198	0.198	0.197	0.192	0.179	1.03	1.03	1.03	1.10	1.10	1.10
130	2.379	0.169	0.169	0.169	0.165	0.155	1.03	1.03	1.03	1.09	1.10	1.09
Mean							1.04	1.05	1.04	1.14	1.15	1.14
Standard Deviation							0.02	0.03	0.03	0.06	0.07	0.06

Table 6.11 Comparison of numerical results and GB 50017-2003 (2003) for H columns about major axis

λ_u	$\bar{\lambda}_u$	χ_u					Ratio			Ratio		
		H-6	H-7	H-8	a curve	b curve	H-6/a curve	H-7/a curve	H-8/a curve	H-6/b curve	H-7/b curve	H-8/b curve
20	0.366	0.937	0.932	0.932	0.954	0.921	0.98	0.98	0.98	1.02	1.01	1.01
30	0.549	0.908	0.915	0.913	0.913	0.851	0.99	1.00	1.00	1.07	1.07	1.07
40	0.732	0.880	0.883	0.878	0.849	0.762	1.04	1.04	1.03	1.15	1.16	1.15
50	0.915	0.800	0.816	0.809	0.749	0.654	1.07	1.09	1.08	1.22	1.25	1.24
60	1.098	0.682	0.690	0.685	0.621	0.541	1.10	1.11	1.10	1.26	1.28	1.27
70	1.281	0.545	0.549	0.547	0.499	0.441	1.09	1.10	1.09	1.24	1.24	1.24
80	1.464	0.433	0.435	0.434	0.401	0.360	1.08	1.08	1.08	1.20	1.21	1.20
90	1.647	0.349	0.350	0.349	0.326	0.297	1.07	1.07	1.07	1.18	1.18	1.18
100	1.830	0.286	0.287	0.286	0.269	0.248	1.06	1.06	1.06	1.15	1.16	1.15
110	2.013	0.238	0.239	0.238	0.226	0.210	1.06	1.06	1.06	1.14	1.14	1.14
120	2.196	0.201	0.202	0.202	0.192	0.179	1.05	1.05	1.05	1.12	1.13	1.13
130	2.379	0.172	0.173	0.173	0.165	0.155	1.05	1.05	1.05	1.11	1.12	1.12
Mean							1.05	1.06	1.06	1.16	1.16	1.16
Standard Deviation							0.03	0.04	0.04	0.07	0.07	0.07

Table 6.12 Comparison of numerical results and Eurocode 3 (2005) for box columns

λ	$\bar{\lambda}$	χ					Ratio			Ratio		
		B-7	B-10	B-13	a_0 curve	a curve	B-7/a_0 curve	B-10/a_0 curve	B-13/a_0 curve	B-7/a curve	B-10/a curve	B-13/a curve
20	0.366	0.943	0.938	0.940	0.976	0.962	0.97	0.96	0.96	0.98	0.98	0.98
30	0.549	0.911	0.915	0.913	0.940	0.908	0.97	0.97	0.97	1.00	1.01	1.00
40	0.732	0.867	0.869	0.871	0.884	0.832	0.98	0.98	0.99	1.04	1.04	1.05
50	0.915	0.794	0.797	0.803	0.786	0.724	1.01	1.01	1.02	1.10	1.10	1.11
60	1.098	0.676	0.680	0.681	0.650	0.597	1.04	1.05	1.05	1.13	1.14	1.14
70	1.281	0.542	0.543	0.544	0.517	0.481	1.05	1.05	1.05	1.13	1.13	1.13
80	1.464	0.431	0.432	0.432	0.413	0.388	1.05	1.05	1.05	1.11	1.11	1.11
90	1.647	0.348	0.348	0.348	0.334	0.317	1.04	1.04	1.04	1.10	1.10	1.10
100	1.830	0.285	0.285	0.286	0.275	0.262	1.04	1.04	1.04	1.09	1.09	1.09
110	2.013	0.238	0.238	0.239	0.229	0.220	1.04	1.04	1.04	1.08	1.08	1.08
120	2.196	0.201	0.202	0.202	0.194	0.187	1.03	1.04	1.04	1.07	1.08	1.08
130	2.379	0.172	0.173	0.172	0.167	0.161	1.03	1.04	1.03	1.07	1.07	1.07
Mean							1.02	1.02	1.02	1.07	1.08	1.08
Standard Deviation							0.03	0.03	0.03	0.04	0.05	0.05

Table 6.12 (Cont.) Comparison of numerical results and Eurocode 3 (2005) for box columns

λ	$\bar{\lambda}$	χ					Ratio			Ratio		
		B-7	B-10	B-13	b curve	c curve	B-7/b curve	B-10/b curve	B-13/b curve	B-7/c curve	B-10/c curve	B-13/c curve
20	0.366	0.943	0.938	0.940	0.939	0.915	1.00	1.00	1.00	1.03	1.03	1.03
30	0.549	0.911	0.915	0.913	0.862	0.815	1.06	1.06	1.06	1.12	1.12	1.12
40	0.732	0.867	0.869	0.871	0.765	0.705	1.13	1.14	1.14	1.23	1.23	1.24
50	0.915	0.794	0.797	0.803	0.651	0.591	1.22	1.22	1.23	1.34	1.35	1.36
60	1.098	0.676	0.680	0.681	0.536	0.485	1.26	1.27	1.27	1.39	1.40	1.40
70	1.281	0.542	0.543	0.544	0.436	0.397	1.24	1.25	1.25	1.36	1.37	1.37
80	1.464	0.431	0.432	0.432	0.356	0.326	1.21	1.21	1.21	1.32	1.32	1.32
90	1.647	0.348	0.348	0.348	0.293	0.271	1.19	1.19	1.19	1.28	1.28	1.28
100	1.830	0.285	0.285	0.286	0.245	0.228	1.16	1.16	1.17	1.25	1.25	1.26
110	2.013	0.238	0.238	0.239	0.207	0.194	1.15	1.15	1.15	1.22	1.22	1.23
120	2.196	0.201	0.202	0.202	0.177	0.167	1.13	1.14	1.14	1.20	1.21	1.21
130	2.379	0.172	0.173	0.172	0.153	0.145	1.12	1.13	1.13	1.19	1.19	1.19
Mean							1.16	1.16	1.16	1.25	1.25	1.25
Standard Deviation							0.07	0.07	0.07	0.10	0.10	0.10

Table 6.13 Comparison of numerical results and Eurocode 3 (2005) for H columns about the minor axis

λ_v	$\bar{\lambda}_v$	χ_v					Ratio			Ratio		
		H-6	H-7	H-8	a_0 curve	a curve	H-6/a_0 curve	H-7/a_0 curve	H-8/a_0 curve	H-6/a curve	H-7/a curve	H-8/a curve
20	0.366	0.937	0.945	0.940	0.976	0.962	0.96	0.97	0.96	0.97	0.98	0.98
30	0.549	0.921	0.927	0.924	0.940	0.908	0.98	0.99	0.98	1.01	1.02	1.02
40	0.732	0.881	0.896	0.886	0.884	0.832	1.00	1.01	1.00	1.06	1.08	1.07
50	0.915	0.801	0.820	0.809	0.786	0.724	1.02	1.04	1.03	1.11	1.13	1.12
60	1.098	0.669	0.677	0.671	0.650	0.597	1.03	1.04	1.03	1.12	1.13	1.12
70	1.281	0.531	0.534	0.531	0.517	0.481	1.03	1.03	1.03	1.10	1.11	1.10
80	1.464	0.422	0.423	0.421	0.413	0.388	1.02	1.03	1.02	1.09	1.09	1.09
90	1.647	0.340	0.341	0.340	0.334	0.317	1.02	1.02	1.02	1.07	1.08	1.07
100	1.830	0.280	0.280	0.279	0.275	0.262	1.02	1.02	1.02	1.07	1.07	1.06
110	2.013	0.233	0.234	0.233	0.229	0.220	1.02	1.02	1.02	1.06	1.06	1.06
120	2.196	0.198	0.198	0.197	0.194	0.187	1.02	1.02	1.01	1.05	1.06	1.05
130	2.379	0.169	0.169	0.169	0.167	0.161	1.02	1.02	1.02	1.05	1.05	1.05
Mean							1.01	1.02	1.01	1.06	1.07	1.07
Standard Deviation							0.02	0.02	0.02	0.04	0.04	0.04

Table 6.13 (Cont.) Comparison of numerical results and Eurocode 3 (2005) for H columns about the minor axis

λ_v	$\bar{\lambda}_v$	χ_v					Ratio			Ratio		
		H-6	H-7	H-8	b curve	c curve	H-6/b curve	H-7/b curve	H-8/b curve	H-6/c curve	H-7/c curve	H-8/c curve
20	0.366	0.937	0.945	0.940	0.939	0.915	1.00	1.01	1.00	1.02	1.03	1.03
30	0.549	0.921	0.927	0.924	0.862	0.815	1.07	1.08	1.07	1.13	1.14	1.13
40	0.732	0.881	0.896	0.886	0.765	0.705	1.15	1.17	1.16	1.25	1.27	1.26
50	0.915	0.801	0.820	0.809	0.651	0.591	1.23	1.26	1.24	1.36	1.39	1.37
60	1.098	0.669	0.677	0.671	0.536	0.485	1.25	1.26	1.25	1.38	1.40	1.38
70	1.281	0.531	0.534	0.531	0.436	0.397	1.22	1.23	1.22	1.34	1.35	1.34
80	1.464	0.422	0.423	0.421	0.356	0.326	1.19	1.19	1.18	1.29	1.30	1.29
90	1.647	0.340	0.341	0.340	0.293	0.271	1.16	1.16	1.16	1.25	1.26	1.25
100	1.830	0.280	0.280	0.279	0.245	0.228	1.14	1.14	1.14	1.23	1.23	1.22
110	2.013	0.233	0.234	0.233	0.207	0.194	1.13	1.13	1.13	1.20	1.20	1.20
120	2.196	0.198	0.198	0.197	0.177	0.167	1.12	1.12	1.11	1.18	1.19	1.18
130	2.379	0.169	0.169	0.169	0.153	0.145	1.11	1.11	1.11	1.17	1.17	1.17
Mean							1.15	1.15	1.15	1.23	1.24	1.24
Standard Deviation							0.07	0.07	0.07	0.10	0.10	0.10

Table 6.14 Comparison of numerical results and Eurocode 3 (2005) for H columns about the major axis

λ_u	$\bar{\lambda}_u$	χ_u					Ratio			Ratio		
		H-6	H-7	H-8	a_0 curve	a curve	H-6/a_0 curve	H-7/a_0 curve	H-8/a_0 curve	H-6/a curve	H-7/a curve	H-8/a curve
20	0.366	0.937	0.932	0.932	0.976	0.962	0.96	0.95	0.96	0.97	0.97	0.97
30	0.549	0.908	0.915	0.913	0.940	0.908	0.97	0.97	0.97	1.00	1.01	1.00
40	0.732	0.880	0.883	0.878	0.884	0.832	1.00	1.00	0.99	1.06	1.06	1.05
50	0.915	0.800	0.816	0.809	0.786	0.724	1.02	1.04	1.03	1.11	1.13	1.12
60	1.098	0.682	0.690	0.685	0.650	0.597	1.05	1.06	1.06	1.14	1.16	1.15
70	1.281	0.545	0.549	0.547	0.517	0.481	1.05	1.06	1.06	1.13	1.14	1.14
80	1.464	0.433	0.435	0.434	0.413	0.388	1.05	1.05	1.05	1.12	1.12	1.12
90	1.647	0.349	0.350	0.349	0.334	0.317	1.05	1.05	1.05	1.10	1.11	1.10
100	1.830	0.286	0.287	0.286	0.275	0.262	1.04	1.04	1.04	1.09	1.09	1.09
110	2.013	0.238	0.239	0.238	0.229	0.220	1.04	1.04	1.04	1.08	1.08	1.08
120	2.196	0.201	0.202	0.202	0.194	0.187	1.04	1.04	1.04	1.08	1.08	1.08
130	2.379	0.172	0.173	0.173	0.167	0.161	1.03	1.04	1.04	1.07	1.07	1.07
Mean							1.02	1.03	1.03	1.08	1.08	1.08
Standard Deviation							0.03	0.03	0.03	0.05	0.05	0.05

Table 6.14 (Cont.) Comparison of numerical results and Eurocode 3 (2005) for H columns about the major axis

λ_u	$\bar{\lambda}_u$	χ_u				Ratio		
		H-6	H-7	H-8	b curve	H-6/b curve	H-7/b curve	H-8/b curve
20	0.366	0.937	0.932	0.932	0.939	1.00	0.99	0.99
30	0.549	0.908	0.915	0.913	0.862	1.05	1.06	1.06
40	0.732	0.880	0.883	0.878	0.765	1.15	1.15	1.15
50	0.915	0.800	0.816	0.809	0.651	1.23	1.25	1.24
60	1.098	0.682	0.690	0.685	0.536	1.27	1.29	1.28
70	1.281	0.545	0.549	0.547	0.436	1.25	1.26	1.25
80	1.464	0.433	0.435	0.434	0.356	1.22	1.22	1.22
90	1.647	0.349	0.350	0.349	0.293	1.19	1.19	1.19
100	1.830	0.286	0.287	0.286	0.245	1.17	1.17	1.17
110	2.013	0.238	0.239	0.238	0.207	1.15	1.15	1.15
120	2.196	0.201	0.202	0.202	0.177	1.14	1.14	1.14
130	2.379	0.172	0.173	0.173	0.153	1.13	1.13	1.13
Mean						1.16	1.17	1.16
Standard Deviation						0.08	0.08	0.08

Table 6.15 Comparison of numerical results and ANSI/AISC 360-10 (2010) for box columns

λ	$\bar{\lambda}$	χ				Ratio		
		B-7	B-10	B-13	curve	B-7/ curve	B-10/ curve	B-13/ curve
20	0.366	0.943	0.938	0.940	0.945	1.00	0.99	0.99
30	0.549	0.911	0.915	0.913	0.881	1.03	1.04	1.04
40	0.732	0.867	0.869	0.871	0.799	1.09	1.09	1.09
50	0.915	0.794	0.797	0.803	0.704	1.13	1.13	1.14
60	1.098	0.676	0.680	0.681	0.604	1.12	1.13	1.13
70	1.281	0.542	0.543	0.544	0.503	1.08	1.08	1.08
80	1.464	0.431	0.432	0.432	0.408	1.06	1.06	1.06
90	1.647	0.348	0.348	0.348	0.323	1.08	1.08	1.08
100	1.830	0.285	0.285	0.286	0.262	1.09	1.09	1.09
110	2.013	0.238	0.238	0.239	0.216	1.10	1.10	1.10
120	2.196	0.201	0.202	0.202	0.182	1.10	1.11	1.11
130	2.379	0.172	0.173	0.172	0.155	1.11	1.11	1.11
Mean						1.08	1.08	1.09
Standard Deviation						0.04	0.04	0.04

Table 6.16 Comparison of numerical results and ANSI/AISC 360-10 (2010) for H columns about the minor axis

λ_v	$\bar{\lambda}_v$	χ_v				Ratio		
		H-6	H-7	H-8	curve	H-6/ curve	H-7/ curve	H-8/ curve
20	0.366	0.937	0.945	0.940	0.945	0.99	1.00	0.99
30	0.549	0.921	0.927	0.924	0.881	1.04	1.05	1.05
40	0.732	0.881	0.896	0.886	0.799	1.10	1.12	1.11
50	0.915	0.801	0.820	0.809	0.704	1.14	1.16	1.15
60	1.098	0.669	0.677	0.671	0.604	1.11	1.12	1.11
70	1.281	0.531	0.534	0.531	0.503	1.05	1.06	1.06
80	1.464	0.422	0.423	0.421	0.408	1.03	1.04	1.03
90	1.647	0.340	0.341	0.340	0.323	1.05	1.06	1.05
100	1.830	0.280	0.280	0.279	0.262	1.07	1.07	1.07
110	2.013	0.233	0.234	0.233	0.216	1.08	1.08	1.08
120	2.196	0.198	0.198	0.197	0.182	1.09	1.09	1.08
130	2.379	0.169	0.169	0.169	0.155	1.09	1.09	1.09
Mean						1.07	1.08	1.07
Standard Deviation						0.04	0.04	0.04

Table 6.17 Comparison of numerical results and ANSI/AISC 360-10 (2010) for H columns about the major axis

λ_u	$\bar{\lambda}_u$	χ_u				Ratio		
		H-6	H-7	H-8	curve	H-6/ curve	H-7/ curve	H-8/ curve
20	0.366	0.937	0.932	0.932	0.945	0.99	0.99	0.99
30	0.549	0.908	0.915	0.913	0.881	1.03	1.04	1.04
40	0.732	0.880	0.883	0.878	0.799	1.10	1.10	1.10
50	0.915	0.800	0.816	0.809	0.704	1.14	1.16	1.15
60	1.098	0.682	0.690	0.685	0.604	1.13	1.14	1.14
70	1.281	0.545	0.549	0.547	0.503	1.08	1.09	1.09
80	1.464	0.433	0.435	0.434	0.408	1.06	1.07	1.06
90	1.647	0.349	0.350	0.349	0.323	1.08	1.08	1.08
100	1.830	0.286	0.287	0.286	0.262	1.09	1.10	1.09
110	2.013	0.238	0.239	0.238	0.216	1.10	1.10	1.10
120	2.196	0.201	0.202	0.202	0.182	1.11	1.11	1.11
130	2.379	0.172	0.173	0.173	0.155	1.11	1.12	1.12
Mean						1.09	1.09	1.09
Standard Deviation						0.04	0.04	0.04

Table 6.18 Comparison of the proposed DAM and advanced analysis method for box columns

λ	P_{DAM} (kN)			P_a (kN)			Ratio		
	B-7	B-10	B-13	B-7	B-10	B-13	B-7	B-10	B-13
20	5620.0	8150.0	10230.0	5838.5	8185.6	10299.6	0.96	1.00	0.99
30	5540.0	7879.9	9899.9	5643.7	7984.9	9999.1	0.98	0.99	0.99
40	5149.1	7249.1	9108.9	5370.1	7581.6	9540.5	0.96	0.96	0.95
50	4545.4	6367.8	7997.8	4919.3	6956.4	8792.4	0.92	0.92	0.91
60	3761.6	5234.5	6574.5	4188.9	5935.0	7457.8	0.90	0.88	0.88
70	2889.7	4078.4	5070.0	3354.6	4738.0	5960.4	0.86	0.86	0.85
80	2194.1	3117.5	3946.4	2670.6	3766.1	4734.1	0.82	0.83	0.83
90	1735.1	2451.2	3087.1	2153.1	3035.0	3814.1	0.81	0.81	0.81
100	1386.4	1973.9	2480.5	1765.5	2488.0	3138.5	0.79	0.79	0.79
110	1137.2	1605.7	2042.3	1471.1	2072.9	2613.4	0.77	0.77	0.78
120	947.7	1356.3	1704.7	1243.5	1759.5	2208.0	0.76	0.77	0.77
130	788.4	1146.8	1445.5	1064.7	1505.5	1889.3	0.74	0.76	0.77
Mean							0.86	0.86	0.86
Standard Deviation							0.08	0.08	0.08

Table 6.19 Comparison of the proposed DAM and advanced analysis method for H columns about the minor axis

λ_v	P_{DAM} (kN)			P_a (kN)			Ratio		
	H-6	H-7	H-8	H-6	H-7	H-8	H-6	H-7	H-8
20	6960.0	8040.0	8830.0	6949.5	8097.9	8834.4	1.00	0.99	1.00
30	6709.9	7759.8	8509.9	6830.4	7939.5	8690.2	0.98	0.98	0.98
40	6168.7	7128.5	7818.7	6530.5	7678.4	8334.1	0.94	0.93	0.94
50	5436.2	6285.6	6912.5	5941.5	7023.3	7607.4	0.91	0.89	0.91
60	4490.8	5190.4	5699.9	4961.5	5801.3	6309.9	0.91	0.89	0.90
70	3455.6	4018.1	4406.7	3935.3	4576.9	4991.5	0.88	0.88	0.88
80	2622.3	3066.9	3364.9	3126.4	3625.6	3959.6	0.84	0.85	0.85
90	2063.8	2393.1	2640.6	2523.7	2922.7	3195.0	0.82	0.82	0.83
100	1675.3	1924.5	2113.7	2073.1	2399.4	2623.7	0.81	0.80	0.81
110	1356.5	1585.7	1734.7	1730.0	2001.6	2189.8	0.78	0.79	0.79
120	1147.1	1316.6	1455.8	1464.7	1694.2	1854.2	0.78	0.78	0.79
130	957.8	1126.9	1236.7	1255.4	1451.6	1590.7	0.76	0.78	0.78
Mean							0.87	0.86	0.87
Standard Deviation							0.08	0.07	0.07

Table 6.20 Comparison of the proposed DAM and advanced analysis method for H columns about the major axis

λ_u	P_{DAM} (kN)			P_a (kN)			Ratio		
	H-6	H-7	H-8	H-6	H-7	H-8	H-6	H-7	H-8
20	6910.0	7980.0	8760.0	6947.3	7981.6	8767.2	0.99	1.00	1.00
30	6670.0	7730.0	8480.0	6730.9	7836.4	8581.4	0.99	0.99	0.99
40	6139.6	7109.4	7809.2	6527.3	7564.0	8252.3	0.94	0.94	0.95
50	5369.0	6248.0	6848.2	5934.1	6987.1	7601.7	0.90	0.89	0.90
60	4357.6	5115.6	5615.6	5054.2	5914.8	6444.6	0.86	0.86	0.87
70	3333.3	3980.8	4360.9	4044.2	4704.6	5140.8	0.82	0.85	0.85
80	2583.0	3067.0	3364.9	3213.0	3728.2	4079.0	0.80	0.82	0.82
90	2063.8	2393.1	2640.6	2588.5	3001.1	3284.3	0.80	0.80	0.80
100	1675.3	1924.5	2113.7	2121.2	2457.5	2690.7	0.79	0.78	0.79
110	1366.5	1585.7	1735.1	1767.2	2046.6	2241.8	0.77	0.77	0.77
120	1147.0	1316.6	1446.0	1493.3	1728.9	1895.4	0.77	0.76	0.76
130	957.8	1126.9	1236.7	1278.1	1479.9	1625.2	0.75	0.76	0.76
Mean							0.85	0.85	0.86
Standard Deviation							0.08	0.08	0.08

Table 6.21 Comparison of the proposed DAM with modified factors and advanced analysis method for box columns

λ	P_{DAM} (kN)			P_a (kN)			Ratio		
	B-7	B-10	B-13	B-7	B-10	B-13	B-7	B-10	B-13
20	5620.0	8150.0	10230.0	5838.5	8185.6	10299.6	0.96	1.00	0.99
30	5550.0	7950.0	9980.0	5643.7	7984.9	9999.1	0.98	1.00	1.00
40	5259.3	7399.4	9299.3	5370.1	7581.6	9540.5	0.98	0.98	0.97
50	4717.2	6618.5	8308.5	4919.3	6956.4	8792.4	0.96	0.95	0.94
60	4013.8	5596.7	7036.5	4188.9	5935.0	7457.8	0.96	0.94	0.94
70	3215.6	4438.9	5578.5	3354.6	4738.0	5960.4	0.96	0.94	0.94
80	2453.2	3483.3	4405.1	2670.6	3766.1	4734.1	0.92	0.92	0.93
90	1924.6	2739.3	3452.0	2153.1	3035.0	3814.1	0.89	0.90	0.91
100	1546.0	2193.4	2778.2	1765.5	2488.0	3138.5	0.88	0.88	0.89
110	1266.8	1795.1	2281.6	1471.1	2072.9	2613.4	0.86	0.87	0.87
120	1057.3	1515.7	1894.2	1243.5	1759.5	2208.0	0.85	0.86	0.86
130	888.1	1276.5	1624.6	1064.7	1505.5	1889.3	0.83	0.85	0.86
Mean							0.92	0.92	0.93
Standard Deviation							0.05	0.05	0.05

Table 6.22 Comparison of the proposed DAM with modified factors and advanced analysis method for H columns about the minor axis

λ_v	P_{DAM} (kN)			P_a (kN)			Ratio		
	H-6	H-7	H-8	H-6	H-7	H-8	H-6	H-7	H-8
20	6959.8	8050.0	8830.0	6949.5	8097.9	8834.4	1.00	0.99	1.00
30	6867.2	7839.9	8609.8	6830.4	7939.5	8690.2	1.01	0.99	0.99
40	6299.1	7278.9	7988.7	6530.5	7678.4	8334.1	0.96	0.95	0.96
50	5647.3	6535.9	7166.4	5941.5	7023.3	7607.4	0.95	0.93	0.94
60	4813.0	5562.7	6111.8	4961.5	5801.3	6309.9	0.97	0.96	0.97
70	3824.7	4395.5	4823.6	3935.3	4576.9	4991.5	0.97	0.96	0.97
80	2949.5	3413.9	3760.0	3126.4	3625.6	3959.6	0.94	0.94	0.95
90	2322.6	2690.3	2957.7	2523.7	2922.7	3195.0	0.92	0.92	0.93
100	1854.8	2153.6	2362.7	2073.1	2399.4	2623.7	0.89	0.90	0.90
110	1535.8	1765.1	1953.6	1730.0	2001.6	2189.8	0.89	0.88	0.89
120	1276.5	1485.6	1635.2	1464.7	1694.2	1854.2	0.87	0.88	0.88
130	1096.9	1246.6	1385.9	1255.4	1451.6	1590.7	0.87	0.86	0.87
Mean							0.94	0.93	0.94
Standard Deviation							0.05	0.04	0.04

Table 6.23 Comparison of the proposed DAM with modified factors and advanced analysis method for H columns about the major axis

λ_u	P_{DAM} (kN)			P_a (kN)			Ratio		
	H-6	H-7	H-8	H-6	H-7	H-8	H-6	H-7	H-8
20	6910.0	7980.0	8760.0	6947.3	7981.6	8767.2	0.99	1.00	1.00
30	6730.0	7790.0	8540.0	6730.9	7836.4	8581.4	1.00	0.99	1.00
40	6269.8	7259.6	7969.5	6527.3	7564.0	8252.3	0.96	0.96	0.97
50	5589.2	6478.9	7118.8	5934.1	6987.1	7601.7	0.94	0.93	0.94
60	4678.4	5477.2	6017.1	5054.2	5914.8	6444.6	0.93	0.93	0.93
70	3675.5	4340.6	4770.1	4044.2	4704.6	5140.8	0.91	0.92	0.93
80	2871.3	3413.8	3760.2	3213.0	3728.2	4079.0	0.89	0.92	0.92
90	2274.1	2690.3	2957.7	2588.5	3001.1	3284.3	0.88	0.90	0.90
100	1854.8	2153.6	2362.7	2121.2	2457.5	2690.7	0.87	0.88	0.88
110	1535.8	1765.1	1953.6	1767.2	2046.6	2241.8	0.87	0.86	0.87
120	1276.6	1485.6	1635.2	1493.3	1728.9	1895.4	0.85	0.86	0.86
130	1087.1	1246.6	1385.9	1278.1	1479.9	1625.2	0.85	0.84	0.85
Mean							0.91	0.92	0.92
Standard Deviation							0.05	0.05	0.05

CHAPTER 7

CONCLUSIONS AND RECOMMENDATIONS

7.1. Conclusions

This thesis proposes advanced analysis and design methods for axial compression members fabricated with high-strength steel. In the proposed advanced analysis method, the PEP element and refined plastic hinge model are used to consider geometric nonlinearity and simulate the plastic behavior of members. To consider residual stress effects, two types of cross-sectional yield surfaces generated by a section analysis technique that is based on the quasi-Newton iterative algorithm are employed in the refined plastic hinge model. The sectioning method is used to measure the residual stress distribution of Q690 welded box and H columns. Then, two residual stress models for such columns are proposed on the basis of the analysis for experimental results. An experiment on the overall buckling behavior of box and H columns fabricated from Q690 high-strength steel is conducted. The experimental results for the columns are compared with the predictions indicated in the Chinese (GB 50017-2003, 2003), European (Eurocode 3, 2005), and American (ANSI/AISC 360-10, 2010) codes. To validate the accuracy and efficiency of the proposed advanced analysis method, the experimental results are compared with the numerical results derived by the method. Parametric analyses for the Q690 box and H columns with different slenderness ratios and sectional dimensions are carried out by the advanced analysis method. A refined second-order elastic analysis method, namely, the DAM, is also proposed for the design of Q690 welded box and H columns. The DAM is based on the proposed advanced analysis technique. The comparison of the numerical results of the proposed DAM and advanced analysis method verify the feasibility of the former for box and H columns that are welded using Q690 high-strength steel. Moreover, suggestions are provided for the first-order linear design of these columns in GB 50017-2003 (2003), Eurocode 3 (2005) and ANSI/AISC 360-10 (2010).

The conclusions drawn are as follows.

1) An advanced analysis method is proposed for analyzing and designing high-strength steel columns. The diverse effects of initial imperfections (i.e., initial geometric imperfections and residual stress), geometric and material nonlinearities can be simulated in the method. During analysis, the adopted PEP element can accurately reflect the P-δ effect due to initial geometric imperfections. The residual stress models based on the test results can be applied in the sectional analysis for arbitrary steel sections. The residual stress and material nonlinearity effects can be explicitly considered by combing the two types of yield surfaces determined from the sectional analysis and refined plastic hinge method. The applicability of the proposed advanced method in analyzing welded high-strength steel columns is confirmed by the comparison of the load-deflection curves obtained in the test and numerical analysis.

2) For welded box and H columns of identical sectional dimensions, sensitivity to initial geometric imperfections gradually decreases with increasing steel grade. The buckling reduction factors of Q690 welded box and H columns are higher than those of Q460 columns that possess reduction factors that are higher than those of Q235 columns.

3) The presence of residual stresses decreases the buckling reduction factors of Q690 welded box and H columns in non-dimensional slenderness ratios that range from 0.5 to 1.2. For stub or slender columns that suffer from strength failure or elastic instability, residual stresses slightly influence ultimate bearing capacity.

4) For the first-order design of Q690 welded box columns with a less than 20 width-to-thickness ratio under axial compression, the buckling curve “a” specified in the Chinese code (GB 50017-2003, 2003) is suggested. For Q690 welded flame-cut H columns with plates of less than 40 mm, the columns that buckle about the minor and major axes can be designed with reference to the buckling curve “a” indicated in GB 50017-2003 (2003).

5) For the safety of stocky columns, the design of Q690 welded box columns with a less than 30 width-to-thickness ratio and welded flame-cut H columns (plate thickness < 40 mm) can conservatively use the buckling curve “a” indicated in the European code (Eurocode 3, 2005). In the American

specification (ANSI/AISC 360-10, 2010), the single buckling curve can be used to design box and H columns fabricated with Q690 high-strength steel.

6) To facilitate the design of Q690 welded box and H columns, a refined second-order elastic analysis method (i.e., DAM) based on the proposed advanced technique is put forward. In the method, initial geometric imperfections and P-δ effects can be considered using the PEP element. To take into account partial yielding and residual stress effects, a stiffness reduction formula based on ANSI/AISC 360-10 (2010) is proposed. The feasibility of the proposed second-order elastic analysis method is verified by comparing analysis results with those obtained by the proposed advanced analysis method. The method can be used to design Q690 welded box and H columns under axial compression.

7.2. Recommendations for future work

This thesis discusses an experimental investigation on the residual stress distributions and overall buckling behavior of Q690 welded box and H columns under axial compression. A second-order elastic design method and advanced analysis are proposed for Q690 welded box and H columns. The results derived using the two methods are validated through testing. The succeeding research directions are recommended to promote the application of Q690 high-strength steel in engineering practice.

1) For Q690 welded box and H columns, the residual stress magnitudes and distributions of members with high width-to-thickness ratios should be explored. Aside from these two sectional columns, circular, channel, and tee sections should be analyzed in terms of residual stress. Each section that corresponds to the most unfavorable distribution of residual stresses should be identified and applied in analysis.

2) On the basis of the aforementioned residual stress pattern, the overall buckling behavior of other sectional members with Q690 high-strength steel under static loads should be studied with respect to theory and experimentation. The mechanical performance of structural systems with Q690 steel subjected to static loads should be investigated.

3) For other sectional members fabricated with Q690 steel, the practicability of adjusted stiffness factors, with consideration for partial yielding and residual stress effects in the proposed second-order elastic design method, should be confirmed.

4) For the application of Q690 steel in the construction industries of seismic regions, the hysteretic behavior and models of flexural members fabricated with Q690 steel should be determined and examined. Because joints are critical structural components, the ductility and fatigue behavior of member joints fabricated with Q690 steel should be studied.

5) For comprehensive investigations into Q690 high-strength steel, the partial material factors and reliabilities of members and structures made of Q690 steel should be considered.

REFERENCES

Alvarenga, A. R. d., and Silveira, R. A. d. M. (2009). Second-order plastic-zone analysis of steel frames. Part I: numerical formulation and examples of validation. *Latin American Journal of Solids and Structures, 6*, 131-152.

Alvarez, R. J., and Birnstiel, C. (1969). Inelastic analysis of multistory multibay frames. *Journal of the Structural Division, 95*(ST11), 2477-2503.

ANSI/AISC 360-10. (2010). ANSI/AISC 360-10: Specification for structural steel buildings. *AISC, Inc., One East Wacker Driver, Suite 700, Chicago, Illinois 60601-1802*.

Attalla, M. R., Deierlein, G. G., and Mcguire, W. (1994). Spread of plasticity-quasi-plastic-hinge approach. *Journal of Structural Engineering-Asce, 120*(8), 2451-2473.

Ban, H. Y. (2012). *Research on the overall buckling behavior and design method of high strength steel columns under axial compression.* (Ph.D.), Tsinghua University

Ban, H. Y., Shi, G., Shi, Y. J., and Wang, Y. Q. (2013a). Residual stress of 460MPa high strength steel welded box section: Experimental investigation and modeling. *Thin-Walled Structures, 64*, 73-82.

Ban, H. Y., Shi, G., Shi, Y. J., and Bradford, M. A. (2013b). Experimental investigation of the overall buckling behaviour of 960 MPa high strength steel columns. *Journal of Constructional Steel Research, 88*, 256-266.

Ban, H. Y., Shi, G., Shi, Y. J., and Wang, Y. Q. (2008). Study on the residual stress distribution of ultra-high-strength-steel welded sections. *Eng. Mech, 25*, 57-61.

Ban, H. Y., Shi, G., Shi, Y. J., and Wang, Y. Q. (2011). Research progress on the mechanical property of high strength structural steels. *Advanced Materials Research, 250-253*, 640-648.

Ban, H. Y., Shi, G., Shi, Y. J., and Wang, Y. Q. (2012). Overall buckling behavior of 460MPa high strength steel columns: Experimental investigation and design method. *Journal of Constructional Steel Research, 74*, 140-150.

Barroso, A.*, et al.* (2010). Prediction of welding residual stresses and displacements by simplified models. Experimental validation. *Materials & Design, 31*(3), 1338-1349.

Barsan, G. M., and Chiorean, C. G. (1999). Computer program for large deflection elasto-plastic analysis of semi-rigid steel frameworks. *Computers & Structures, 72*(6), 699-711.

Barsoum, Z., and Gustafsson, M. (2009). Fatigue of high strength steel joints welded with low temperature transformation consumables. *Engineering Failure Analysis, 16*(7), 2186-2194.

Barth, K. E., White, D. W., and Bobb, B. M. (2000). Negative bending resistance of HPS70W girders. *Journal of Constructional Steel Research, 53*(1), 1-31.

Bathe, K. J., and Bolourchi, S. (1979). Large displacement analysis of 3-dimensional beam structures. *International Journal for Numerical Methods in Engineering, 14*(7), 961-986.

Batoz, J. L., and Dhatt, G. (1979). Incremental displacement algorithms for nonlinear problems. *International Journal for Numerical Methods in Engineering, 14*(8), 1262-1267.

Beg, D., and Hladnilk, L. (1996). Slenderness limit of class 3 I cross-sections made of high strength steel. *Journal of Constructional Steel Research, 38*, 201-217.

Bergan, P. G., Horrigmoe, G., Bråkeland, B., and Søreide, T. H. (1978). Solution techniques for non-linear finite element problems. *International Journal for Numerical Methods in Engineering, 12*(11), 1677-1696.

Bjorhovde, R. (2001). *Structural steel selection considerations: A guide for students, educators, designers, and builders*: ASCE Publications.

Bjorhovde, R. (2004). Development and use of high performance steel. *Journal of Constructional Steel Research, 60*(3-5), 393-400.

Bresler, B. (1960). *Design criteria for reinforced columns under axial load and biaxial bending.* Paper presented at the ACI Journal proceedings.

Bridge, R. Q., Clarke, M. J., Hancock, G. J., and Trahair, N. S. (1990). *Trends in the analysis and design of steel building frames.* Paper presented at the Second National Structural Engineering Conference.

Brondum-Nielsen, T. (1985). Ultimate flexural capacity of cracked polygonal concrete sections under biaxial bending. *Journal of the American Concrete Institute, 82*(6), 863-869.

Cao, X. L. (2010). *Study on stability capacity of Q460 high-strength steel single-angle compression members.* (Doctor of Philosophy), Xi'an University of Architecture and Technology.

Capper, P. (2008). Millau viaduct. Retrieved July 15, 2013, from http://commons.wikimedia.org/wiki/File:Millau_Viaduct,_Aveyron,_France,_2008_-_Flickr_-_PhillipC_(2).jpg?uselang=zh-cn

Chan, S. L., and Chui, P. P. T. (1997). A generalized design-based elastoplastic analysis of steel frames by section assemblage concept. *Engineering structures, 19*(8), 628-636.

Chan, S. L. (1988). Geometric and material non-linear analysis of beam-columns and frames using the minimum residual displacement method. *International Journal for Numerical Methods in Engineering, 26*(12), 2657-2669.

Chan, S. L., and Cho, S. H. (2008). Second-order analysis and design of angle trusses Part I: Elastic analysis and design. *Engineering Structures, 30*(3), 616-625.

Chan, S. L., and Gu, J. X. (2000). Exact tangent stiffness for imperfect beam-column members. *Journal of Structural Engineering-Asce, 126*(9), 1094-1102.

Chan, S. L., and Kitipornchai, S. (1987). Geometric nonlinear analysis of asymmetric thin-walled beam-columns. *Engineering Structures, 9*(4), 243-254.

Chan, S. L., and Zhou, Z. H. (1994). Pointwise equilibrating polynomial element for nonlinear analysis of frames. *Journal of Structural Engineering, 120*(6), 1703-1717.

Charalampakis, A. E., and Koumousis, V. K. (2008). Ultimate strength analysis of composite sections under biaxial bending and axial load. *Advances in Engineering Software, 39*(11), 923-936.

Chen, J., Young, B., and Uy, B. (2006). Behavior of high strength structural steel at elevated temperatures. *Journal of Structural Engineering, 132*(12), 1948-1954.

Chen, S. F., Teng, J. G., and Chan, S. L. (2001). Design of biaxially loaded short composite columns of arbitrary section. *Journal of Structural Engineering, 127*(6), 678-685.

Chen, W. F., and Chan, S. L. (1995). 2nd-order inelastic analysis of steel frames using element with midspan and end springs. *Journal of Structural Engineering, 121*(3), 530-541.

Chen, W. F., and Lui, E. M. (1987). *Structural stability* (Vol. 198): Elsevier New York.

Chiew, S. P., Zhao, M. S., and Lee, C. K. (2014). Mechanical properties of heat-treated high strength steel under fire/post-fire conditions. *Journal of Constructional Steel Research, 98*, 12-19.

Chiorean, C. (2010). Computerised interaction diagrams and moment capacity contours for composite steel–concrete cross-sections. *Engineering Structures, 32*(11), 3734-3757.

Cho, S. H., and Chan, S. L. (2008). Second-order analysis and design of angle trusses, Part II: Plastic analysis and design. *Engineering Structures, 30*(3), 626-631.

Chu, K., and Pabarcius, A. (1964). Elastic and inelastic buckling of portal frames. *Journal of the Engineering Mechanics Division*, *90*(5), 221-250.

Collin, P., and Johansson, B. (2005). *Design of welds in high strength steel.* Paper presented at the Proceedings of the 4th European Conference on Steel and Composite Structures.

Collin, P., and Johansson, B. (2006). *Bridges in high strength steel.* Paper presented at the IABSE Symposium Report.

Connor, J. J., Logcher, R. D., and Chan, S. C. (1967). *Nonlinear analysis of elastic framed structures*: Department of Civil Engineering, Massachusetts Institute of Technology.

Corbett, K., Bowen, R., and Petersen, C. (2003). High-strength steel pipeline economics. *International Journal of Offshore and Polar Engineering, 14*(1), 105-112.

Costa, J., Ferreira, J., and Abreu, L. (2010). Fatigue behaviour of butt welded joints in a high strength steel. *Procedia Engineering, 2*(1), 697-705.

Crisfield, M. A. (1981). A faster Incremental/iterative solution procedure that handles snap-through. *Computers and Structures, 13*, 55-62.

Crisfield, M. A. (1983). An arc-length method including line searches and accelerations. *International Journal for Numerical Methods in Engineering, 19*(9), 1269-1289.

Cruise, R. B., and Gardner, L. (2008). Residual stress analysis of structural stainless steel sections. *Journal of Constructional Steel Research, 64*(3), 352-366.

Cruz, A., Simões, R., and Alves, R. (2012). Slip factor in slip resistant joints with high strength steel. *Journal of Constructional Steel Research, 70*, 280-288.

Cuong, N. H., Kim, S. E., and Oh, J. R. (2007). Nonlinear analysis of space steel frames using fiber plastic hinge concept. *Engineering Structures, 29*(4), 649-657.

da Silva, L. S., Jordão, S., and Simões, R. (2007). *Numerical Behaviour of Internal Joints with Beams of Different Heights.* Paper presented at the ICASS07—5th International conference on advances in steel structures, National University of Singapore and Singapore Structural Steel Society, Singapore.

Dafalias, Y. F., and Popov, E. P. (1975). A model of nonlinearly hardening materials for complex loading. *Acta Mechanica, 21*(3), 173-192.

Dancette, S., *et al.* (2012). Investigation of the tensile shear fracture of advanced high strength steel spot welds. *Engineering Failure Analysis, 25*, 112-122.

De Freitas, J. A. T., and Ribeiro, A. C. B. S. (1992). Large displacement elastoplastic analysis of space trusses. *Computers & Structures, 44*(5), 1007-1016.

De Vivo, L., and Rosati, L. (1998). Ultimate strength analysis of reinforced concrete sections subject to axial force and biaxial bending. *Computer Methods in Applied Mechanics and Engineering, 166*(3), 261-287.

Deng, C. S., Shi, G., Zhang, Y., Shi, Y. J., and Wang, Y. Q. (2010). Finite element analysis on the hysteretic behavior of high strength steel columns under cyclic loading. *Journal of Building Structures*, (S1), 28-34.

Driver, R., Abbas, H., and Sause, R. (2002). Local buckling of grouted and ungrouted internally stiffened double-plate HPS webs. *Journal of Constructional Steel Research, 58*(5), 881-906.

Dubina, D., Stratan, A., and Dinu, F. (2008). Dual high-strength steel eccentrically braced frames with removable links. *Earthquake Engineering & Structural Dynamics, 37*(15), 1703-1720.

Dubina, D*., et al.* (2010). *Application of high strength steel to seismic resistant multi-storey buildings.* Paper presented at the Urban Habitat Constructions under Catastrophic Events (Proceedings), London.

Dusicka, P., and Lewis, G. (2010). High strength steel bolted connections with filler plates. *Journal of Constructional Steel Research, 66*(1), 75-84.

Earls, C. (1999). On the inelastic failure of high strength steel I-shaped beams. *Journal of Constructional Steel Research, 49*(1), 1-24.

Earls, C. (2000). *Suitability of current design practice in the proportioning of high performance steel girders and beams.* Paper presented at the Proceedings of the 17th International Bridge Conference. Pittsburgh: Engineers' Society of Western Pennsylvania.

Earls, C., and Shah, B. (2002). High performance steel bridge girder compactness. *Journal of Constructional Steel Research, 58*(5), 859-880.

Earls, C. J. (2000). Influence of material effects on structural ductility of compact i-shaped beams. *Journal of Structural Engineering, 126*(11), 1268-1278.

Earls, C. J. (2001). Constant moment behavior of high-performance steel I-shaped beams. *Journal of Constructional Steel Research, 57*(7), 711-728.

Ekhande, S. G., Selvappalam, M., and Madugula, M. K. (1989). Stability functions for three-dimensional beam-columns. *Journal of Structural Engineering, 115*(2), 467-479.

El-Tawil, S., and Deierlein, G. G. (2001a). Nonlinear analysis of mixed steel-concrete frames. I: Element formulation. *Journal of Structural Engineering-Asce, 127*(6), 647-655.

El-Tawil, S., and Deierlein, G. G. (2001b). Nonlinear analysis of mixed steel-concrete frames. II: Implementation and verification. *Journal of Structural Engineering-Asce, 127*(6), 656-665.

El-Zanaty, M. H., Murray, D. W., and Bjorhovde, R. (1980). *Inelastic behavior of multistory steel frames*: Department of Civil Engineering, University of Alberta.

Eurocode 3. (2005). *Eurocode 3: Design of steel structures: Part 1-1: General rules and rules for buildings*: European Committee for Standardization (CEN).

Fang, L. X., Chan, S. L., and Wong, Y. L. (1999). Strength analysis of semi-rigid steel-concrete composite frames. *Journal of Constructional Steel Research, 52*(3), 269-291.

Fang, L. X., Chan, S. L., and Wong, Y. L. (2000). Numerical analysis of composite frames with partial shear-stud interaction by one element per member. *Engineering Structures, 22*(10), 1285-1300.

Fisher, J. W., and Wright, W. J. (2001). High performance steel enhances the fatigue and fracture resistance of steel bridge structures. *International Journal of Steel Structures, 1*(1), 1-7.

Fleming, J. F., and Werner, S. D. (1965). *Design of columns subjected to biaxial bending.* Paper presented at the ACI Journal Proceedings.

Fong, M., Chan, S. L., and Uy, B. (2011). Advanced design for trusses of steel and concrete-filled tubular sections. *Engineering Structures, 33*(12), 3162-3171.

Fong, M., Cho, S. H., and Chan, S. L. (2009). Design of angle trusses by codes and second-order analysis with experimental verification. *Journal of Constructional Steel Research, 65*(12), 2140-2147.

Fong, M., Liu, Y. P., and Chan, S. L. (2010). Second-order analysis and design of imperfect composite beam-columns. *Engineering Structures, 32*(6), 1681-1690.

Freuhan, J. (1998). *The Making, Shaping and Treating of Steel 11th Edition—Steelmaking and Refining Volume*: Pittsburgh, Pa.: The AISE Steel Foundation.

Fukumoto, Y. (1996). New constructional steels and structural stability. *Engineering structures, 18*(10), 786-791.

Furlong, R. W. (1961). Ultimate strength of square columns under axial load and biaxial bending. *ACI Journal, 32*(9), 1129-1140.

Galambos, T. V., Hajjar, J., Earls, C., and Gross, J. L. (1997). *Required properties of high-performance steels*: National Institute of Standards and Technology, Building and Fire Research Laboratory.

Gao, L., Sun, H., Jin, F., and Fan, H. (2009). Load-carrying capacity of high-strength steel box-sections I: Stub columns. *Journal of Constructional Steel Research, 65*(4), 918-924.

GB 50017-2003. (2003). GB 50017-2003 Code for design of steel structures. Beijing China Architecture & Building Press.

GB/T 228-2002. (2002). GB/T 228-2002 Metallic materials: tensile testing at ambient temperature. Beijing Standards Press of China.

GB/T 2975-1998. (1998). GB/T 2975-1998 Steel and steel products: location and preparation of test pieces for mechanical testing. Beijing: Standards Press of China.

Girão Coelho, A. M., and Bijlaard, F. (2010). High strength steel in buildings and civil engineering structures: Design of connections. *Advances in Structural Engineering, 13*(3), 413-429.

Girão Coelho, A. M., and Bijlaard, F. S. K. (2007). Experimental behaviour of high strength steel end-plate connections. *Journal of Constructional Steel Research, 63*(9), 1228-1240.

Girão Coelho, A. M., Bijlaard, F. S. K., and Kolstein, H. (2009). Experimental behaviour of high-strength steel web shear panels. *Engineering Structures, 31*(7), 1543-1555.

Girão Coelho, A. M., Bijlaard, F. S. K., and Simões da Silva, L. (2006). *Deformation considerations for high strength steel moment connections*. Paper presented at the proceedings of Stability and Ductility of Steel Structures, Lisbon, Portugal.

Girão Coelho, A. M., Bijlaard, F. S. K., and Simões da Silva, L. (2004). Experimental assessment of the ductility of extended end plate connections. *Engineering Structures, 26*(9), 1185-1206.

Goto, Y., and Chen, W. F. (1987). Second-order elastic analysis for frame design. *Journal of Structural Engineering, 113*(7), 1501-1519.

Greco, N., and Earls, C. (2003). Structural ductility in hybrid high performance steel beams. *Journal of Structural Engineering, 129*(12), 1584-1595.

Green, P., Sause, R., and Ricles, J. (2002). Strength and ductility of HPS flexural members. *Journal of Constructional Steel Research, 58*(5), 907-941.

Guralnick, S., and He, J. (1992). A finite element method for the incremental collapse analysis of elastic-perfectly plastic framed structures. *Computers & Structures, 45*(3), 571-581.

Haaijer, G. (1963). Economy of high strength steel structural members. *Transactions of the American Society of Civil Engineers, 128*(2), 820-841.

Harstead, G., Birnstiel, C., and Leu, K. (1968). Inelastic H-columns under biaxial bending. *Journal of the Structural Division, 94*(ST10), 2371-2398.

Hsu, C. T. T. (1987). Channel-shaped reinforced concrete compression members under biaxial bending. *Aci Structural Journal, 84*(3), 201-211.

Hsu, C. T. T. (1988). Analysis and design of square and rectangular columns by equation of failure surface. *Aci Structural Journal, 85*(2), 167-179.

Hsu, C. T. T. (1989). T-shaped reinforced concrete members under biaxial bending and axial compression. *Aci Structural Journal, 86*(4), 460-468.

Huang, Y., Onishi, Y., and Hayashi, K. (1996). *Inelastic behavior of high strength steels with weld connections under cyclic gradient stress.* Paper presented at the Proceedings of the 11th Wold Conference on Earthquake Engineering, Acapulco, Mexico.

Izzuddin, B., and Smith, D. L. (1996). Large-displacement analysis of elastoplastic thin-walled frames. I: Formulation and implementation. *Journal of Structural Engineering, 122*(8), 905-914.

Izzuddin, B. A. (1996). Quartic formulation for elastic beam-columns subject to thermal effects. *Journal of Engineering Mechanics, 122*(9), 861-871.

Jiang, X. M., Chen, H., and Liew, J. Y. R. (2002). Spread-of-plasticity analysis of three-dimensional steel frames. *Journal of Constructional Steel Research, 58*(2), 193-212.

Jiao, H., and Zhao, X. L. (2003). Imperfection, residual stress and yield slenderness limit of very high strength (VHS) circular steel tubes. *Journal of Constructional Steel Research, 59*(2), 233-249.

Jiao, H., and Zhao, X. L. (2004). Section slenderness limits of very high strength circular steel tubes in bending. *Thin-Walled Structures, 42*(9), 1257-1271.

Jordao, S., Simoes da Silva, L., and Simoes, R. (2007). Experimental behaviour of internal joints with beams of different heights, steel grade S690. *Proceedings of ICSAS, 7*.

Kakidai. (2012). Tokyo SkyTree 2012. Retrieved July 18, 2013, from http://commons.wikimedia.org/wiki/File:Tokyo_Sky_Tree_2012.JPG

Kalakoutsky, N. (1888). The study of internal stresses in cast iron and steel: London.

Kassimali, A. (1983). Large deformation analysis of elasticplastic frames. *Journal of Structural Engineering, 109*(8), 1869-1886.

Kassimali, A., and Abbasnia, R. (1991). Large deformation analysis of elastic space frames. *Journal of structural Engineering, 117*(7), 2069-2087.

Kato, B. (1990). Deformation capacity of steel structures. *Journal of Constructional Steel Research, 17*(1–2), 33-94.

Kim, D. K.*, et al.* (2014). Strength and residual stress evaluation of stub columns fabricated from 800 MPa high-strength steel. *Journal of Constructional Steel Research, 102*(0), 111-120.

Kim, H. J., and Yura, J. A. (1999). The effect of ultimate-to-yield ratio on the bearing strength of bolted connections. *Journal of Constructional Steel Research, 49*(3), 255-269.

Kim, S. E., and Chen, W. F. (1998). A sensitivity study on number of elements in refined plastic-hinge analysis. *Computers & Structures, 66*(5), 665-673.

Kim, S. E., Lee, J., and Park, J. S. (2002). 3-D second-order plastic-hinge analysis accounting for lateral torsional buckling. *International Journal of Solids and Structures, 39*(8), 2109-2128.

Kim, S. E., Lee, J., and Park, J. S. (2003). 3-D second-order plastic-hinge analysis accounting for local buckling. *Engineering Structures, 25*(1), 81-90.

Kim, S. E., Uang, C. M., Choi, S. H., and An, K. Y. (2006). Practical advanced analysis of steel frames considering lateral-torsional buckling. *Thin-walled structures, 44*(7), 709-720.

King, W. S., White, D. W., and Chen, W. F. (1992). Second-order inelastic analysis methods for steel-frame design. *Journal of Structural Engineering, 118*(2), 408-428.

Kolstein, M., Bijlaard, F., and Dijkstra, O. (2007). *Deformation capacity of welded joints using very high strenght steel*. Paper presented at the Proceedings of the Fifth International Conference on Advances in Steel Structures, Singapore.

Kuwamura, H. (1988). *Effect of yield ratio on the ductility of high-strength steels under seismic loading*. Paper presented at the Proceedings of Annual Technical Session of SSRC, Minneapolis, Minnesota.

Kuwamura, H., and Kato, B. (1989). *Inelastic behaviour of high strength steel members with low yield ratio.* Paper presented at the Pacific Structural Steel Conference, 2nd, 1989, Gold Coast, Queensland, Australia.

Kuwamura, H., and Suzuki, T. (1992). *Low-cycle fatigue resistance of welded joints of high-strength steel under earthquake loading.* Paper presented at the Proc., 10th World Conf. on Earthquake Engineering.

Lazić, V.*, et al.* (2012). Estimates of weldability and selection of the optimal procedure and technology for welding of high strength steels. *Procedia Engineering, 40*, 310-315.

Lee, C. K., Chiew, S. P., and Jiang, J. (2012a). Residual stress study of welded high strength steel thin-walled plate-to-plate joints: Part 1: Experimental study. *Thin-Walled Structures, 56*, 103-112.

Lee, C. K., Chiew, S. P., and Jiang, J. (2012b). Residual stress study of welded high strength steel thin-walled plate-to-plate joints: Part 2: Numerical modeling. *Thin-Walled Structures, 59*, 120-131.

Lee, C. K., Chiew, S. P., and Jiang, J. (2014a). Residual stress of high strength steel box T-joints: Part 1: Experimental study. *Journal of Constructional Steel Research, 93*, 20-31.

Lee, C. K., Chiew, S. P., and Jiang, J. (2014b). Residual stress of high strength steel box T-joints: Part 2: Numerical study. *Journal of Constructional Steel Research, 98*, 73-87.

Lee, H. E., Joo, H. S., Choi, B. H., and Moon, J. H. (2011). Evaluation of flexural ductility of negative moment Region of I-girder with high strength steel. *Procedia Engineering, 14*, 272-279.

LERA, E. (2014). Shanghai world financial centre. from http://commons.wikimedia.org/wiki/File:Shanghai_World_Financial_Center_-_China.jpg?uselang=zh-cn

Li, G. Q., Wang, Y. B., Chen, S. W., Cui, W., and Sun, F. F. (2013a). Experimental study of Q460C high strength steel welded H-section and box-section columns under cyclic loading. *Journal of Building Structures, 34*(3), 80-86.

Li, G. Q., Wang, Y. B., Chen, S. W., and Cui, W. (2013b). Finite element analysis on hysteretic behavior of Q460C high strength steel box-section and H-section columns. *Journal of Building Structures, 34*(3), 87-92.

Li, G. Q., Wang, Y. B., Chen, S. W., and Sun, F. F. (2013c). State-of-the-art on research of high strength structural steels and key issues of using high strength steels in seismic structures. *Journal of Building Structures, 34*(1), 1-13.

Li, G. Q., Wang, Y. B., Chen, S. W., and Sun, F. F. (2011). Parametric analysis of ultimate bearing capacity of Q460 high strength steel welded box columns under axial compression. *Journal of Building Structures, 11*, 019.

Li, Z. L., Liu, H. J., Zhang, D. Y., and Li, M. H. (2008). Application of high-strength steel Q460 in 1000kV transmission towers. *Power System Technology, 24*, 004.

Liew, J. Y. R., Chen, H., Shanmugam, N. E., and Chen, W. F. (2000). Improved nonlinear plastic hinge analysis of space frame structures. *Engineering Structures, 22*(10), 1324-1338.

Liew, J. Y. R., Punniyakotty, N. M., and Shanmugam, N. E. (1997). Advanced analysis and design of spatial structures. *Journal of Constructional Steel Research, 42*(1), 21-48.

Lindner, F. (2005). Sony center Berlin. Retrieved July 14, 2013, from http://commons.wikimedia.org/wiki/File:Sony_Center_Berlin.jpg

Liu, B., Wang, W., Li, G. Q., and Dai, G. X. (2012). Study of fire resistance of high strength Q460 steel columns. *China Civil Engineering Journal, 45*(9), 19-26.

Liu, S. W., Liu, Y. P., and Chan, S. L. (2014a). Direct analysis by an arbitrarily-located-plastic-hinge element: Part 1: Planar analysis. *Journal of Constructional Steel Research, 103*, 303-315.

Liu, S. W., Liu, Y. P., and Chan, S. L. (2014b). Direct analysis by an arbitrarily-located-plastic-hinge element: Part 2: Spatial analysis. *Journal of Constructional Steel Research*, *103*, 316-326.

Liu, S. W. (2014). *Second-order design and advanced analysis of hybrid steel and concrete framed structures.* (Ph.D.), The Hong Kong Polytechnic University, Hong Kong.

Liu, S. W., Liu, Y. P., and Chan, S. L. (2010). Pushover analysis by one element per member for performance-based seismic design. *International Journal of Structural Stability and Dynamics, 10*(01), 111-126.

Liu, S. W., Liu, Y. P., and Chan, S. L. (2012a). Advanced analysis of hybrid steel and concrete frames: Part 1: Cross-section analysis technique and second-order analysis. *Journal of Constructional Steel Research, 70*, 326-336.

Liu, S. W., Liu, Y. P., and Chan, S. L. (2012b). Advanced analysis of hybrid steel and concrete frames: Part 2: Refined plastic hinge and advanced analysis. *Journal of Constructional Steel Research, 70*, 337-349.

Livesley, R. K., and Chandler, D. B. (1956). *Stability functions for structural frameworks*: Manchester University Press.

Long, H. V., Jean-François, D., Lam, L. D. P., and Barbara, R. (2011). Field of application of high strength steel circular tubes for steel and composite columns from an economic point of view. *Journal of Constructional Steel Research, 67*(6), 1001-1021.

Lücken, H., Kern, A., and Schriever, U. (2008). *High-performance steel grades for special applications in ships and offshore constructions.* Paper presented at the Proceedings of the Eighteenth International Offshore and Polar Engineering Conference; Canada.

Chen, L. R. (2007). The characteristics of structural steel for the main building in new location of China central television station. *Steel Construction, 22*(91), 1-4.

Lwin, M. M. (2002). *High performance steel designers' guide*. San Francisco: U.S. Department of Transportation, Federal Highway Administration, Western Resource Center.

Mang, F., Bucak, O., and Stauf, H. (1993). *Fatigue behaviour of high-strength steels, welded hollow section joints and their connections*. Paper presented at the Proceedings of the 12th International Conference on Offshore Mechanical and Arctic Engineering (OMAE 1993), Glasgow, Scotland.

Ma, J. L., Chan, T. M., and Young, B. (2015). Material properties and residual stresses of cold-formed high strength steel hollow sections. *Journal of Constructional Steel Research, 109*, 152-165.

McDermott, J. (1969a). Local plastic buckling of A514 steel members. *J. Struct. Div. ASCE, 5*(9), 1837-1850.

McDermott, J. (1969b). Plastic bending of A514 steel beams. *J. Struct. Div, 95*(9), 1851-1871.

Meek, J. L., and Lin, W. J. (1990). Geometric and material nonlinear analysis of thin-walled beam-columns. *Journal of Structural Engineering, 116*(6), 1473-1490.

Meek, J. L., and Tan, H. S. (1984). Geometrically nonlinear analysis of space frames by an incremental iterative technique. *Computer methods in applied mechanics and engineering, 47*(3), 261-282.

MEng, G. P. (2006). Evening meeting-High strength steel use in Australia, Japan & the US. *Structural Engineer, 84*(21), 27-31.

Michael. (2006). Flughafenbruecke (Airport Bridge). Retrieved July 15, 2013, from http://commons.wikimedia.org/wiki/File:Flughafenbruecke_ein_Pylon.JPG?uselang=zh-cn

MIIT. (2014). The economic status of steel industry in 2013. from http://www.miit.gov.cn/n11293472/n11293832/n11294132/n12858402/n12858492/15891265.html

Miki, C., and Kawakami, T. (2011). *Tokyo gate bridge an application of bridge high-performance steel*. Paper presented at the 6th International Symposium on Steel Structures, Seoul, Korea.

Moreadith, F. L. (1978). *Design of reinforced concrete for combined bending and tension.* Paper presented at the ACI Journal Proceedings.

Morita, K., Keii, M., and Matsumoto, S. (2011). *Applications of high performance structural steels to high-rise steel buildings*. Paper presented at the 6th International Symposium on Steel Structures, Seoul, Korea.

Može, P., and Beg, D. (2010). High strength steel tension splices with one or two bolts. *Journal of Constructional Steel Research, 66*(8-9), 1000-1010.

Može, P., and Beg, D. (2011). Investigation of high strength steel connections with several bolts in double shear. *Journal of Constructional Steel Research, 67*(3), 333-347.

Može, P., Beg, D., and Lopatič, J. (2007). Net cross-section design resistance and local ductility of elements made of high strength steel. *Journal of Constructional Steel Research, 63*(11), 1431-1441.

Muntean, N., Stratan, A., and Dubina, D. (2009). *Strength and ductility performance of welded connections between high strength and mild carbon steel components - experimental evaluation*. Paper presented at the Proceedings of the 11th WSEAS International Conference on Sustainability in Science Engineering.

Neuenhofer, A., and Filippou, F. C. (1998). Geometrically nonlinear flexibility-based frame finite element. *Journal of Structural Engineering, 124*(6), 704-711.

Niceno, B. (2002). EasyMesh: A two-dimensional quality mesh generator, version 1.4. *Trieste University, Italy*.

Nishino, F., and Tall, L. (1970). Experimental investigation of the strength of T-1 steel columns: Fritz Engineering Laboratory, Department of Civil Engineering Lehigh University.

of plates with residual stresses. *ASTM special technical publication*(419), 12-30.

Nishino, F., Ueda, Y., and Tall, L. (1967). Experimental investigation of the buckling of plates with residual stresses. In e. Materials ASfTa (Ed.), *Test Methods for Compression Members* (pp. 12-30). Philadelphia, PA: ASTM special technical publication.

Nukala, P. K. V. V., and White, D. W. (2004). A mixed finite element for three-dimensional nonlinear analysis of steel frames. *Computer Methods in Applied Mechanics and Engineering, 193*(23–26), 2507-2545.

Odar, E., and Nishino, F. (1965). Residual stresses in welded built-up T-1 shapes: Fritz Engineering Laboratory, Department of Civil Engineering, Lehigh University.

Olden, V., Zhang, Z. L., Østby, E., Nyhus, B., and Thaulow, C. (2002). *Notch tensile testing of high strength steel weldments*. Paper presented at the 2nd International Symposium on High Strength Steel, Verdal, Norway.

Ons. (2006). JR East main office. Retrieved July 14, 2013, from http://commons.wikimedia.org/wiki/File:JR_East_main_office.jpg

Oran, C. (1973a). Tangent stiffness in plane frames. *Journal of the Structural Division, 99*(6), 973-985.

Oran, C. (1973b). Tangent stiffness in space frames. *Journal of the Structural Division, 99*(6), 987-1001.

Ozturk, F., Toros, S., and Kilic, S. (2009). Tensile and spring-back behavior of DP600 advanced high strength steel at warm temperatures. *Journal of Iron and Steel Research, International, 16*(6), 41-46.

Papanikolaou, V. K. (2012). Analysis of arbitrary composite sections in biaxial bending and axial load. *Computers & Structures, 98*, 33-54.

Peter. (2011). Beijing national stadium. Retrieved July 14, 2013, from http://en.wikipedia.org/wiki/File:Beijing_national_stadium.jpg

Pi, Y. L., Bradford, M. A., and Uy, B. (2006a). Second order nonlinear inelastic analysis of composite steel–concrete members. I: Theory. *Journal of structural engineering, 132*(5), 751-761.

Pi, Y. L., Bradford, M. A., and Uy, B. (2006b). Second order nonlinear inelastic analysis of composite steel–concrete members. II: Applications. *Journal of Structural Engineering, 132*(5), 762-771.

Pi, Y. L., and Trahair, N. (1994a). Nonlinear inelastic analysis of steel beam-columns. I: Theory. *Journal of Structural Engineering, 120*(7), 2041-2061.

Pi, Y. L., and Trahair, N. (1994b). Nonlinear inelastic analysis of steel beam-columns. II: Applications. *Journal of Structural Engineering, 120*(7), 2062-2085.

Proffer, D. (2008). New CCTV building in Beijing. Retrieved July 14, 2013, from http://commons.wikimedia.org/wiki/File:New_CCTV_building_in_Beijing_(3020040244).jpg

Puthli, R., and Fleischer, O. (2001). Investigations on bolted connections for high strength steel members. *Journal of constructional steel research, 57*(3), 313-326.

Qiang, X., Bijlaard, F. S. K., and Kolstein, H. (2013). Post-fire performance of very high strength steel S960. *Journal of Constructional Steel Research, 80*(0), 235-242.

Qiang, X. H., Bijlaard, F. S. K., and Kolstein, H. (2012a). Dependence of mechanical properties of high strength steel S690 on elevated temperatures. *Construction and Building Materials, 30*, 73-79.

Qiang, X. H., Bijlaard, F. S. K., and Kolstein, H. (2012b). Post-fire mechanical properties of high strength structural steels S460 and S690. *Engineering Structures, 35*, 1-10.

Ramm, E. (1981). *Strategies for tracing the nonlinear response near limit points*: Springer.

Randwicked. (2005). Latitude Sydney. Retrieved July 14, 2013, from http://en.wikipedia.org/wiki/File:Latitude_Sydney.jpg

Raoul, J., and Günther, H.-P. (2005). *Use and application of high-performance steels for steel structures* (Vol. 8): Iabse.

Rasmussen, K. J. R., and Hancock, G. J. (1992). Plate slebderness limits for high strength steel sections. *Journal of Constructional Steel Research, 23*, 73-96.

Rasmussen, K. J. R., and Hancock, G. J. (1995). Tests of high strength steel columns. *Journal of Constructional Steel Research, 34*(1), 27-52.

Rex, C. O., and Easterling, W. S. (2003). Behavior and modeling of a bolt bearing on a single plate. *Journal of Structural Engineering, 129*(6), 792-800.

Ricles, J. M., Sause, R., and Green, P. S. (1998). High-strength steel: implications of material and geometric characteristics on inelastic flexural behavior. *Engineering structures, 20*(4), 323-335.

Riks, E. (1979). An incremental approach to the solution of snapping and buckling problems. *International Journal of Solids and Structures, 15*(7), 529-551.

Rodriguez, J., and Aristizabal-Ochoa, J. D. (1999). Biaxial interaction diagrams for short RC columns of any cross section. *Journal of Structural Engineering, 125*(6), 672-683.

Saberwyn. (2011). The star casino front. Retrieved July 14, 2013, from http://commons.wikimedia.org/wiki/File:The_Star_Casino_front.jpg

Santathadaporn, S., and Chen, W. F. (1968). Interaction curves for sections under combined biaxial bending and axial force: Fritz Engineering Laboratory, Department of Civil Engineering, Lehigh University.

Sause, R., Abbas, H., Kim, B.-G., and Driver, R. (2001). *Innovative high performance steel bridge girders.* Paper presented at the Proceedings of 2001 Structures Congress, ASCE, Reston, Va.

Sause, R., and Fahnestock, L. A. (2001). Strength and ductility of HPS-100W I-girders in negative flexure. *Journal of Bridge Engineering, 6*(5), 316-323.

Sfakianakis, M. G. (2002). Biaxial bending with axial force of reinforced, composite and repaired concrete sections of arbitrary shape by fiber model and computer graphics. *Advances in Engineering Software, 33*(4), 227-242.

SG. (2009). The first transmission line made of high-strength steel towers successfully energized in Henan province. from http://www.sgcc.com.cn/xwzx/gsxw/2009/12/214167.shtml

Shi, G., Ban, H. Y., and Bijlaard, F. S. K. (2012a). Tests and numerical study of ultra-high strength steel columns with end restraints. *Journal of Constructional Steel Research, 70*, 236-247.

Shi, G*., et al.* (2012b). Experimental study on hysteretic behavior of high strength steel box-section columns. *Journal of Building Structures, 33*(3), 1-7.

Shi, G*., et al.* (2012c). Experimental and modeling study of high-strength structural steel under cyclic loading. *Engineering Structures, 37*, 1-13.

Shi, G., and Bijlaard, F. (2007). *Finite element analysis on the buckling behaviour of high strength steel columns.* Paper presented at the Proceedings of the Fifth International Conference on Advances in Steel Structures, Singapore.

Shi, G., Shi, Y. J., and Wang, Y. Q. (2008). Engineering application of ultra-high strength steel structures. *Progress in Steel Building Structures, 10*(4), 32-38.

Shi, G., Zhou, W., Bai, Y., and Lin, C. (2014). Local buckling of 460MPa high strength steel welded section stub columns under axial compression. *Journal of Constructional Steel Research, 100*, 60-70.

Sivakumaran, K. S., and Yuan, B. (1998). Slenderness limits and ductility of high strength steel sections. *J. Construct. Steel Res., 46*(1-3), 149-151.

So, A. K. W., and Chan, S. L. (1991). Buckling and geometrically nonlinear analysis of frames using one element/member. *Journal of Constructional Steel Research, 20*(4), 271-289.

Spacone, E., Ciampi, V., and Filippou, F. (1996). Mixed formulation of nonlinear beam finite element. *Computers & Structures, 58*(1), 71-83.

Sun, F. F*., et al.* (2013). Experimental study on material properties of Q460 high strength steel under monotonic and cyclic loading. *Journal of Building Structures, 34*(1), 30-35.

Tashiro, D. (2011). Tokyo gate bridge. Retrieved July 15, 2013, from http://commons.wikimedia.org/wiki/File:Tokyo_Gate_Bridge-3.jpg?uselang=zh-cn

Tebedge, N., Alpsten, G., and Tall, L. (1973). Residual-stress measurement by the sectioning method. *Experimental Mechanics, 13*(2), 88-96.

Teh, L. H. (2001). Cubic beam elements in practical analysis and design of steel frames. *Engineering structures, 23*(10), 1243-1255.

Teh, L. H., and Clarke, M. J. (1999). Plastic-zone analysis of 3D steel frames using beam elements. *Journal of Structural Engineering, 125*(11), 1328-1337.

Thomas, S., and Earls, C. (2003). Cross-sectional compactness and bracing requirements for HPS483W girders. *Journal of Structural Engineering, 129*(12), 1569-1583.

Toma, S., and Chen, W. F. (1992). European calibration frames for second-order inelastic analysis. *Engineering Structures, 14*(1), 7-14.

Tominaga, T., Homma, K., Takagi, M., and Tanaka, M. (2011). *Development of BHS, bridge high-performance steels, in Japan*. Paper presented at the 6th International Symposium on Steel Structures, Seoul, Korea.

Tyoron. (2006). NTV tower. Retrieved July 14, 2013, from http://commons.wikimedia.org/wiki/File:NTV_Building.JPG

Tyoron. (2008). Yokohama landmark tower. Retrieved July 14 2013, from http://commons.wikimedia.org/wiki/File:Yokohama_Landmark_Tower_2008.JPG

Usami, T., and Fukumoto, Y. (1982). Local and overall buckling of welded box columns. *Journal of the Structural Division, 108*(3), 525-542.

Usami, T., and Fukumoto, Y. (1984). Welded box compression members. *Journal of Structural Engineering, 110*(10), 2457-2470.

Veljkovic, M., and Johansson, B. (2004). Design of hybrid steel girders. *Journal of Constructional Steel Research, 60*(3-5), 535-547.

Wang, F., Shi, G., Dai, G., Shi, Y., and Wang, Y. (2010). Research advance of influence of yield-to-tensile strength ratio on seismic behavior of steel frames. *Journal of Building Structures*, (S1), 18-22.

Wang, Y. B. (2012). *Experimental and theoretical study on the ultimate strength of welded Q460 high strength steel columns.* (Doctor of Philosophy), Tongji University.

Wang, Y. B., Li, G. Q., and Chen, S. W. (2012a). The assessment of residual stresses in welded high strength steel box sections. *Journal of Constructional Steel Research, 76*, 93-99.

Wang, Y. B., Li, G. Q., and Chen, S. W. (2012b). Residual stresses in welded flame-cut high strength steel H-sections. *Journal of Constructional Steel Research, 79*, 159-165.

Wang, Y. B., Li, G. Q., Chen, S. W., and Sun, F. F. (2012c). Experimental and numerical study on the behavior of axially compressed high strength steel columns with H-section. *Engineering Structures, 43*, 149-159.

Wang, Y. B., Li, G. Q., Chen, S. W., and Sun, F. F. (2014). Experimental and numerical study on the behavior of axially compressed high strength steel box-columns. *Engineering Structures, 58*, 79-91.

Wang, Y. Q., Lin, Y., Zhang, Y. N., Shi, Y. J., and Chen, H. (2011). Experimental study on the mechanical properties of Q460C the high strength construction steel at low temperature. *Journal of Shenyang Jianzhu University (Natural Science), 27*(4), 646-652.

Wheeler, A., and Russell, B. (2005). Behaviour and design of webs in high strength steel under flexural loading. In Z. Y. Shen, G. Q. Li, S. L. Chan (Eds.), *Fourth International Conference on Advances in Steel Structures* (pp. 137-142). Oxford: Elsevier Science Ltd.

White, D. W. (1985). *Material and geometric nonlinear analysis of local planar behavior in steel frames using interactive computer graphics*: Cornell University, Aug.

Williams, J. G., Anley, R. E., Nash, D. H., and Gray, T. G. F. (2009). Analysis of externally loaded bolted joints: Analytical, computational and experimental study. *International Journal of Pressure Vessels and Piping, 86*(7), 420-427.

Wong, M. B., and Tin-Loi, F. (1990). Analysis of frames involving geometrical and material nonlinearities. *Computers & Structures, 34*(4), 641-646.

WSA. (2014). *World Steel in Figures 2014* (pp. 30).

Yan, J. B., Liew, J. Y. R., Zhang, M. H., and Wang, J. Y. (2014). Mechanical properties of normal strength mild steel and high strength steel S690 in low temperature relevant to Arctic environment. *Materials & Design, 61*, 150-159.

Yan, X. L., Li, G. Q., and Chen, S. W. (2013). Numerical analysis of the ultimate bearing capacity of welded box-section columns using Q460 high strength steel in bending and axial compression. *Progress in Steel Building Structures, 15*(3), 12-18.

Yang, T. Y., and Saigal, S. (1984). A simple element for static and dynamic response of beams with material and geometric nonlinearities. *International Journal for Numerical Methods in Engineering, 20*(5), 851-867.

Yau, C. Y., Chan, S. L., and So, A. K. W. (1993). Biaxial bending design of arbitrarily-shaped reinforced-concrete column. *ACI Structural Journal, 90*(3), 269-278.

Yen, J. Y. R. (1991). Quasi-newton method for reinforced-concrete column analysis and design. *Journal of Structural Engineering, 117*(3), 657-666.

Zhou, Z. H., and Chan, S. L. (2004). Elastoplastic and large deflection analysis of steel frames by one element per member. I: One hinge along member. *Journal of Structural Engineering, 130*(4), 538-544.

Zrilic, M., Grabulov, V., Burzic, Z., Arsic, M., and Sedmak, S. (2007). Static and impact crack properties of a high-strength steel welded joint. *International journal of pressure vessels and piping, 84*(3), 139-150.